Ph.D. thesis

Electrochemically synthesized functional polymers in macromolecular architectures and diagnostics

Nabila Yasmeen

Supervisors
Prof. Wlodzimierz Kutner, Ph.D., D.Sc. (IPC PAS, Warsaw, Poland)
Dr. hab. Piyush Sindhu Sharma, Ph.D. (IPC PAS, Warsaw, Poland)
Dr. Mathieu Etienne, Ph.D. (CNRS, LCPME, Nancy, France)

To

Rahmatul lil Alameen

(Mercy for all the worlds)

and

my Lovely Parents,

Mr. Malik Khuda Bakhsh (late) & Mrs. Gul Mahtab

Erratum

to the Ph.D. thesis of Nabila Yasmeen, entitled:
"Electrochemically synthesized functional polymers
in macromolecular architectures and diagnostics"

Item No.	The present text	The revised text
E1	Page 127, Figures 4a and 4b show cell viability as a function of the NPs' concentration.	Page 127, Figures 3.4-9a and 3.4-9b show cell viability as a function of the NPs' concentration.
E2	Page 50 **Figure 2-1.** Schematic representation of DLS operation principle. (Reference missing)	Page 50 **Figure 2-1.** Schematic representation of DLS operation principle. (Chaudhary, R. "Synthesis and characterization of monodispersed microgel." *Doctoral dissertation* 2011.)
E3	Page 51 **Figure 2-2.** Schematic representation of an SEM microscope. (Reference missing)	Page 51 **Figure 2-2.** Schematic representation of an SEM microscope. (https://en.wikipedia.org/wiki/File:Schema_MEB_(en).svg)

Declaration of originality

I declare that the research included within this thesis was carried out by myself or with support from others included in the acknowledgments.

I state that I have exercised care to ensure that the work is original and contains no previously published material or written by another person, except where citations have been made in the text. The content provided here does not violate any copyrights to the best of my knowledge.

I accept that the Polish Academy of Sciences has the right to use plagiarism detection software to ensure the thesis's legitimacy.

I certify that no part of my thesis has been or will be submitted for obtaining a degree or diploma by the Institute of Physical Chemistry, Polish Academy of Science, or any other educational institution.

This thesis's copyright rests with the author, and no information derived from it may be published without the author's consent.

Warsaw, April 2022   Signature

Acknowledgments

I acknowledge several key persons; I am indebted to many for their lasting contribution to completing my Ph.D. thesis.

Especially, I am deeply thankful to **Prof. Wlodzimierz Kutner** for introducing me to the molecularly imprinted polymer field, improvisation of scientific reports, and the manuscript's writing style. I would also like to thank him for teaching me the art of professional presentation of research work in weekly seminars and international conferences. Moreover., I want to thank him for his motivation, guidance, and fatherly support in all administrative and group matters.

I thank **Dr. hab. Piyush Sindhu Sharma**, primary research advisor, for research training and support in learning many new scientific techniques and completing different research projects. Moreover, I want to thank him for his scientific advice on the best description of research data and for helping me establish scientific collaborations within and outside our institute.

I give special thanks to my secondment supervisor, **Dr. Mathieu Etienne**, for helping me complete my research work on time in Covid 19 pandemic year (2020) and for arranging urgent documentation required for my unplanned flight to my home country because of the sudden death of my father.

Moreover, I thank all members of Molecular Films Research (IPC PAS), functional polymers (IPC PAS), and LCPME teams for their kindness, help, and scientific and emotional support throughout my Ph.D. studies. Significantly, **M.Sc. Jakub Kałęcki** (IPC PAS), for helping me in many lab affairs, from finding lost electrodes to scanning electron microscopy imaging of the highest resolutions.

Besides, I express my gratitude to:
- Prof. Francis D'Souza (University of Texas, Denton TX, USA) and Dr. Marta Sosnowska (IPC PAS) for synthesizing functional monomers.
- Dr. Francius Grégory (LCPME) for providing bacteria strains.
- Dr. Xie Wang (LCPME) for basic training in bacteria culture.
- Dr. Krzysztof Noworyta (IPC PAS) and Dr. Sofiane El-Kirat-Chatel (LCPME) for AFM imaging.
- Dr. Karina Kwapiszewska and MSc Aneta Karpinska (IPC PAS) for introducing me to cell biology and performing MTT assays and confocal microscopy experiments.

1. Funding

2. List of publications

2.1 Yasmeen, N., Etienne, M., Sharma, P. S., El-Kirat-Chatel, S., Helú, M. B., and Kutner, W., "Molecularly imprinted Polymer as a synthetic receptor mimic for capacitive impedimetric selective recognition of *Escherichia coli* K-12," Anal. Chim. Acta 1188 (2021) 339177.

2.2 Yasmeen, N., Kalecki, J., Borowicz, P., Kutner, W., and Sharma, P. S., "Electrochemically controlled synthesizing of polyacrylic microgel particles as well as microgel shell grafting over inorganic cores," ACS Applied Polymer Materials, 4 (2022) 452-462.

2.3 Yasmeen, N., Sharma, P. S., Piechowska, J., Noworyta, K., D'Souza F., and Kutner, W., "Electropolymerized molecularly imprinted polymer for chemosensing of a gamma-aminobutyric acid autism biomarker," (2022) submitted.

2.4 Yasmeen N., Karpinska A., Kalecki J., Kutner W., Kwapiszewska K., Sharma P. S, "Electrochemically synthesized polyacrylamide gel and core-shell nanoparticles for 3D cell culture formation," (2022) submitted.

3. Active participation in scientific conferences

3.1   **Yasmeen, N.**, Sharma, P .S., Etienne, M., D'Souza, F., Kutner, W., "Electropolymerized molecularly imprinted polymer towards chemosensing of an autism biomarker" presented as a short oral communication at the 9th International Workshop on Surface Modification for Chemical and Biochemical Sensing, SMCBS'2019, Żelechów (near Warsaw), Poland, 8-12 November 2019, Abstract No. SC17, Programme, and Book of Abstracts, p. 156, Warsaw, 2019, ISBN: 978-83-939295-2-8.

3.2   **Yasmeen, N.,** Sharma, P. S., Noworyta, K., Kalecki, J, Kutner, W, "Electrochemical polymerization of microgels with and without core-shell support," oral communication at the ACS Fall 2020 Virtual Meeting & Expo, 17 - 20 August 2020.

3.3   **Yasmeen, N.**, Karpinska, A., Kalecki, J., Kutner, W., Kwapiszewska, K., Sharma, P. S., Electrochemically synthesized polyacrylamide gel and core-shell nanoparticles for 3D cell culture formation, poster presented at the IPC-PAS Micro Symposium, Warsaw, Poland, 25-26 January 2022.

4. Research visits and training online

4.1 A one-week course, 'Training Course and Seminar on Broadband Dielectric and Impedance Spectroscopy and Its Applications,' 17th - 21st March 2019, Montabaur, Germany.

4.2 Visiting Research Scholar, Laboratoire de Chimie Physique et Microbiologie pour l'Environnement (LCPME), for the research project,' Electrochemical chemosensors for the *Escherichia coli* K-12 determining with molecularly imprinted polymer recognition units,' Dec 2019 - Dec 2020, CNRS, Nancy, France.

4.3 A one-month training course, 'Introduction to Molecular Modelling Concepts for Polymers: a Schrödinger Online,' 21st April - 26th May 2021.

5. List of abbreviations

AA – acrylamide
ABDV – 2,2'-azobis(2,4-dimethylvaleronitrile)
ACN – acetonitrile
AFM – atomic force microscopy
Ag43 – antigen 43 protein
2-APBA – 2-aminophenylboronic acid
ANI – aniline
AIBN – azobisisobutyronitrile
APS – ammonium persulfate

BIS – *N,N´*- methylenebisacrylamide.
B3LYP – Becky-Lee-Yang-Parr's three-parameter
BET – Brunauer-Emmett-Teller theory

CE – counter electrode
CI – capacitive impedimetry
CP – conducting polymer
CV – cyclic voltammetry

3D – three-dimensional
2D – two-dimensional
DCM – dichloromethane
DFT – density functional theory
DTGA –differential thermogravimetric analysis
DMF – *N,N'*-dimethylformamide
DMSO – dimethyl sulfoxide
DPV – differential pulse voltammetry
DLS – dynamic light scattering

E. coli K-12 – *Escherichia coli* K-12
EIS – electrochemical impedance spectroscopy
ECM – extracellular matrix
EDOT – 3,4-ethylenedioxythiophene
ELISA – enzyme-linked immunological assay
EPR – electron paramagnetic resonance
EPS – extracellular polymeric substance

FM – functional monomer
FM1– *p*-bis(2,2'-bithien-5-yl)methyl-*o*-catechol
FM2 – *p*-bis(2,2'-bithien-5-yl)methylbenzoic acid
FM3 – *p*-bis(2,2'-bithien-5-yl)methylaniline acetate
FM4 – *p*-bis(2,2'-bithien-5-yl)methyl phenol 2-hydroxy acetamide ether
FM5 – *p*-bis(2,2'-bithien-5-yl)methyl aniline
FTIR – Fourier-transform infrared spectroscopy
FIA – flow injection analysis

GABA – gamma-aminobutyric acid
GCE – glassy carbon electrode

GC-MS – gas chromatography-mass spectrometry

HeLa – cervical cancer cell lines
HPLC – high-performance liquid chromatography
HSA – human serum albumin

IC_{50} – half-maximal inhibitory concentration
IDE – interdigitated electrode
ITIES - interface between two immiscible electrolyte solution
IF – imprinting factor
IR – infrared spectroscopy
IUPAC – International Union of Pure and Applied Chemistry

LCST – lower critical solution temperature
LOD – limit of detection
LOQ – limit of quantification
LPS – lipopolysaccharide
LSV – linear sweep voltammetry
LUMO – lowest unoccupied molecular orbital

MAA – methacrylic acid
MDA-MB-231 – triple-negative breast cancer cell line
MIP– molecularly imprinted polymer
MNP – magnetic nanoparticle
MR-1 (SWMR-1) – *Shewanella oneidensis*
MS – mass spectrometry
MWCNT – multi-walled carbon nanotube
MTT – 3-(4,5-dimethylthiazol-2-yl)-2,5-diphenyl-2*H*-tetrazolium bromide

NP – nanoparticle
NIP – non-imprinted polymer
NIPAM – *N*-isopropyl acrylamide
NMR – nuclear magnetic resonance (spectroscopy)

OS – oligosaccharides

PANI – polyaniline
PCR – polymerase chain reaction PCR
PEDOT – poly(3,4-ethylenedioxythiophene)
PenG – penicillin G
PM-IRRAS – polarization-modulation infrared reflection-absorption spectroscopy
PNIAM – poly-*N*-isopropyl acrylamide
POC – point-of-care

RAFT – reversible addition-fragmentation chain transfer
RE – reference electrode
RGD – arginine-glycine-aspartic acid
SEM – scanning electron microscopy
STEM – scanning transmission electron microscopy
SPE – solid-phase extraction

SPR – surface plasmon resonance
SWV – square wave voltammetry

(TBA)ClO$_4$ – tetra-*n*-butylammonium perchlorate
TGA – thermogravimetric analysis

UV-vis – ultraviolet-visible (spectroscopy)

WE – working electrode

XPS – X-ray photoelectron spectroscopy

7. List of symbols

A – active electrode surface area, cm^2

C_{dl} – electrical double-layer capacitance, μF
c – concentration, M
$CPE1$ – constant phase element (paralleled with R_{ct1})
$CPE2$ – constant phase element (paralleled with R_{ct2})

D – diffusion coefficient, $cm^2\ s^{-1}$

ΔE_p – pulse amplitude
E – potential, V vs. reference electrode
E_f – final potential, V vs. reference electrode
E_i – initial potential, V vs. reference electrode
E_{pa} – anodic peak potential, V vs. reference electrode
E_{pc} – cathodic peak potential, V vs. reference electrode
E_t – potential at the time, t

F – Faraday constant, $96\ 500\ C\ mol^{-1}$
f – frequency, Hz

ΔG – Gibbs free energy change, $kJ\ mol^{-1}$

h – Planck constant, $6.63 \times 10^{-34}\ J\ Hz^{-1}$

I_p – peak current
I_{pa} – anodic peak current, A
I_{pc} – cathodic peak current, A
n – number of electrons exchanged in the elementary electrode reaction
α – selectivity

λ – wavelength, nm

ϕ – phase angle, degree

q – charge, C

ω - angular frequency, $rad\ s^{-1}$

R – molar gas constant, $8.31\ J\ mol^{-1}K^{-1}$
R_{ct} – charge-transfer resistance, Ω

S/N – signal-to-noise ratio

T – absolute temperature, K
t – time, s
t_{max} - maximum time of alternating waveform (in EIS), s

V – voltage, V

v – potential scan rate, mV s^{-1}

W – Warburg impedance, Ω

Z – impedance, Ω
Z_{real} – real component of impedance, Ω
Z_{img} – imaginary component of impedance, Ω

Abstract (Eng.)

The present Ph.D. thesis describes fundamental research on molecular imprinting, which was oriented towards devising, fabricating, and testing electrochemical sensors for sensitive and selective determination of gamma-aminobutyric acid (GABA), a biomarker of autism spectrum disorder, and *Escherichia coli* K-12 bacterium. Moreover, procedures were developed to synthesize biocompatible polyacrylamide gel and (inorganic core)-(gel shell) particles in aqueous systems.

An MIP film was deposited on a Pt disk electrode and an Au interdigitated electrode (IDE) array to engineer a chemosensor for GABA biomarker detection and selective determination. The *bis*-bithiophene derivatized functional monomers were chosen to devise an MIP for GABA. The stability of the pre-polymerization complexes of the GABA template with *bis*-bithiophene derivatized functional monomers was estimated with the density functional theory (DFT) at the B3LYP level. Different electrochemical transductions, including differential pulse voltammetry (DPV), capacitive impedimetry (CI), and electrochemical impedance spectroscopy (EIS), were tested to evaluate the MIP chemosensor performance. XPS measurements confirmed the GABA template complete extraction from the MIP film. The morphology of the MIP film deposited on IDEs was unraveled and characterized by AFM. For DPV, CI, and EIS electrochemical transductions, the sensitivity, selectivity, and limit of detection (LOD) of the MIP chemosensors were calculated. Furthermore, GABA in artificial serum samples was determined to confirm the chemosensor suitability for clinical analysis. The EIS transduction appeared most suitable for potential point-of-care GABA determinations.

A modified Gram-negative strain of *Escherichia coli* K-12, i.e., E2152, was determined using the herein devised CI based MIP chemosensor. The extracellular matrix (ECM) of E2152 strongly interacted with a boronic acid group because of the porous and flexible polymers of the cell wall. The scanning electron microscopy (SEM) and atomic force microscopy (AFM) imaging confirmed E2152 template entrapment in the MIP and then the effectiveness of the template extraction. Moreover, the X-ray photoelectron spectroscopy (XPS) measurements, as well as DPV and EIS transductions, confirmed the E2152 template extraction. The E2152 analyte binding was then demonstrated using CI. The interference study, performed using *E. coli* variants expressing different surface appendages (type 1 *fimbriae* or Antigen 43 protein) or *Shewanella oneidensis* MR-1, another Gram-negative bacterium, demonstrated that the bacterial surface composition notably impacts sensing properties of the E2152-templated MIP chemosensor.

A one-step electrochemically initiated gelation was used to synthesize biocompatible polyacrylamide gel microparticles and core-shell nanoparticles. In this gelation, electrochemical decomposition of ammonium persulphate initiated copolymerization of the *N*-isopropylacrylamide, methacrylic acid, and *N,N'*-methylenebisacrylamide monomers under hydrodynamic conditions. SEM and TEM imaging confirmed the fabrication of gel particles. The particles were thoroughly characterized with NMR spectroscopy, TGA, BET, and DLS measurements. They were explored to prepare 3D cell-like structures.

The lyophilized polyacrylamide gel microparticles and core-shell nanoparticles were applied to form a 3D culture of MDA-MB-231 and HeLa cells using gel embedment. The nanoparticles' biocompatibility and IC_{50} values were confirmed using MTT assays. The confocal microscopy showed that core-shell nanoparticles provided superior support for complex 3D tissue structures.

Abstract (Pol.)

W niniejszej rozprawie doktorskiej przedstawione są podstawowe badania wdrukowania molekularnego, ukierunkowane na praktykę, obejmujące opracowanie, wytworzenie i sprawdzenie nowych czujników elektrochemicznych do czułego i selektywnego oznaczania kwasu gamma-aminobutanowego (GABA), biomarkera zaburzeń ze spektrum autyzmu, i bakterii *Escherichia coli* K-12. Jako elementy rozpoznające tych czujników zostały zaprojektowane, zsyntetyzowane i zastosowane polimery wdrukowane molekularnie (MIP-y). Ponadto opracowano syntezy biozgodnego żelu poliakrylamidowego i drobin typu (nieorganiczny rdzeń)-(żelowa powłoka) w układach wodnych.

Aby skonstruować chemosensor do wykrywania i selektywnego oznaczania GABA, warstwy MIP-ów osadzono na platynowej elektrodzie dyskowej i złotych elektrodach naprzemiennego układu elektrodowego (IDE). Do opracowania MIP-u rozpoznającego GABA wybrano sfunkcjonalizowane monomery *bis*-bitiofenowe. Za pomocą teorii funkcjonału gęstości (DFT) w przybliżeniu B3LYP oszacowano trwałość kompleksów pre-polimeryzacyjnych szablonu GABA z monomerami funkcyjnymi. W celu oceny działania chemosensora MIP sprawdzono różne sposoby elektrochemicznego przetwarzania sygnału rozpoznawania na sygnał analityczny, w tym różnicową woltamperometrię pulsową (DPV), impedymetrię pojemnościową (CI) i elektrochemiczną spektroskopię impedancyjną (EIS). Pomiary XPS potwierdziły całkowitą ekstrakcję szablonu GABA z warstwy MIP-u. Za pomocą mikroskopii sił atomowych (AFM) scharakteryzowano morfologię warstwy MIP-u osadzonej na IDE. Dla chemosensorów MIP, w których sygnał był przetwarzany za pomocą DPV, CI i EIS wyznaczono czułość, selektywność i granicę wykrywalności (LOD) pomiarów. Aby potwierdzić przydatność chemosensora w analizie klinicznej, GABA oznaczono w próbkach sztucznej surowicy. Przetwarzanie EIS okazało się najbardziej odpowiednie do potencjalnych oznaczeń GABA przy łóżku pacjenta.

Opracowany chemosensor MIP z przetwarzaniem sygnału za pomocą CI zastosowano do oznaczania zmodyfikowanego Gram-ujemnego szczepu E2152 bakterii *Escherichia coli* K-12. Matryca zewnątrzkomórkowa (ECM) tego szczepu silnie oddziaływała z resztą kwasu boronowego monomeru funkcyjnego z uwagi na porowaty i elastyczny charakter cienkich warstw peptydoglikanów i celulozy w strukturze błony komórkowej E2152. Skaningowa mikroskopia elektronowa (SEM) i mikroskopia sił atomowych (AFM) potwierdziły unieruchomienie szczepu E2152 w MIP-ie, a następnie skuteczną ekstrakcję tego szczepu z MIP-u. Co więcej, pomiary rentgenowskiej spektroskopii fotoelektronów (XPS) oraz przetwarzania sygnału za pomocą DPV i EIS potwierdziły ekstrakcję E2152 z MIP-u. Następnie, za pomocą CI, wykazano oddziaływanie analitu E2152 z MIP-em. Badania zakłóceń oznaczania E2152 przez odmiany *E. coli* z różnymi cechami powierzchniowymi (*fimbrii* typu 1 lub białka Antygenu 43) lub *Shewanella oneidensis* MR-1, innych bakterii Gram-ujemnych wykazały, że skład powierzchni bakterii w sposób znaczący wpływa na właściwości wykrywania za pomocą chemosensora warstwą MIP-u wdrukowaną szczepem E2152.

Syntezy biozgodnych mikrodrobin żelu poliakrylamidowego i nanocząstek typu rdzeń-powłoka przeprowadzono z zastosowaniem elektrochemicznie inicjowanego żelowania jednoetapowego. W żelowaniu tym elektrochemiczny rozkład nadsiarczanu amonu inicjował kopolimeryzację monomerów *N*-izopropyloakryloamidu, kwasu metakrylowego i *N*,*N′*-metylenobisakryloamidu w warunkach hydrodynamicznych. Obrazowanie SEM i TEM potwierdziło tworzenie drobin żelu. Drobiny te scharakteryzowano za pomocą spektroskopii NMR, pomiarów TGA, BET i DLS, aby ocenić ich przydatność do przygotowania struktur przypominających komórki 3D.

Liofilizowane mikrodrobiny żelu i nanodrobiny typu rdzeń-powłoka zastosowano do trójwymiarowego hodowania komórek HeLa i MDA-MB-231 za pomocą metody osadzenia w żelu. Biozgodność drobin i wartości IC_{50} potwierdzono za pomocą testów MTT. Pomiary mikroskopii konfokalnej wykazały, że nanodrobiny typu rdzeń-powłoka znakomicie sprawdziły się jako podłoże złożonych trójwymiarowych struktur tkankowych.

Table of contents

1. Introduction

Functional polymers are macromolecules often determined by reactive functional chain-end, in-chain, block, star or hyper branched groups, or graft structures. Integrating intermolecular interactions can lead to supramolecular structures.[1, 2] Forces integrating into supramolecular self-assemblies is ideal for preparing functional polymer materials.[3] The macroscopic properties and microscopic computational modeling of functional polymers are essential tools to engineer optimum structures of these materials playing a decisive role in fabricating novel devices.[5] Therefore, the performance of functional polymers can reasonably be achieved if the processing aspect is taken into account at the synthesis level.[4] Thus, constructing a novel polymer architecture of desired properties is one of the essential thrusts of modern polymer science.[4]

Functional polymers are promising for materials science because they often incur electric conductivity, photosensitivity, and catalytic, biological, and pharmacological activity.[5] Moreover, they are highly responsive to external physical, chemical, and biological stimuli, such as changes in electric/magnetic fields,[6] temperature,[7] pH,[8, 9] and enzymatic activity.[10] Therefore, functional polymers are extensively used for therapeutic and sensing applications.[11]

The supramolecular self-assembly resulting in synthetic functional polymers is widely exploited in molecular imprinting.[12] That involves the pre-polymerization complex formation of a template with functional monomers via covalent binding or noncovalent interactions in the solution. These interactions result in the functional monomer molecules' pre-organization using its recognizing sites around the template molecule offering binding sites.[13] After polymerization, removing template molecules from the resulting polymer generates molecular cavities featuring recognizing sites capable of interacting with the target analyte molecule via its binding sites.[14] Because of this simplicity of biomimetic synthesis strategy, molecular imprinting became an exciting research area in many fields, including chromatographic separation, catalysis, organic synthesis, chemosensing, and diagnostics.[13-20]

Another significant research area of functional polymers usage is polymer gel matrices.[21] Polymer gels combine typical characteristics of macromolecules and colloidal gel particles. Moreover, polymer hybrid gels offer multi-functionality being excessively used in biotechnology and biomedicine.[22,23, 24] However, polymer preparation is critical for a wide range of applications, such as optoelectronic instrument devising,[25] drug delivery,[26,

[27] tissue engineering,[28, 29] thin-film coating,[30] selective sensing,[31] and diagnosing.[32] Recently, synthetic polymers in the form of scaffolds and gels are employed as an excellent alternative to the natural extracellular matrix (ECM) and Matrigel microenvironments for 3D cell culture.[29, 33]

Consequently, functional polymer materials have become an essential cornerstone of advanced technology. In the present work, we focussed on two major issues, i.e., the supramolecular responsive, functional polymers in use as imprinting matrices and as synthetic base membranes to provide a microenvironment for three-dimensional (3D) cell culture formation.

1.1 Molecularly imprinted polymers (MIPs)

In 1987, the Nobel Prize laureates Donald J. Cram, Jean-Marie Lehn, and Charles J. Pedersen introduced the idea of supramolecular self-assembly application for dedicated molecular recognitions. To date, this powerful biomimetic strategy has increasingly been applied for various biotechnological and bioanalytical purposes.[34-36] The concept of molecular recognition is governed by biological processes of transformation and translocations. The molecular recognition simplicity enables regenerating artificial biomimetic receptors as substitutes for natural biomolecules or bioreceptors.

In this respect, molecular imprinting, which leads to molecularly imprinted polymers (MIPs), is one of the simple biomimetic strategies. The concept of molecular imprinting is usually related to Fischer's lock and key model. Wulff et al.[37] and Mosbach et al.[38] proposed this imprinting idea.

In molecular imprinting, the template molecule is entrapped within the polymer due to chemical and physical interactions with the polymer recognizing sites, including heteroatoms, π-conjugated system, etc., and functional groups. These sites originate from the functional monomers used to form a stable pre-polymerization complex. Generally, interactions of the template with functional monomers leading to molecular imprinting are classified as covalent, semi-covalent, metal-ion exchange, and non-covalent molecular interactions.[13, 39-41]

Wulff et al. first proposed the covalent template-monomer binding.[37] In this binding, well-defined homogenous recognizing sites are formed to bind target molecules via their binding sites. However, only a few functional monomers, including boronic acid derivatives, form covalent bonds with template molecules reversibly.[42] Moreover, harsh

template removal conditions and slow binding kinetics during the imprinting often make covalent imprinting difficult.[43]

Fujii et al.[44] first proposed metal-ion exchange imprinting. Here, coordinative bonds are formed between metals and functional monomers, facilitating the interaction with the template molecule. In this imprinting, a stable pre-polymerization complex is formed by varying the metals' oxidation state and the functional monomers' characteristics. The strategy has strong imprinting potential but is limited to only functional groups capable of metal complex formation.

Mosbach et al.[45] introduced the non-covalent binding that predominantly involves charge-dipole, cation-π, dipole-dipole, electrostatic, π-stacking, hydrogen bonding, hydrophobic, and van der Waals molecular interactions. Here, the proper porogen solvent selection along with the excessive use of monomers are vital requirements. Mainly, monounsaturated functional monomers, including acrylic and vinyl, are used with excessive cross-linking monomers. The main advantages of this strategy include favorable binding kinetics and easy and rapid template removal under mild conditions. However, this strategy's drawbacks embrace the heterogeneous distribution of functional monomers, a high excess of cross-linking monomers, and the reversibility of the formation of the pre-polymerization complex.[46]

In the 1990s., Sellergen et al.[47] proposed semi-covalent imprinting to overcome the above deficiencies. The template complex with the functional monomer is first formed through covalent bonds in this imprinting. Then, after template extraction associated with those covalent bonds cleaving, the target molecule binding to the cavity is governed by noncovalent interactions. Still, a steric hindrance between the template and the monomers may arise in this imprinting.

Template attachment to the functional monomer through a sacrificial spacer overcomes this difficulty. This spacer, such as carbamate or carbonate ester, can readily be removed during template extraction.[48, 49] The mixed semi-covalent strategy provides highly precise cavities and strong template binding by these cavities that are only affected by template diffusion without any kinetic hindrance. Scheme 1-1 illustrates different stepwise MIPs formation strategies.
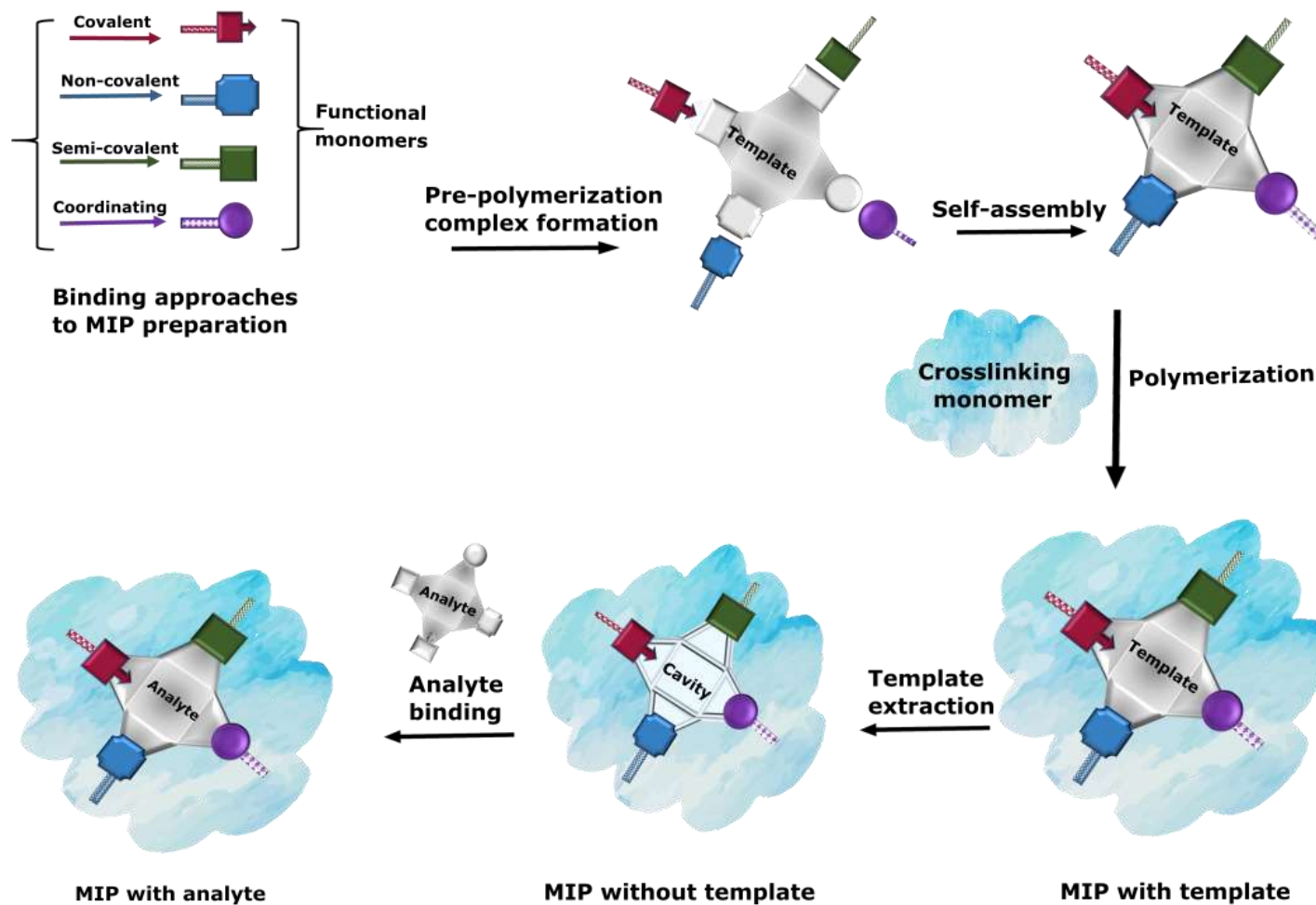
Scheme 1-1. An illustration of different strategies of molecularly imprinted polymer (MIP) syntheses.

1.1.1 MIPs' preparation strategies

MIPs have gained considerable attention because of their high stability, sensitivity, selectivity, unique recognition abilities, and ease of preparation.[50] Many polymerization strategies were developed for MIPs syntheses. Interestingly, the strategy choice is decisive for preparing MIPs of desired properties. For instance, one can generate a rigid MIP block with limited or no accessibility of low binding performance imprinted cavities. Various methods are proposed for preparing different MIP structures, including thin films, beads, nanoparticles (NPs), core-shell particles, and self-assembled monolayers. Precipitation polymerization,[51] surface imprinting,[52] sol-gel condensation,[53] photopolymerizations,[54] self-assembly,[55] and electropolymerization[50] can be used to prepare these structures.

Precipitation polymerization is the universal method well-suited for preparing efficient MIP beads and NPs.[51] In this method, MIPs with desirable features are synthesized with reasonable control over polymerization conditions. This method leads to MIP beads and NPs with a high surface-to-volume ratio of uniformly distributed imprinted cavities. Subsequent template removal from the resulting MIP is relatively easy. However, the deficiency includes a relatively large solvent consumption, low yield, and low control of the polymerization rate.[56, 57]

Traditional bulk polymerization is a quick synthetic method.[58, 59] This method is most common because of its simplicity and the possibility of using a wide range of solvents and temperatures. After grinding, then sieving, the prepared MIP particles are primarily applied as a stationary phase in chromatography and solid-phase extraction (SPE). However, this method is time-consuming and laborious.[59] Moreover, the prepared MIPs deficiencies included irregular shape, a wide range of particles' size, limited production efficiency, and non-uniform imprinted cavities distribution.[59]

A one-step sol-gel MIP preparation is a relatively more straightforward, quite conventional method. In this method, material heterogeneity, thermal stability, intrinsic conversion efficiency, and high solvent stability are attained.[60] Moreover, mild synthesis conditions, ease of preparation, and significantly high selectivity of the prepared MIP films make this method attractive.[61]

Another polymerization method, the reversible addition-fragmentation chain transfer (RAFT)[62] polymerization method, initiated by free radicals, is promising for preparing MIPs. Its advantages consist of rapid and straightforward MIP preparation.[63] It serves as

an alternative to the pre-existing conventional methods. The imprinting efficiency of MIPs synthesized by RAFT polymerization is significantly higher than those prepared by traditional polymerization.[64] Moreover, this method affords excellent recognition ability and sufficiently high-affinity recognizing sites.[65]

Notably, the highly selective MIPs with large molecular cavities of high sorption capacity are primarily prepared using surface imprinting.[66, 67] In this imprinting, the imprinted cavities are mainly distributed outside the MIP film. Thus, a large surface area increases the analyte sorption capacity by increasing the density of imprinted cavities. Moreover, it circumvents the shortcomings of traditional/conventional methods, i.e., incomplete template removal, as well as slow binding kinetics and low mass transfer rates.[68, 69] However, the ultrathin film stability and the thickness control are the most typical difficulties in this method.

Photopolymerization is another method of preparing MIP thin films of controlled thickness at a nanoscale level, with few limitations. These include insufficient control over the polymer chain lengths and the size of MIP NPs formed.[54] In principle, this light-sensitive approach involves photon absorption leading to reactive species that initiate the polymerization of monomers.[70] However, the possibility of template degradation is one limitation of using this approach, overcome by formulating the photoinitiator in low molar amounts.[71] Moreover, a low-temperature requirement for stable MIPs synthesis is met by initiating the polymerization photochemically in the presence of an immobilized template.[72] This method involves a multi-step polymerization that requires subsequent proper purification and fractionation of the fabricated MIP particles. The immobilized template can be used several times, which is particularly advantageous if the template is expensive.[72]

Lastly, the most straightforward and facile method for preparing MIPs is electropolymerization.[73, 74] Either a direct or indirect electropolymerization method is used. Thin MIP films are deposited on conducting or semiconducting substrates directly.[73] In the indirect method, MIP NPs are first synthesized using alternative approaches, e.g., precipitation polymerization or solid-phase synthesis. Then, a conductive substrate is coated with these MIP NPs to fabricate the chemosensor ultimately.[72, 75, 76] Because of the preparation ease and high detectability, sensitivity, and selectivity, MIPs prepared by electropolymerization are most extensively used for sensing purposes.[74, 77]

1.1.2 Electrochemical MIPs synthesizing

MIPs, as surrogates of bio-recognition probes in electrochemical chemosensors, offer some analytical parameters superior to other surrogates.[78, 79] In recent years, electrochemical MIPs MIP chemosensors have developed considerably. Direct electrosynthesis[50, 73, 74] and immobilization of the pre-prepared MIP NPs[75, 76, 80] in polymer films were applied to fabricate electrochemical chemosensors. This MIP-electrode integration, stable during measurements, is essential for the efficient recognition event transducing into a sound analytical signal. For that purpose, MIP NPs were prepared via precipitation polymerization, then immobilized on the transducer, offering a high surface-to-volume ratio with improved binding kinetics.[43, 81-83] Moreover, MIP films are prepared by simultaneous electropolymerization and deposition directly on the electrode surface by applying electropolymerizable functional and cross-linking monomers. Electropolymerization is a one-step procedure allowing firm film adherence to the transducer surface.[73, 74, 84]

Because of the above strategy's simplicity, different nanomaterials are easily incorporated into the MIP film.[85] Moreover, MIP film thickness can readily be tuned by controlling the charge passed.[86] For that, components' concentrations and electropolymerization conditions can adequately be adjusted.

Template removal from the MIP is relatively easy. For that, an external stimulus like changing the solution pH or polymer overoxidation can be used. As a result, many homogenously distributed molecular cavities with predetermined recognizing sites are generated.[86] The critical requirement is optimizing over potential oxidation windows for stable and precise MIP cavities preparation.[87] The monomers commonly used in MIPs syntheses involving electropolymerization include aniline, thiophene, 3,4-ethylenedioxythiophene (EDOT), and pyrrole in their pristine or derivatized forms.[73, 74] This electropolymerization reveals several advantages, i.e., low reagent consumption, low cost, and relatively high reproducibility. The resulting MIPs are stable and easy to miniaturize. They are considered outstandingly sensitive materials for detecting analytes in real samples.[88] Prepared by electropolymerization, MIPs have both recognition and transduction properties.[89] They can help transform the interaction of their recognizing imprinted cavities with an analyte into a quantifiable analytical signal, such as the current, charge, capacitance, conductivity, potential, and impedance change.[90]

Moreover, computational modeling is widely used to optimize pre-polymerization complexes' structures and MIP cavities interactions with the molecules of analytes and

interferences to build high-affinity MIPs with appreciably high imprinting factors. Then these parameters are experimentally verified.[91] The computational methods provide deep insight into screening functional monomers, selecting the most appropriate porogenic solvent, and the template-to-monomer ratios.[41, 76, 92] Broad quantum chemistry-based
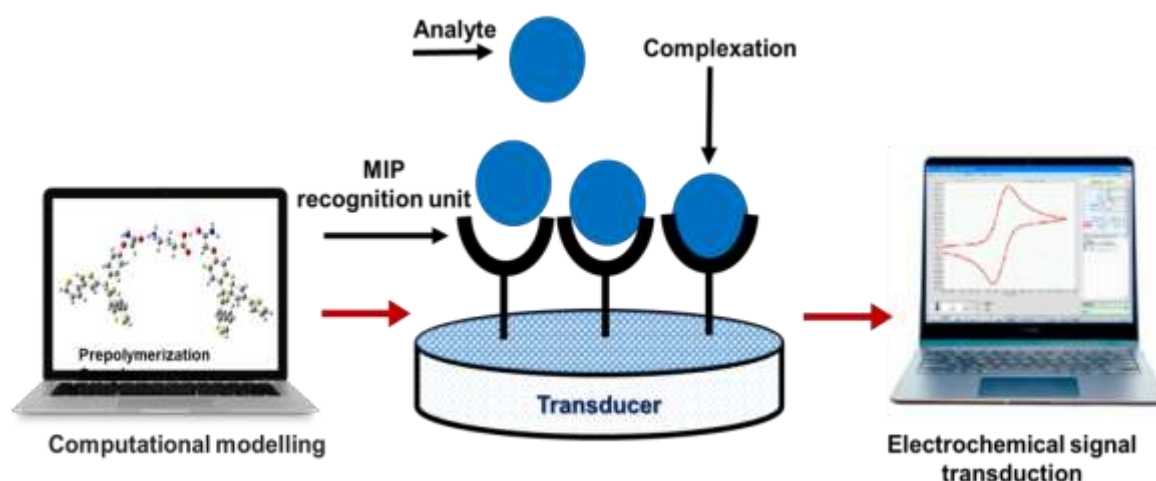
Scheme 1-2. A sketch of an MIP film-based electrochemical chemosensor preparation and operation.

techniques, such as density functional theory (DFT) methods, are primarily used for theoretically optimizing MIP synthesis composition.[93] The advantage of the theoretical approach is a significant shortening of the time of laboratory experiments and decreasing chemicals consumption. This optimization can suggest a stable pre-polymerization complex resulting in highly selective MIP materials. Scheme 1-2 shows a sketch of the MIP-based electrochemical chemosensor preparation and operation protocol.

1.1.3 Molecularly imprinted polymers for biomarkers determining

MIPs for sensing biomarkers, i.e., indicators of various biological and pharmacological processes for proper health assessment, are successfully synthesized.[94] Biomarkers can be classified into two categories, i.e., small-molecule biomarkers ranging between ~0.1 and ~10 nm to macromolecular biomarkers, such as proteins and even whole bacteria.[52]

1.1.3.1 Small biocompounds imprinting

Small (low molecular weight) biocompounds, including amino acids, fatty acids, hormones, vitamins, neurotransmitters, and their metabolites, are responsible for essential life

processes, e.g., neural signal transmission, and play essential roles in healthy body metabolism.[95] The alteration of these biocompounds concentrations in living organisms highly affects normal physiological processes.[79] Therefore, several conventional methods are reported for their rapid and reliable determination, including high-performance liquid chromatography (HPLC),[96] fluorimetry,[97] mass spectrometry (MS),[98] immunoassays,[99] etc. However, these physicochemical methods have limitations, including prevailingly expensive multistep sample preparation procedures, limited sensitivity, and low selectivity. Therefore, in the context of stability, cost, and ease of preparation, MIP chemosensors are becoming more and more popular for biocompounds determination. Among them, chemosensors with MIP recognizing units prepared by electropolymerization are considered the most practical and reliable.[52, 100, 50]

MIPs are difficult to prepare for small biocompounds' metabolites because of their small size.[50, 101, 102] Among all, very few studies report identifying clinically relevant low-molecular-weight biocompounds, such as dopamine, melatonin, and catecholamine.[102,103,86] One of the primary inhibitory neurotransmitters is a small-molecule electroinactive neurotransmitter,[104] gamma-aminobutyric acid (GABA), necessary for the central nervous system.[105, 106] Alteration in GABA neurochemical level is responsible for many neurological disorders.[105, 106] Moreover, GABA is considered a biomarker for autism.[107] Usually, GABA is determined after chemical modification via biosensing[108-110] and HPLC (Table 1-1).[111, 112, 113]

The vital advantage of MIPs is that they can also determine electroinactive analytes, however, in the presence of an auxiliary redox probe.[114] In this system, the probe activity change in the presence of the target analyte is measured as an analytical signal.[115] However, biosensors using biological molecular recognizing units are insufficiently suitable for point-of-care (POC) clinical diagnostics.[116] Hence, applying MIP recognizing units to fabricate POC devices can be a valuable alternative for selective and sensitive determination of low-molecular-weight biomarkers.[117]

Table 1-1. Analytical parameters of sensors reported for GABA determination.

Sensor	Sensing substrate	Analytical signal	Linear dynamic concentration range	Limit of detection	Ref.
Biosensor	Anti-GABA antibody	Piezoelectric microgravimetric	-	~42 μM	[118]
Optical	Negatively charged AgNPs probe	Surface plasmon	$100 - 500$ mg L^{-1}	57.7 mg L^{-1}	[119]
Optical	Fe$_3$O$_4$@SiO$_2$@meso SiO$_2$ microspheres	Refractive index	$10^{-11} - 10^{-3}$ M	3.51×10^{-13} M	[120]
Chemosensor	GCE/CuO NPs probe	Current–voltage (I–V) progression	100 pM to 100 mM	11.7 pM	[121]
Biosensor	GABA-antibody modified silicon nanowire	Electrical	970 fM - 9.7 μM	-	[122]
Chemosensor	Dibenzo-18-crown-6 nano-ITIES pipet electrode	CV	0.25 to 1.0 mM	-	[123]
Chemosensor	Au electrode/GO-cysteamine-2-mercapto ethanol-o-phthalaldehyde	CV	0.25 - 100 μM	98 nmol L^{-1}.	[124]
Optical	Chitosan-gold nano shell particles	Surface-enhanced Raman spectroscopy	$5 - 30$ mM		[125]
Microbiosensors	(Pt electrode)-GABase enzyme	Amperometry	$5 - 80$ μM	2 ± 0.12 μM	[126]
Optical	AgNP probe	Surface-enhanced Raman spectroscopy	$10 - 90$ μM	8 μM	[127]
Optical	carbon dots-GABase	Fluorescence quenching	$10 - 90$ μM	6.46 μM	[128]
Optical	CdS/ZnSe QDs-3-aminophenyl boronic acid-NADP$^+$	QD fluorescence quenching	-	2 nM	[129]
Optical	Au nano bipyramids/polypyrrole core-shell	Surface-enhanced Raman spectroscopy	-	116 nM	[130]
Biosensor	GABase-carbon film electrode	Amperometry	-	30 nM	[131]
Chemosensor	CNTs/electropolymerized thin film of 5-fluorouracil-N-acetylacrylamide	DPV, CV	$0.75 - 205.19$ ng mL^{-1}	0.28 ng mL^{-1}	[132]
Chemosensor	Molecularly imprinted o-phenylene polymer	DPV, CV, LSV, EIS	$0.2 - 20$ μM	0.08 mM	[133]

ITIES - Interface between two immiscible electrolyte solutions.

Health care requires cheap, non-invasive chemosensing devices to screen the population targeted at the risk of diseases.[134, 135] MIP-based POC devices show the possibility of meeting this requirement.[136] One alternative may involve disposable interdigitated electrodes (IDEs) [137] over conventional disk electrodes.[138, 139] The IDEs consist of paired planar interconnected microband electrodes in variant geometries. They demonstrated their usefulness as very effective sensing platforms. At IDEs, a steady-state current is quickly attained because of the enhanced diffusion of redox species.[140] Furthermore, they need a small sample volume due to their small size.

1.1.3.2 Macromolecular biocompounds imprinting

Macromolecular biocompounds are organic compounds of biological relevance with molecular weights of tens of thousands of daltons or more.[141] Because of the unstable structure and mass, these biocompounds' determination was always challenging. Proteins, nucleic acids, cells, and microbes are considered the most critical biological macromolecules and micro-organisms to be exploited as disease biomarkers.[142-144] Typically, macromolecular compounds are imprinted via bulk imprinting. The section above lists several limitations of bulk imprinting, including slow template removal, high mass transfer resistance, diffusion hindrance, and limited recognizing availability.

Bacterial strains detection and determination, necessary for biosafety and biosecurity reasons, include food safety, medical diagnostics, and environmental monitoring. Several analytical methods using, e.g., colorimetry, polymerase chain reaction (PCR), enzyme-linked immunological assay (ELISA), and MS techniques, are already well developed to quantify pathogenic and non-pathogenic microorganisms.[145-147] These methods' only limitations are the requirement of expensive instruments and highly skilled operators. The conventional antibody-antigen host-guest systems determining pathogenic microorganisms lack specificity and stability towards the exposed surface peptidoglycan strands in these microorganisms.[148]

Molecular imprinting in polymers is a fast and inexpensive procedure for rapidly identifying and quantifying macromolecular compounds, e.g., proteins, membrane glycolipids, and even whole bacteria cells.[149, 150] Traditional recognizing bacterial components procedures require a high infectious dose and extra reagents for sample processing, increasing the cost and time of adequate diagnosis.[151, 152] Therefore, the chemosensors encapsulating microorganisms are more desirable for rapid testing.[152-154]

This encapsulation provides a high control over the imprinting, enabling effective template removal, then analyte binding in MIP nanofilms.[80, 155-159] Indeed, the whole bacteria cells encapsulation provides an efficient way to imprint all microbial features present on the microbial surface, including antigenic properties, genomic elements, as well as all biochemical, electromechanical, and morphological features potentially beneficial for the fast and effective determination of target microorganisms in a given sample.[154] Some successful MIPs have already been devised to imprint the bacteria using synthetic functional monomers. For instance, biodegradable chitosan polymer has been used for MIP fabrication.[160]

Synthetic functional monomers featuring boronic acid derivatives were proposed as a bio-recognition mimic to imprint whole bacteria. Boronic acid groups can strongly interact with a porous and flexible polymer present on the bacteria surface. Thus, they help in the fabrication of whole bacteria cell imprinting.

1.2 Polymer gels

Polymer gels, defined as cross-linked polymer networks self-assembled into soft materials with tailored super adsorbent properties, were first devised in the 1970s.[161] However, functional polymer gels with volume phase transition phenomena were introduced by Tanaka in 1978.[162] Since then, functional polymer gels have become an essential topic of polymer and material chemistry because of their high effectiveness and diverse and valuable properties.[5, 163] Most importantly, the stimuli-responsive polymer gels acquire biochemists' attention in the biomedical field because these gels can potentially be used in drug delivery and tissue engineering.[26, 27, 28, 29]

Polymer gels are generally classified into different categories depending upon the intermolecular linkages, morphology, material, size, and monomer composition (Scheme 1-3). The commonly used methodologies for functional polymer gel polymerizations are direct polymerization in homogenous or self-assembly mixtures, emulsion or suspension systems,[101] template-based nano-fabrication,[164] or use of large polymer building blocks as polymer precursors.[165] Polymerization is initiated in all these methods using free radicals initiators, such as ammonium persulphate and azobisisobutyronitrile. These initiators break thermally or photochemically by applying ultraviolet radiation.[166-168] Scheme 1-4 summarizes the advantages and limitations of these traditional polymerization methods.

1.3 Advances in gel polymerization

A functional polymer is a molecular macro chain composed of many small repeating monomer units. Most of these macro chains are linear polymers formed by the reaction of the same monomers or with mono/bi-functionality. However, the presence of the two different active functional groups, e.g., amino and carboxyl groups, in the same monomer often leads to branched polymerization. Furthermore, if branching is extensive, macromolecular chains form a highly cross-linked 3D network structure. Those 3D cross-linked polymers are insoluble in solvents used for polymerization, thus precipitating polymer gels.[169]

According to composition, functional polymer gels are further classified as homopolymers (same monomers), copolymers (different monomers), and hybrid gels (same/different monomers and inorganic cores).[170] This versatility makes polymer gels attractive candidates for different applications. Thus, many improvements have to date been made to advance traditional polymerization systems. Various synthetic systems are used for polymer synthesis, broadly divided into two sub-classes, i.e., homogenous and heterogeneous reaction systems.

The homogenous phase's cross-linking units, or self-assembling monomer units, are called homogenous polymerization, further categorized as bulk or solution polymerization.[171] These reactions are usually carried out by addition or condensation polymerization, less dense, and mildly exothermic.[172]

Heterogeneous polymerization is usually divided into many subcategories. However, precipitation, suspension, emulsion, RAFT, and electrochemical polymerization are the most commonly used polymer gel syntheses procedures.[173] The significant advantages and limitations of these subcategories are briefly described in Scheme 1-4.

- In principle, polymer macro chains appear as precipitates during the precipitation polymerization. That is easy for gel preparation, but precipitation occurs only when growing polymer chains are sufficiently long to become insoluble in the solvent used for the synthesis. So, an excessive amount of monomers is required for size-controlled gel preparations. This method is widely used for thermosensitive polymer gels preparation.[174, 175]
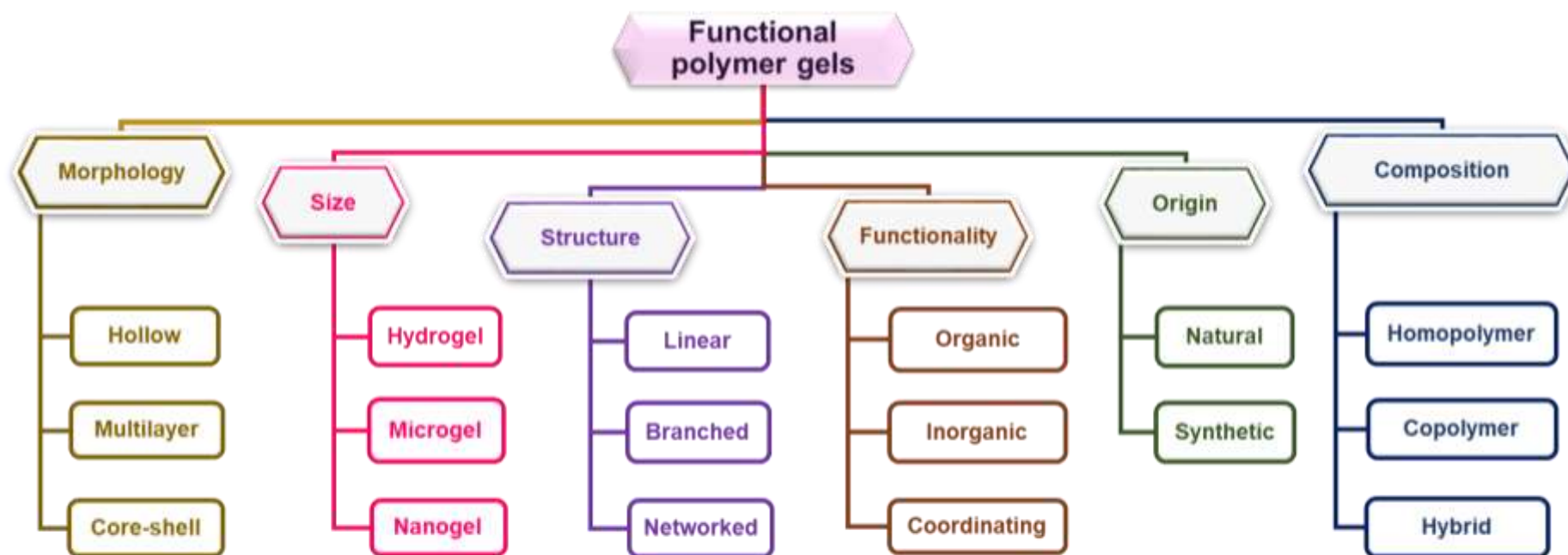
Scheme 1-3. The general classification of polymer gels based on intermolecular monomer linkages, morphology, material type, size, and composition.

- The other approach is suspension polymerization.[176] Organic and aqueous phases in contact are used. The monomer and initiator are in the organic phase, while the polymer stabilizer is in the aqueous phase. The dispersed monomers and initiators react to form dispersed solid microparticles in an aqueous phase during the polymerization.[177] This polymerization is limited to hydrophobic initiators and monomers. Moreover, the presence of a stabilizer and surfactant is mandatory.[178]

- In emulsion polymerization, the initiator is dissolved in the aqueous phase, unlike in suspension polymerization; emulsifiers surround the macro chains to form polymer micelles and thus can be easily separated from the organic phase.[172, 179, 180] It is a stabilizer- and surfactant-free process, but hydrophobic monomers and hydrophilic initiators are required along with emulsifier agents.[181]

- The most advanced polymerization system is RAFT polymerization. It uses chain-transfer agents, e.g., thiocarbonyl compounds, to pursue the reaction by a reversible chain transfer known as living or controlled polymerization. The advantage of RAFT polymerization is the low dispersity index, pre-chosen molecular weight, and complex polymer architectures.[182] Moreover, RAFT polymerization allows preparing tailor-made polymers and copolymers, including block copolymers, without using hazardous or toxic solvents of various topologies.[183] Furthermore, photo-RAFT polymerization has recently been introduced to control the polymerization leading to NPs of the desired shape and size at low temperatures. Moreover, this method helps control the dispersity of molecular weights but suffers from a few limitations. One is a low rate of polymerization on a large scale. Another limitation is the dead-end absence. Even after polymerization, a dormant end group in the polymer architecture leads to the degeneration of polymer chains with time.[184]

- Polymer gel synthesis by electrochemical polymerization is the most recent, not undermined approach.[185] Its main advantages include no need for additives, surfactants, and hazardous solvents. Moreover, this polymerization can proceed at low temperatures. It is referred to as the "green" synthesis. The polymer chain grows after forming an active center, i.e., a nucleation site.[186] The monomer's active forms are generated using initiators under controlled electrochemical parameters in an inert environment.

1.3.1 Macromolecular gel architecture

One vital versatility of functional polymer gels is their ability to confine in various architectures, i.e., hollow microgels, core-shell structures, nanowires, thin porous films, interpenetrating networks, scaffolds, and soft shells of metallic and inorganic NP cores. This characteristic feature of structural diversity enhances these gels' applicability in numerous biotechnological and industrial sectors.

The non-homogenous monomers' distribution, because of differences in monomers reaction kinetics, monomer concentrations, and physical parameters like polymerization temperature, is mainly responsible for different types of the morphology of colloidal gel particles.[187]

The most commonly used polymer colloidal gel architecture comprises copolymer core-shell particles. The reaction rate kinetics plays a decisive role in preparing this architecture.[188] For example, the monomer of a higher polymerization rate constant reacts faster than other monomers during polymerization, forming the interior colloidal core. The monomers polymerizing slower usually form fuzzy dangling chains over the core particles. This attractive versatility of stimuli-responsive gels is used for dedicated applications. For instance, in the case of temperature-responsive gels, the core of the gel produced by polymerization of monomers with lower critical solution temperature (LCST) shrinks earlier, thus effectively compressing the colloidal gel upon increasing the external temperature stimulus.[189, 190]

Similarly, the pH change can trigger the sol-gel transition of the copolymer's core-shell structure. The targeted drug delivery systems could potentially benefit from this property. Another attractive structural design is a polymer nanowire, prepared through electrospinning,[191] templating,[192] and nanolithography.[193] It is widely used in nanoelectronics because of its desired electrical, optical, and chemical properties.

3D polymer thin films play a significant role in electronic devices. Especially, a thin film of functional polymer gels has potential applications in portable power devices.[194] To increase the power density for enabling sufficient mass loading of electrochemically active materials, electrodes of high surface areas are required. That is mainly achieved using 3D polymer films, the best alternative to traditional electrodes. They are also used as electrolytes in electronic devices.[195-197] Another vital use of thin films is tissue engineering as a synthetic biomimetic cell culture microenvironments.[198]
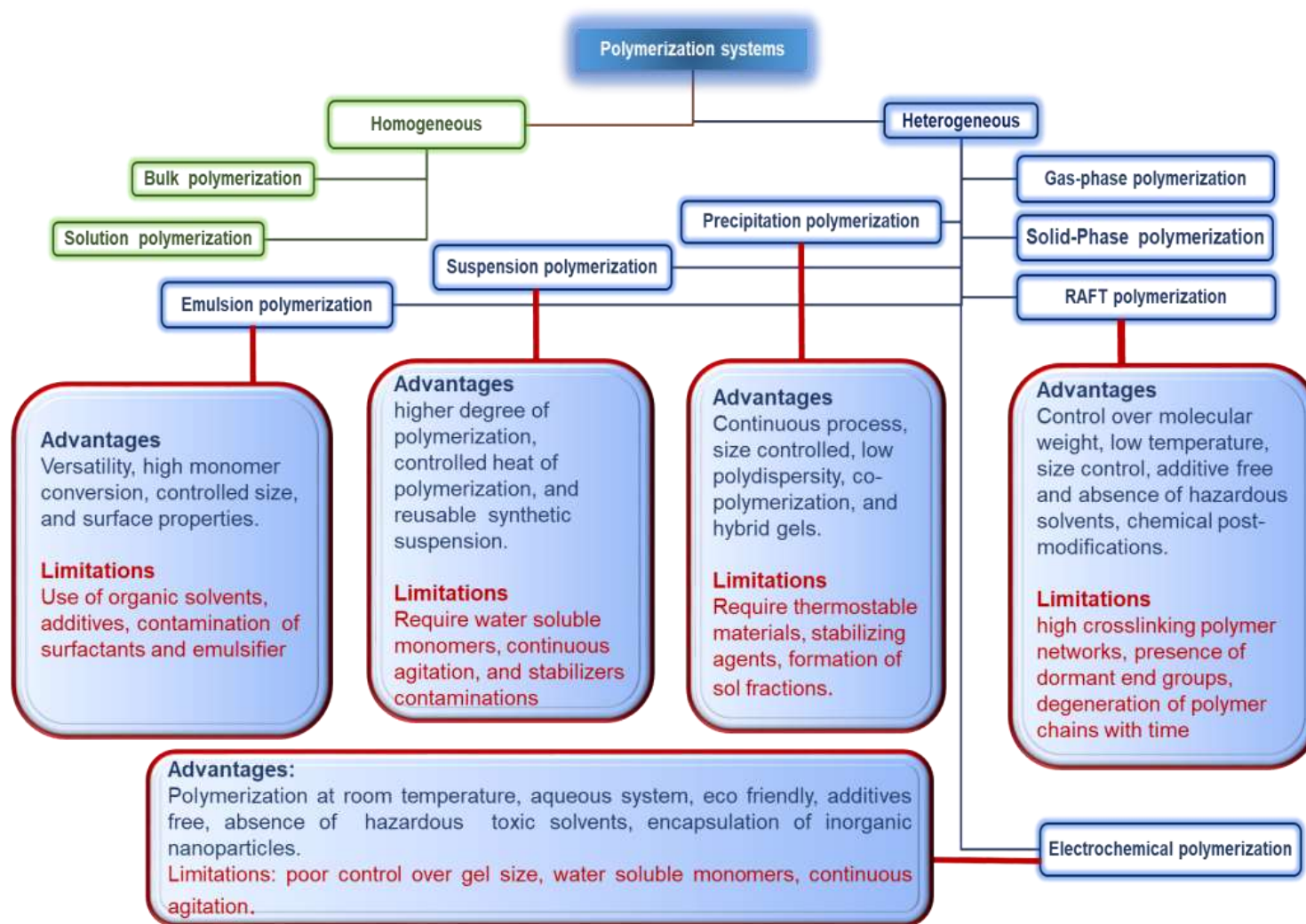
Scheme 1-4. General classification, limitations, and advantages of commonly used polymerization methods for polymer gel preparation.

Likewise, nanowires and polymer 3D thin films are extensively used as transducers for analytical, optical, and chemical sensing.[199-201]

Finally, the responsive microgels can be used to incorporate inorganic NPs. Microgels exist in these hybrids as collapsed inner cores or swollen outer shells. After surface modification or functionalization, the inorganic NPs are integrated into the sol-gel matrix. The microgel surface functionalization provides the binding sites for monomer precursors and improves the stability of inorganic particles in the sol-gel matrix. These responsive hybrid polymer gels are primarily applied for catalytic and photocatalytic,[202] and biomedical purposes.[203] Moreover, because of the high porosity, these gels are used for chromatographic sorption, phase separation, and toxins' adsorption.[204-206]

1.3.2 Nano- and microgels for biological applications

Polymeric smart nano- and microgels form colloidal submicron networks with dimensions ranging from nano- to micrometers.[207] Physical or chemical cross-linking is involved in this networking. In the former, the nanogels are bound via hydrophobic or electrostatic interactions, while the latter occurs via covalent, semi-covalent, or coordinate linkages.[208] Therefore, the physically cross-linked polymers are considered unstable and impractical for in vivo applications.[209]

The nanogel particles' high surface-to-volume ratio is the reason for their high mass loading capacity. Moreover, their shape and size are essential for in vivo applications, with the accepted preferred size of 70-200 nm. Prevailingly, larger-size particles aggregate.[210] Furthermore, the nanogel external gel-sol transition stimulus is the main characteristic of incorporating various guest molecules.[211] However, the biodegradable and biocompatible properties of nanogels are crucial for their efficient use in biomedical therapeutics and the pharmaceutical industry.[212, 213] Therefore, polyacrylamide nanogels are considered the best candidates for these applications (Scheme 1-5).

1.3.3 Polyacrylamide nano- and microgels

Polyacrylamide nano- and microgels are tuneable potential delivery systems whose remarkable characteristics can be utilized to encapsulate molecules of a wide range of guest compounds, including oligonucleotides, peptides, and other macromolecular compounds, often being drug substances.[212, 214-216] Therefore, polyacrylamide nanogels have increasingly been intensively studied. Essential uses are "nanomedicines carriers" and "3D

cell culture tissue/organoids (see below)" formation due to biocompatibility, biodegradability, and active integration of NPs as cores or net of nanodots with the shells.[211, 217-220] That is because they have enhanced capability of tissue permeation for controlled delivery of hydrophilic and hydrophobic drugs and for providing a basement membrane for 3D cell culture formation.
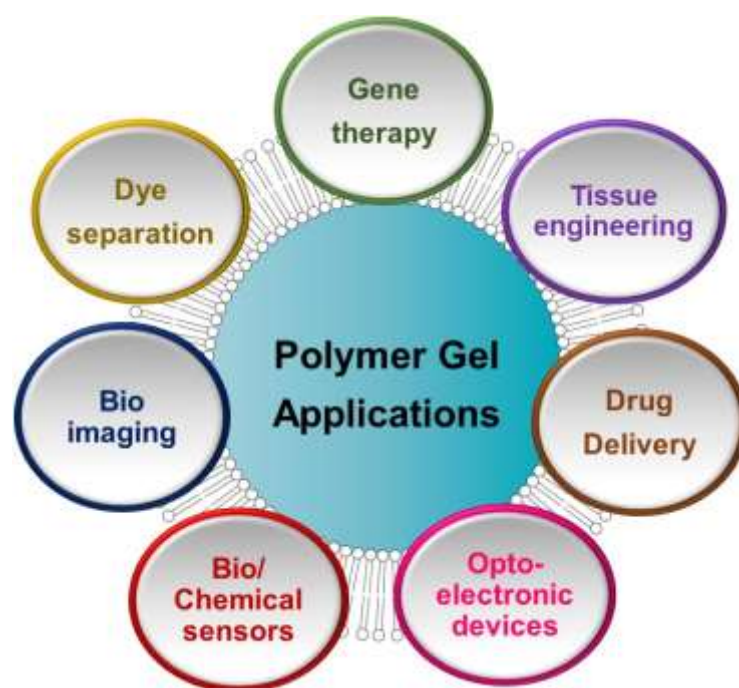
Scheme 1-5. Typical applications of polymer gels.

The drug release from nanogels either consists of drug diffusion from the nanogel matrix or is externally triggered by energy stimuli (changes in the magnetic or electric field), pH or temperature changes, or the counter ions displacement (Scheme 1-6).[221] Moreover, the gel cross-linking extent and surface functionalization indirectly control the drug release mechanisms.[222] Because of the low pH of the tumor microenvironment, the pH-sensitive nanogels reveal superior antitumor efficacy, accelerating the drug release in the tumor microenvironment.[223, 224]

Additionally, the polyacrylamide sensitivity to environmental parameters, such as light, temperature, and pH, highly depends on its functional counterpart.[225] Incorporating the carboxyl group functionality into intelligent polymer components may efficiently enhance the bioinspired mechanisms triggered in response to external environmental stimuli.[133]

Thus, cross-linked polymer gels containing carboxyl groups, such as a copolymer of poly-*N*-isopropyl acrylamide (PNIPAM) and methacrylic acid (MA), are highly responsive to pH and temperature changes.[226] These copolymer functional nanogels may respond to appropriate pH changes with volume transition. Additionally, the acrylic monomer's ability to adhere to the biological tissue enhances the capability of intracellular drug sorption and release.[222]

PNIPAM nanogels are potential nanocarriers in delivering low-molecular-weight drugs, e.g., cisplatin, doxorubicin, 5-fluorouracil, methotrexate, then releasing their cargo upon even a slight change in pH or temperature.[219, 224, 227-229]

1.3.4 Polymer gels as basement membranes for 3D cell culture

The two-dimensional (2D) cell culture workflows and animal models are limited by lack of signaling pathways, accessibility of imaging for observation, limited usability, and, most importantly, the vast differences between animal and human biology.[230] To better understand cellular and non-cellular environments, the model systems derived from human cells are required.[231] Tumor cell aggregates, tissue slices, or spheroids may transiently capture physiologically relevant cell-cell and cell-matrix interactions. However, they still lack relevant tissue organization and relevant stem cell populations required in maintaining the 3D culture systems for cell proliferation and differentiation.[232 233]

The cellular microenvironment, capable of assembling complex cell structures as organ alternatives, is required to overcome the gap between the current model systems.[234] Complex cell structures self-assembled in 3D clusters are known as organoids.[235] Organoids are mainly derived from embryonic stem cells, primary tissue-specific cells, induced pluripotent stem cells, and adult stem/progenitor cells.[236-238] The spatially organized organoid models can self-renew and self-organize.[239] The physiologically relevant organoids are invaluable to study organogenesis, disease modeling, and patient-specific therapies.[240]

Moreover, in vitro 3D miniature versions can recapitulate human life processes.[241] The 3D environment encompassing the advantages of 2D cell culture and in vivo animal models is widely used to investigate physiological processes for translational medicine.[143] They closely mimic in vivo 3D environments, overcoming the limitations of 2D cell culture.

Recent advances in micro- and nanotechnology have driven organoid research progress. However, a high-quality microenvironment is still required to incorporate 3D

structures into cell culture workflows. Moreover, physical parameters, such as porosity, permeability, surface chemistry, and mechanical characteristics are crucial for successful organoid growth.[242] Few scientifically confirmed methods are available for organoids' preparation. These include magnetic suspension culture formation, crypt isolation method, air-liquid interface method, embryonic model, bioreactor, and extracellular matrix (ECM) method.[148,149]

The most commonly used microenvironments are natural hydrogel systems, i.e., ECM and Matrigel® matrix, providing a proper biological environment for cell survival and proliferation for organoid formation. The Matrigel® matrix or ECM-based basement membrane is enriched with growth factors and compounds crucial for cell proliferation and differentiation, i.e., laminin, heparin sulfate proteoglycan, and nidogen/nidogen/entactin.[243] Moreover, these components help activate signaling pathways to control angiogenesis, cancer cell motility, and drug sensitivity.[239, 244]

The natural hydrogel systems for organoid formation are engineered using 3D bioprinting with precise geometries. Nevertheless, the crucial requirements of bioactive growth factors emphasize the development of some alternatives for 3D cell culture applications. Moreover, natural animal-derived controlled hydrogel matrix systems are not well defined and always at a high risk of batch-to-batch variability.[245] Therefore, the best alternative is a synthetic polymer scaffold capable of providing a pathogen-free, biologically inert, highly tuneable microenvironment for the growth of organoid systems of choice.[246] Generally, synthetic hydrogels incorporate the signaling proteins, specific bio-functionalities, and growth arginine-glycine-aspartic acid (RGD) motifs to mimic the natural microenvironment.[247-249] The synthetic polymer gels provide a more physiologically relevant chemical composition, which helps support biologically relevant functions, i.e., enhancing cell attachment or regulating cellular proliferation.[155,250, 251]

Additionally, hydrophilicity and porosity of smart polyacrylamides provide similarity to the cellular microenvironments, including Matrigel® or ECM, to promote cell-cell interactions.[252 251, 253, 254] Likewise, stiffness, stability, cell adhesivity (incurred by the addition of RGD peptides) are vital biochemical parameters for tissue formations.[255-257] Moreover, the cross-linking and mechanical properties of the gels significantly influence cell adhesion, in turn regulating cell proliferation and migration in the cellular microenvironment.[258] Unfortunately, the biocompatibility of currently available gels is low, and their mechanical properties are weak.[259]
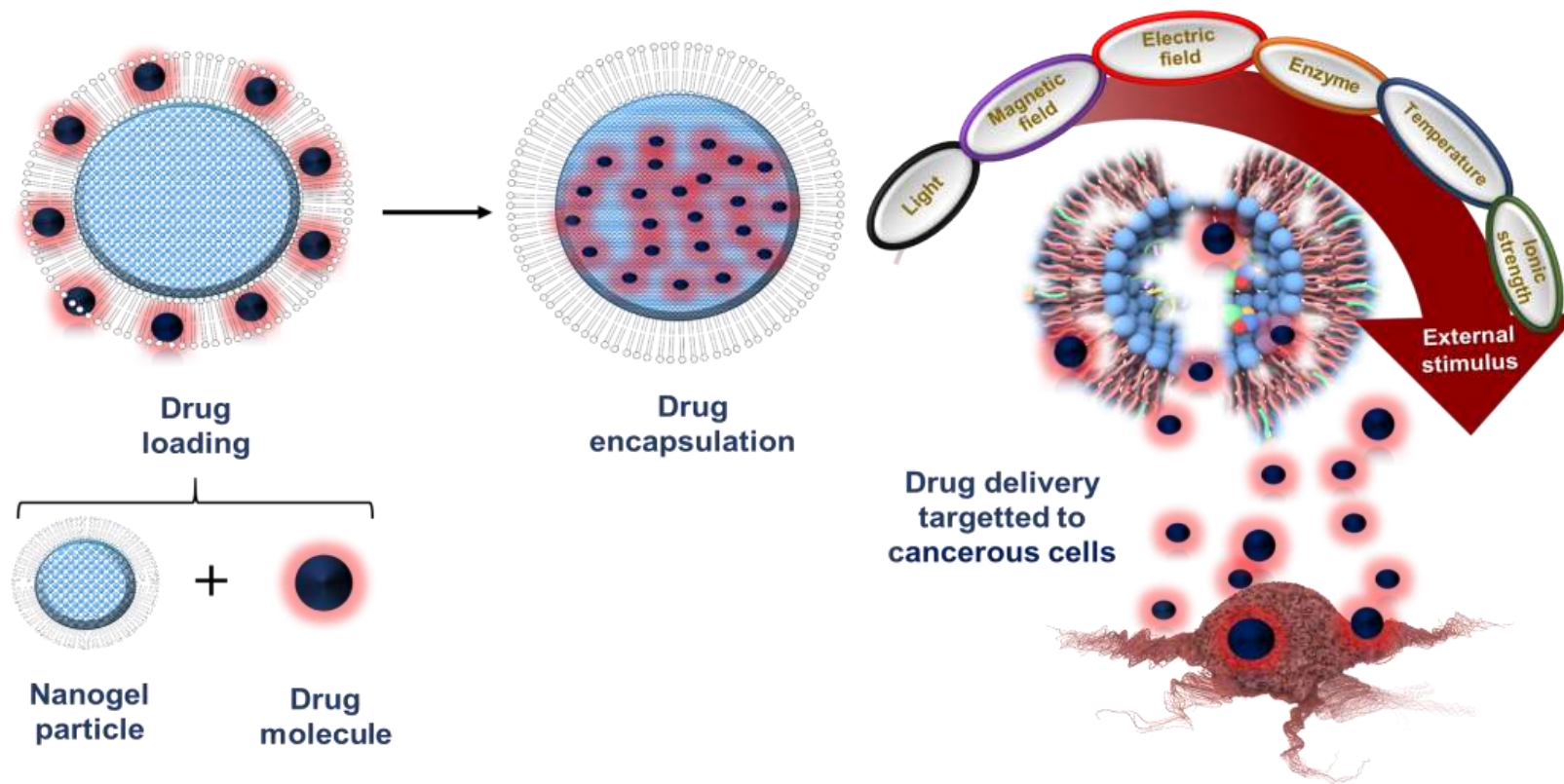
Scheme 1-6. The steps of a nanogel application for drug delivery.

These two factors are usually tuned by adjusting cross-linking monomers, adding co-monomers featuring the desired functionalities, changing solvents for syntheses, or varying synthetic strategies.[260]

Critical organoid applications (Scheme 1-7) include stem cell biology (investigating life processes), disease mechanisms (disease-relevant mutations and regenerative medicines), toxicology (drug-induced toxicities), and drug discovery (drug screening and profiling mechanisms), and studying infectious diseases (pathophysiological response). Thus, developing organoid study has driven biological researchers to investigate human pathologies and life processes cost-effectively and profoundly.
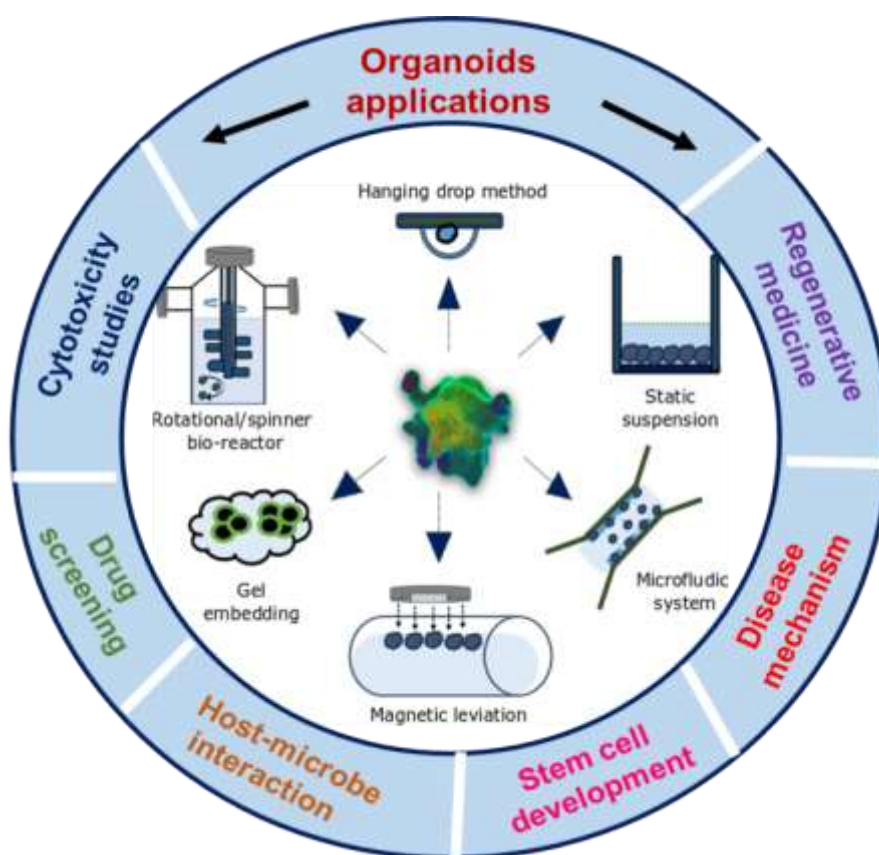
Scheme 1-7. Commonly used methods of organoid synthesis and application.

1.4 Thesis objectives

As reviewed above, the functional polymers are used for biomarkers' molecular imprinting and microgels' synthesizing. Most reported approaches using functional monomers to synthesize molecular receptor biomimetics for biomarkers encountered several challenges,

including functional complexity, fragile structures, harsh conditions for template removal, and low selectivity. However, the electrochemical MIP chemosensors are the breakthrough in biotech sensors.

The current research goal is to synthesize functional polymers and nano- or microgels oriented toward clinical analyses under electrochemical conditions. The research plan includes electrochemical synthesizing sensitive MIP films to selectively determine a gamma-aminobutyric acid (GABA) autism biomarker (an electroinactive neurotransmitter) and *Escherichia coli* K-12 bacteria. Moreover, the thesis describes the electrochemically initiated hydrodynamic syntheses of polyacrylamide gel particles and shells on selected inorganic cores and the application of these particles for cell culture.

First, the MIP electrochemical sensor for GABA was devised, engineered, and tested. To this end, the MIP for GABA was prepared in the form of a nanometer-thin film by using chosen designed functional monomers to mimic receptors on the electrode, i.e., the transducer surface.

Moreover, as GABA is electroinactive, the hexacyanoferrate/hexacyanoferrate(II) redox probe was used for the indirect electroanalytical determination of GABA. The computational simulations provided the stability of the pre-polymerization complexes to be formed. Five different *bis*-bithiophenes and monomers with different functional moieties were used. The density functional theory (DFT) calculations provided the negative Gibbs free energy gains accompanying the formation of the most stable pre-polymerization complexes. Moreover, computational modeling helped select functional monomers suitable for preparing MIPs of the highest selectivity.

Furthermore, a stepwise procedure for determining the GABA analyte rapidly was developed. Different transduction techniques were employed to evaluate MIP-based chemosensor performance and then propose a technique suitable for the MIP-based POC analysis.

Food pathogens became a global concern when Gram-negative *E. coli* was reported as a significant cause of the severe European health pandemic in 2011. To date, several methods have been developed for *E. coli* specific identifications. However, an essential need persists in replacing traditional laborious *E. coli* determinations with robust, convenient, and cost-effective determinations. Therefore, here, an MIP film-based recognition unit was prepared to determine the E. coli E2152 strain selectively. A (boronic acid)-functionalized monomer was used to imprint this strain molecularly. This monomer was used because of its ability to form five- or six-membered rings of cyclic esters

with the negatively charged glycoproteins of the *E. coli* cell membrane surface. The thin MIP film deposited was cross-linked with aniline.

Progress in polymer gel synthesis requires developing novel gel materials of controllable shape and size. Though currently available methods for polymer gel synthesis are highly developed, they still face some limitations, such as incompatibility with hydrophobic organic solvents, lack of tolerance to toxic additives, and high temperature and or pressure, as mentioned above in detail.

Still, better solutions are required to develop novel green approaches for efficient polymer gels' use in biological systems. Here, therefore, we made an effort to develop a comparatively green approach for a 3D intra-molecularly cross-linked microgel. The *N*-isopropyl acrylamide (NIPAM) and MA were used as the main monomers. Under hydrodynamic conditions, electrochemical initiation allowed preparing different morphology microgels at room temperature. Importantly, neither heating nor UV-light illumination was needed to initiate the polymerization. Moreover, microgel shells were electrochemically grafted over inorganic core support, including silica and iron-oxide magnetic NPs. This study used the green synthetic approach in controlled drug delivery and cell encapsulation.

First, biocompatibility studies were performed using the cervical and HeLa cell lines. The prepared nanogels were further used for 3D cell culture/organoid synthesis to be subsequently used for drug screening and organ transplanting.

Chapter 2

2. Experimental

2.1 Chemicals

N-isopropyl acrylamide (NIPAM), methacrylic acid (MA), *N*,*N*'-methylenebisacrylamide, and (50 – 100)-nm size iron oxide magnetic nanoparticles (MNPs), acetonitrile, gamma-aminobutyric acid, *N*-acetyl-L-aspartate, 2-aminobutanoic acid, 5-aminopentanoic acid**,** tryptic soy broth (TSB), 2-aminophenyl boronic acid (2-APBA), aniline (ANI), glucose, tetrabutylammonium perchlorate (TBA)ClO$_4$, Luria-Bertani (LB) broth, lysozyme, Triton X 100, Tris-HCl buffer (pH = 7.4) were purchased from Sigma Aldrich. Potassium hexacyanoferrate(II), K$_4$[FeCN)$_6$], and potassium hexacyanoferrate(III), K$_3$[FeCN)$_6$], were procured from Chempur, while sodium hydroxide was from Roth Chemicals. All reagents and solvents were of analytical grade and used as received. The Fiber Optic Centre provided the 500-nm diameter silica beads. Deionized Ultrapure Merck Millipore Milli-Q$^®$ water (18.2 MΩ cm) was used to prepare all aqueous solutions.

2.2 Biological materials

The 3-(4,5-dimethylthiazol-2-yl)-2,5-diphenyltetrazolium bromide (MTT) reagent was from Thermo Fischer Scientific. MDA-MB-231 and HeLa cells came from the American Type Culture Collection (ATCC, Manassas, USA). Both cell lines were cultured as standard monolayers in a complete growth medium, supplemented with fetal bovine serum (FBS, Gibco), L-glutamine (1%, *v/v*) from Sigma-Aldrich, and the antibiotics, vis., streptomycin [10,000 U/mL] and penicillin [10 mg/mL] (1%, *v/v*) from Sigma-Aldrich. Standard conditions (37 °C, 5% CO$_2$) were applied for cells' culturing. HeLa cell lines were cultured in Dulbecco's Modified Eagle Medium (DMEM) with low glucose content (Institute of Immunology and Experimental Technology, Wrocław, Poland), while the culture medium for MDA-MB-231 was RPMI 1640 with sodium bicarbonate and without L-glutamine (Sigma-Aldrich). Cells were maintained in a logarithmic growth phase using regular passages. They were detached from the surface using a 0.25% trypsin-EDTA solution (Sigma-Aldrich). The trypsinization process was controlled by optical microscopy.

2.3 Bacterial strains and growth conditions

The *E. coli* K-12 strains were constructed from *Escherichia coli* MG1655 (*E. coli* genetic stock center CGSC #6300) by transforming the red linear DNA gene inactivation method using the pKOBEG plasmid.[261] All strains contained the gfpmut3 gene linked to the bla ampicillin-resistance gene (ampR, 100 g/mL) to make them fluorescent. Our study used three mutants, vis., E2146, E2152, and E2498, expressing different surface appendages of different scales.[261] E2152 shows a simple surface with no type 1 fimbria and antigen 43 protein (Ag43). E2146 displays external ultrastructure type 1 fimbriae, 1 to 10 μm long, and E2498 expresses a dense layer of the Ag43 protein merely 10 nm long. Moreover, *Shewanella oneidensis* MR1 (ATCC 700550) was used as an interferent.

The modified Gram-negative strains of *Escherichia coli* bacterium, i.e., *E. coli* K-12 strains of E2146, E2152, and E2498, were pre-grown overnight (~12 h) in the LB broth at 37 °C and 160 r.p.m., in the presence of appropriate antibiotics to select the strains. The next day, a fresh culture was inoculated with that overnight pre-grown to an optical density of ~0.08, measured at 600 nm, and then cultivated under the same conditions. The cultured bacteria cells were collected by triple centrifugation at 5000 r.p.m. for 10 min. Afterward, a pellet was collected and re-suspended in a sterilized 1 mM KCl. The same procedure was repeated for the SWMR-1 strain except for the change in growth medium conditions characteristic of the strain used, i.e., the TSB broth at 30 °C.

For the preparation of the bacterium imprinted polymer (the experimental work performed at LCPME, Villers-lès-Nancy, France), TSB, LB broth, lysozyme, Triton X100, NaOH, KCl, $K_3[Fe(CN)_6]$, $K_4[Fe(CN)_6]$, Tris-HCl buffer (pH = 7.4), 2-APBA, and ANI were used.

2.4 Techniques

2.4.1 Dynamic light scattering (DLS)

Dynamic light scattering (DLS), also known as photon correlation spectroscopy, is a highly sensitive technique used to characterize solid particles by determining their charge, shape, size, and profile.

Particles in suspension are always in random Brownian motion because of their thermal energy. The DLS operation principle is based on the momentum transferring to the suspended particles.[262] Light is scattered upon the electromagnetic field interaction with the matter. The incoming incident laser beam induces the electric dipoles oscillation (Brownian

motion) as it passes through the matter. This motion imparts momentum to the suspended particles, whose magnitude and direction fluctuate with time.[263] This scattered wave electric field effect is responsible for the experimental realization of this technique. The light scattering can be either elastic or inelastic. The elastic scattering is further classified into a static measure of the molecular weight, second virial coefficient, and radius of gyration of polymers, while dynamic scattering provides information about the diffusion coefficient of colloidal particles and suspended particles of, e.g., biopolymers and gels.[264] Most importantly, the diffusion coefficient defines the colloidal particle hydrodynamic radius and polydispersity parameters.[265] Figure 2.1 schematically represents the DLS phenomenon.
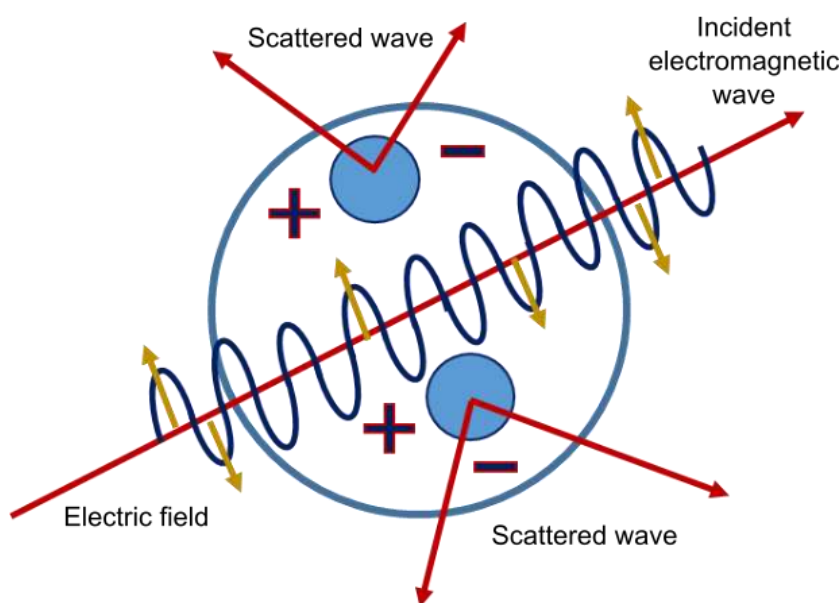
Figure 2-1. Schematic representation of DLS operation principle.

2.4.2 Scanning electron microscopy (SEM)

The maximum human eye resolution reaches two dots/points 0.2 mm apart. Therefore, the microscope is an efficient alternative magnifying tool to overcome this resolution limitation. The source used to increase the microscope's resolution is visible light or an electron beam. However, the optical microscope resolution is lower than that of the electron microscope because of light diffraction properties. As the electrons' wavelength is much shorter than that of visible light, the electron microscope's optimal resolution is many orders of magnitude higher than that of an optical microscope. Therefore, the highly accelerated and focussed electron beam is used to investigate the morphological properties of the specimen.

Scanning electron microscopy (SEM) is an effective imaging technique for analyzing solid organic and inorganic specimens scaled from nanometres to micrometers. In principle, SEM uses a high-energy beam of primary electrons to produce an image of very high magnification, i.e., up to 300,000 times (1,000,000 times in some modern SEM microscope models).[266]
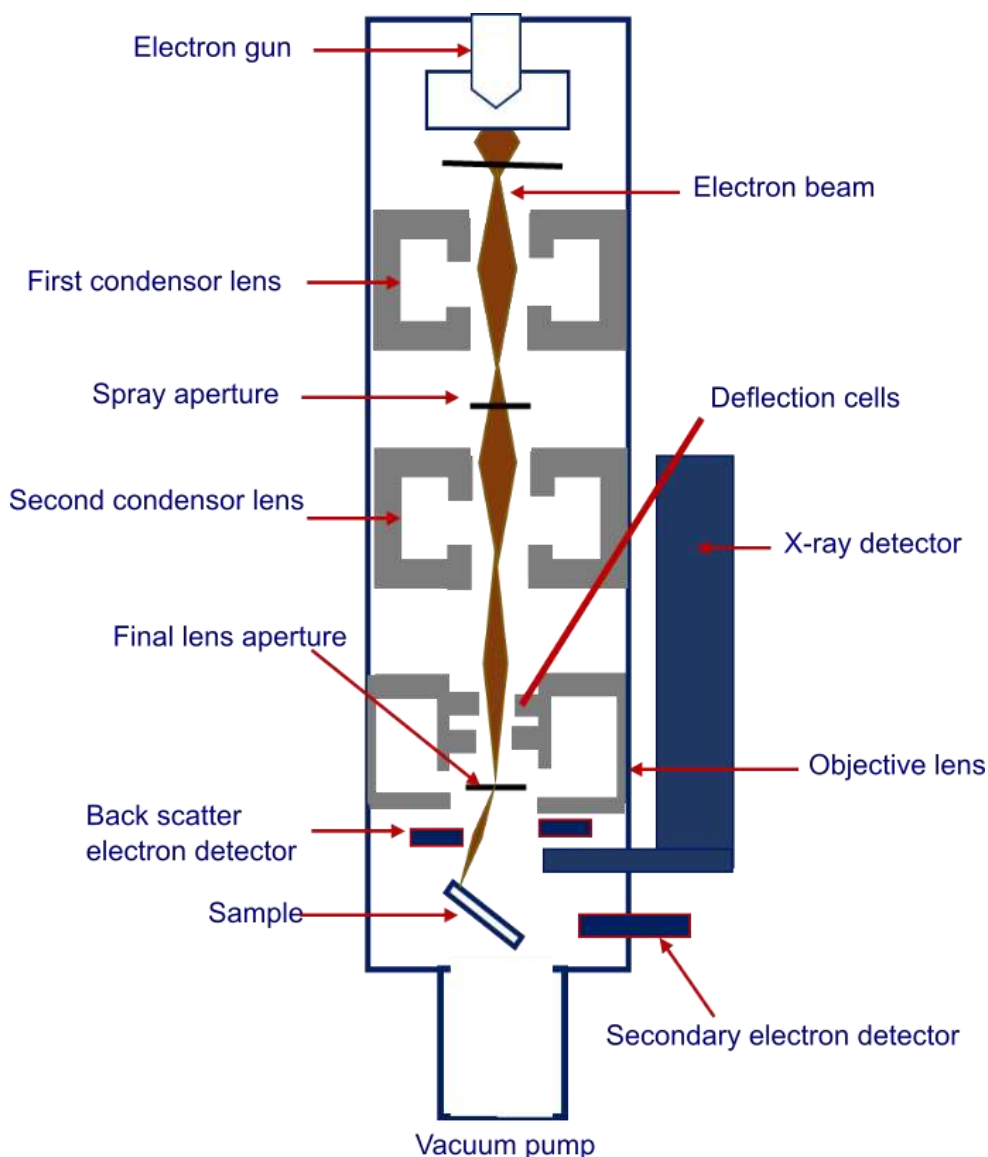
Figure 2-2. Schematic representation of an SEM microscope.

The impinging primary electrons accelerated towards the specimens have substantial quantities of kinetic energy. They transfer this energy inside the sample, scatter it back, and generate signals. Moreover, this scattering depends upon the angle of incidence of the

51

electron beam; the angle larger than 90°, the smaller is the interaction area. The high accelerating voltage generates high-energy electrons (100 to 30,000 eV) that penetrate the sample deeply. Overall, because of the Coulomb interactions, the interactions of the primary electrons' beam with the specimen generate many signals upon scattering.

The incoming high-energy electron beam interactions with the sample's atoms can be divided into elastic and inelastic.[267] Elastic scattering results from the deflection of the incident beam by outer-shell electrons of similar energy. The incident electrons scattered through an angle exceeding 90° (backscattered electrons) yield a useful signal for sample imaging. While incident electrons interact with the sample's atoms and electrons differently in inelastic scattering, the generated secondary electrons of less than 50 eV are used to analyze the sample morphology.[268] These backscattered signaling electrons are gathered by detectors in the SEM microscope and then manipulated by the computer to produce the required image.

A modern SEM instrument is additionally equipped with the energy-dispersive X-ray (EDX) spectroscopy unit. This unit separates the characteristic backscattered X-ray signals of various elements within the sample into the energy spectrum and analyses it by EDX system software.[269] The SEM and EDX combination can provide high qualitative and semi-quantitative results of scanned samples, e.g., material morphology, size, shape, and composition. Figure 2-2 is a schematic representation of a typical SEM instrument.

2.4.3 Scanning transmission electron microscopy (STEM)

In scanning transmission electron microscopy (STEM), the high-resolution electron beam analyses quantum wells, wires, and dots' quality, shape, size, and density. STEM determines material sciences' deposited film thickness, growth layers, and morphology. The fundamental principle is quite similar to that of SEM; the main difference is using an electron beam in STEM instead of photons to illuminate the basic features of the specimen. However, STEM is more informative because it provides a deep understanding of internal specimen structure, magnetic domains, and surface morphology and composition. The STEM detects the transmitted electrons, while SEM detects the backscattered electrons. The accelerated voltage is at most 40 kV in SEM, while it exceeds 100 kV in STEM. Moreover, the material thickness of less than 100 nm can be determined using STEM. Thus STEM is quite helpful in understanding the most subtle details of internal specimen structure.

The electron gun in STEM focuses a narrow electron beam over the specimen. The high-angle electron beam striking the specimen reveals its thickness and electron transparency. The beam transmitted through the specimen is focused on an image of the objective lens's charge-coupled device. Finally, the enlarged image (with the help of intermediate and projector lenses all the way) strikes the phosphorus screen allowing the user to observe it. STEM images' dark and bright areas appear because of the difference in electrons transmitted through a variant thickness and morphology specimen.

2.4.4 Atomic force microscopy (AFM)

Atomic force microscopy (AFM) uses force measurement for topographic imaging (three-dimensional imaging), measurement of mechanical (Young's modulus), and electrical (conductivity or surface potential) properties of the sample.[270] The forces involved in AFM are van der Waals, capillary, electrostatic, magnetic, and solvation forces. The primary AFM modes of operation include the static/contact mode and dynamic non-contact/tapping mode at a given applied frequency. Precise scanning information is gathered using the piezoelectric elements in the mechanical probe.[271]

In principle, AFM follows Hook's law. A sharp tip (typically made of silicon) of the cantilever is brought into the proximity of the specimen surface. Forces between the tip and the specimen lead to cantilever deflection as the tip approaches the solid sample specimen surface. The repulsive forces increase and deflect the cantilever away. The laser beam detects these deflections. The reflection angle of the laser beam depends upon the cantilever displacement. A photodiode collects the laser beam angle changes and then converts them to an electric signal. This signal appears as a colored map expressing the sample topography.[272] Figure 2-3 shows a schematic of the AFM working principle.

2.4.5 Confocal microscopy (CM)

Confocal microscopy (CM)[273] is a high-resolution imaging technique based on the fluorescence optics principle. It is used for live cells imaging and tissue engineering.[273] In CM, instead of illuminating the whole sample at once, a laser beam is focused onto a defined spot at a specific sample depth, leading to fluorescent light emission at the precisely required point. A pinhole inside the optical pathway cuts off signals out of focus, thus allowing only the fluorescence signals from the illuminated spot to enter the light detector and scan the images of one single optical plane. CM operates on the point illumination principle and

generates focused illumination of every point. Therefore, the focussed light scans the whole specimen to build a complete image.
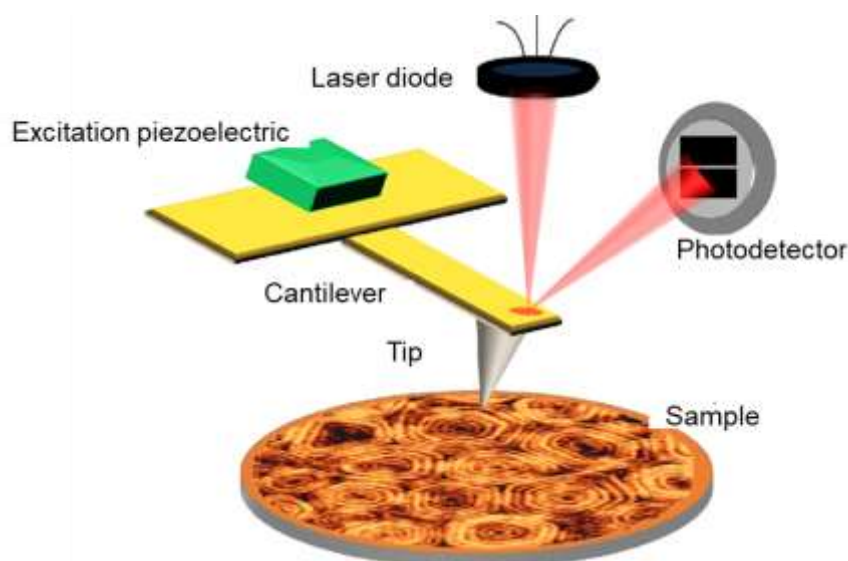
Figure 2-3. Schematic representation of an AFM microscope operating in a tapping mode.[272]

The use of fluorochrome is one of the necessary CM requirements. The laser beam is focussed at a particular point over fluorochrome, producing an illumination, eventually collected by the objective lens. In modern CM, the objective numerical aperture is 0.25 to 0.8 µm in diameter and 0.5 to 1.5 µm in depth. Finally, the detector measures the illumination signal and produces an image in a computerized system.

The main advantage of CM is to detect only the object which is in the focus point; objects outside this point appear black. Thus CM essentially removes the limitation of conventional wide-field fluorescence microscopy out of "*focus light*." Another advantage of CM is scanning the specimen at several optical planes and then stacking them using a suitable microscopy deconvolution software. Therefore, it is helpful for 3D sample visualization. Moreover, CM's additional possibility is adding several lasers to analyze multicolor immunofluorescence staining. Figure 2-4 shows the CM operation principle.

2.4.6 Electrochemical measurements

The simplicity of electrochemical measurements and their ease with measuring kinetic and thermodynamic parameters of electrochemical reactions make them powerful for electrochemical sensing and polymer synthesizing. These reactions involve the electrode processes, i.e., heterogeneous oxidation-reduction reactions, where voltage is applied from an external source to the electrical conductor or semiconductor for modulating the chemical energy into an electrical output.
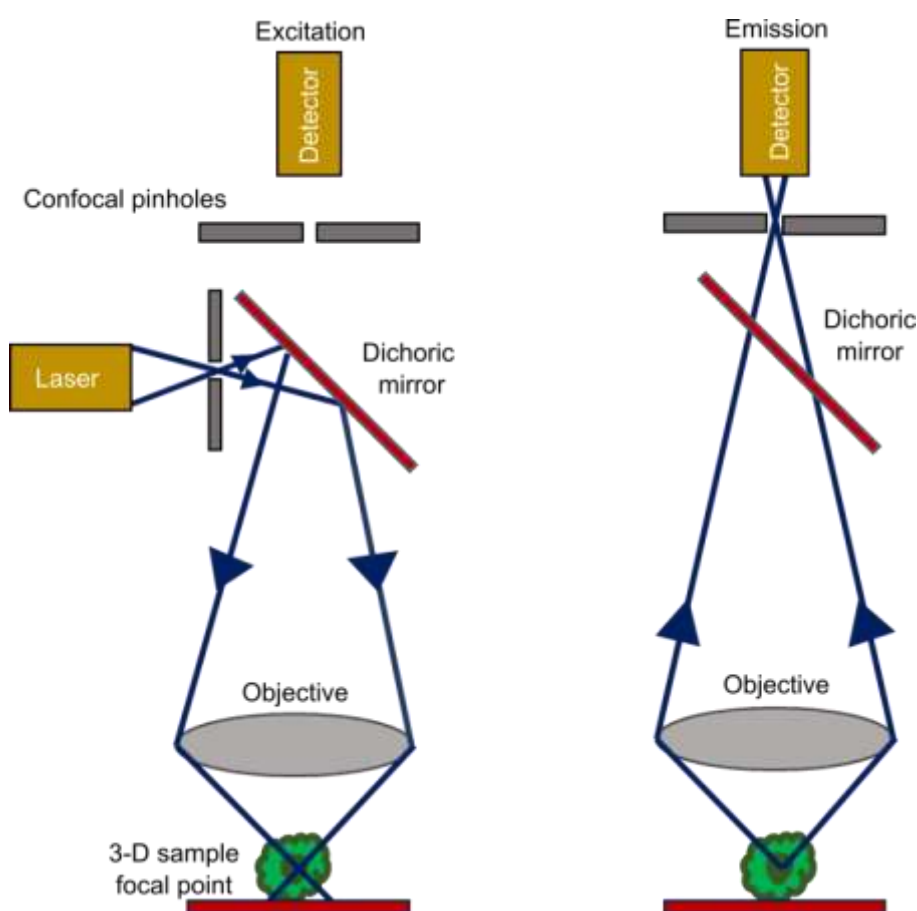
Figure 2-4. Schematic representation of confocal microscopy[273] operation principle.

The three-electrode cell system (Figure 2-5) is typically used for electrochemical measurements involving aqueous, non-aqueous, and molten salt systems. It consists of a working electrode (WE), a counter electrode (CE), and a reference electrode (RE) generating electrode reactions. These electrodes are submerged in an electrolyte solution or liquid

electrolyte. The potentiostat or galvanostat is an external device generating respective excitation potential or current signals and recording output signals.

The potentiodynamic and potentiostatic techniques are the most common electrochemical techniques used to synthesize MIPs, while the most common techniques used to study MIPs' electrochemical properties include electrochemical impedance spectroscopy (EIS) and electroanalytical techniques, such as cyclic voltammetry (CV) and differential pulse voltammetry (DPV).

2.4.6.1 Cyclic voltammetry (CV)

Cyclic voltammetry is an electroanalytical technique used for analytical and physicochemical purposes to determine the analyte concentration as well as the kinetics and thermodynamics of electrochemical processes, respectively. The CV measurements are most often accomplished using a three-electrode cell system. A computerized potentiostat linearly scans the WE's potential against the RE's potential until it reaches a pre-set limit. Then, the potential is scanned in the opposite direction. A cyclic voltammogram is a graph recorded by scanning the potential forth and back between the chosen limits (Figure 2-6). The voltammogram provides information about compound redox properties, including the formal redox potential, diffusion coefficient, rate-limiting factor, energy levels of semiconductors, system reversibility, i.e., reversible, irreversible, and quasi-reversible electrode reactions, and the charge transfer coefficient of the irreversible process.[274] The current generated by applying linearly scanned potential is limited by the rate of mass transport of a redox species from the solution bulk to the electrode-solution interface. At 25 °C, the peak current, i_p, of the reversible redox process is described by the Randles-Ševčik equation in the form

$$i_p = (2.69 \times 10^5)\, n^{3/2} A c D^{1/2} v^{1/2} \qquad\qquad \text{Eq. 2.1}$$

where A is the electrode surface area (cm^2), n is the number of electrons transferred, D is the diffusion coefficient of the redox analyte ($cm^2 \cdot s^{-1}$), c is the analyte concentration ($mol \cdot cm^{-3}$), and v is the potential scan rate ($V \cdot s^{-1}$).

The redox process at the WE generates the current of an electrochemical reaction. The potential applied to the WE creates an electrical double-layer by arranging ions and orienting electric dipoles on the WE. The response measured due to this effect is described by a combination of Faraday's law and Fick's first law (Eq. 2.2).

a
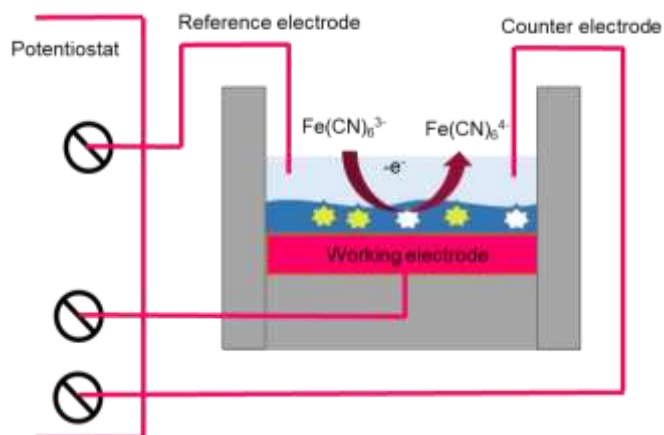
b
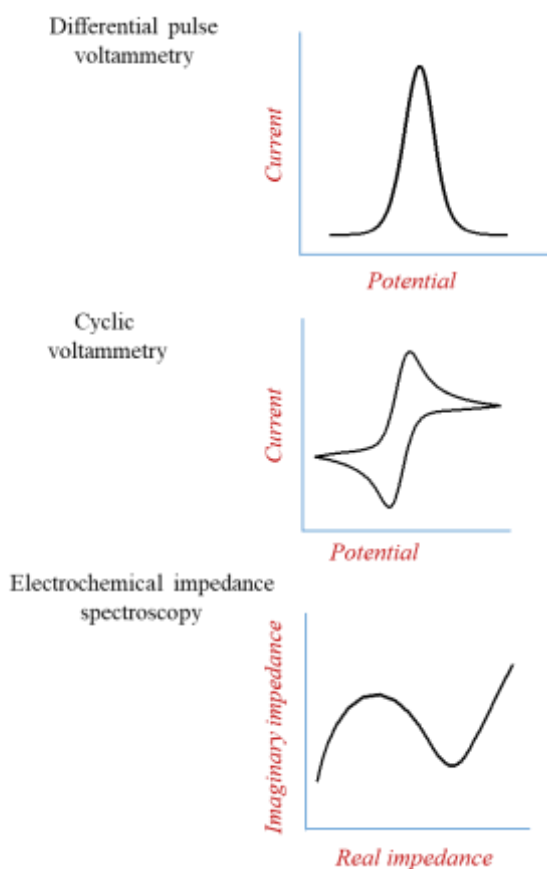
Figure 2-5. (a) Schematic representation of a three-electrode cell system for chemosensing. The working electrode is modified with a molecularly imprinted polymer. (b) Techniques most commonly used in electrochemical MIP chemosensors.

$$i_d = n \, F \, A \, D \, (\partial c_0 / \partial x) \qquad\qquad \text{Eq. 2.2}$$

where i_d is the diffusion-limited current, F is the Faraday constant, and $(\partial c_0 / \partial x)$ is the analyte concentration gradient.
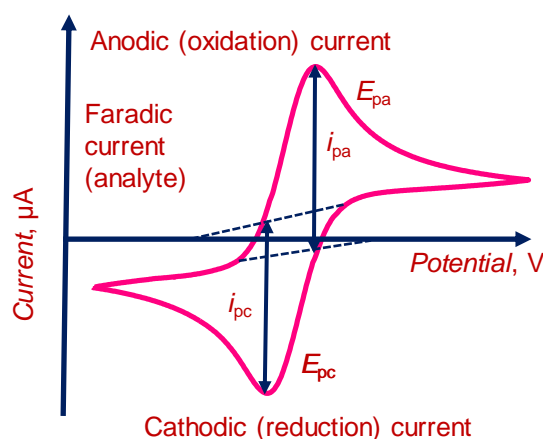
Figure 2-6. A typical cyclic voltammogram for a reversible electrode process.

2.4.6.2 Differential pulse voltammetry

A differential pulse voltammetry (DPV) potential excitation waveform is shown in Figure 2-7a. In DPV, the difference in current sampled at the end and before the applied potential pulse is measured, then presented as a function of the base potential, stepwise increased with small increments between pulses. Eliminating the capacitive current component during electrochemical measurements is a significant DPV advantage. The pulse height is maintained between 10 and 100 mV above the base potential. This base potential serves to refresh analyte diffusion to WE.

The measured current difference against the base potential plot takes a peak-shaped form (Figure 2-7b), described by Eq. 2.3

$$\delta i = i(\tau) - i(\tau')$$
<div align="right">Eq. 2.3</div>

where i is the current, τ and τ' are pre-pulse and post-pulse widths recorded at each time interval (Figure 2-7a).

For reversible systems, the peak potential (E_p) corresponds to the half-wave potential ($E_{1/2}$) in hydrodynamic voltammetry or voltammetry at a microelectrode, while the peak height (i_p) corresponds to the concentration of the analyte. However, the more E_p deviates from $E_{1/2}$, the more irreversible the electrode process is. Under those conditions, the peak width increases, and its height decreases. Being more sensitive than linear scan voltammetry (LSV) and CV because of capacitive current minimizing, DPV is used for quantitative while LSV and CV are mainly used for qualitative determinations.
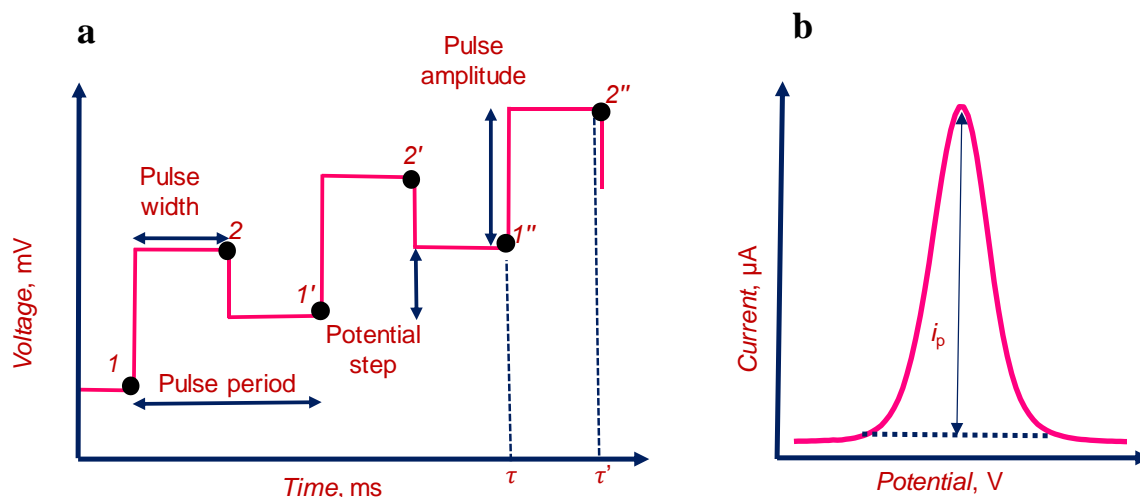
Figure 2-7. A DPV (a) potential-time waveform; each filled circle indicates the current sampling time (τ') just before pulse (1, 1', and 1") and (τ) just before the end of the pulse (2, 2', and 2"), and (b) a typical DPV voltammogram of a reversible redox system.

2.4.6.3 Electrochemical impedance spectroscopy (EIS)

Electrochemical impedance spectroscopy (EIS) is effective and sensitive in characterizing the electrode-electrolyte interface, which cannot be deeply understood using direct current (dc) techniques, including LSV, CV, and DPV. A capacity current, considered noise, always accompanies the faradaic current in electrochemical redox reactions. Enormous efforts have been made to minimize non-faradaic currents to understand electrochemical redox reactions better. For instance, CV was replaced with normal pulse voltammetry (NPV), square wave voltammetry (SWV), and DPV.[275] However, an effective approach to determine or separate faradaic current from that non-faradaic is possible only by EIS. EIS characterizes an electrochemical system at different constant potentials applied over a broad frequency range.[276] The electrode-electrolyte interface comprises a thin parallel capacitor built of the charged electrode and the lined up solution counter ions and solvent molecule dipoles. In a simple case of redox reactions, this interface is represented by the Randles equivalent circuit (Figure 2-8).[277] This circuit features four main components, vis., solution resistance, R_s, connected to electrical double-layer capacitance, C_{dl}, in parallel connected to a Warburg impedance, W, in series to the charge transfer resistance, R_{ct}. Impedance is a complex resistance that an alternating current (ac) encounters if flowing through an electric circuit. The ac magnitude and the phase angle shift (caused by ac wave perturbations) depend on the electrical components' configuration in a circuit. Electrochemical impedance is the

applied voltage-to-current ratio for an ac system. Like electrical resistance, impedance is the circuit's ability to resist the ac current flow.
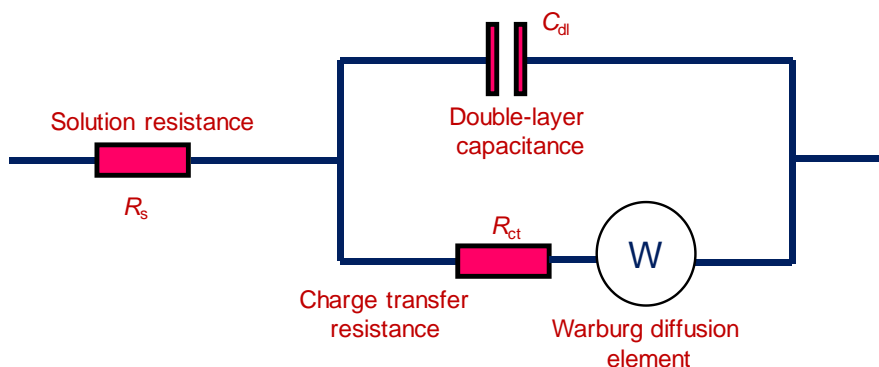
Figure 2-8. A Randles equivalent circuit.

Because of the ac wave nature, impedance is defined by two parameters, vis., the total impedance Z (in ohms) and the phase angle shift Φ (in degrees or radians). The Z value is a complex number expressed with the real, Z', and imaginary, Z'', impedance components. The Φ is defined as the constant-time shift between the two periodic waves of current and voltage in its unit's degrees. The impedance components and phase angle shift are depicted in the respective Nyquist (Figure 2-9a) and Bode (Figure 2-9b) plots.

The phase angle shift of a sinusoidal waveform is the angle Φ that the ac waveform has shifted from a certain reference point along the horizontal zero axis. The Φ value of an alternating waveform can vary from zero to its maximum time, t_{max}, of the waveform during one complete cycle. Moreover, it can be expressed as a *time shift* in seconds, representing a fraction of t_{max}.

Like voltammetric measurements, the impedance and the phase shift are measured with a computer-operated potentiostat by applying a constant potential and an ac voltage of small amplitude at different frequencies to the WE, then recording the resulting current wave. The potentiostat records the spectrum by calculating the Z, Φ, Z', and Z'' values for potential waves with different frequencies (Eq. 2.4)

$$E_t = E_0 \sin(\omega t) \qquad\qquad \text{Eq. 2.4}$$

where E_t is the potential at time t, E_0 is the potential amplitude, and ω (radian s^{-1}) is the angular frequency. Eq. 2.5 relates the angular frequency ω to frequency f (Hz).

a
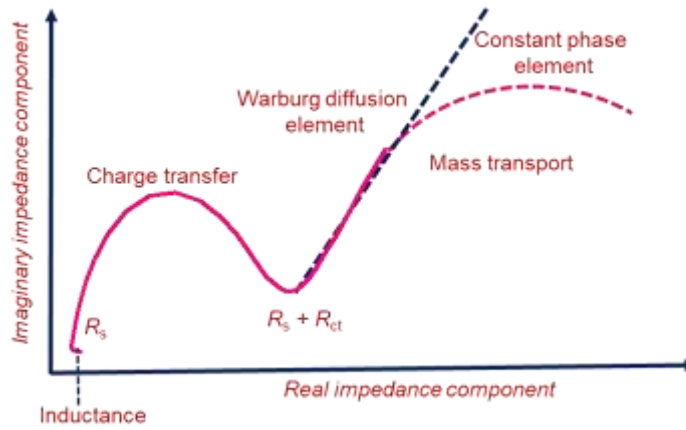
b
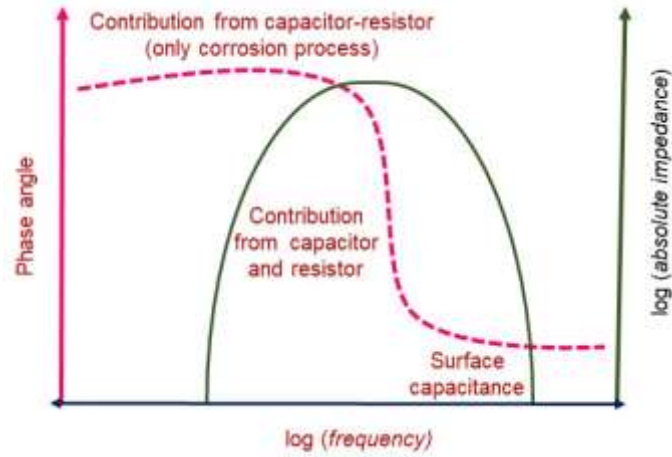
Figure 2-9. A typical (a) Nyquist and (b) Bode plot generated in an electrochemical impedance spectroscopy measurement.

$$\omega = 2\pi f \qquad\qquad \text{Eq. 2.5}$$

while in a linear system, the current signal at time t, I_t, is shifted in phase Φ and has a different amplitude, I_0 (Eq. 2.6).

$$I_t = I_0 \sin(\omega t + \Phi) \qquad\qquad \text{Eq. 2.6}$$

An expression analogous to Ohm's law (Eq. 2.7) allows calculating the impedance of the system:

$$Z = E_t/I_t = E_0 \sin(\omega t)/I_0 \sin(\omega t + \Phi) = Z_0 \sin(\omega t)/\sin(\omega t + \Phi) \qquad\qquad \text{Eq. 2.7}$$

So, the impedance, Z, is expressed in terms of the impedance amplitude, Z_0, and the phase shift, Φ.

For deep analysis of the EIS spectrum involving the R_{ct} and C_{dl} calculations, the Nyquist (Figure 2-9a) and Bode (Figure 2-9b) plots are analyzed by adopting a cell model represented by a suitable equivalent circuit. The equivalent circuit model can be partially or entirely empirical. Moreover, the equivalent circuit components may not directly be related to physical processes in the electrochemical cell. An empirical simplified Randles equivalent circuit represents the most common model adopted for the diffusion rate-controlled kinetic process. The R_s can be calculated for this circuit by reading the abscissa Z' value at the high-frequency intercept, while the low-frequency intercept provides the sum of the R_{ct} and R_s (Figure 2-9a). Moreover, this physical model can be modified based on the electrode process nature and electrode surface coating. The Warburg coefficient is added to the simplified Randles model for combining kinetic and diffusion processes.

The EIS is the most sensitive tool for measuring the current response to applied ac voltage, at different frequencies, for measuring the changes in electrode capacitance at the frequency and potential and at low electrolyte concentrations, but the potential-step amperometry or capacitive impedimetry (CI) is most commonly employed.[278] The CI is an effective tool to measure the changes in double-layer capacitance at an electrode and electrolyte interface under steady-state and flow-injection analysis conditions.

2.4.7 Computational calculations and simulations

The recent trend in analytical chemistry involves implementing green chemistry principles and procedures.[279] Among them, a growing interest is in using MIPs as green tools for developing analytical methods for determining biologically and environmentally important analytes for pharmaceutical and biotechnological applications. For that, a deep knowledge of the underlying processes of MIP preparation and operation, including its advantages and limitations, is necessary for the best implementation in analytical chemistry.

The optimum MIP devising requires appropriate instrumentation and considerable optimization input, generating significant waste products. Therefore, the preliminary computational simulation for the pre-polymerization complex formation in MIPs is helpful in significantly less use of solvents and reagents for preparing an optimized MIP.[280] The appropriate software allows performing theoretical computations and simulations of the MIP pre-polymerization complex composition and stoichiometry, and the molecular cavity, imprinted in the MIP, selectivity of interaction with the analyte and interferences molecules.

The most common modeling methods for optimizing MIPs are ab initio and semi-empirical methods.[281]

2.5 Instruments and procedures

2.5.1 Pretreatment of bare electrodes and preparation of MIP film-coated electrodes

Before electrochemical deposition of GABA-templated MIP films, typical Pt disk electrodes and Au ring-array thin-film IDEs [137] were cleaned, and then MIP films were deposited. The Pt electrodes were cleaned with the "piranha" solution for 10 min and then polished with a 0.05-μm diameter alumina slurry. Later, the electrodes were thoroughly washed with acetone, then deionized water to remove alumina particles before electrochemical measurements. The IDEs were electrochemically activated in 0.5 M H_2SO_4 by ten times potential linear cycling between 0 and 1.50 V vs. Ag quasi-reference electrode at a potential scan rate of 100 mV s^{-1} (Figure 2-10).
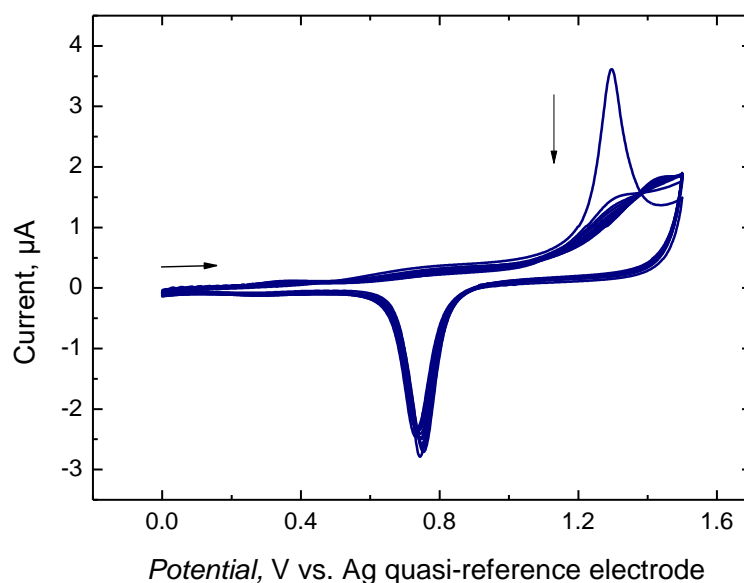
Figure 2-10. The CV curve of activation of the IDE in 0.5 M H_2SO_4 by ten times potential cycling between 0 and 1.50 V vs. Ag quasi-reference electrode at a potential scan rate of 100 mV s^{-1}.

Before electrochemical deposition of an (*E. coli* K-12)-templated MIP film, a glassy carbon electrode (GCE) disk of 7 mm in diameter was consecutively polished with the 1.0, 0.3, and 0.05-μm diameter alumina slurry, next rinsed with deionized water and then sonicated in ethanol for ~15 min. Then, GCE was dipped in the "piranha" solution for 10 min for reusing.

The Au-layered glass slides (7 × 21 mm) were prepared at the Institute of Electronic Materials Technology (Warsaw, Poland) by vapor depositing a thin (100 nm thick) Au layer over a thin (15 nm thick) Ti underlayer. Before each determination, the Au layered-glass slides were cleaned with oxygen plasma for 10 minutes. These slides were then used as supports for the deposition of MIP films for SEM, AFM, and IR spectroscopy characterizations.

2.5.2 Instrumentation and procedures for SEM, STEM, AFM, and CM characterizing of GABA- and (*E. coli* K-12)-templated MIP films, and polyacrylamide gels

The nano- and microgels were first dispersed in water and then drop-coated onto Au-layered glass slides to prepare gel films. The films were then SEM imaged at the 5-kV acceleration voltage and a working distance of 5 mm without coating the samples. The EDX spectra were recorded for at least 50 s with an acceleration voltage of 5 kV and a working distance of 5 mm. A NanoSEM 450 microscope (FEI Nova) was used to examine the morphology of the micro- and nanogel films.

The STEM was used to analyze the nano- and microgels with and without core-shell colloidal particles. Samples for the STEM analysis were prepared by dropping the respective colloid on an amorphous carbon film supported on a 300-mesh copper grid. The samples were STEM imaged on an FEI Talos F200X transmission microscope at the 200-kV acceleration voltage in the scanning mode using a high-angle annular dark-field (HAADF) detector. Moreover, the EDX spectroscopy experiments were carried out on a Brucker BD4 instrument to map the sample's elemental distribution.

The (*E. coli* K-12)-templated MIP films were SEM imaged, and EDX spectra recorded on a JMS-IT500HR microscope (JEOL, Japan) equipped with the Ultim Max 170 EDS detector (Oxford Instruments, UK).

The thickness and roughness of GABA-templated MIP films were determined using a MultiMode 8 AFM microscope equipped with a Nanoscope V controller and Multimode v 8.15 software, both from Bruker. Phosphorous-doped Si tip and RTESP cantilevers of 350-kHz resonant frequency and the force constant, $k = 43.3$ N m^{-1} (Bruker), were used with the ScannAssyst™ mode sample imagining. For roughness measurements, four sample points were imaged at (6×6) μm^2. Then average roughness was calculated from the results for each image. The as-prepared, (*E. coli*)-extracted, and (*E. coli*)-bound MIP film-coated

GCEs were AFM imaged in the air using a Bioscope Resolve AFM microscope (Bruker) with SNL-C tips at the Peak Force Tapping (PFT) mode.

For confocal microscopy (CM) imaging, cells were stained with calcein-AM (Merck) and propidium iodide (Merck). Calcein-AM is a green dye staining living cells selectively; it was added to the medium at a final cell concentration of 1 µg/mL. In dead cells, propidium iodide stains nucleic acids red. Its final concentration was 0.1 mg/mL. Samples were incubated with the dyes for 20 min and then imaged with CM on a Nikon A1 inverted confocal microscope (Nikon Instruments) and NIS-Elements software (Nikon Instruments). The signals from viable and dead cells were recorded using FITC and TRITC settings, respectively. The 3D images were recorded using the Z-stack mode of NIS Elements software. The 3D images were further analyzed and processed using Imaris software (Oxford Instruments).

2.5.3 Instrumentation and preparation of polyacrylamide microgel dispersions for DLS measurements

The hydrodynamic microgel particle diameters were determined with DLS using a Zetasizer NS instrument (Malvern Instruments, Ltd.). The microgel suspension (0.1%, *w/v*) was prepared using Milli-Q water (pH = 7.4) and then sonicated for 15 min before the DLS analysis. The 0.1% *w/v* gel suspension was chosen to avoid concentration-dependent effects, e.g., mutual particle interactions, etc., as the Zetasizer Nano User Manual recommends for relatively big particles. The measurements were repeated thrice for each sample, and the average size value, Z_{avg}, was reported.

2.5.4 Quantum-chemistry calculations for GABA molecular imprinting

Quantum-chemistry calculations for optimizing the composition and structure of the GABA pre-polymerization complex were performed using the workstation with four Intel dual-core processors and Gaussian 09 software (Gaussian, Inc., CT, USA).[282] The Gibbs free energy changes associated with pre-polymerization complex formation were obtained using the density functional theory (DFT) with the B3LYP functional and 6-31G* basis set. These computations were performed for five functional monomers (Scheme 2.1), namely, *p*-bis(2,2'-bithien-5-yl)methyl-*o*-catechol **FM1**, *p*-bis(2,2'-bithien-5-yl)methylbenzoic acid **FM2**, *p*-bis(2,2'-bithien-5-yl)methylaniline acetate **FM3**, *p*-bis(2,2'-bithien-5-yl)methyl phenol 2-hydroxy acetamide ether **FM4**, and *p*-bis(2,2'-bithien-5-yl)methyl aniline **FM5**.
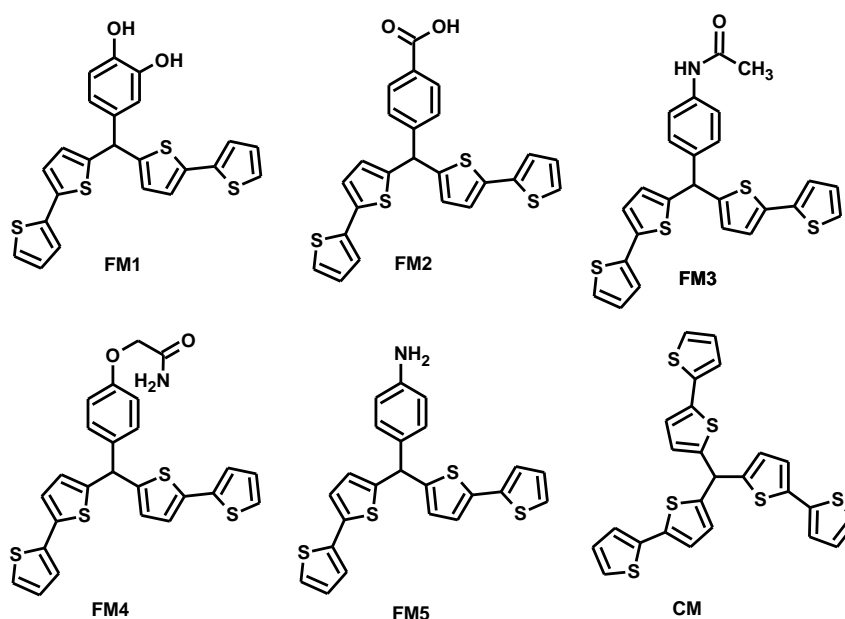
Scheme 2.1. Structural formulas of **FM1** to **FM 5** functional monomers, as well as the 5,5',5"-methanetriyltris(2,2'-bithiophene) cross-linking monomer **CM**.

2.5.5 Synthesis of functional monomer FM4

The *p*-bis(2,2'-bithien-5-yl)methyl phenol 2-hydroxy acetamide ether **FM4** functional monomer was synthesized, first, by mixing 4-bis(2,2'-bithiophen-5-yl)methylphenol (1.3 mmol), and K_2CO_3 (13.1 mmol) in acetone (80 mL) in a round-bottom flask for 30 min under continuous N_2 purge. Next, 2-bromoacetamide (4 mmol) was added to the reaction mixture and then stirred for another 16 h at 60 °C. Afterward, this mixture was filtered, and then the solvent was evaporated at room temperature. Finally, a crude solid product was purified by liquid chromatography on a silica gel column using hexane as the eluate.

The 5,5',5"-methanetriyltris(2,2'-bithiophene) **CM** synthesis is described elsewhere.[283]

2.5.6 In vitro cytotoxicity assays for polyacrylamide nanogels

The viability assays were performed using MTT proliferation/metabolic activity assays, a culture medium including 1 mM MTT. The cytotoxicity assays were carried out for polyacrylamide nanogels using two different cancer cell lines, MDA-MB-231 (triple-negative breast cancer) and HeLa (cervical cancer).

The MTT assay was executed using ~5000 cells/well for MDA-MB-231 and 10,000 cells/well for HeLa (controlled with a Countess II Cell Counter) and seeded into a 96-well plate (Greiner Bio-One). Next, cells were incubated for 24 h at 37 °C in an incubator. Afterward, the medium was removed, and microgel particles at different concentrations (20,000 ng/mL – 39 ng/mL) were added to the cell fresh medium. The experiments were thrice repeated for each concentration. Subsequently, the medium was replaced with a culture medium, which was 1 mM in MTT. Moreover, negative controls were made with 1% Triton-X 100. Cells were incubated for 4 h at 37 °C. Then, the solutions were replaced with DMSO and incubated for 10 min. The absorbance of each well was measured at 540 nm using a Synergy HTX multimode reader (BioTek). The schematic of the spectrophotometer is shown in Figure 2-11.

2.5.7 Instrumental details and electrochemical conditions for preparation of GABA- or (*E. coli* K-12)-templated MIP films and polyacrylamide microgels particles

2.5.7.1 Electrochemical conditions for preparing GABA-templated MIP films

Electrochemical measurements were conducted to fabricate a GABA-templated MIP using a BioLogic SP150 potentiostat controlled by EC-Lab BioLogic software. The IDEs were purchased from MicruX Technologies. The ring array electrode contained 12 pairs of gold IDEs (10/10 μm, electrode/gap). A 0.7-mm diameter Pt disk electrode, a Pt wire, and an Ag wire were used as the WE, CE, and quasi-reference electrode, respectively.

The GABA-templated MIP film was prepared using *bis*-bithiophene derivatized functional monomer, i.e., *p*-bis(2,2'-bithien-5-yl)methyl phenol 2-hydroxy acetamide ether **FM4**, to fabricate an artificial polymer receptor for GABA.

The MIP thin films were deposited on Pt disk electrodes and IDEs using the solution of 0.1 mM GABA, 0.2 mM **FM4**, 0.1 mM **CM**, and 0.1 M (TBA)ClO$_4$ in acetonitrile and 0.1 M H$_2$SO$_4$ (9 : 1, *v/v*) under potentiodynamic conditions. The potential was cycled six times between 0.0 and 1.30 V vs. Ag quasi-reference electrode at a scan rate of 50 mV s^{-1}. The non-imprinted polymer films were deposited on the Pt electrode and IDEs under similar conditions but without the GABA template.
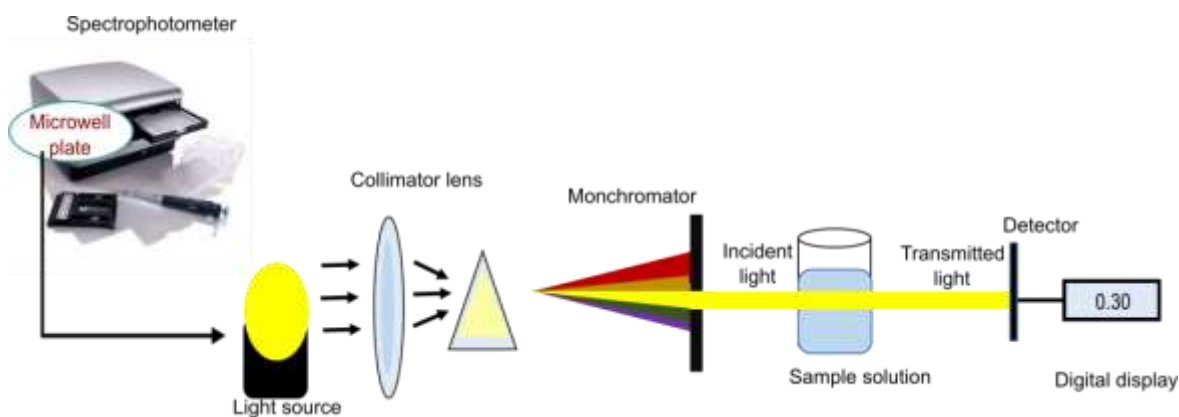
Figure 2-11. A schematic of a spectrophotometer setup.

2.5.7.2 Electrochemical conditions for preparing (*E. coli* K-12)-templated MIP

For the (*E. coli* K-12)-templated MIP film-coated electrodes, the electrochemical measurements were carried out with a BioLogic SP-50 potentiostat. The three-electrode cell system was used for simultaneous electropolymerizing and depositing (*E. coli* K-12)-templated MIP films. A 7-mm diameter disk GCE was used as the WE, and a Pt wire coil and an Ag wire as the CE and quasi-reference electrode, respectively. The selective to the *E. coli* K-12 strain MIP was fabricated using 2-aminophenyl boronic acid (2-APBA) as the primary functional monomer and aniline (ANI) as the cross-linking monomer.

The E2152 was used to template the MIP. The three-electrode cell system was used for simultaneous electropolymerizing and depositing E2152-templated MIP films. A 7-mm diameter disk GCE, a Pt wire coil, and an Ag/AgCl electrode (1 M KCl) were used as the respective WE, CE, and RE. The MIP and NIP thin films were potentiodynamically deposited on the GCE by cycling the potential between -0.20 and 1.10 V vs. Ag/AgCl at 25 mV s $^{-1}$ in the 5-mL sample solution of 2.5 mM 2-APBA and 10 mM ANI monomers, and 0.01 M KCl supporting electrolyte, with a 200-µL sample of E2152 of optical density of 0.08.

2.5.7.3 Electrochemically initiated synthesis of polyacrylamide microgels

A BioLogic SP-300 potentiostat was used for potentiostatic initiating the polymerization of polyacrylic microgels. Electrochemical experiments were carried out using a ~30-mL homemade conically-shaped three-neck glass cell. A 1-mm diameter Pt wire, an Ag/AgCl electrode, and a seamless Pt cylinder electrode were used as respective WE, RE, and CE.

For electrochemically initiated microgel preparation, first, CV properties of the 25 mM NIPAM, 25 mM MA, 50 mM BIS, 25 mM APS, and 0.1 M KNO_3 solution were examined under an oxygen-free atmosphere. For that, the WE potential was linearly cycled between 0 and -1.40 V vs. Ag quasi-reference electrode at a scan rate of 50 mV s^{-1} (Figure 2-12). An irreversible cathodic peak appeared at ~0.80 V vs. Ag quasi-reference electrode. It corresponded to APS electroreduction. In effect, soluble persulfate free radicals were formed at the electrode surface. These radicals initiated the polymer chain growth upon interaction with monomers present. A cathodic current was pronounced at very high negative potentials. After determining the APS decomposition potential, electrochemical conditions of the microgel synthesis were established.

For electrochemical polymerization initiation, the WE potential was kept at -0.60 V vs. Ag quasi-reference electrode. Typically, the solution of 25 mM NIPAM, 25 mM MA, 25 mM APS, and 50 mM BIS was used for the microgel synthesis. Sufficiently high solution conductivity was afforded with the 0.1 M KNO_3 supporting electrolyte. Before electrochemically initiating the polymerization, the solution was deoxygenated with the 20-min argon purge. Moreover, during all experiments, argon was continuously purged through the solution. Monomers of a similar combination were polymerized in a neutral solution.

The core support NPs coated with the microgel shell were centrifuged at 20,000 r.p.m. for 20 min. This centrifugation was thrice repeated to remove the unreacted substrates completely. Finally, the microgels were stored in Milli-Q water for further characterization. Without electrochemical initiation, the solution for polymerization has not gelated.

For the electrosynthesis of gel films over MNPs, a 2.5-mL sample of 3 mg mL^{-1} MNPs dispersion was added to a 25-mL sample of the solution for polymerization, which was 25 mM in MA, 25 mM in NIPAM, and 50 mM in BIS.

A 0.5-mL sample of a silica NPs suspension was added to the 20-mL sample of the 25 mM MA, 25 mM NIPAM, and 50 mM BIS solution during core-shell particle synthesis. Before synthesizing a microgel film, 500-nm diameter silica NPs were first modified using the 3-(trimethoxysilyl)propyl methacrylate to prepare the acrylate functionalized silica NPs. For that, ethanol (15 mL) and ammonia solution (1.5 mL) were placed in a round-bottom flask (100 mL) connected to a refluxing system. After adding 3-(trimethoxysilyl)propyl methacrylate (10 μL) and silica NPs (400 mg), the system was refluxed at 90 °C overnight to ensure covalent attachment of the coupling agent to the surface of the silica NPs. After this modification, the resulted surface-modified silica NPs were suspended in anhydrous ethanol by vigorous shaking in an ultra-sonication bath (10 min, room temperature). Then,

dispersed silica NPs were centrifuged at 10,000 r.p.m. for 10 min, and then the supernatant solution was discarded. This procedure was repeated five times for purification and dehydration of the NPs, and then those were stored in anhydrous ethanol (2.5 mL).
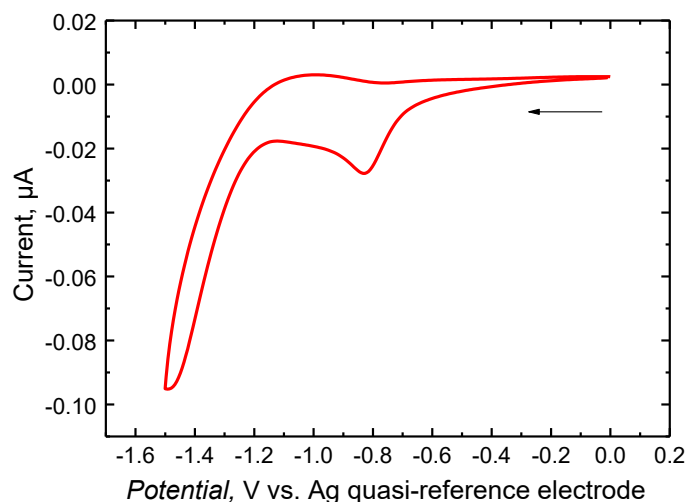
Figure 2-12. The cyclic voltammogram recorded at the 0.7-mm diameter Pt disk electrode in the solution of 25 mM MA, 25 mM NIPAM, 50 mM BIS, 25 mM APS, and 0.1 M KNO$_3$ at a scan rate of 50 mV s^{-1}.

Electrosynthesis conditions were optimized to improve the size and morphology of microgels further. Toward that, the APS initiator and BIS cross-linking monomer concentrations were optimized. Moreover, the electrolyte effect was evaluated by synthesizing microgel in the presence of two different electrolytes, i.e., 0.1 M KNO$_3$ and 0.1 M KCl. Finally, the solution of 20 mM NIPAM, 20 mM MA, 10 mM BIS monomers, and 10 mM APS initiator was used for nanogel electrosynthesis. A similar monomer combination was used to prepare polymer shells over inorganic NPs cores. Once again, the NPs were surface modified before the electrodeposition of the polymer shell, as mentioned above.

2.5.8 Other instrumentation and procedures

The microgels' thermal stability was investigated using a Mettler Toledo TGA/DSC1 thermogravimetric analyzer. In the thermogravimetric analysis (TGA), the sample mass change is measured as a function of temperature. During this analysis, a sample is heated in a controlled gaseous environment, and the temperature is increased at a programmed rate for a known initial mass of the sample. Consequently, the sample mass changes are recorded

periodically at regular intervals as a function of temperature. The resulting thermogravimetric curve shows the mass loss against temperature.

The microgel samples were first dried in a vacuum at room temperature for 24 h. Next, an alumina crucible was used to place samples in the furnace. During measurements, samples were purged with nitrogen at a flow rate of 10 mL min^{-1} and heated from room temperature to 1000 °C at a constant temperature gradient of 10 °C min^{-1}. The sample mass varied between 5 and 10 mg.

PM-IRRAS spectra were recorded with a Vertex 80v spectrophotometer equipped with a PMA50 module and a nitrogen-cooled MCT (Hg-Cd-Te) detector (Bruker). The angle of incidence of the *p*-polarized light beam was 83° against the normal to the plane of the Au-(polymer film) coated glass slide. This slide was mounted in a dedicated holder. Fourier-transform infrared (FTIR) spectroscopy with one-reflection ATR apparatus was used for analyzing microgel samples. For PM IRRAS investigations, polymer film's spectra were recorded with a 2 cm^{-1} resolution. For each spectrum, 1024 scans were acquired. Measurements were performed under decreased (6 hPa) pressure.

For X-ray photoelectron spectroscopy (XPS) characterizing the GABA-imprinted and non-imprinted polymer films, samples were potentiodynamically deposited on gold-layered glass slides by 6 potential cycles between 0 to 1.30 V at 50 mV s^{-1}. Similarly, (*E. coli*)-templated MIP films were deposited on 7-mm diameter disk GCEs by applying potential cycles between 0 and 1.0 V at 25 mV s^{-1}. The XPS experiments were performed with monochromatic Al K α (*hv* = 1486.4 eV) radiation using a PHI 5000 Versa Probe-Scanning ESCA microprobe instrument (ULVAC-PHI).

Chapter 3

3. Results and Discussion

3.1 Molecularly imprinted polymer as a synthetic receptor mimic for capacitive impedimetric selective recognizing *Escherichia coli* K-12

3.1.1 Selecting functional monomer for MIP preparation

We selected 2-aminophenylboronic acid (2-APBA) for electrochemical fabrication of an MIP film templated with *E. coli* (E2152) bacteria (Scheme 3.1). The aminophenyl boronic functional groups are often used for imprinting biomolecules and cells.[284] Basically, the presence of the boronic acid group is of primary importance due to its chemical recognition abilities.[285] The synergistic interactions of boronic acid groups with *cis*-diol groups of a microbe membrane allow the formation of a polymeric network around specific bacteria cells.[286] The boronic acid groups to bacteria membrane surface affinity arises from their interactions with *cis*-diols of the surface enriched peptidoglycans and lipopolysaccharides. A particularly appreciated feature of using aminophenyl boronic groups is the reversibility of the (*cis*-diol)-boronic group complex, helpful in easy template removal, thus the regeneration of the recognition cavities and chemical affinities in MIPs.[287, 288]

2-Aminophenylboronic acid
Functional monomer

Aniline
Cross-linking monomer
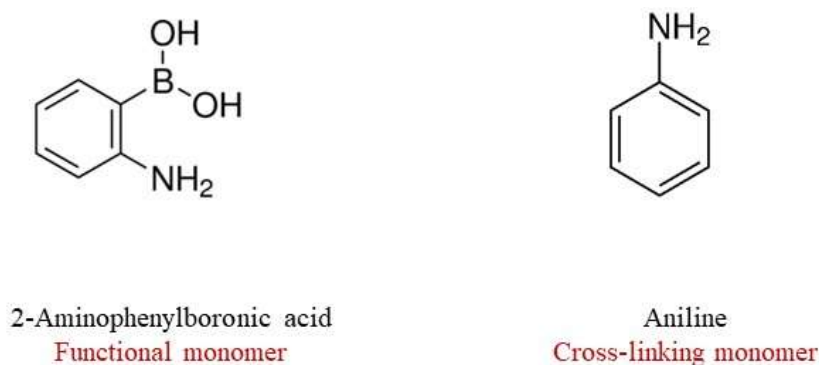
Scheme 3.1-1. The structural formulas of 2-aminophenylboronic acid (2-APBA) and aniline (ANI) monomers.

The role of aniline (ANI) was to cross-link functional monomer molecules for molecular imprinting of the *E. coli* (E2152) strain (Scheme 3.1-1). A low MIP selectivity often results from the lack of defined analyte binding sites. Then, non-specific interactions involved generate responses similar to interactions in chemosensors. Therefore, boronate functionalized conducting polyANI is used to generate selective binding sites.[289] However, they are highly unsuitable for encapsulating bacteria because the synthesis of conductive polyANI requires an acidic solution condition.[290] Moreover, the binding affinity of the phenylboronic acid group is decreased as solution pH is lowered below neutral solution pH.[291] Therefore, here, a conductive MIP film was prepared using 2-aminophenylboronic acid (2-APBA), the synthetic receptor most suitable for saccharides, and ANI as the cross-

linking monomer in a neutral solution for selective enzyme-free detection and determination of the E2152 strain of *E. coli* (Scheme 3.1-2)
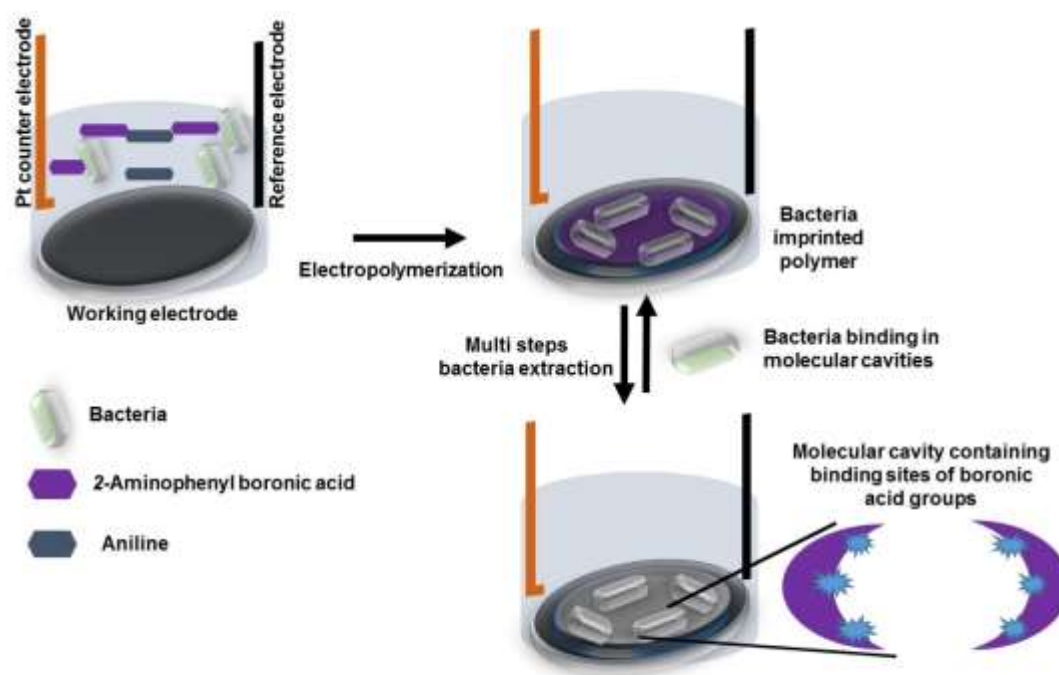
Scheme 3.1-2. The flowchart of *E. coli* E2152 imprinting by electro-copolymerization of ANI and 2-APBA in 0.01 M KCl on a 7-mm diameter disk glassy carbon electrode (GCE).

3.1.2 Preparing a film of a polymer molecularly imprinted with *E. coli* E2152 cells

The multi-cyclic potentiodynamic curve in Figure 3.1-1a represents electro-oxidation of the 2-APBA and ANI monomers in the presence of the E2152 cells. A broad irreversible anodic peak at ~0.85 V vs. Ag/AgCl corresponds to 2-APBA electropolymerization.[292] The non-conducting reduced leucoemeraldine form conversion into the conducting intermediate oxidized emeraldine form started at 0.20 V vs. Ag/AgCl. Subsequently, it turned to fully oxidized pernigraniline form at 0.65 V vs. Ag/AgCl.[292] However, only one anodic peak at 0.65 V vs. Ag/AgCl in successive cycles indicated the emeraldine-base form presence with a relatively low protonation and deprotonation rate in a neutral solution.[293]

This cycling was accomplished to attain full coverage of the MIP film surface with bacteria cells and generate the MIP film of sufficient conductivity. The potentiodynamic anodic and cathodic peak currents increased in the potential range of -0.20 to 0.85 V vs. Ag/AgCl after the 5th cycle (Figure 3.1-1b). This increase indicates that more than 5 potential cycles are required to prepare electroactive conductive MIP film. Moreover, the goal was

to prepare the MIP to recognize bacteria concerning their size, shape, and surface functionalities. Therefore, the potential was continuously cycled 12 times to deposit an MIP film capable of entrapping the bacteria cells.
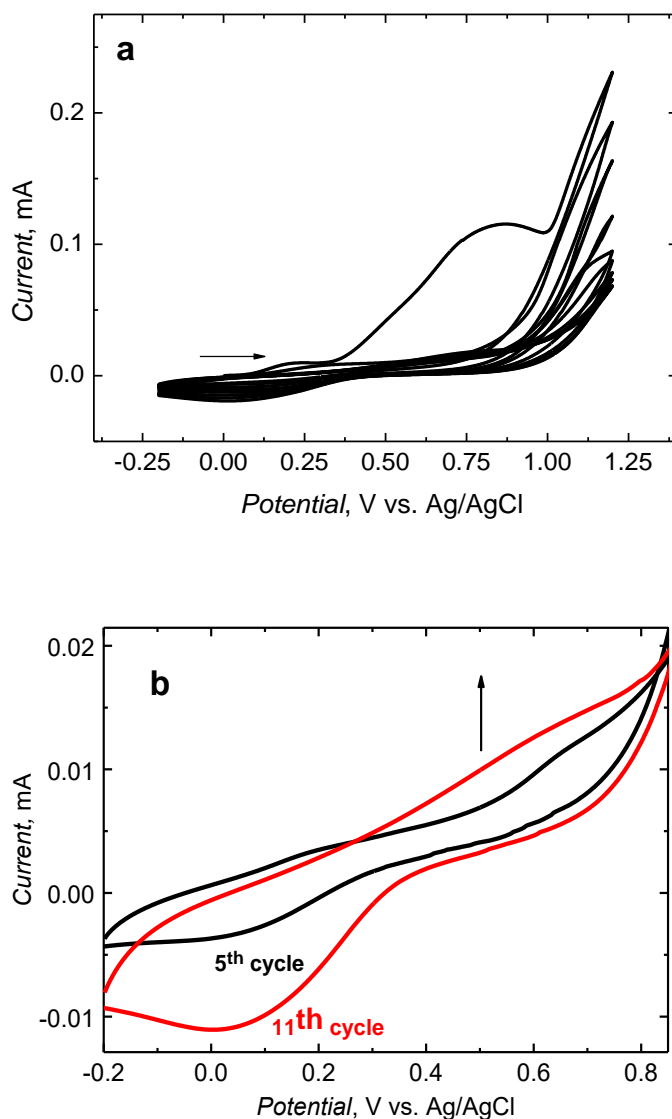
Figure 3.1-1. (a) The multi-cyclic potentiodynamic curve for the GCE (0.38 cm^2) in the 5 mL 0.01 M KCl solution of 2.5 mM 2-APBA, 10 mM ANI, and 200 µL of 5×10^9 cells mL^{-1} E2152 suspension at a scan rate of 25 mV s^{-1}. (b) The selected potentiodynamic curves showing the change in MIP film conductivity with the number of potential scans. The cycle number is indicated at each curve.

3.1.3 Imaging of bacteria-imprinted film

MIP film partial covering with bacteria cells evidences their successful imprinting. The AFM and SEM images clearly show effective E2152 embedding in the MIP (Figure 3.1-2).

The MIP layers partially covering the 3 µm long 0.8 µm diameter rod-shaped E2152 are seen in the SEM (Figure 3.1-2a and 2a') and AFM (Figure 3.1-2b and 2b') images. During the electropolymerization, the boronic acid residues interact with the bacterial outer membrane (*cis*-diol)-containing molecules, including sugar molecules.[294] That increases the cell adhesion to the polymer surface.[295] This reversible covalent affinity helped capture the bacteria cells within the MIP network during imprinting. Hence, after bacteria template removal, the MIP film was expected to recognize target bacteria by their shape, size, and molecular interactions between its boronic acid groups and surface glycoproteins of the bacteria.
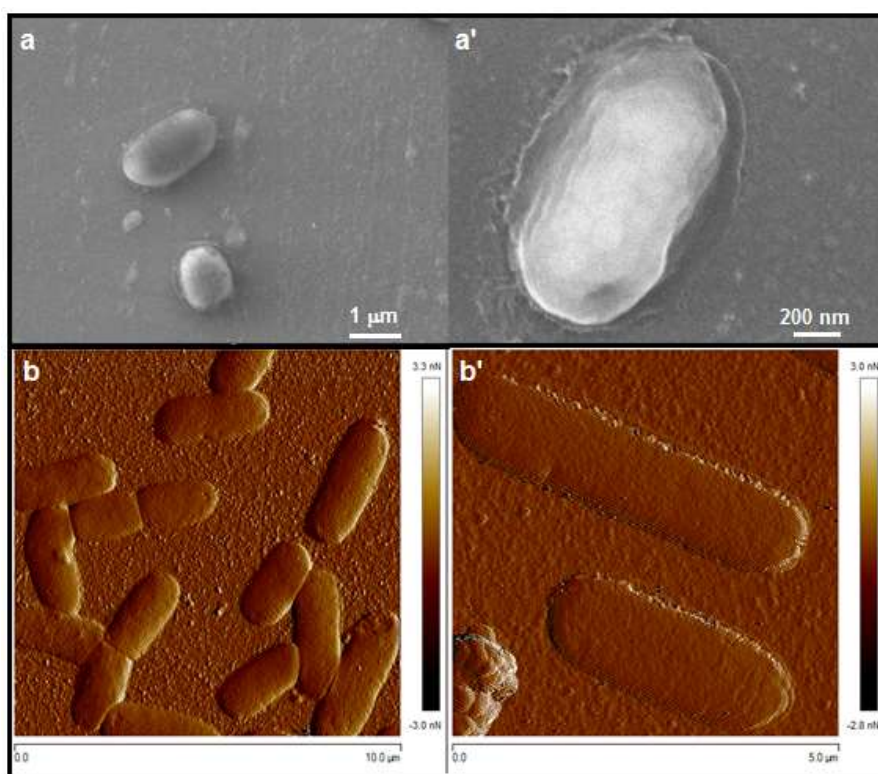
Figure 3.1-2. (a, a') SEM and (b, b') AFM images of the GCE coated with the *E. coli* E2152 imprinted film before washing.

At the early stage of the present research, another bacteria surface imprinting approach was examined. In this approach, first, bacteria cells were immobilized on the electrode surface, and then polymer film was grown around the bacteria immobilized. However, it appeared that the polymer was also growing on top of the bacteria. That was supported by the EDX measurement of the bacteria imprinted polymer. The boron element was present on the top of the bacteria imprinted (Figure 3.1-3b). Surprisingly, the boron element was

absent in the close vicinity of the bacteria cells (Figure 3.1-3c). In this imprinting, bacteria removal was difficult. Therefore, this approach was abandoned (Figure 3.1-3).
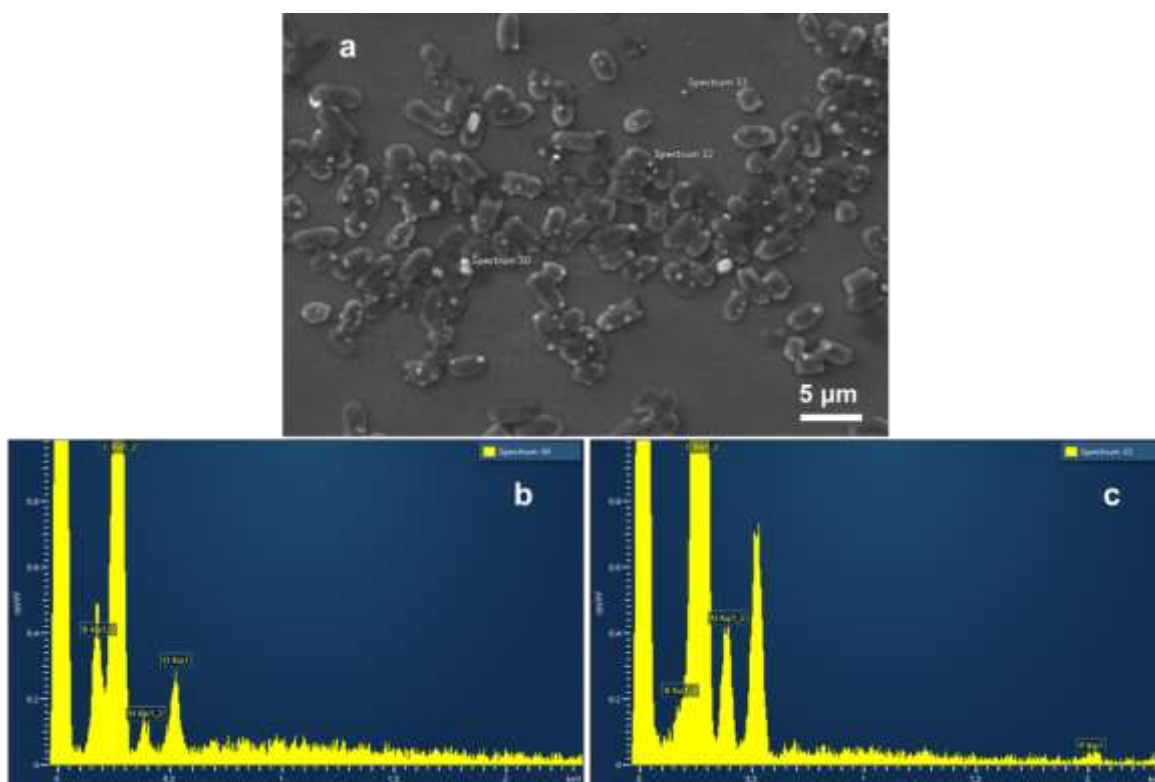
Figure 3.1-3 (a) The SEM image of surface-imprinted *E. coli* E2152 before bacteria extraction. EDX spectra of the bacteria-templated MIP with the boron element mapping (b) at the top of bacteria and (c) in the close bacteria vicinity.
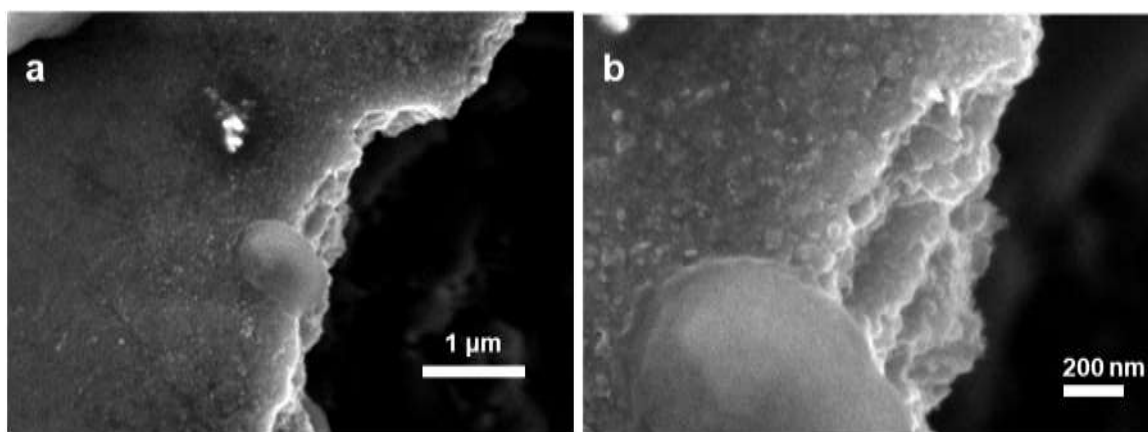
Figure 3.1-4. Different-magnification SEM images of the E2152-templated MIP film-coated GCE confirming that the bacteria protrude the polymer surface. The sample was imaged after scratching the MIP surface with a Teflon^TM spatula.

Furthermore, to confirm the bacteria encapsulation inside the film and not sitting on its top, the sample was SEM imaged after scratching the polymer surface with a Teflon™ spatula (Figure 3.1-4). However, images were recorded after the 3rd, 6th, and 12th potentiodynamic cycles of electropolymerization to ensure partial surface coverage. In the case of 12 cycles, the polymer film overgrowth around bacteria was visible (Figure 3.1-2a and 2a'). During the 3rd and 6th cycles, bacteria stayed on top of the thin polymer film (Figure 3.1-5).
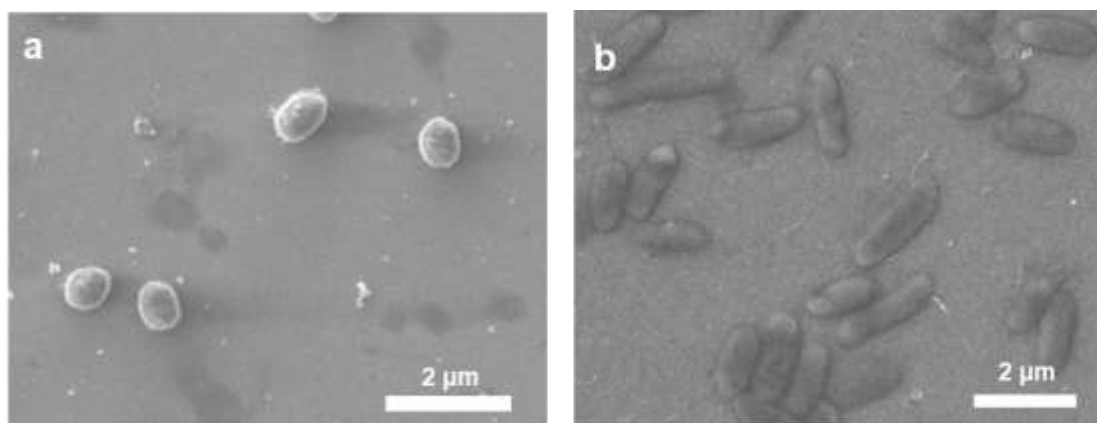
Figure 3.1-5. SEM images of the E2152-templated MIP film-coated GCE prepared after (a) the 3rd and (b) the 6th potential cycle at a scan rate of 50 mV s^{-1}.

3.1.4 Bacteria cells removing from the MIP film for emptying imprinted cavities

After MIP film preparation, many mild conditions were attempted for the encapsulated bacteria template extraction, including sonication and washing in water,[296] soaking in alkaline or acidic solutions, incubating with fructose solution (20 mM) as fructose has a strong affinity for boronic acid groups.[288] Unfortunately, these mild conditions were ineffective for removing encapsulated bacteria cells.

Therefore, the following harsher multistep extraction procedure was adopted. First, the MIP film was 2 h treated with 2 mg mL^{-1} lysozyme enzyme in PBS (pH = 7.4) for lysing the *E. coli* E2152 strain. The lysozyme helped break the intermolecular bonding of boronic acid residues of MIP with glycoproteins on the *E. coli* surface (Figure 3.1-6a). The electrode was then immersed in 10% Triton X to remove the bacteria membrane debris and the lysozyme enzyme excess from the MIP film surface. Afterward, the MIP film was extensively rinsed with deionized water. Finally, it was overoxidized at +0.98 V vs.

Ag/AgCl in 0.1 M NaOH for 20 min to completely remove the bacteria cells. Each extraction step was monitored with SEM imaging.
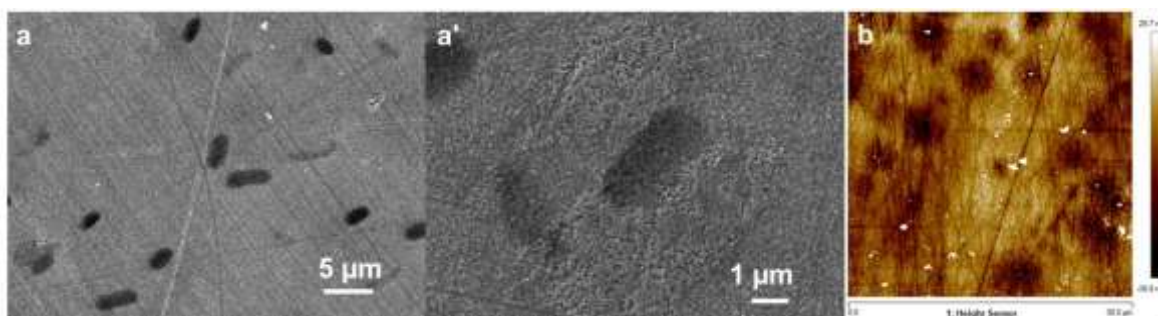
Figure 3.1-6. (a and a') The SEM image at two different resolutions and (b) the AFM image of the E2152-extracted MIP film-coated GCE.
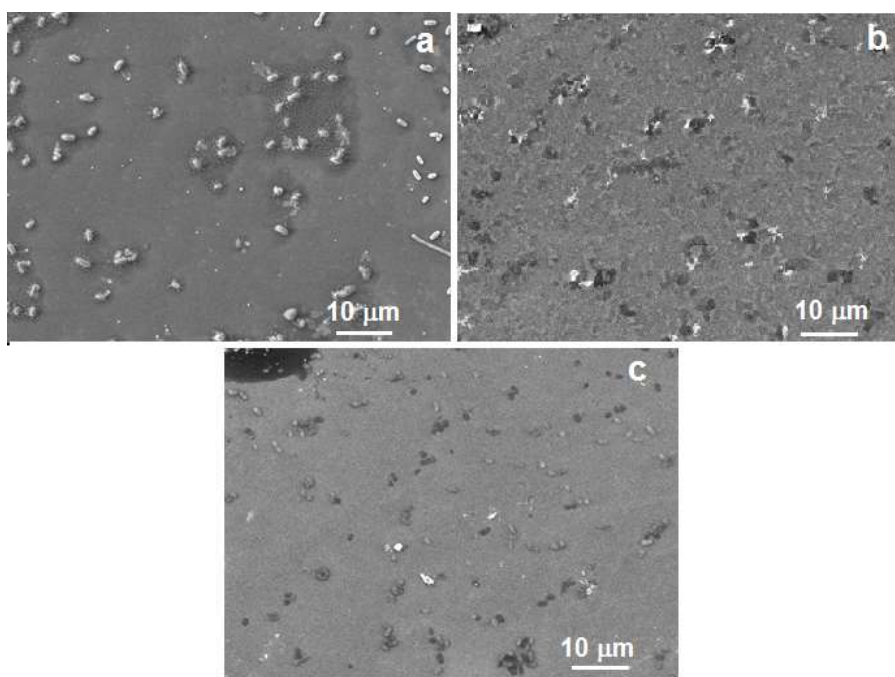
Figure 3.1-7. SEM images of the E2152-templated MIP film-coated GCE after different attempts of bacteria extraction, including (a) overoxidation at +0.98 V vs. Ag/AgCl for 20 min in 0.1 M NaOH, (b) lysozyme treatment followed by rinsing with ethanol, and then Triton X-100, and (c) lysozyme treatment followed by rinsing with ethanol.

Worth mentioning, missing any step in the above extraction procedure, such as direct overoxidation of the MIP film at a constant potential of +0.98 V vs. Ag/AgCl for 20 min in 0.1 M NaOH (Figure 3.1-7a) or its only treatment in 2 mg mL^{-1} lysozyme for 2 h (Figure 3.1-7b), or lysozyme treatment followed by rinsing with ethanol (Figure 3.1-7c), resulted in no bacteria extraction. As the consequence of efficient bacteria template removal from the

MIP film, the SEM (Figures 3.1-6a and 6a') and AFM images (Figure 3.1-6b) show the complementary cavities vacated.

GCEs coated with the bacteria-extracted MIP films were stored in 0.1 M PBS (pH = 7.4) until further use.

3.1.5 Electrochemical characterizing of E2152-templated and E2152-extracted MIP films

Further, EIS and DPV were used to characterize the E2152-templated and E2152-extracted MIP films. Figures 4a, 4b, and 4c show changes in the charge transfer resistance and DPV peak incurred by the presence of 5 mM $K_3[Fe(CN)_6]$ and 5 mM $K_4[Fe(CN)_6]$ in 0.1 M PBS (pH=7.4), for the MIP film-coated electrode before and after bacteria removal. The MIP film's charge transfer resistance determined from the Nyquist plot before bacteria extraction was high (Figure 3.1-8a). Presumably, the E2152 cells' entrapment in the film blocked the electron transfer between the redox probe molecules in the solution and the electrode substrate. In contrast, the charge transfer resistance of this film-coated electrode with E2152 cells removed was relatively small (Figure 3.1-8b). A reason could be that the removal resulted in the MIP film poration, causing the oxidation current of the redox probe to increase (Figure 3.1-8c).

Moreover, insets to Figures 3.1-8a and 3.1-8b propose equivalent circuits for the MIP film-coated electrode system before and after E2152 extraction. The solid curves represent the best-fit curves based on the proposed circuits. For the best simulation, two Randles type circuits were connected in series to represent the contribution of the interface parameters, including bulk solution resistance (R_s), double-layer capacitance (C_{dl}), contact capacitance (C_c), the charge transfer resistance (R_{ct}), and the Warburg diffusion element (W) for the MIP film-coated glassy carbon electrodes (GCEs). In these circuits, both the C_{dl} and C_c are in parallel connected with R_{ct} to represent the faradic transport processes and the charge transfer kinetics of the redox probe ions transition at the polymer-electrolyte solution interface. Moreover, because of expected porosity in the MIP film, the pseudocapacitive element, vis., the constant phase element (CPE), represents the pure capacitive elements C_{dl} and C_c.[297] The determined R_{ct} value before and after E2152 extraction was 38.54 and 1.20 kΩ, respectively, for the MIP film-coated electrodes. This noticeable R_{ct} decrease appreciably contributed to the double-layer capacitance change due to bacteria encapsulation within the MIP film and then extraction. Moreover, a significant decrease in

R_{ct} reflects the considerable increase in the rate of diffusion of redox probe ions through the MIP because of the cavities present in the MIP.
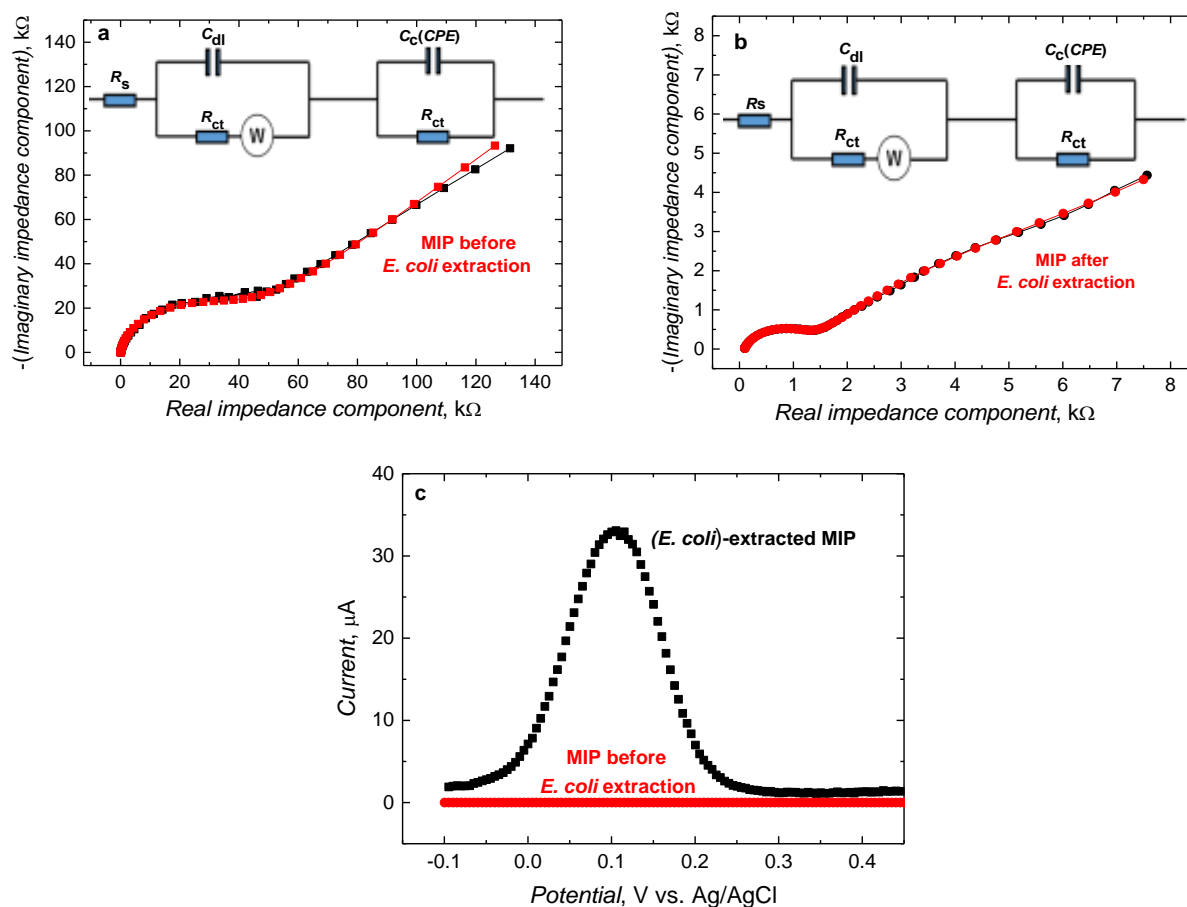
Figure 3.1-8. The Nyquist plots for the (a) E2152-templated MIP film-coated GCE and (b) E2152-extracted MIP film-coated GCE. (c) The DPV curves for the E2152-templated and E2152-extracted MIP film-coated GCE in 5 mM $K_4[Fe(CN)_6]$ and 5 mM $K_3[Fe(CN)_6]$ in 0.1 M PBS (pH=7.4).

3.1.6 XPS analyzing E2152-templated and E2152-extracted MIP films

Surprisingly, the boron band is absent in the high-resolution XPS spectrum of the MIP film before bacteria extraction. However, this band appears only after bacteria removal (Figure 3.1-9), confirming the boron presence in bacteria stamps. Evidently, the bacteria present in the film mask the boron band. A possible explanation may come from the strong interaction of these residues with a bacterial surface that would induce a concentration gradient between the bacteria and the polymer; boron becoming then undetectable in the XPS analysis before extracting the bacterial cells and emptying the cavities (the XPS depth of surface analysis is limited to ~10 nm).
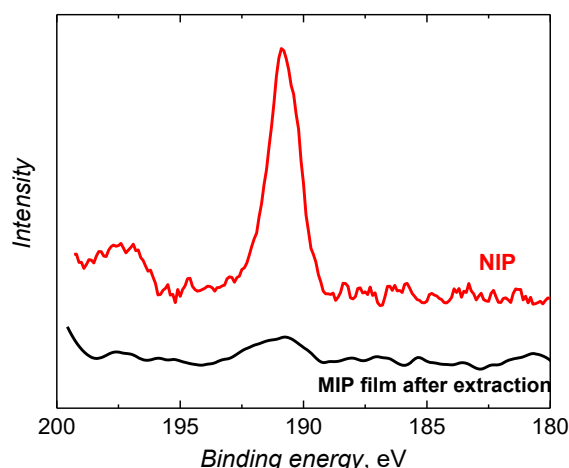
Figure 3.1-9. The XPS spectra for the MIP film-coated GCE after *E. coli* E2152 template extraction and the NIP film with the boron B 1s band manifested.

3.1.7 Recognizing efficiency of the E2152-templated MIP film

The MIP's boronic acid binding sites are expected to reversibly interact with the bacterial outer membrane *cis*-diol surface groups during electropolymerization. This covalent affinity aids in capturing bacteria cells within the MIP network during imprinting. Therefore, it is anticipated that the MIP film after the bacteria template removal would recognize the target bacteria by shape and size and molecular interactions between the MIP boronic acid residues and bacteria surface glycoproteins. The E2152-extracted MIP film-coated GCEs were used for *E. coli* determination by capacitive impedimetry (CI) under steady-state solution conditions.

For the *E. coli* CI determination under steady-state solution conditions, the 100 mM Tris-HCl buffer (pH =7.4) was used as the supporting electrolyte solution at the applied frequency and potential of $f = 20$ Hz and $E_{appl} = 0.60$ V vs. Ag/AgCl, respectively. The steady-state analysis's first step is to attain the time-independent capacitance to confirm stable electric double layer formation at the electrode-solution interface. Afterward, the analyte is introduced to the test solution.

The *E. coli* binding in molecular cavities is mainly governed by electrostatic attractions of positively charged *E. coli* surface groups and negatively charged porous MIP film boronic acid residues. This *E. coli* binding affects the electric permittivity of the electric double layer. Therefore, the capacitance and phase angle change with successive addition of *E. coli* of different concentrations (Figure 3.1-10). The linear dynamic concentration range for the *E. coli* extended from 2.9×10^4 to 3.1×10^7 cells mL^{-1} with the calibration plot obeying a semi-

logarithmic linear regression equation of C [nF] = 0.46($\pm$0.04) [nF/log (cells mL^{-1})] $\times$ $c_{E.\,coli}$ [log (cells mL^{-1})] – 2.0($\pm$0.19) (Figure 3.1-11). The correlation coefficient was R^2 = 0.984 while the sensitivity was 0.46($\pm$0.04) [nF/log (cells mL^{-1})].
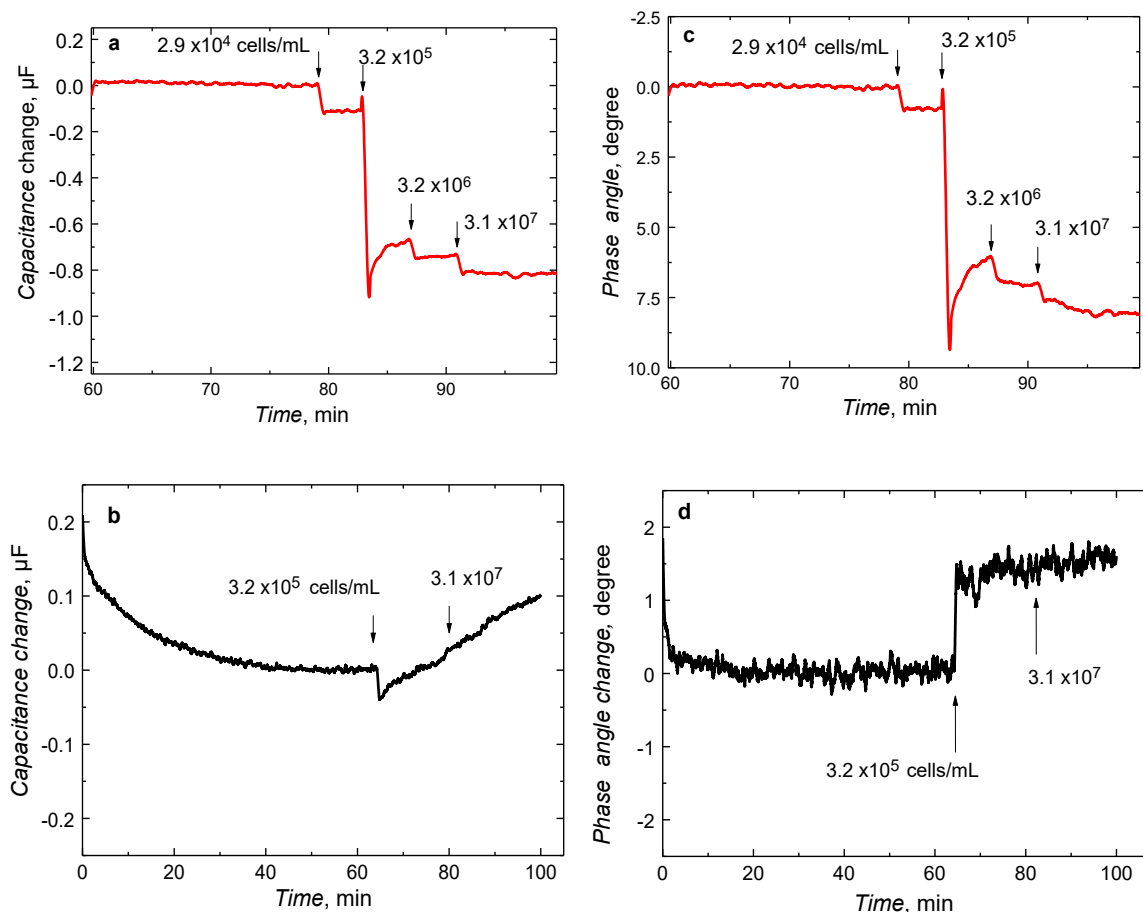
Figure 3.1-10. The time dependence changes of (a and b) capacitance and (c and d) phase angle after the addition of *E. coli* E2152 of different concentrations to 100 mM Tris-HCl buffer (pH = 7.4) measured at the (a and c) E2152-templated MIP and (b and d) NIP film-coated electrodes under steady-state solution conditions. GCEs were kept at the potential of +0.60 V vs. Ag/AgCl and a frequency of 20 Hz.

Moreover, the *E. coli* E2152 binding was evidenced with SEM imaging of the (*E. coli* E2152)-extracted MIP film-coated electrode after adding the bacteria cells (Figure 3.1-12). Expectedly, the cells mainly settled at the bacteria-imprinted cavities instead of the unimprinted MIP film surface (Figure 3.1-12). The bacteria binding was governed by the boronic acid residue present in the cavities, which could be detected with the XPS measurement only if the cavities were vacated (Figure 3.1-12).
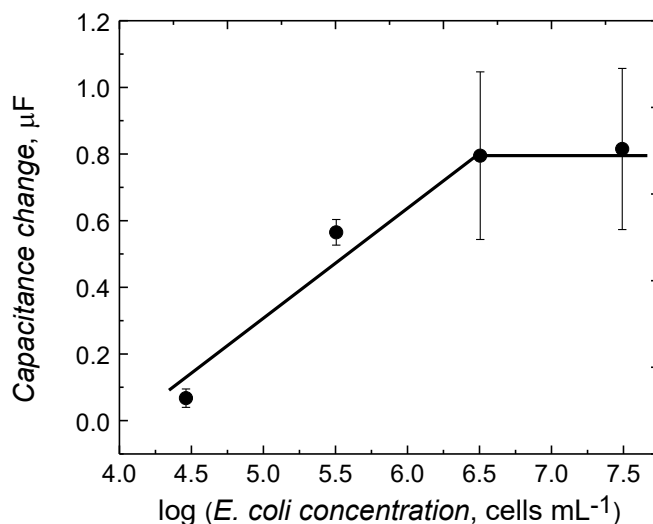
Figure 3.1-11. The semi-logarithmic calibration curve of the capacitance change at the MIP film-coated GCE after adding *E. coli* E2152 of different concentrations to 100 mM Tris-HCl buffer (pH = 7.4). For capacitance determination, the electrode was kept at a constant potential of 0.60 V vs. Ag/AgCl and a frequency of 20 Hz.

Gram-negative pathogens, including multidrug-resistant *E. coli* strains, are enclosed by an outer membrane, essential for cell viability and a protective barrier against antibodies. This asymmetric outer core comprises lipopolysaccharides (LPSs), phospholipids, and lipoproteins, playing a crucial role in sensing and antimicrobial activity.[298] The most abundant and vital structural lipoproteins covalently bound to the peptidoglycan layer via the ε-amino group are responsible for the outer core's stability and integrity. In comparison, the glycolipids and phosphorylated oligosaccharides (OS) are the major components of LPS making the strain highly hydrophobic.[299] However, the *E. coli* E2152 outer core is highly anionic because it is enriched with phosphate groups and 3-deoxy-D-manno-octulosonic acid and lacks *o*-polysaccharides. Because of this highly anionic surface nature, the boronic acid residues form *cis*-diol bonds with exposed glycolipids to firmly encapsulate the whole bacteria cell within the film during electropolymerization. Subsequently, the template-extracted MIP gains a positive charge because of the MIP film overoxidation during extraction in a highly alkaline solution (0.1 M NaOH). This cationic surface of the MIP helps bind the negatively charged *E. coli* E2152 cells into the imprinted cavities generated. Herein, this binding event was transduced into an analytical signal with CI. However, to confirm this hypothesis, the binding behavior of three interferences, namely, *Shewanella oneidensis* MR-1 (SWMR-1) and two *E. coli* strains, E2146 (with type 1 fimbriae), and E2498 (with Ag43 protein) were studied under steady-state solution conditions using the

same test solution, namely, 100 mM Tris-HCl buffer (pH = 7.4) (Figure 3.1-13). The interferences of known concentrations were separately added to the test solution under the same conditions for CI determination, i.e., the frequency and potential were kept constant at $f = 20$ Hz and $E_{appl} = 0.60$ V vs. Ag/AgCl, respectively. Clearly, the bacteria surface composition significantly impacts the prepared MIP sensing properties.
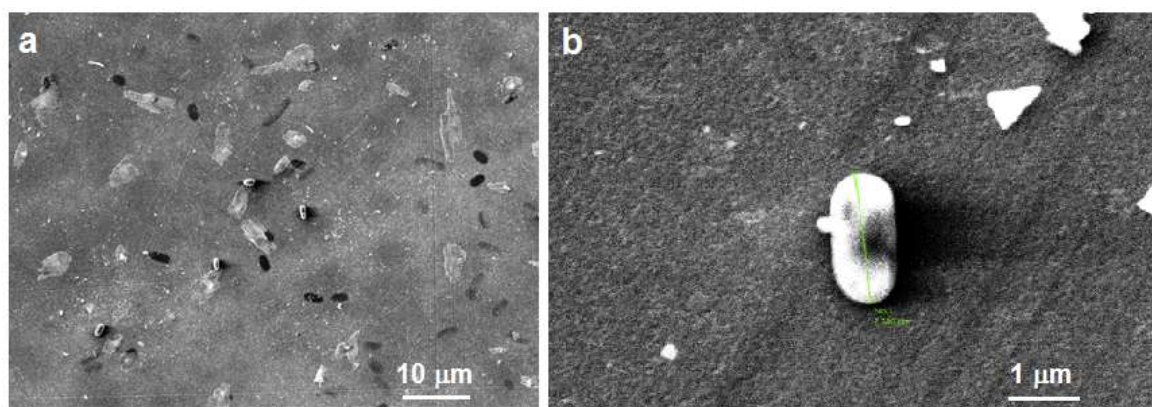
Figure 3.1-12. SEM images at (a) 10 μm (b) 1 μm magnification recorded after binding fresh *E. coli* E2152 on an MIP film-coated GCE.

As shown in Figure 3.1-13, no changes in capacitance were found for the E2498 interference. Seemingly, this arises from the presence of an additional dense peripheral thin layer of auto-transported adhesion Ag43 protein, a product of the *flu* gene on the *E. coli* K-12 chromosome.[261] *E. coli* Ag43 is a short and rigid monomeric appendage composed of a C-terminal integral outer membrane *β* domain that exports an *N*-terminal passenger *α* domain.[300, 301] Interestingly, Ag43 variants display a twisted L-shaped *β*-helical structure that facilitates auto-aggregation and cell-cell interactions via a molecular "Velcro-type" mechanism.[302] At pH = 7.4, the Ag43 domains' aggregation reaches maximum.[303] Therefore, the drastic change induced on the bacterial surface by this bacteria's auto-aggregations and additional coverage results in the lack of recognition that eventually appeared as no CI analysis response. Simultaneously, capacitance and phase angle pronouncedly changed for the E2146 mutant adsorption on the E2152-extracted MIP film. The E2146 mutant comprises a rod-shaped 100- to 200-nm thick layer of partially bent fimbriae. Moreover, the repeating fimbriae subunits with lectin group endings play an essential role in biofilm formation and bacterial virulence.[304] The unwinding of these tiny fimbriae extensions increases with the pH increase and reaches a pronounced maximum elongation at pH = 7.4.[305]

This surface modification is much less dense than that with Ag43 expression of E2498.[261] Therefore, it seems that the appreciable binding of E2146, comparable to E2152, might correlate with the more limited surface modification compared to E2498.
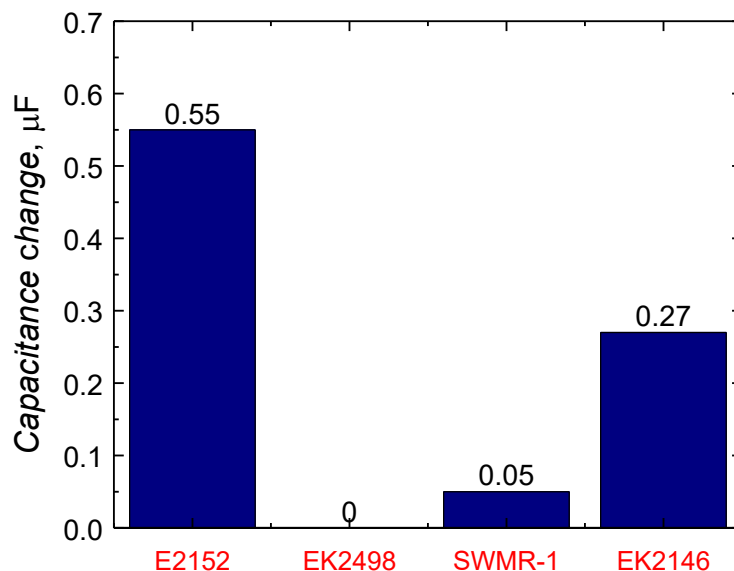
Figure 3.1-13. The histogram of the capacitance changes of the MIP film-coated GCE after the addition of 3.2×10^5 cells mL^{-1} of E2152, E2498, SWMR-1, or E2146 to 100 mM Tris HCl buffer (pH = 7.4) under steady-state conditions. The electrode was kept at a constant potential of 0.60 V vs. Ag/AgCl and a frequency of 20 Hz for capacitance measurements.

The third interference selected was Gram-negative SWMR-1, commonly known as metal-reducing bacteria externally surrounded by extracellular polymeric substances.[306] The extracellular polymer matrix [290] mainly comprises polysaccharides (~90%), including galactose, glucose, mannose, *N*-acetyl glucosamine, and glucuronic acids with smaller protein ratios, nucleic acids, cellulose, and amyloid formations.[307, 308] A very minute change in capacitance and phase angle values for just one higher concentration of SWMR-1 depicts that the binding most likely depends on the arrangement of exposed surface proteins. Moreover, it depends on the surface charge density of binding agents, which in the case of Gram-negative SWMR-1 is smaller compared to *E. coli* K-12 strains.[309, 310]

During the imprinting of microbes, their surface groups play a role. Therefore, proper selection of functional monomers is crucial in generating functionally adapted cavities. In our work, the excess of the cross-linking monomer maintained the shape of the cavities after template removal from the MIP and helped functional monomers position in these cavities. Moreover, bacteria binding was controlled via electrostatic and hydrophobic interactions

and reversible covalent bonding with boronic functional groups. That way, boronic diester saccharides complexes were formed. The SEM image (Figure 3.1-12) showed a well-defined fingerprint left after removing the imprinted *E. coli* single bacterium. Because of the presence of boronic functional groups and the size and shape of the cavities generated, the bacteria analyte cells entrapment by combined size-shape discrimination and affinity recognition was possible.

All strains other than the template bacteria yielded low capacitance signals, thus pointing out the unique recognition characteristics of cavities generated during molecular imprinting. However, it is difficult to control the shape and size of a specific strain, especially that of *E. coli* multiplying by every 30 min; therefore, *E. coli* collected after log phase from nutritional media were suspended in a KCl solution extensively vortexed to get a homogenous mixture before use.

Chapter 3

3.2 Electropolymerized molecularly imprinted polymer for chemosensing of gamma-aminobutyric acid autism biomarker

3.2.1 Molecular structures optimizing

The molecular imprinting is here used to synthesize selective recognition units of chemosensors for GABA selective determination. Initially, computational calculations were performed for five functional monomers, namely, *p*-bis(2,2'-bithien-5-yl)methyl-o-catechol **FM1**, *p*-bis(2,2'-bithien-5-yl)methylbenzoic acid **FM2**, *p*-bis(2,2'-bithien-5-yl)methylaniline acetate **FM3**, *p*-bis(2,2'-bithien-5-yl)methyl phenol 2-hydroxy acetamide ether **FM4**, and *p*-bis(2,2'-bithien-5-yl)methyl aniline **FM5** (Scheme 2). The Gibbs free energy change (ΔG) values were calculated for GABA complexes formed with all functional monomers to find the most suitable (Scheme 2.1-1). Apparently, GABA can form the most stable pre-polymerization complexes with **FM4** because of their lowest ΔG values (Table 3.2-1). Therefore, **FM4** was used to prepare the MIP.

Table 3.2-1. The DFT B3LYP/6-31G calculated Gibbs free energy (ΔG) changes accompanying the formation of the pre-polymerization complexes of GABA with different functional monomers.

Functional monomer	Complex stoichiometry (Template: Functional monomer)	Gibbs free energy change due to complex formation in vacuum (kJ/mol)
FM1	1 : 1	-19.8
FM2	1 : 1	-47.5
FM3	1 : 1	-38.0
FM4	1 : 1	-60.0
FM4	1 : 2	-144.0
FM5	1 : 1	-0.4

Table 3.2-2. The DFT, at the B3LYP/6-31G level, calculated Gibbs free energy (ΔG) changes corresponding to the formation of the pre-polymerization complexes of the GABA template with the **FM4** functional monomer at different molar ratios in acetonitrile.

Complex stoichiometry (GABA: FM4)	Gibbs free energy change due to complex formation in solution (kJ/mol)
1 : 2	-54
1 : 3	-25
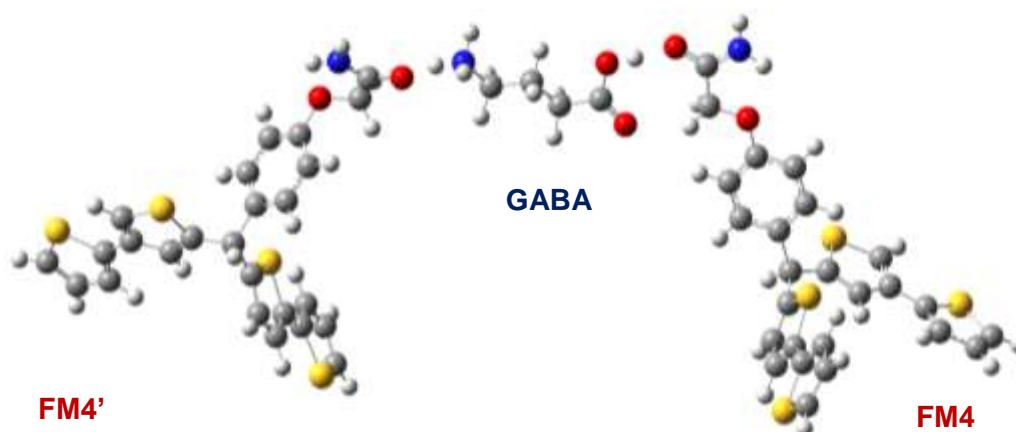
Scheme 3.2-2. The DFT optimized GABA-**FM4** pre-polymerization complex structure of the 1 : 2 molar ratio.

As the GABA biomolecule has two binding sites, i.e., the amide and carbonyl groups, the DFT calculations were further performed by keeping the GABA-to-**FM4** molar ratio of 1 : 2 (Scheme 3.2-2). The negative ΔG value was higher for this higher GABA-to-**FM4** molar ratio. The GABA protonated form was used for all DFT calculations because neutral GABA is weakly soluble in the acetonitrile solvent selected. This solubility was increased using a 90% acetonitrile and 10% 0.1 M H_2S0_4 solution. The ΔG values in a vacuum (Table 3.2-1) and the solution (Table 3.2-2) were calculated using the same DFT B3LYP/6-31G energy set. The ΔG value for the complex formation in the solution was smaller than in a vacuum (Table 3.2-2), presumably because of solvent-complex interactions.

3.2.2 Electrochemical MIP and NIP films synthesizing

MIP (Figure 3.2-1a and 3.2-1c) and NIP (Figure 3.2-1b and 3.2-1d) films were prepared and simultaneously deposited on the Pt disk electrodes (Figure 3.2-1a and 3.2-1b) and IDEs (Figure 3.2-1c and 3.2-1d) by potentiodynamic electropolymerization. An anodic and cathodic peak at ~0.90 V and 0.20 V vs. Ag quasi-reference electrode, respectively, were seen during the MIP film deposition (Figure 3.2-1a). Anodic currents appeared at slightly higher potentials with each successive potential cycle, and the current peaks decreased, thus suggesting non-conductive MIP film deposition. This current decreased with each potential cycle. A control NIP film was deposited by following the same procedure except for the absence of the GABA template Figure 3.2-1b and Figure 3.2-1d. However, the NIP film deposition current was higher than that of the MIP film. Possibly, the pre-polymerization

complex formation in solution hampered the electropolymerization. For MIP (Figure 3.2-1c) and NIP films depositions on IDEs (Figure 3.2-1d), two anodic peaks were present at 0.80 V and 1.10 V vs. Ag quasi-reference electrode. Anodic currents appeared at slightly higher potentials during the successive potential cycle. However, the current was almost negligible, thus showing non-conductive MIP film deposition. Moreover, the Pt electrode and IDEs surfaces' complete coating with the MIP film was confirmed by DPV experiments with 25 mM $K_4[Fe(CN)_6]$ and 25 mM $K_3[Fe(CN)_6]$.
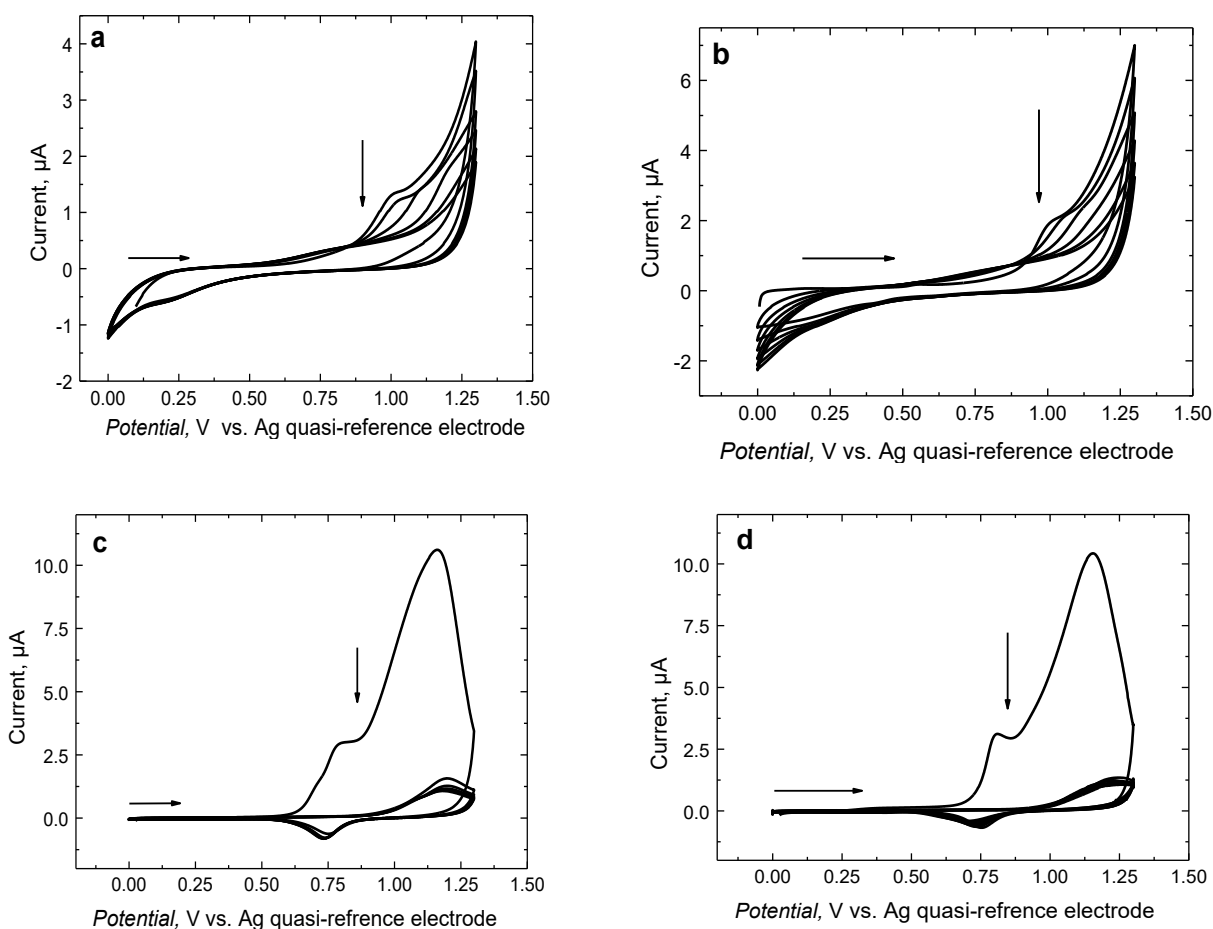
Figure 3.2-1. (a) and (c) MIP as well as (b) and (d) NIP film deposition by potentiodynamic electropolymerization on (a) and (b) the Pt disk electrode, and (c) and (d) Au IDEs in the 90% acetonitrile and 10% 0.1 M H_2SO_4 solution of 0.1 mM GABA, 0.2 mM **FM4**, 0.6 mM **CM**, and 0.1 M TBAClO$_4$. A potential scan rate was 50 mV s^{-1}.

3.2.3 GABA template removal from the MIP

The "gate effect" at the MIP film-coated electrodes was examined to confirm the GABA template removal from the MIP. For that, electro-oxidation of the 25 mM $K_4[Fe(CN)_6]$ and mM $K_3[Fe(CN)_6]$ redox probe was followed by DPV measurements at the MIP film-coated

Pt electrode (Figure 3.2-2). Because of the non-conducting polymer film formation, the redox activity of the probe was hampered, and the peak current of $K_4[Fe(CN)_6]$ electro-oxidation was low. However, the current substantially increased when the GABA template was extracted from the MIP (Figure 3.2-2a). At least 2 to 3 h were needed to extract the MIP film completely. That resulted in emptying the MIP molecular cavities. Similar template extraction from the NIP did not affect the anodic current (Figure 3.2-2b), indirectly indicating molecular cavities formation only in the MIP.
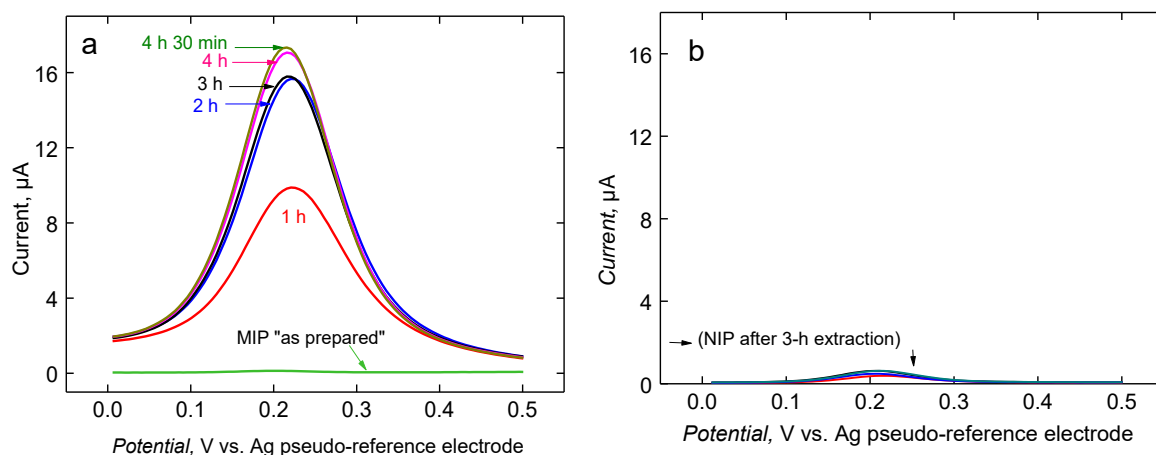
Figure 3.2-2. Differential pulse voltammetry (DPV) curves for 25 mM $K_3[Fe(CN)_6]$ and 25 mM $K_4[Fe(CN)_6]$ in 0.1 M PBS (pH 5) at the (a) MIP and (b) NIP film-coated Pt disk electrode after GABA template extraction with 50 mM NaOH for different time intervals indicated at curves with numbers.

Likewise, the "gate effect" at the MIP film-coated IDEs was examined using DPV and EIS measurements to confirm the GABA template removal from the MIP. For that, electro-oxidation of the 25 mM $K_4[Fe(CN)_6]$ and 25 mM $K_3[Fe(CN)_6]$ redox probe was followed by DPV at the MIP film-coated IDEs (Figure 3.2-3).

3.2.4 XPS confirming GABA template removal from the MIP

Moreover, XPS was used to confirm GABA template removal (Figure 3.2-4). The presence of the protonated GABA template in the MIP was confirmed with the high-resolution N 1s spectrum. Before GABA extraction, bands characteristic of the **FM4** amide group and charged amine moiety of GABA at ~400 and ~402 eV, respectively, contributed to this spectrum.[311, 312] After GABA extraction, the charged amine N 1s band at ~402 eV disappeared (Figure 3.2-4a). The XPS spectra for the NIP film showed only one N 1s band

at ~400 eV assigned to the **FM4** amide group (Figure 3.2-4b). This band remained after
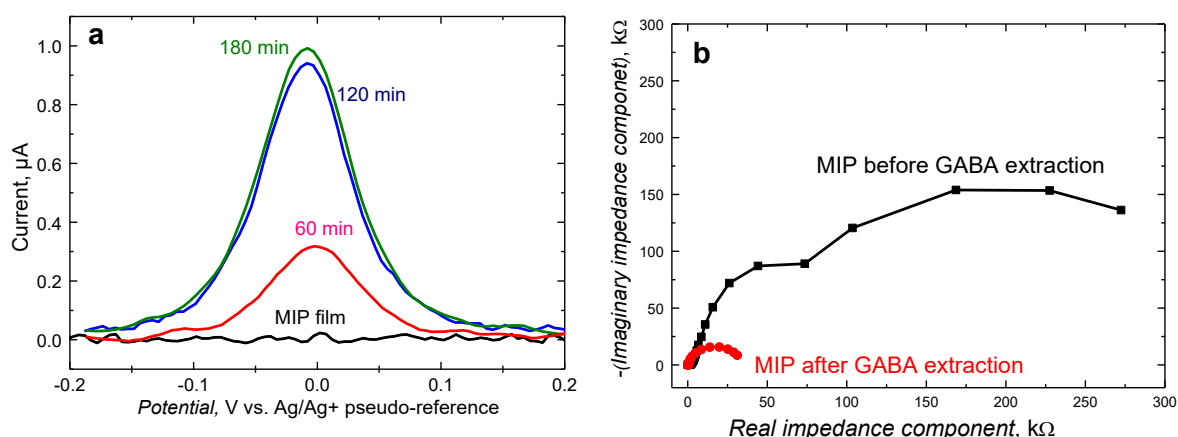
washing the NIP film with 50 mM NaOH (Figure 3.2-4b).

Figure 3.2-3. (a) Differential pulse voltammetry (DPV) curves and (b) Nyquist plots for 25 mM $K_4[Fe(CN)_6]$ and 25 mM $K_3[Fe(CN)_6]$ in 0.1 M phosphate buffer solution (pH = 5) for the MIPs film-coated IDEs before and after GABA template extraction with 50 mM NaOH for different time intervals.

3.2.5 Differential pulse voltammetric GABA sensing with MIP and NIP film-coated Pt electrodes

GABA template extracting from the MIP enabled binding of the GABA analyte molecules by the empty molecular cavities of MIP. That allowed determining the GABA analyte in the test solution using DPV. Once again, the "gate effect" was exploited for that. In the GABA absence in the test solution, the DPV peak at 0.18 V vs. Ag quasi-reference electrode for the redox probe was high (Figure 3.2-5a) because of the efficient probe diffusion through the MIP film. However, the peak decreased the more (Figure 3.2-5a), the higher was the GABA concentration. Presumably, the GABA molecules were bound in MIP molecular cavities, thus blocking the redox probe diffusion through the MIP film. This DPV peak decrease was linearly dependent on the GABA concentration increase (Figure 3.2-5a, curve 1). The apparent imprinting factor for GABA, calculated from the ratio of the calibration plot slope for the MIP to that of the NIP, exceeded 2 (Table 3.2-3), thus, in addition, substantiating the presence of molecular cavities in the MIP.
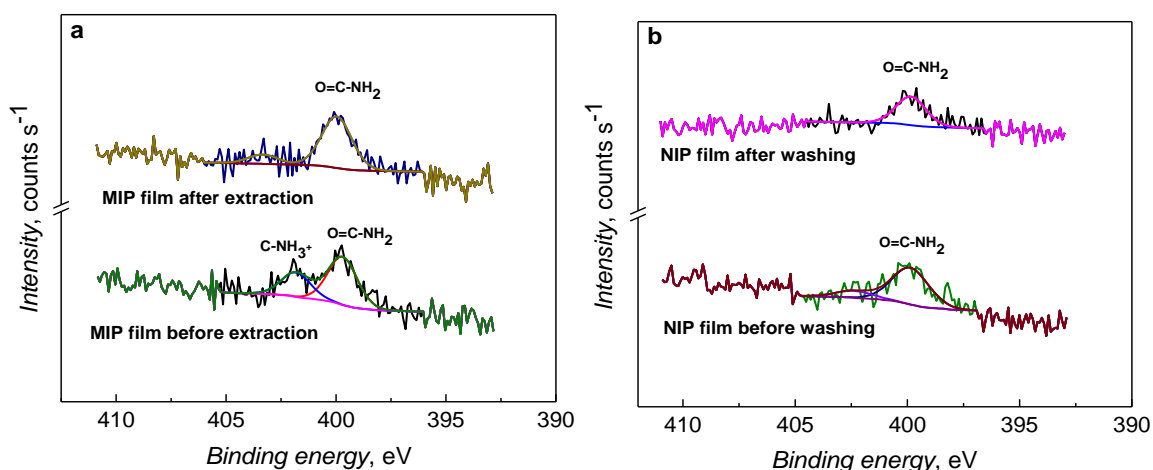
Figure 3.2-4. The XPS spectra in the N 1s electron binding energy region for (a) MIP and (b) NIP films before and after GABA template extraction with 50 mM NaOH. Assignments of nitrogen atom electrons for deconvoluted peaks are indicated in the spectra.

3.2.6 Electrochemical impedance spectroscopic GABA sensing with MIP and NIP film-coated Pt electrodes

Along with the DPV studies, EIS has been employed to elucidate the MIP film-coated electrodes' behavior. The Nyquist plots (Figure 3.2-5b) manifest MIP film-coated Pt disk electrode impedance alterations with the GABA analyte concentration increase. The charge transfer resistance (R_{ct}) increased with the GABA concentration increase (Figure 3.2-5b), indicating the decrease in the film conductivity. The experiments were repeated thrice to study the MIP film-coated Pt disk electrode repeatability. The averaged data were used to construct the calibration plots (Figure 3.2-5b). The apparent imprinting factor, calculated from the ratio of the calibration plot slope for the MIP to that for the NIP close to 3 (Table 3.2-3), additionally confirms the presence of molecular cavities in the MIP film.

Table 3.2-3. Sensitivity and the imprinting factor of MIP chemosensors obtained by DPV and EIS transductions.

Analyte	DPV		EIS	
	Sensitivity	Imprinting factor	Sensitivity	Imprinting factor
GABA	-0.13	-	0.24	-
GABA	-0.06	2.16	0.09	2.66

94
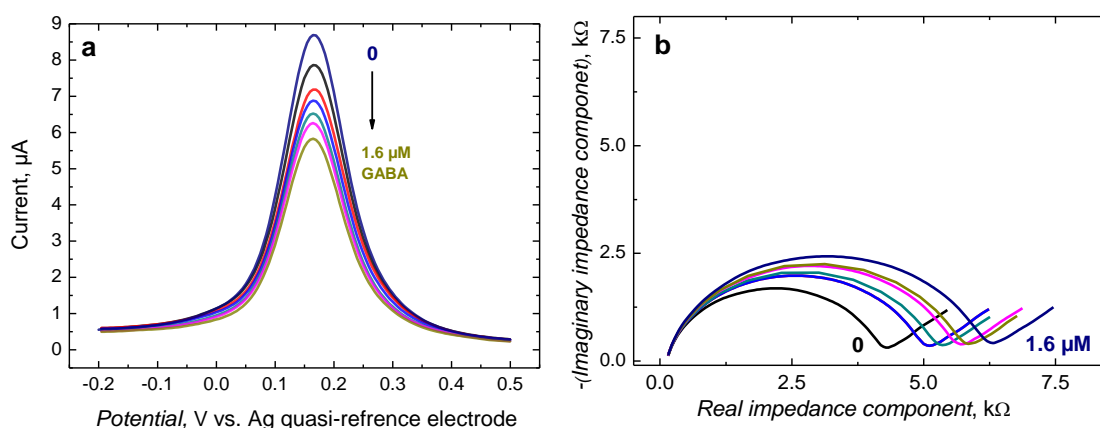
Figure 3.2-5. (a) DPV curves and (b) Nyquist plots at the MIP film-coated Pt disk electrode in the GABA solutions of concentrations indicated with numbers at curves, in 25 mM $K_4[Fe(CN)_6]$ and 25 mM $K_3[Fe(CN)_6]$, in 0.1 M phosphate buffer (pH = 5.0). For the EIS measurements, the potential was kept constant at 0.20 V vs. Ag quasi-reference electrode, and the frequency was varied in the range of 100 mHz to 1 MHz.

3.2.7 Interferences determining with the MIP film-coated Pt disk electrode

The GABA recognizing DPV (Figure 3.2-5a) and EIS (Figure 3.2-5b) results show that the MIP film-coated Pt disk electrode determined the GABA analyte in the 190 to 1600 nM concentration range. Further, this electrode selectivity to GABA structural analogs, vis., 5-aminopentanoic acid, and 2-aminobutanoic acid, was determined. The MIP's "gate effect" in the presence of GABA structural analogs was less pronounced, except for 5-aminopentanoic acid, for which the DPV and EIS responses were opposite to those for GABA (curves *3* and *3'* in Figures 3.2-6a and 3.2-6b, respectively). Nevertheless, there were differences in the electrode behavior in the presence of the GABA analyte and its structural analogs.

3.2.8 Electrochemical impedance spectroscopic GABA sensing with MIP and NIP film-coated IDEs

Next, the above set of experiments was repeated using IDEs. The normalized R_{ct} values for the MIP film-coated IDE increased with the GABA concentration increase (Figure 3.2-7a). The linear dynamic GABA concentration range stretched from 12 to 432 µM (Figure 3.2-7c). Under similar determination conditions, the R_{ct} for the NIP film-coated IDEs was much smaller (Figure 3.2-7b).
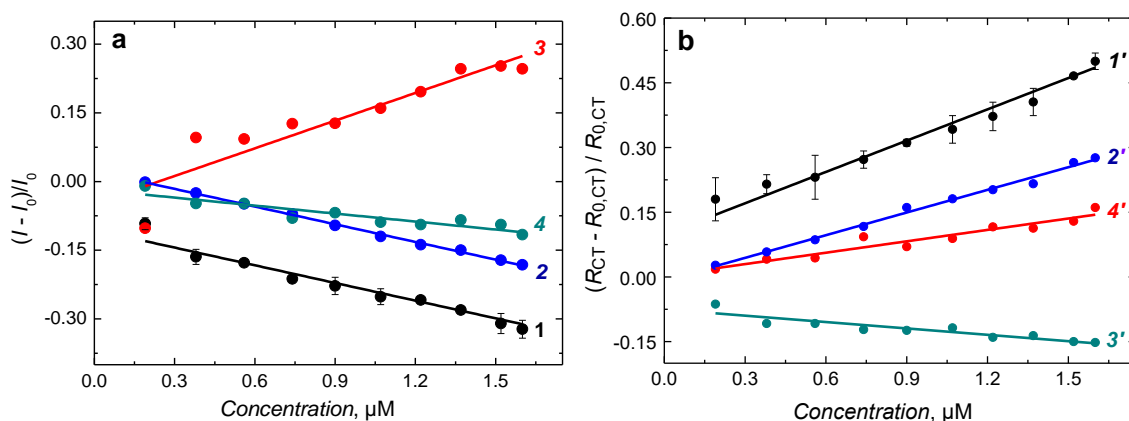
Figure 3.2-6. Calibration plots for 25 mM $K_3[Fe(CN)_6]$ and 25 mM $K_4[Fe(CN)_6]$ in 0.1 M phosphate buffer (pH = 5.0) of changes in the normalized (a) DPV peak and (b) charge transfer resistance with the concentration change of (curves *1* and *1'*) GABA, (curves *2* and *2'*) 2-aminobutanoic acid, (curves *3* and *3'*) 5-aminopentanoic acid recorded at the MIP film-coated Pt electrodes. Curves *4* and *4'* are calibration plots for GABA at the NIP film-coated Pt electrodes.

In the Nyquist plots, semicircles with diameters corresponding to the redox probe R_{ct} were well pronounced (Figure 3.2-7a). The electrode-solution interfaces were modeled with an equivalent circuit composed of solution resistance (R_s) and two *RC* circuits in series (Figure 3.2-7c, inset). The circuit elements were R_s in series connected with (*CPE*1 paralleled with R_{ct1}) and (*CPE*2 paralleled with R_{ct2}). The *CPE*1 corresponds to the capacity and resistivity of various electrical connections, and *CPE*2 refers to faradaic processes. The numerical values obtained from the Nyquist plot fitting revealed an R_{ct} increase with the GABA concentration increase (Figure 3.2-7c). The R_{ct} linearly increased with the logarithm of GABA concentration in buffered solution increase in the 8 to 432 μM GABA concentration range obeying the linear regression equation of R_{ct} = -0.11 (±0.006) log c_{GABA} [μM] - 0.044(±0.013) (Figure 3.2-7c, curve *2*); the correlation coefficient was 0.986. This R_{ct} increase is presumably due to filling resistivity of various electrical connections, and *CPE*2 with the GABA analyte molecules available for these molecules' molecularly imprinted cavities in the MIP, causing the R_{ct} decrease.
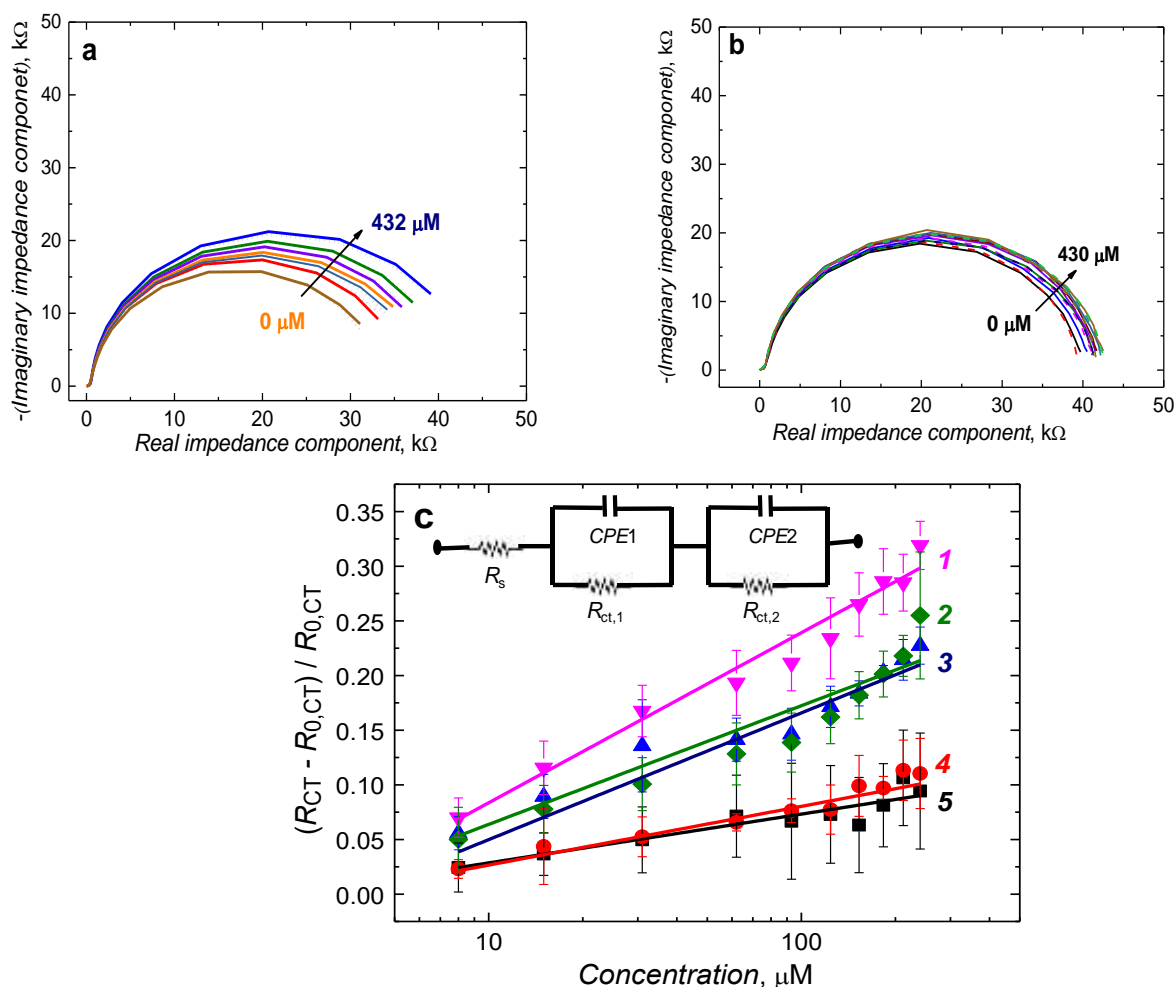
Figure 3.2-7. The Nyquist plots for IDEs coated with the template-extracted films of (a) MIP and (b) NIP, and (c) calibration plots of changes in the normalized charge transfer resistance for (curve *1*) GABA in artificial serum, (curve *2*) GABA in 25 mM $K_4[Fe(CN)_6]$ and 25 mM $K_3[Fe(CN)_6]$, in 0.1 M phosphate buffer (pH = 5.0), (curve *3*) GABA in an equimolar solution of interferences, vis., 5-aminopentanoic acid, 2-aminobutanoic acid, *N*-acetyl aspartate, and glucose, (curve *4*) equimolar mixed solution of interferences, vis., 5-aminopentanoic acid, 2-aminobutanoic acid, *N*-acetyl aspartate, and glucose, and (curve *5*) the GABA calibration plot for the NIP film-coated IDE.

The GABA imprinting was further confirmed using the control NIP thin-film coated IDE (Figure 3.2-7b and Table 3.2-4). This electrode response was smaller than the MIP film-coated IDE over the entire GABA concentration range (Figure 3.2-7c, curve *5*). That indicates the absence of sufficiently strong interactions of binding sites of the analyte molecules with recognizing sites of functional monomer molecules randomly distributed in the NIP (Table 3.2-4). The chemosensor sensitivity to interferences in the solution of equimolar concentrations was much lower than to the GABA alone (Table3.2-4). Moreover, when GABA was present in this equimolar interferences solution, the chemosensor

recognized GABA with the same sensitivity (curves *2* and *3* in Figure 3.2-7c and Table 3.2-4).

Table 3.2-4. The EIS determined MIP-based IDE chemosensor sensitivity and selectivity.

Polymer	Analyte	EIS	
		Normalized sensitivity	**Selectivity/ imprinting factor**
MIP	GABA	0.11	-
	GABA (in serum)	0.16	-
	GABA and 5-aminopentanoic acid, 2-aminobutanoic acid, *N*-acetyl aspartate and glucose	0.12	0.92
	5-Aminopentanoic acid, 2-aminobutanoic acid, *N*-acetyl aspartate and glucose	0.05	2.20
NIP	GABA	0.04	2.75

Further, the devised chemosensor was tested for GABA determining in 100 times diluted artificial serum sample, which was 25 mM in $K_4[Fe(CN)_6]$ and 25 mM in $K_3[Fe(CN)_6]$, and 0.1 M in phosphate buffer (pH = 5.0). The calibration curve for GABA in this complex matrix appeared slightly affected by proteins or other interferences, and analytical features were slightly higher than in the blank buffer solution (Figure 3.2-7c, curve *1*). The calibration curve slope for the control serum was 0.16, while it was 0.11 for the blank buffer solution.

3.2.9 MIP and NIP film-coated IDEs morphology characterizing

The surface morphology of thin MIP and NIP films deposited on IDEs was investigated with AFM (Figure 3.2-8). It appeared that the polymers were composed of nanogranules. This observation was verified by considering the films' surface roughness. Because of polymer chains' staking, the template-extracted MIP film revealed an elongated fibril-like structure. The MIP film was primarily deposited on the IDE strips. Moreover, it was deposited on the dielectric support material between microelectrode strips. After template extraction, loose MIP fragments deposited on the dielectric material were removed.
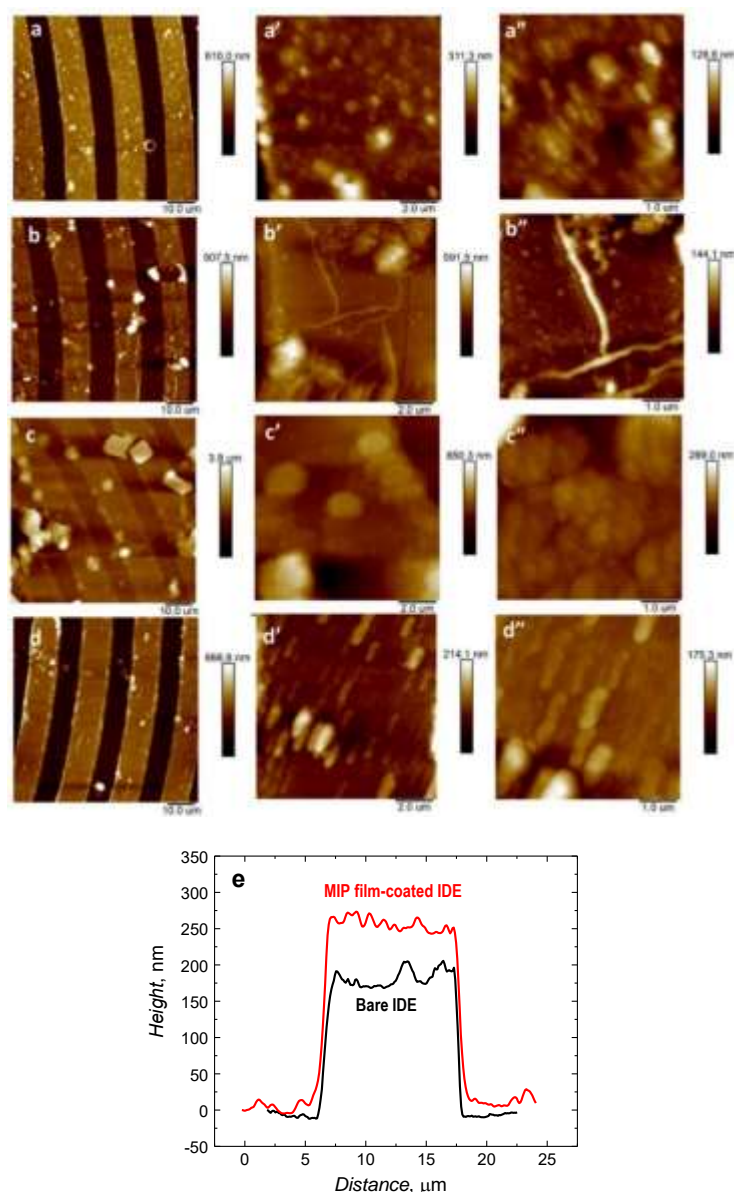
Figure 3.2-8. AFM images of (a, a', a" and b, b', b") MIP and (c, c', c" and d, d', d") NIP films potentiodynamically deposited on IDEs, (a, a', a" and c, c', c") before and (b, b', b" and d, d', d") after GABA extraction with 50 mM NaOH. (e) The cross-sectional profile of the bare and MIP film-coated IDE strip.

The NIP film was much more irregular, revealing many large aggregates. After template extraction, this film appeared to be composed of fibril-like nanogranules. Those were arranged similarly to nanogranules in the MIP film. The MIP film was ~50 nm thick (Figure 3.2-8e), thicker than the NIP film, whose thickness was ~40 nm.

3.2.10 Capacitive impedimentary (CI) GABA determining in 0.01 M KF with MIP film-coated IDEs

Impedance measurements by the above-described frequency scanning are commonly performed using commercially available frequency response analyzers. Those instruments are often bulky and cannot be used as portable sensors components. Therefore, a smaller module targeting one or two chosen constant frequencies and monitoring the impedance at those frequencies is more practical.[139] Hence, a new attempt has here been made using CI transduction to determine an MIP film-coated electrode's double-layer capacitance (C_{dl}). The MIP thin films were deposited on IDEs by potentiodynamic electropolymerization under the already optimized conditions (Figure 3.2-1). The template-extracted MIP film-coated IDEs were used for GABA determining with CI under both steady-state solution and flow-injection analysis (FIA) conditions. The applied frequency and potential were kept constant at $f = 20$ Hz and $E_{appl} = 0.50$ V vs. Ag quasi-reference electrode, respectively.

The 10 mM KF was used for determinations under the steady-state solution conditions. This KF concentration was sufficiently low to ensure high sensitivity of the CI transduction. First, in both the steady-state and FIA experiment, a time-independent C_{dl} was reached, confirming the formation of a stable double layer. Then, the GABA analyte was introduced to the test solution. The GABA molecules binding in the MIP molecular cavities is mainly governed by hydrogen bonding. This binding affects the electric permittivity of the double layer (Figure 3.2-9a). Therefore, the C_{dl} increases with successive additions of GABA sample solutions of different concentrations (Figure 3.2-9a).

Moreover, GABA was determined using the template-extracted MIP film-coated IDEs under FIA conditions with 10 mM KF as the carrier solution. This solution was pumped at the 35 µL min^{-1} flow rate. The 20-µL solution samples of known GABA concentrations in 10 mM KF, i.e., the solution of the same composition as the carrier solution, were injected at different time intervals (Figure 3.2-9b). The C_{dl} measurement conditions for the GABA were kept constant at $f = 20$ Hz and $E_{appl} = 0.50$ V vs. Ag quasi-reference electrode, respectively.

After each sample injection, the C_{dl} initially increased, then returned to its baseline value after sufficient volume of the carrier solution flow. A sample of the same GABA concentration was injected in triplicate for repeatability study. The C_{dl} signals were quite repeatable (Figure 3.2.9b). The C_{dl} increase after consecutive injections of sample solutions of increasing concentrations is presumably due to MIP imprinted molecular cavities binding

of GABA molecules. The linear dynamic concentration range extended from 5 to 250 µM GABA (Figure 3.2.9b, inset). Moreover, the capacitance change with time upon injecting GABA solution samples of different concentrations was measured for the NIP film-coated IDE under steady-state solution conditions (Figure 3.2-10). However, no profound change in C_{dl} was observed on extracted NIP film-coated IDE after successive GABA addition of different concentrations.
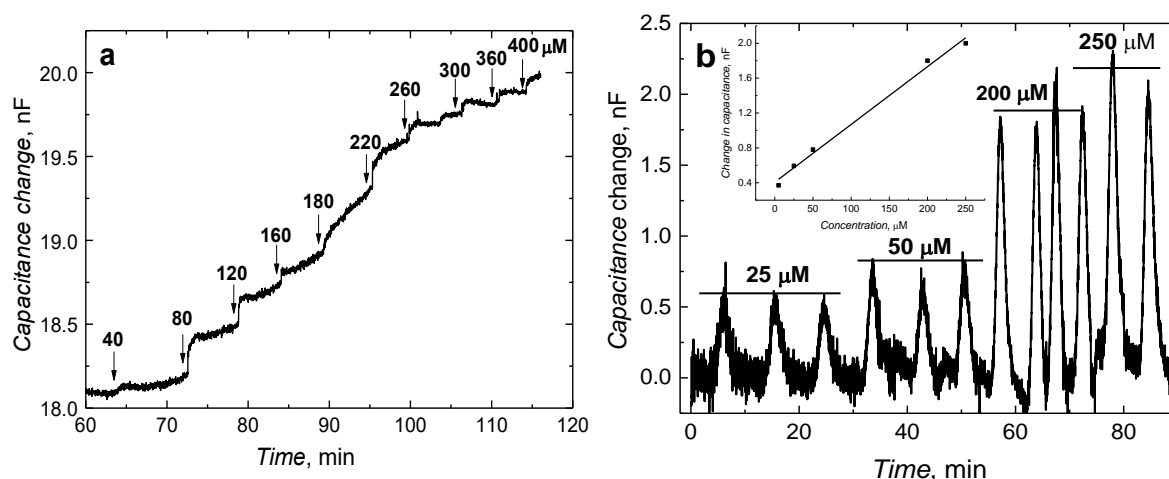
Figure 3.2-9. The MIP film-coated IDEs capacitance changes with time after injection of samples of solutions of different GABA concentrations, indicated with numbers at curves, under (a) steady-state solution conditions in 10 mM KF and (b) FIA conditions with 10 mM KF as the carrier solution; inset being the GABA calibration plot for the MIP film-coated IDE under FIA conditions. For capacitance determination, the potential and frequency were kept constant at 0.50 V vs. Ag quasi-reference electrode and 20 Hz, respectively. The carrier solution flow rate was 35 µL min^{-1}, and the injected GABA solution volume was 20 µL.
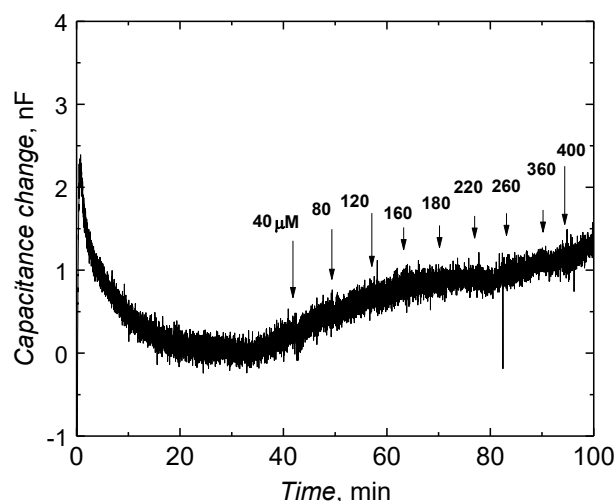
Figure 3.2-10. The capacitance change with time for the NIP film-coated IDE upon injecting GABA solution samples of different concentrations; the IDE was kept at a constant potential of 0.50 V vs. Ag quasi-reference electrode and frequency of 20 Hz. The solution was 10 mM in KF.

3.3 Electrochemically initiated synthesis of polyacrylamide gel microparticles and core-shell nanoparticles

Research background
Polyacrylamide gels are used for drug delivery, sensing, and tissue engineering

Available methods for gel preparation
- Precipitation polymerization
- Bulk polymerization
- Emulsion polymerization
- Suspension polymerization
- Raft polymerization

Limitations
- Require water soluble monomers, continuous agitation, and stabilizers contaminations
- Use of organic solvents, contamination with surfactants, additives and emulsifiers
- Require thermostable materials, stabilizing agents, formation of sol fractions

Valuable alternative

Electrochemically initiated polymerization

Working electrode

Refrence electrode

Counter electrode

SO_4^{-2}

Polymer collidal gel partilce

Research goal
Development of a facile green approach of polyacrylamide gel synthesis without addition of any additives and stabilizers, at room temperature

3.3.1 Electrochemical synthesizing gel microparticles

A simple procedure of polyacrylamide gel synthesizing was developed. The gel was prepared as microparticles, and thin shells on silica and magnetic nanoparticles (MNP) cores, suspended in aqueous solutions. A relatively low constant potential of -0.60 V vs. Ag quasi-reference electrode was selected to generate free radicals by decomposing APS, which resulted in the gelation. A corresponding potentiostatic curve (Figure 3.3-1) shows the current reaching its constant minimum value after 30 min. The present APS concentration in the solution for polymerization was higher than that reported in earlier studies.[313]
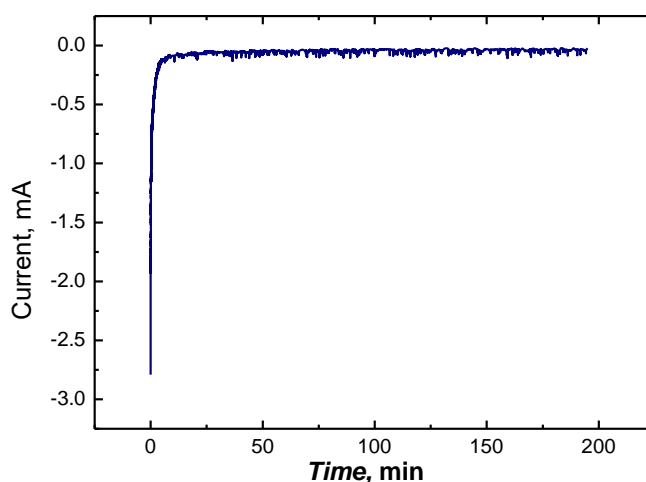
Figure 3.3-1. The potentiostatic current transient at -0.60 V vs. Ag quasi-reference electrode under vigorous magnetic stirring conditions recorded at the 0.7-mm diameter Pt disk electrode in the solution of 25 mM MA, 25 mM NIPAM, 50 mM BIS, 25 mM APS, and 0.1 M in KNO$_3$.

The polymerization mechanism involving the water-soluble NIPAM monomer has widely been studied.[313-315] Similarly, as in the previously described syntheses, in our electrochemically initiated polymerization, the solution for polymerization was initially homogeneous (Scheme 3.3-1). As the potentiostatic synthesis proceeded, the increasing APS amount was cleaved, and the amount of water-soluble free radicals became sufficient for initiating the polymerization (Scheme 3.3-1).[316] A suitable amount of the cross-linking monomer in the solution promotes entropic precipitation.[317, 318]

Moreover, this NIPAM and MA monomers incorporation in the growing polymer chain substantially decreases the polymer's solubility. Usually, the density of no part of the microgel structure is homogeneous. This lack of homogeneity arises from the different

reactivity of the main and cross-linking monomers.[319] The faster-polymerizing monomers generate centers of higher density in the polymer interior, while a fuzzy surface with dangling chains constitutes its outer part. However, at a considerably high concentration of a cross-linking monomer, coverage of carboxyl terminated MA chains can be high, and the number of reactive sites can be sufficient.[320] Thus, Scheme 3.3-1 proposes a tentative electrochemically initiated microgel synthesis mechanism.
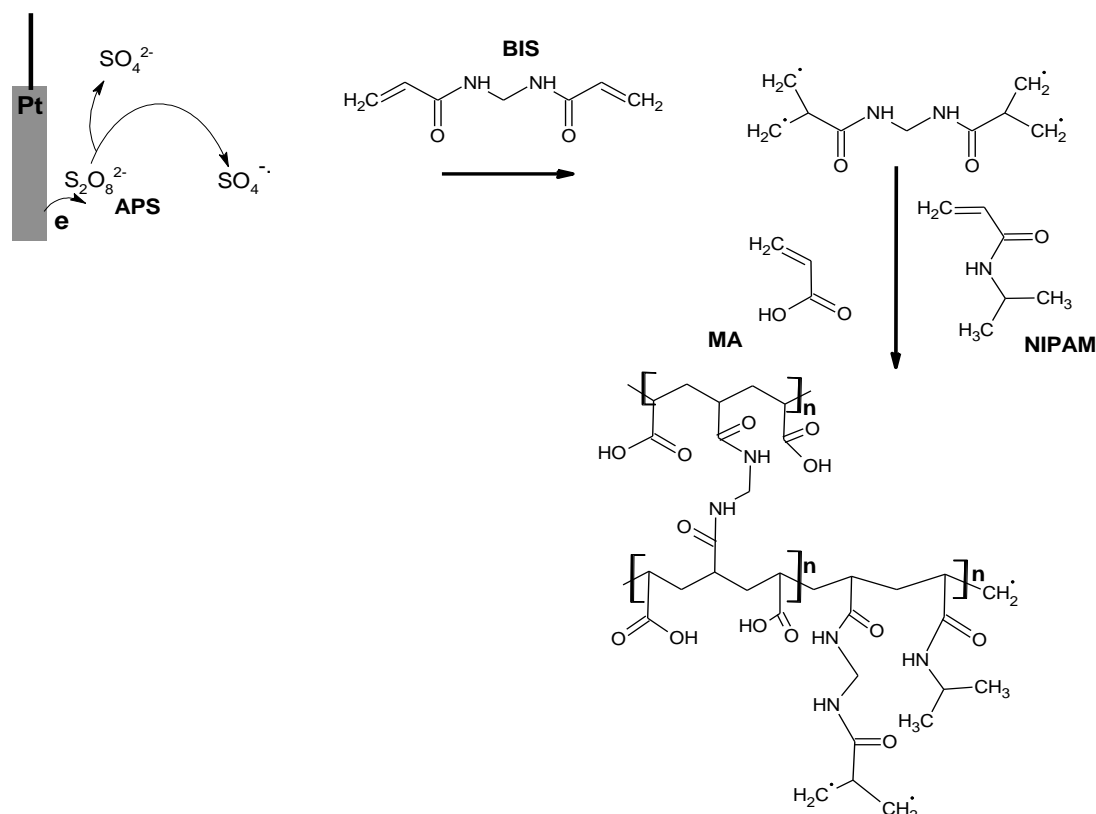
Scheme 3.3.1. The electrochemically initiated mechanism of polyacrylamide microgel synthesis.

3.3.2 SEM and TEM characterizing the morphology of gel microparticles

The microgels, prepared at all monomer combinations, were imaged with SEM and STEM to study their morphology (Figure 3.3-2). These images revealed that the gel microparticles were mainly irregular. Interestingly, the size of the particles prepared by combining NIPAM and BIS (Figure 3.3-2a and 3.3-2a') appeared similar to that by combining NIPAM, MA, and BIS (Figure 3.3-2c and 3.3-2c'). Image closer examination disclosed a globular shape of the MA-BIS microgel (Figure 3.3-2a and 3.3-2a').
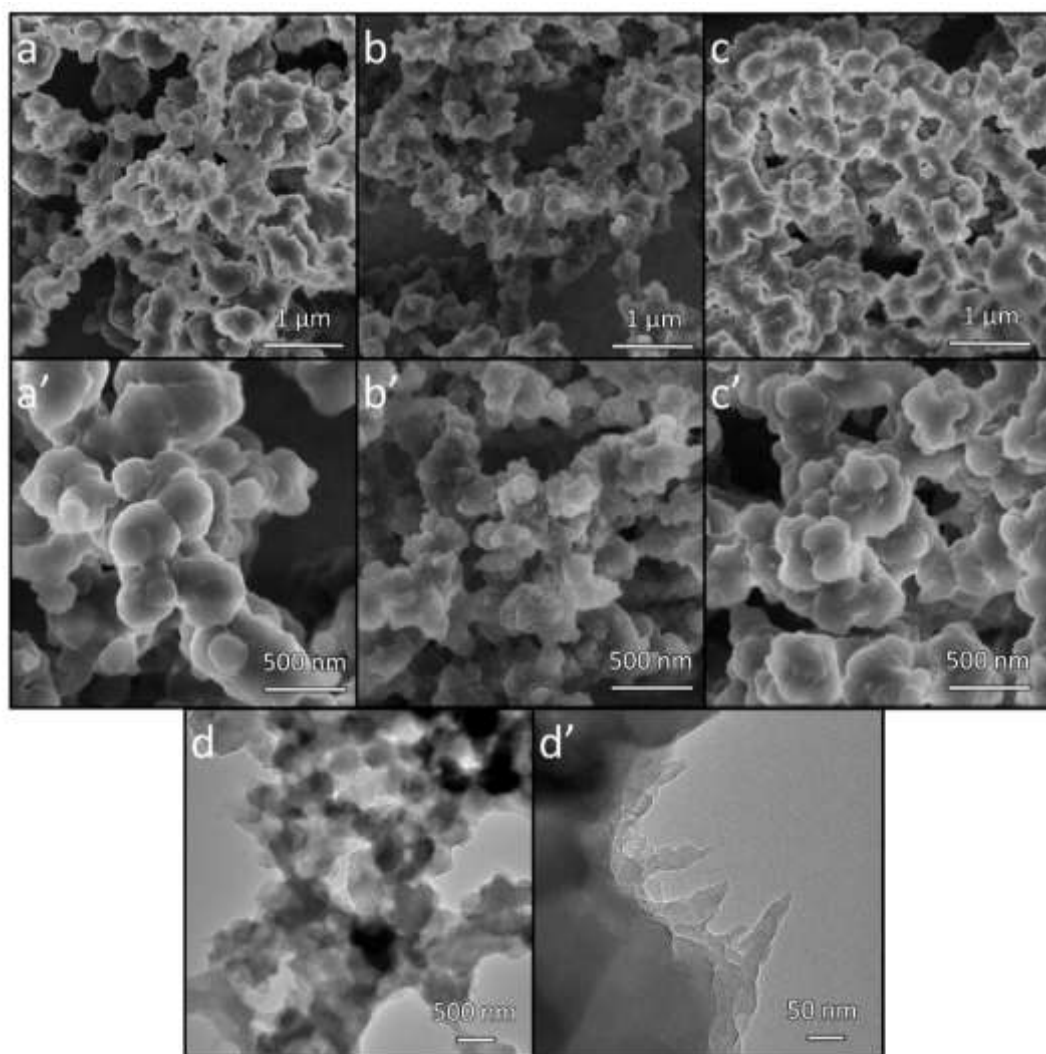
Figure 3.3-2. The SEM images of the microgels prepared at monomer combinations of (a, a') NIPAM-BIS, (b, b') MA-BIS, and (c, c') NIPAM-MA-BIS. (d, d') The STEM image of the NIPAM-MA-BIS microgel.

The MA-BIS particles were small (Figure 3.3-2b and 3.3-2b'). The NIPAM-MA-BIS particle's irregular shape presumably resulted from the aggregation of smaller particles (Figure 3.3-2c and 3.3-2c'). Sharp edges of these particles are clearly seen. This high aggregation likely arises from thorough drying of the microgel during SEM imaging. Moreover, the van der Waals and hydrophobic interactions might contribute to this aggregation.

Presumably, the MA monomer incorporation in the microgel aided in generating globularly shaped gel microparticles. The STEM image of the NIPAM-MA-BIS microgel demonstrates the porosity of the particles with a fuzzy surface (Figure 3.3-2d and 3.3-2d'), in accord with earlier reports.[314, 321, 322]

Interestingly, a microgel morphology was different if the pH of the solution for polymerization exceeded the acid's pK_a (Figure 3.3-3). At high pH, where the acid monomer was negatively charged, the gel microparticles partially interconnected, yielding a soft gel-like soluble material. Consequently, it was difficult to separate this microgel from the aqueous solution. In contrast, the uncharged gel microparticles were densely packed when polymerization was performed at a low solution pH (Figure 3.3-2).
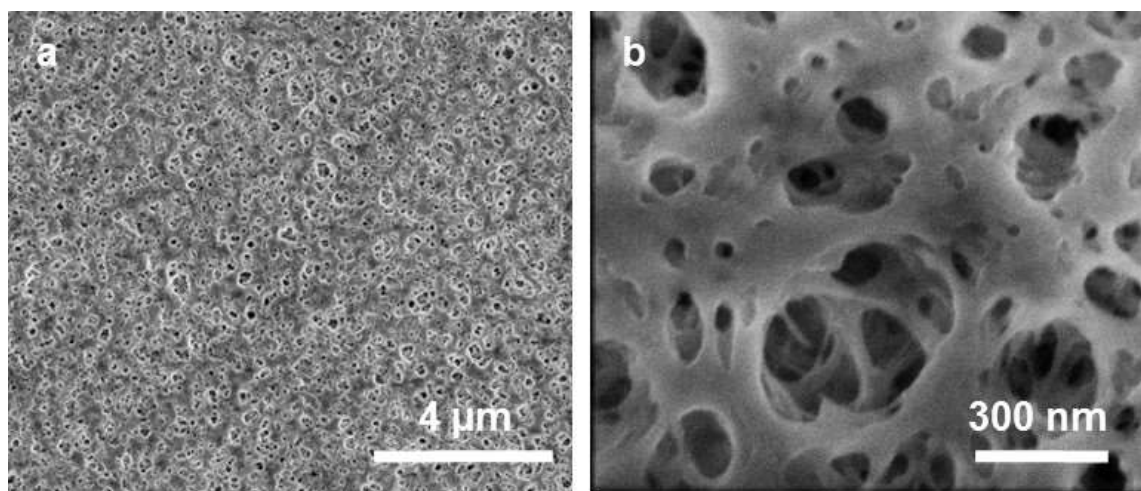
Figure 3.3-3. SEM images of resolution of (a) 10,000 and (b) 100,000 times of a microgel prepared using a solution of 25 mM MA, 25 mM NIPAM, 50 mM BIS, 25 mM APS, and 0.1 M in KNO$_3$, pH = 7.4.

3.3.3 BET analyzing the NIPAM-MA-BIS gel microparticles

Further, the BET analysis was performed for the NIPAM-MA-BIS microgel prepared at low pH to examine its porosity and determine its surface area (Figure 3.3-4). The adsorption isotherms constructed showed a steep increase in the adsorbed N$_2$ volume, typical of IUPAC type IV isotherms. Pore size distribution, calculated by the Barrett-Joyner-Halenda (BJH) method, varied between 2.5 and 15 nm, with a maximum centered at 5 nm. The surface area of the NIPAM-MA-BIS microgel was relatively high, equaling 136 m^2 g^{-1}.
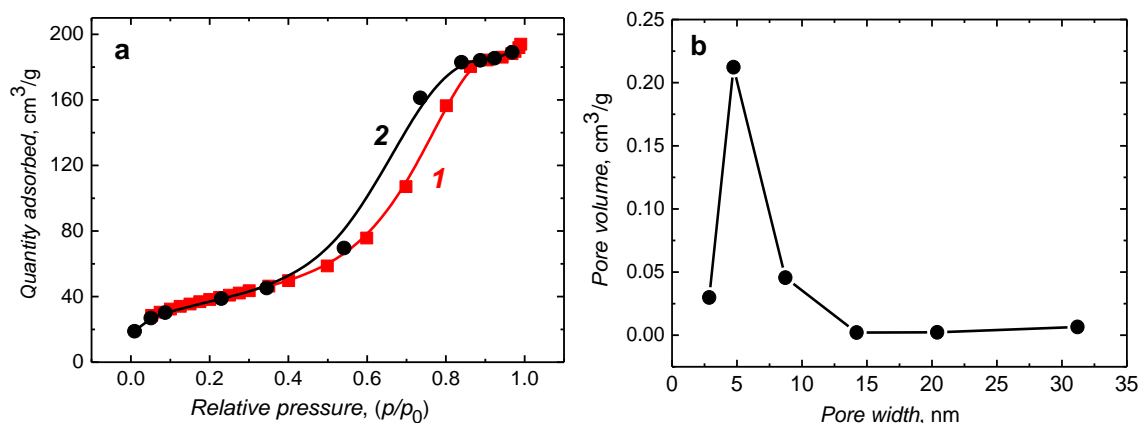
Figure 3.3-4. (a) The BET isotherm of N_2 (curve *1*) adsorption and (curve *2*) desorption for the microgel prepared by electrochemically initiated polymerization of NIPAM**,** MA, and BIS, and (b) the pore width distribution for the resulting NIPAM-MA-BIS gel microparticles prepared at low solution pH.

3.3.4 FTIR and C[13] NMR spectroscopy characterizing gel microparticles

The FTIR transmission spectroscopy was applied to confirm electrochemically initiated polymerization. The structural features of the gel microparticles, prepared by polymerizing NIPAM, MA, and BIS monomers at different combinations, were examined (Figure 3.3-5). The MA monomer incorporation in the polymer manifested itself by a sharp band at ~2990 cm^{-1} (spectra *1* and *2* in Figure 3.3-5). This band is characteristic of the stretching vibration of the -OH bond. The band at ~2930 cm^{-1} corresponds to the stretching vibration of the C-H bond of the -CH$_3$ substituent. It is present in the spectra of all gel microparticles (spectra *1 - 3* in Figure 3.3-5).[323] The band at ~3300 cm^{-1} corresponds to the stretching vibration of the N-H bond. Although this band is pronounced in spectra *1* and *3*, it is barely seen in spectrum *2* in Figure 3.3-5.

The spectrum of the copolymer, prepared with NIPAM, MA, and BIS, contains all the stretching vibration bands (Figure 3.3-5). The band at 1550 cm^{-1}, assigned to the N-H bond bending vibration, was present in the spectra of all microgels (Figure 3.3-5). The C-H bending vibration band of the -CH$_3$ substituent appeared at 1390 cm^{-1} (Figure 3.3-5). This band was characteristically split into two bands for the isopropyl substituent, one at 1388 and the other at 1370 cm^{-1} (spectrum *2* in Figure 3.3-5). Moreover, this band appeared in the NIPAM, MA, and BIS copolymer spectra at similar wavenumbers. However, it was relatively less intense (spectrum *3* in Figure 3.3-5). Sharp bands between 1630 and 1650 cm^{-1} confirm the carbonyl group presence in all polymers (Figure 3.3-5). The band at

~1700cm^{-1}, associated with the stretching vibration of the MA monomer's carbonyl bond, appeared as a shoulder in spectrum *1*, but it was quite intense in spectrum *2* in Figure 3.3-5.
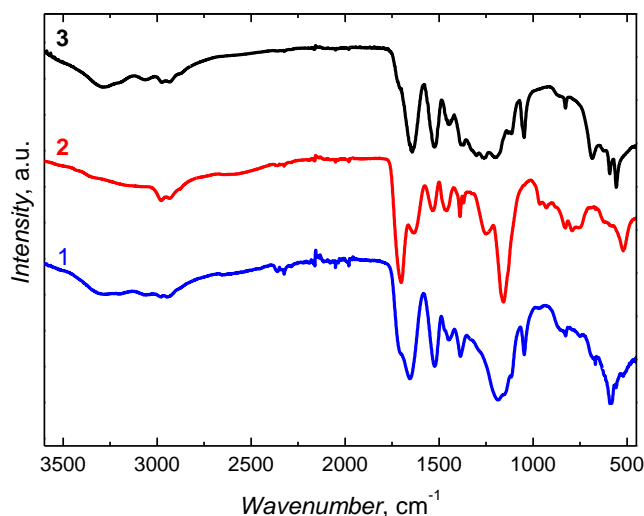
Figure 3.3-5. The FTIR transmission spectra of microgels prepared by electrochemically initiated copolymerization of NIPAM, MA, and BIS at the combination of (spectrum *1*) NIPAM-MA, (spectrum *2*) NIPAM-MA-BIS, and (spectrum *3*) NIPAM-BIS.

Moreover, the microgel structural features were disclosed with the C^{13} NMR spectroscopy measurements (Figure 3.3-6). The gel microparticles prepared by copolymerizing NIPAM and MA reveal a peak at ~178 ppm typical of the amide carbon atom of NIPAM (Figure 3.3-6). The peak at ~181 ppm confirms the presence of the -C=O bond of the MA moiety in the copolymer (spectrum *1* in Figure 3.3-6). The microgel prepared by combining all monomers shows a broad peak between 175 and 180 ppm, thus indicating an overlap of the –C=O and -C-NH carbon peaks (spectrum *2* in Figure 3.3.6). Worth mentioning that this peak was absent in the spectrum for gel microparticles not containing MA (spectrum *3* in the inset to Figure 3.3.6). Peaks at 44 and 21 ppm can be attributed to carbon atoms of the isopropyl and -CH$_3$ substituents of NIPAM, as indicated in earlier reported spectra for these substituents.[324, 325] The FTIR and C^{13} NMR spectroscopy structural analyses confirmed successful electrochemically initiated copolymerization of monomers of different activities.
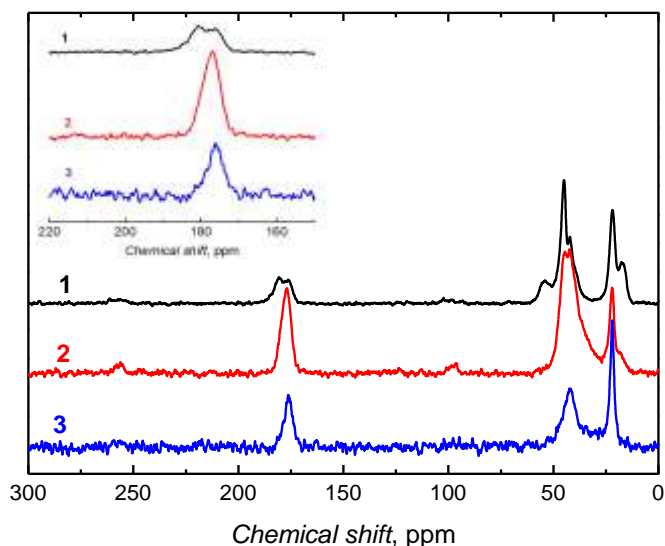
Figure 3.3-6. The ^{13}C NMR spectra of three different microgels prepared by electrochemically initiated copolymerization of NIPAM, MA, and BIS at the combination of (spectrum *1*) NIPAM-MA, (spectrum *2*) NIPAM-MA-BIS, and (spectrum *3*) NIPAM-BIS. Inset shows the magnified spectra in the chemical shift range of 150 to 220 ppm.

3.3.5 Gel microparticles analyzing with dynamic light scattering (DLS)

The dynamic light scattering (DLS) determined the average hydrodynamic diameter of gel microparticles (Figure 3.3-7a). If the particles exhibit random Brownian motion, their diffusion coefficient can be determined from the autocorrelation function's decay (Figure 3.3-7b). The gel microparticles' suspensions were diluted before measurements. The dispersity in aqueous solutions of the NIPAM-MA-BIS, NIPAM-BIS, and NIPAM-MA microgels was high. A relatively high polydispersity index, PDI > 0.1, indicated a broad distribution of particle sizes (Figure 3.3-7a), well matching the SEM imaging (Figure 3.3-2). Because of the anionic APS initiator application in all polymerizations, the zeta-potential of microgels in their swollen state was slightly negative, being -9 to -10 mV. The particle size of the NIPAM-MA-BIS microgel appeared smaller than that of the NIPAM-BIS and NIPAM-MA microgels. Presumably, the incorporation of MA facilitated the formation of a microgel with defined particle size. However, surprisingly, the size of the NIPAM-MA gel microparticles ranged from 1 to 2 μm (curve *3* in Figure 3.3-7a). The particle size distribution of the microgel without MA, i.e., NIPAM-BIS, was broader, ranging from 1 to 2.5 μm (curve *2* in Figure 3.3.7a). The small peaks in DLS (Figure 3.3-7a) for NIPAM-BIS and NIPAM-MA monomer combinations correspond to oligomers.[326]
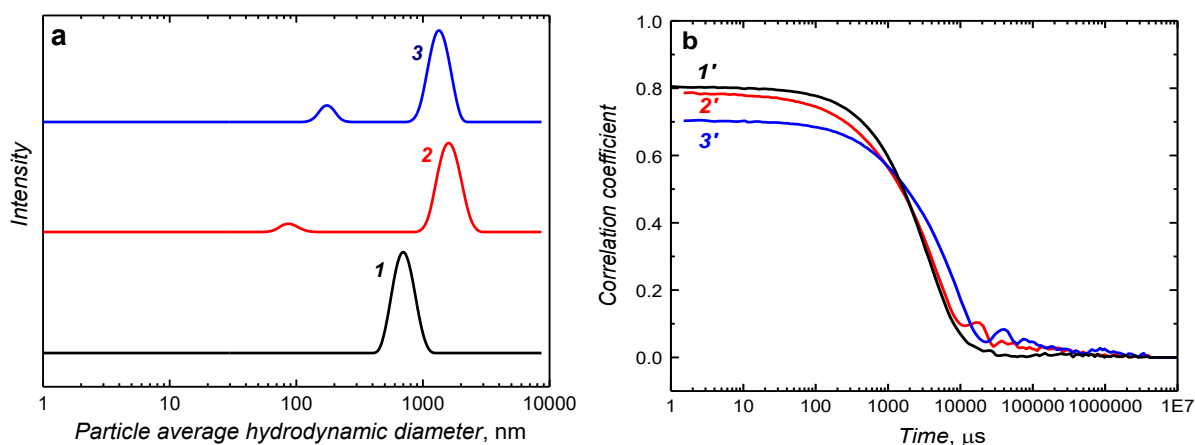
Figure 3.3-7. The (a) DLS size analyses and (b) correlation coefficient vs. time of gel microparticles prepared under hydrodynamic conditions by electrochemically initiated polymerization at the (curve *1*) NIPAM-MA-BIS, (curve *2*) NIPAM-BIS, and (curve *3*) NIPAM-MA monomer combinations.

Moreover, the DLS measurements were performed at different time intervals after ceasing electrochemical initiation and hydrodynamic agitation (Figure 3.3-8) to investigate the gelation progress with time. To this end, the microgel was prepared by combining the NIPAM, MA, and BIS monomers. As a result, the size distribution of gel microparticles collected immediately after seizing the electrochemical initiation was broad (curve *1* in Figure 3.3-8), i.e., ranging from 1000 to 4000 nm. This wide distribution can arise from the presence of growing polymer chains. The gel microparticles' size was further measured after sample collecting at 30 min of gelation. This size was remarkably smaller, i.e., between 500 and 1000 nm (curve *2* in Figure 3.3-8). Finally, the size of particles collected after 1 h was grown again. This size ranged from 1000 to 5000 nm. This size increase with the microgel preparation time can be due to particle aggregation.

The DLS results prompted us to speculate on the following polymerization mechanism. A water-soluble sulfate radical initiates the formation of BIS radicals. Then, these radicals react with other monomers to grow oligomers in the solution until reaching a critical chain length. Afterward, the growing chain collapses to become an unstable colloidal particle. The precursor particles can follow one of at least two competing routes. For instance, they can deposit onto an existing colloidally stable polymer particle or aggregate with other precursor particles until they form a large particle to be colloidally stable.

110
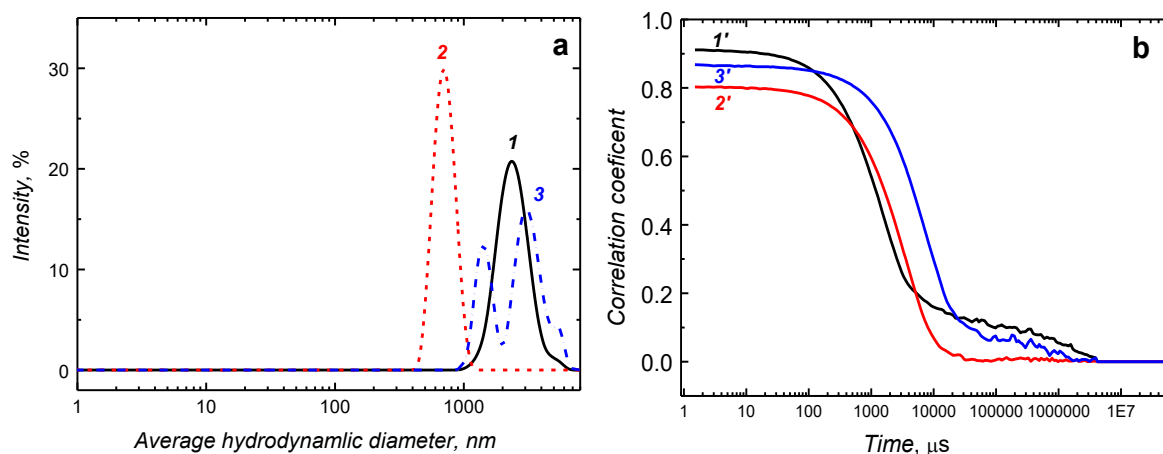
Figure 3.3-8. (a) The microgel hydrodynamic particle size, DLS measured during electrochemically initiated polymerization under hydrodynamic conditions at (curve *1*) 0, (curve *2*) 30 min, and (curve *3*) 1 h after initiating the polymerization. (b) The correlation coefficient for (curve *1'*) 0, (curve *2'*) 30 min, and (curve *3'*) 1 h after initiating the polymerization. The gel microparticles were prepared by combining NIPAM, MA, and BIS monomers.

3.3.6 Thermal stability of gel microparticles

The microgel thermal stability was investigated by thermogravimetric analysis (TGA) and the first derivative TGA (DTGA). Thermograms in Figures 3.3-9a and 3.3-9b present the microgel mass loss in the TGA and DTGA experiments, respectively. Mainly, the DTGA thermograms determined the temperatures of the most significant mass losses. The first mass loss of ~12 to 15% at ~70 °C indicates water removal. The second and the third losses between 200 and 450 °C were caused by the decomposition of the NIPAM-MA polymer backbone (thermogram *1* in Figure 3.3-9). Three corresponding endothermic DTGA peaks (thermogram *1'* in Figure 6a) confirmed the presence of three successive stages in the thermal decomposition of this polymer. The first significant decomposition above ~200 °C was assigned to the cleaving of easily breakable groups, followed by complete polymer degradation at ~390 °C.

Interestingly, thermograms *2* and *2'* in Figure 3.3-9a and 3.3-9b, respectively, for the NIPAM-BIS gel microparticles were slightly shifted to a higher temperature of ~400 °C. The smallest mass loss for the NIPAM-MA-BIS microgel combining all monomers indicated that this microgel was thermally most stable (thermogram *3* in Figure 3.3-9a) while the NIPAM-MA was the least stable microgel (thermogram *2* and *2'* in Figure 3.3-9a and 3.3-9b, respectively). The decomposition of this microgel involved three steps. The absence of any cross-linking monomer was likely the reason for this microgel's lower stability. Other

111

gel microparticles decomposed via four stages (thermograms *2* and *3* in Figure 3.3-9a as well as *2'* and *3'* in Figure 3.3-9b).
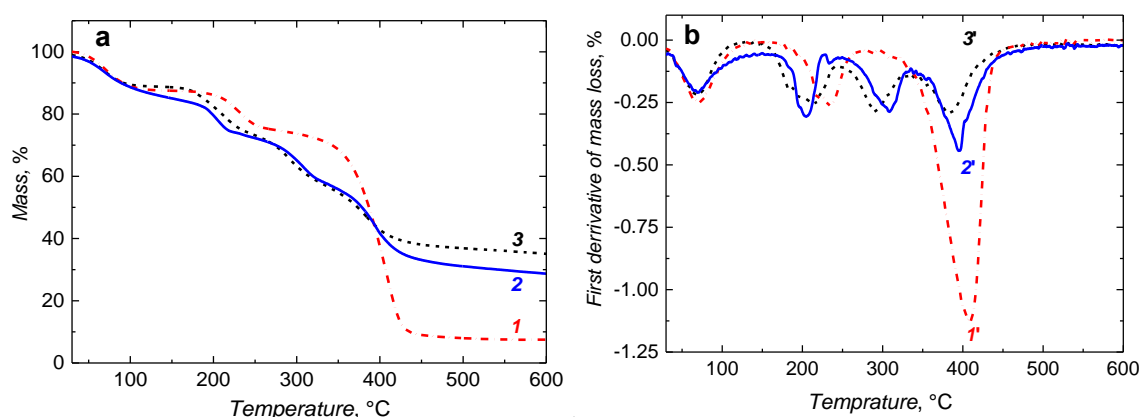
Figure 3.3-9. The (a) TGA and (b) DTGA thermograms for dried (curves *1* and *1'*) NIPAM-MA, (curves *2* and *2'*) NIPAM-BIS, and (curves *3* and *3'*) NIPAM-MA-BIS gel microparticles. The microparticles were heated up to 1000 °C at a constant rate of 10 °C min^{-1}.

3.3.7 Electrochemical synthesizing and characterizing gel films grafted over silica nanoparticle and magnetic nanoparticle cores

Multi-step polymerization conditions have already been applied to coat different inorganic core particles with films of the PNIPAM shell alone or combined with a cross-linking monomer.[327-333] For instance, a PNIPAM shell was grafted over selected cores via multi-step reversible addition-fragmentation transfer polymerization.[330, 331] These hybrid NPs combine the properties of an inorganic core and a gel shell. In effect, they provide appealing catalytic[334] and nontoxic drug delivery systems.[335]

Toward that, silica NPs and MNPs were herein coated with thin polyacrylamide gel films by electrochemically initiated polymerization. Originally developed for coating MNP cores, this procedure was slightly modified to coat the silica NP cores. For gel film grafting over silica NPs, the acidity of the solution for polymerization was adjusted to pH = 7.0. It appeared that a macroporous film was formed at this pH value. This film was favorable in the coating of silica NPs. Finally, the monomers at different combinations and MNPs were added to the solution for polymerization to prepare the MNPs coated with gel films. The pH of this solution was not adjusted.
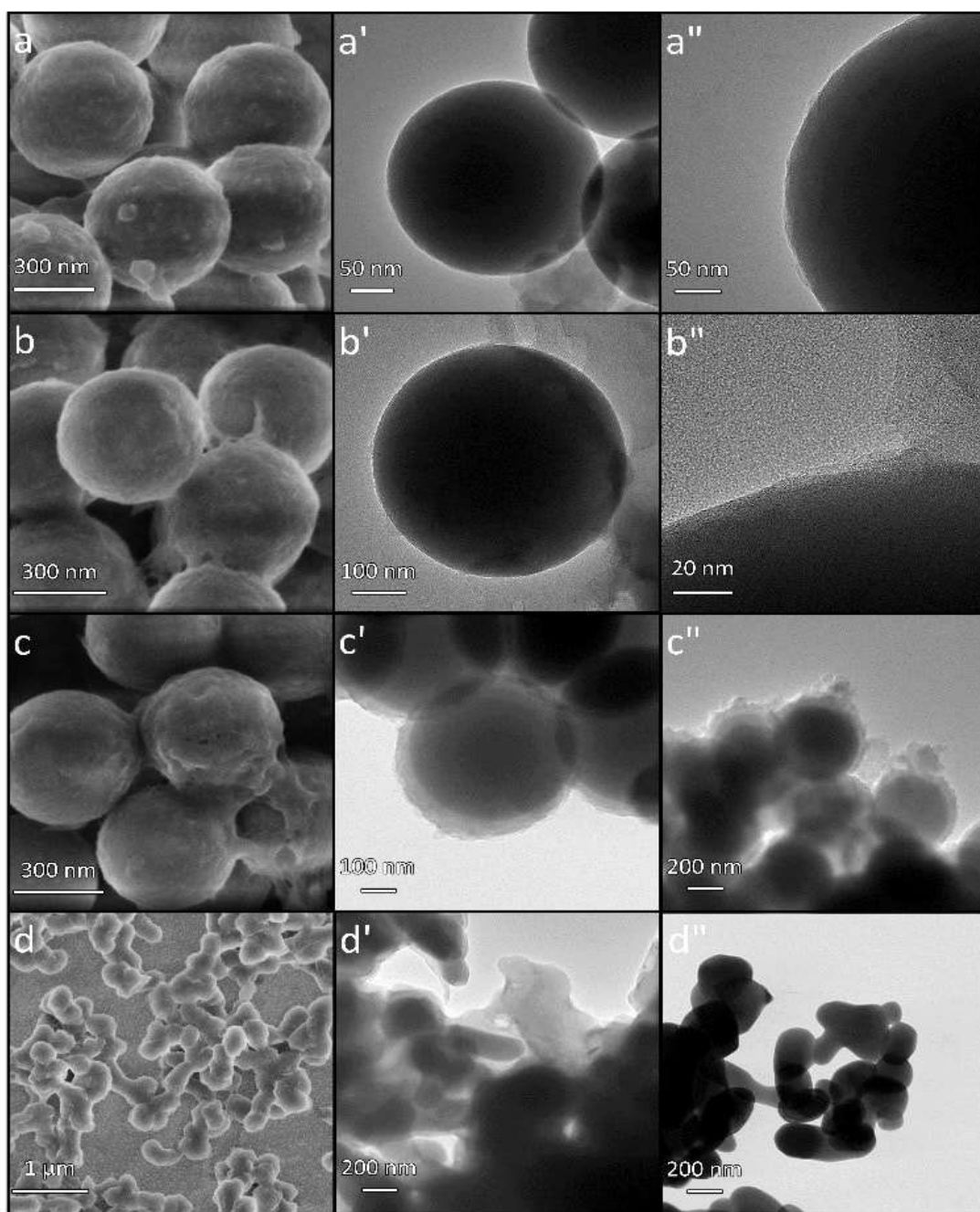
Figure 3.3-10. The (a, b, and c) SEM and (a', a'', b', b'' and c' and c'') STEM images of gel films deposited on silica NPs cores. The films were prepared by combining different supports and monomers, i.e., (a, a', and a'') (silica nanoparticle)-(NIPAM-MA-BIS), (b, b', and b'') (silica nanoparticle)-(NIPAM-BIS), and (c, c', and c'') (silica nanoparticle)-(MA-BIS). The (d) SEM and (d') TEM images of (magnetic nanoparticle)-(NIPAM-MA-BIS), and (d'') STEM image of bare magnetic nanoparticles.

113

3.3.8 SEM and STEM characterizing the morphology of gel films grafted over silica nanoparticle and magnetic nanoparticle cores

The SEM image clearly shows that the gel film at the NIPAM-MA-BIS monomer combination coats the silica NP cores (Figure 3.3-10). The STEM image indicates that this film is relatively thin (Figure 3.3-10a' and a"). The NIPAM-BIS gel coating presents itself similarly (Figure 3.3-10b, b' and b"). Both SEM and STEM imaging confirmed the formation of a thick gel film for the MA-BIS combination (Figure 3.3-10c, c', and c"). The SEM (Figure 3.3-11a) and STEM (Figure 3.3-11b, c) images of NIPAM-MA gel film-coated silica NPs were not seen clearly, suggesting that the film was very thin. Figure 3.3-10d shows the image of MNPs coated with the gel film at the NIPAM-MA-BIS combination. The STEM image confirms the inclusion of MNPs in the gel net (Figure 3.3-10d'). However, the morphology of film-coated MNPs differed from that of bare MNPs (image d" in Figure 3.3-10).
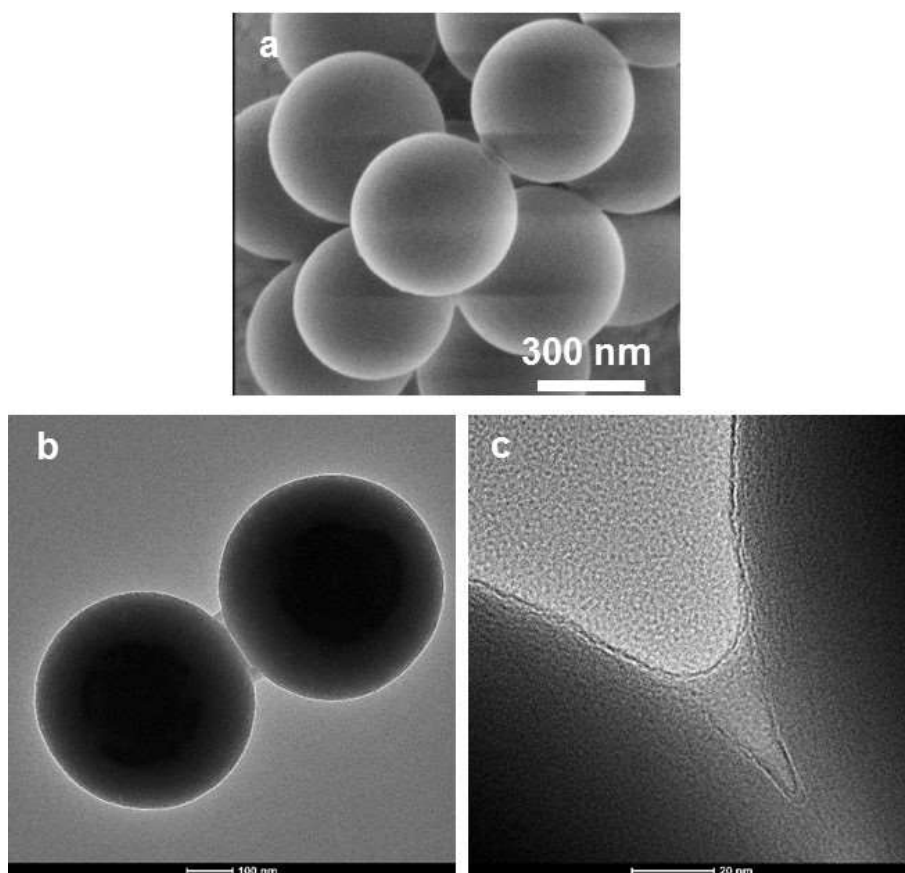
Figure 3.3-11. The (a) SEM and (b, c) TEM images of the (silica nanoparticle)-(**NIPAM-MA**) core-shell nanoparticles.

The EDX spectroscopy mapping indicates the elemental distribution of the MA-BIS and NIPAM-MA gel film-coated silica NPs (Figures 3.3-12a and 3.3-12a'). Figure 3.3-12 shows elemental maps of representative NPs revealing a core-shell structure of the SiO₂ core (olive-yellow), as well as the C (blue) and N (red) containing gel shells. This result supports the deposition of over ~50 nm thick gel films on the silica NP cores (Figure 3.3-12a and 3.3-12a'). These results postulated that the reactivity of monomers in different combinations was different. The SEM and TEM imaging revealed that the polymer film shell growth over the core substrate was pronounced in the presence of MA and BIS monomers. At another combination, the films were thinner (Figure 3.3-10b', 3.3-10b", and 3.3-11b).
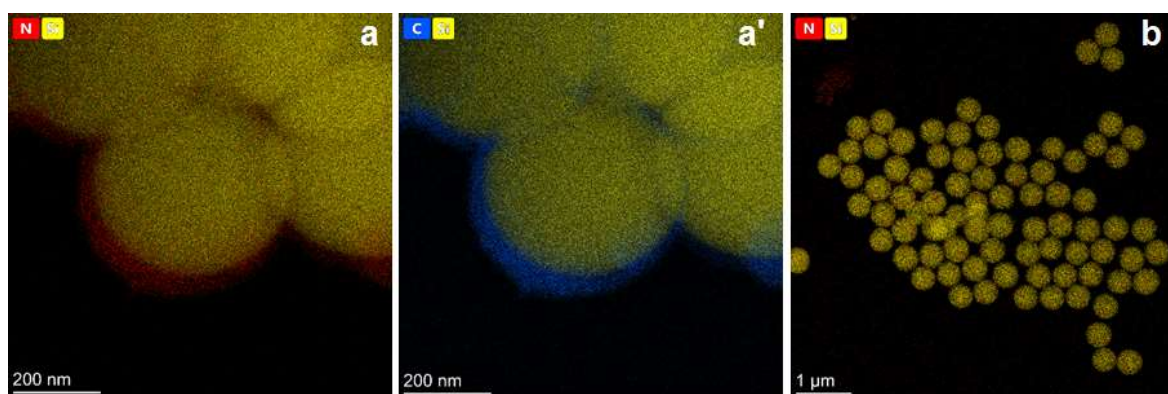
Figure 3.3-12. Energy-dispersive X-ray (EDX) spectroscopy mapping of elemental distribution over the (a, a') (silica nanoparticle)-(MA-BIS) and (b) (silica nanoparticle)-(NIPAM-MA) gel film.

3.3.9 Thermal stability of gel films grafted over silica and MNPs cores

Similarly, as the gel particles' stability (Figure 3.3.9), the stability of the gel films deposited on the silica NP and MNP cores was investigated with both TGA and DTGA (Figure 3.3-13). The first mass loss, associated with water removal from both the (silica nanoparticle)-(MA-BIS) and MNP-(NIPAM-MA-BIS) core-shell nanostructures, was ~10% at ~110 °C. For (silica nanoparticle)-(NIPAM-BIS), this loss was lower, equalling 5%, thus indicating less water content in the shell. Moreover, the water loss was slower. The second and the third mass loss in the TGA thermogram was in the range of 200 - 450 °C. They arose from the thermal decomposition of the polymer shell. Interestingly, MNP-(NIPAM-MA-BIS) decomposition (thermogram *3* in Figure 3.3-13a) was more extensive than those of silica NPs coated with gel films (thermograms *1 and 2* in Figure 3.3-13a), presumably,

because of decomposition of the magnetic core NPs above 450 °C for the former. Apparently, the gel shell deposited on silica NP cores by combining the MA and BIS monomers (thermogram *2* in Figure 3.3-13a) than that prepared by combining the NIPAM and BIS monomers (thermogram *1* in Figure 3.3-13a).
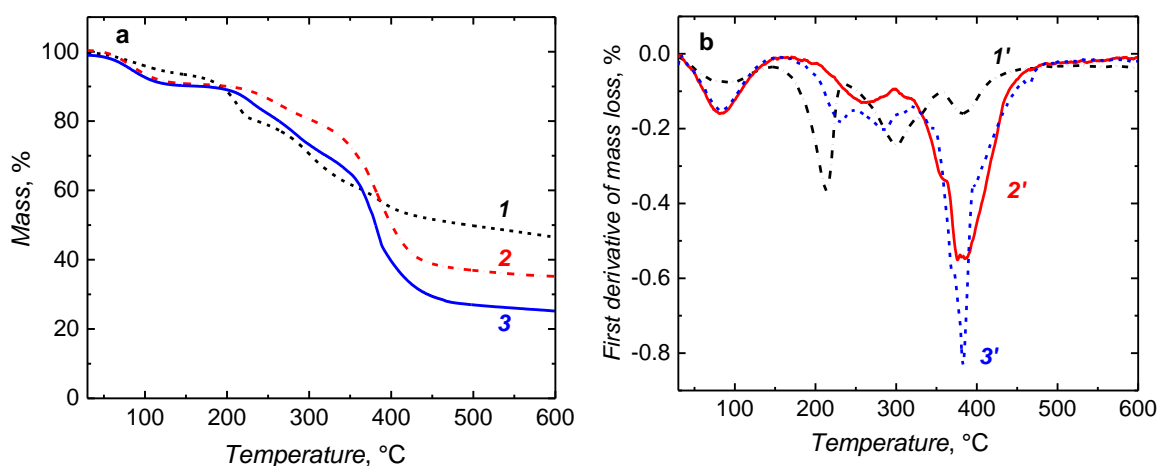
Figure 3.3-13. The (a) TGA and (b) DTGA thermograms for dried gel core-shell particles of (curves *1* and *1'*) (silica nanoparticle)-(NIPAM-BIS), (curves *2* and *2'*) (silica nanoparticle)-(MA-BIS), and (curves *3* and *3'*) (magnetic nanoparticle)-(NIPAM-MA-BIS). The samples were heated up to 1000 °C at a constant rate of 10 °C min^{-1}.

3.3.10 Fourier-transform infrared spectroscopy characterizing gel shells

The presence in the FTIR spectrum of the bands at ~1650 and 1520 cm^{-1} corresponding to the C=O bond stretching and N-H bond bending vibration, respectively, of the amide group, confirms the gel shells deposition on the silica NP cores (spectra *1* and *2* in Figure 3.3-14), as well as on the MNPs (spectrum *3* in Figure 3.3-14). The band appearing as a shoulder at ~1710 cm^{-1} originates from the stretching vibration of the carboxyl group in the shell containing the MA moiety (spectrum *1* in Figure 3.3-14). The band at 1100 cm^{-1} is related to the Si-O bond stretching vibration (spectra *1* and *2* in Figure 3.3-14). All the spectra contain main bands at ~2930 cm^{-1} assigned to the C-H bond stretching vibration of the -CH$_3$ substituent (spectra *1 - 3* in Figure 3.3-14). The N-H bond stretching vibration appeared as the band at ~3300 cm^{-1} (spectra *1 - 3* in Figure 3.3-14). Similarly, as above, the presence of a sharp band at ~2990 cm^{-1} of the -OH bond stretching vibration (spectra *1* and *3* in Figure 3.3-14) confirms the MA monomer incorporation in the shell. These characteristic

bands evidence the successful deposition of the gel shells at different monomer combinations.
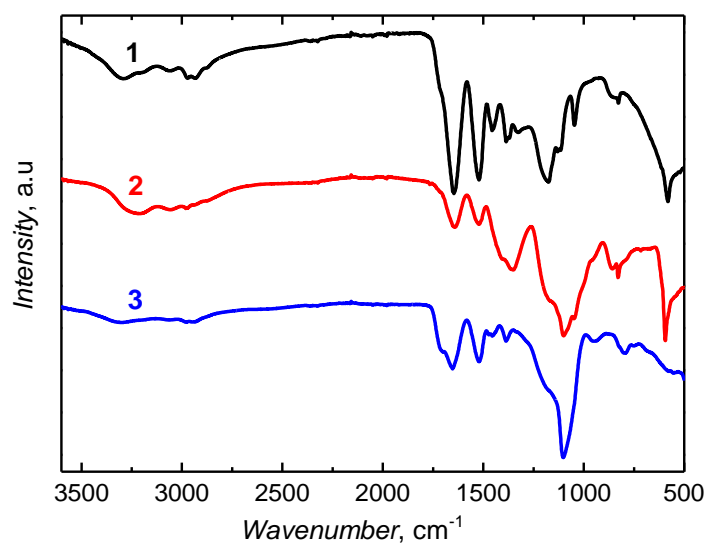
Figure 3.3-14. The FTIR transmission spectra of thin gel films grafted over inorganic cores at the monomer composition of (curve *1*) (silica nanoparticle)-(MA-BIS), (curve *2*) (silica nanoparticle)-(NIPAM-BIS), and (curve *3*) (magnetic nanoparticle)-(NIPAM-MA-BIS) by electrochemically initiated copolymerization.

Chapter 3

3.4 Electrochemically synthesized polyacrylamide gel and core-shell nanoparticles for 3D cell culture formation

3.4.1 Electrochemical gel particles synthesizing

In Chapter 3.3, an electrochemically initiated synthesis of polyacrylamide with and without core support using amphiphilic and hydrophilic monomers is discussed in detail.[336] Overall, it led to micro-sized gel particles with irregular morphology. Therefore, further optimization was needed to improve the morphology and size of these particles. That was because the uniform nano-sized gel particles are best suited for, e.g., biomedical applications.

Herein, we report the improvement of the gel particles' architecture. Because of a relatively high monomer solubility, the solvent for gel synthesis was not changed, and an aqueous solution was chosen. The chain transfer efficiency increased during aqueous polymerization because of strong intermolecular hydrogen bonding between the monomers' amide ($O=C-NH_2$) groups and water molecules.

Later, another critical factor, i.e., the electroinitiation potential, was optimized. For that, potentials different than -0.60 V, i.e., -0.70 and -0.80 V vs. Ag quasi-reference electrode, were applied for 3 h while monomer concentrations were 25 mM NIPAM, 25 mM MA, and 50 mM BIS, as previously reported.[336] When a higher potential of -0.80 V was applied, the gel appearance in the solution was extended over 24 h. This time shortened when the potential of -0.70 V vs. Ag quasi-reference electrode was selected. The shortest gel formation time was needed when the potential of -0.60 V vs. Ag quasi-reference electrode was applied to break APS to generate free sulfate radicals in the solution.[336]

An alternative factor that controls the morphology of gel particles is monomers' composition. Therefore, gels were synthesized using cross-linking monomers of different concentrations. It appeared that the BIS cross-linking monomer concentration increase up to 50 mM in the solution for polymerization nearly did not change the morphology of the resulting gel particles. However, the polymer morphology was substantially changed at concentrations exceeding 50 mM BIS. Another solution was used to polymerize 20 mM MA, 20 mM NIPAM, and 10 mM BIS. In this polymerization, monomers' concentrations were slightly lower than those reported previously.[336] Surprisingly, under these monomers and cross-linking monomers concentration conditions, the gelation commenced after only 20 min of electrochemical initiation.

Nevertheless, the potentiostatic experiment was continued for 1 h at -0.60 V vs. Ag quasi-reference electrode in an aqueous solution of 25 mM NIPAM, 25 mM MA, and 50 mM BIS monomers. After 30 min, we collected the gel particles by centrifuging and dispersing them in the water again. This cycle has thrice been repeated to obliterate unreacted substrates.

Core particles were dispersed in a solution of monomers and cross-linking monomers of the composition similar to that described above to synthesize core-shell particles.

3.4.2 Morphological characterizing of gel microparticles and core-shell nanoparticles

The morphology of the gel microparticles, prepared at different electroinitiation potentials (Figure 3.4-1) and different cross-linking monomer concentrations, was examined by SEM imaging (Figure 3.4-2). The gels were prepared as separate microparticles at lower potentials, whereas at higher potentials, they were more bulk-like (Figure 3.4-1). Therefore, a lower electroinitiation potential was chosen for further study. Figure 3.4-2 shows SEM images of NIPAM-MA-BIS gel particles synthesized using the BIS cross-linking monomer of different concentrations. It appeared that the BIS concentration increase up to 50 mM nearly did not change the morphology of the resulting gel particles. However, this morphology was substantially changed at concentrations exceeding 50 mM BIS (e.g., 100 mM). More deformed particles were obtained at increased BIS concentration (Figure 3.4-2). An increase in the BIS concentration decreased gel porosity and solubility.

This radical polymerization might not be sufficiently quenched after seizing the electrochemical reaction. Therefore, a polymerization inhibitor, vis., hydroquinone monomethyl ether, was added after stopping electroinitiation.[337] Three different inhibitor concentrations were used, vis., 5, 15, and 25 mM, to study the polymerization chain inhibition effect on the gel particles' morphology (Figure 3.4-3). Nevertheless, globular gel particles of different sizes were obtained in each case.

The SEM image of the solution for polymerization, which was 20 mM in MA, 20 mM in NIPAM, and 10 mM in BIS, justified the tuning of electropolymerization conditions (Figure 3.4-4). Decreasing the cross-linking monomer concentration resulted in successfully preparing nanometre-sized gel particles (Figure 3.4-4a'). These results suggest that the gel's overall morphology depends upon the cross-linking monomer concentration. In a way, a low concentration can be beneficial for improving the swelling property, porosity, and mechanical stability of the gel NPs prepared.[338]

The EDX mapping indicates the elemental distribution of the NIPAM-MA-BIS gel NPs (Figure 3.4-4c and 4c'). It reveals that the NPs contained carbon (green) and nitrogen (yellow) elements, and these elements were evenly distributed in the gel NPs. Core-shell particles, such as NIPAM-MA-BIS gel film-coated MNPs, were imaged to confirm thin gel film coating. The SEM image clearly shows that the gel film of the NIPAM-MA-BIS monomer combination

coats the inorganic core (Figure 3.4-5a, 5a', 5b, and 5b'). The TEM image visualizes that this film is thin (Figure 3.4-5b and 5b'). Moreover, the EDX profile supports this observation (Figure 3.4-5c and 5c'). This mapping reveals that the Fe core particle (yellow) is coated with a film containing carbon (green) and nitrogen (blue) elements.
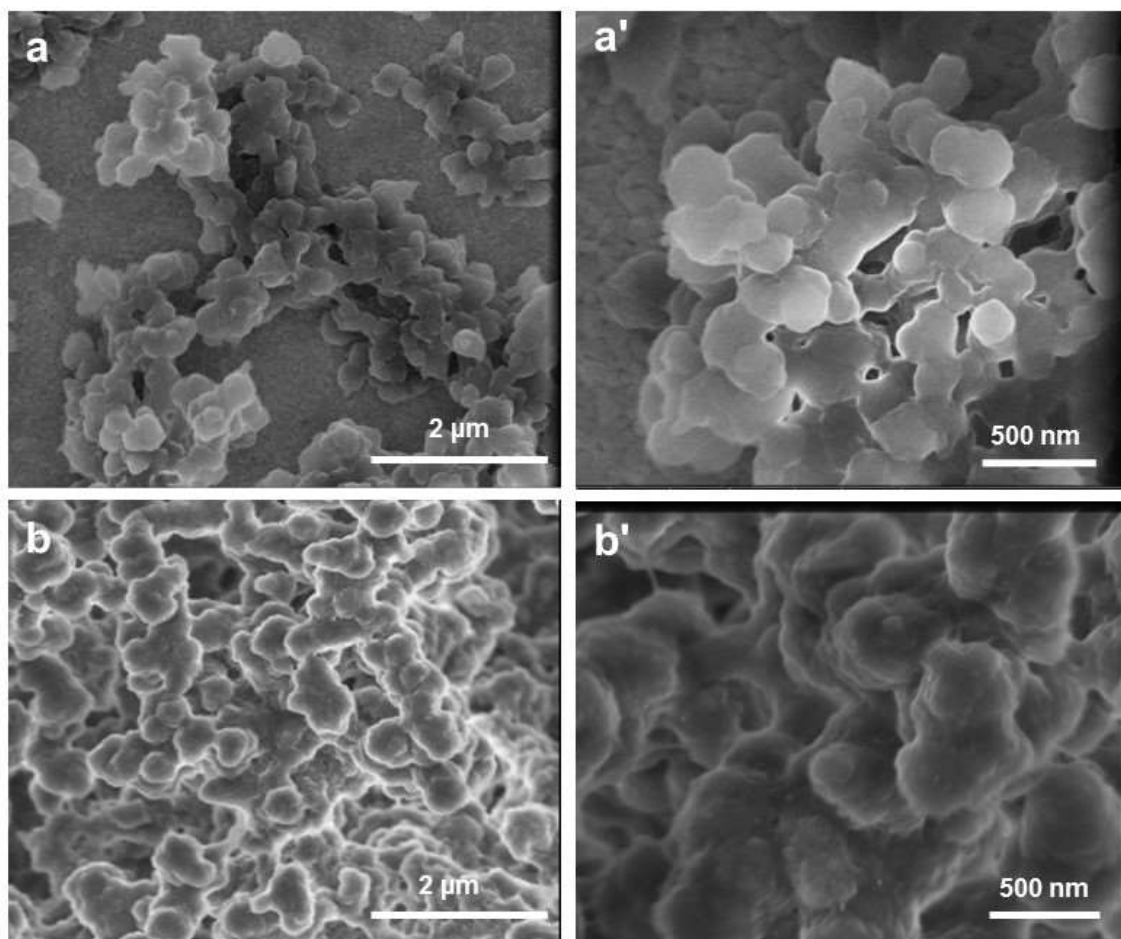
Figure 3.4-1. The SEM images at different magnifications of NIPAM-MA-BIS gels synthesized at the electroinitiation potential of (a, a') -0.70 and (b, b') -0.80 V vs. Ag quasi-reference electrode from the aqueous solution of 25 mM NIPAM, 25 mM MA, and 50 mM BIS.
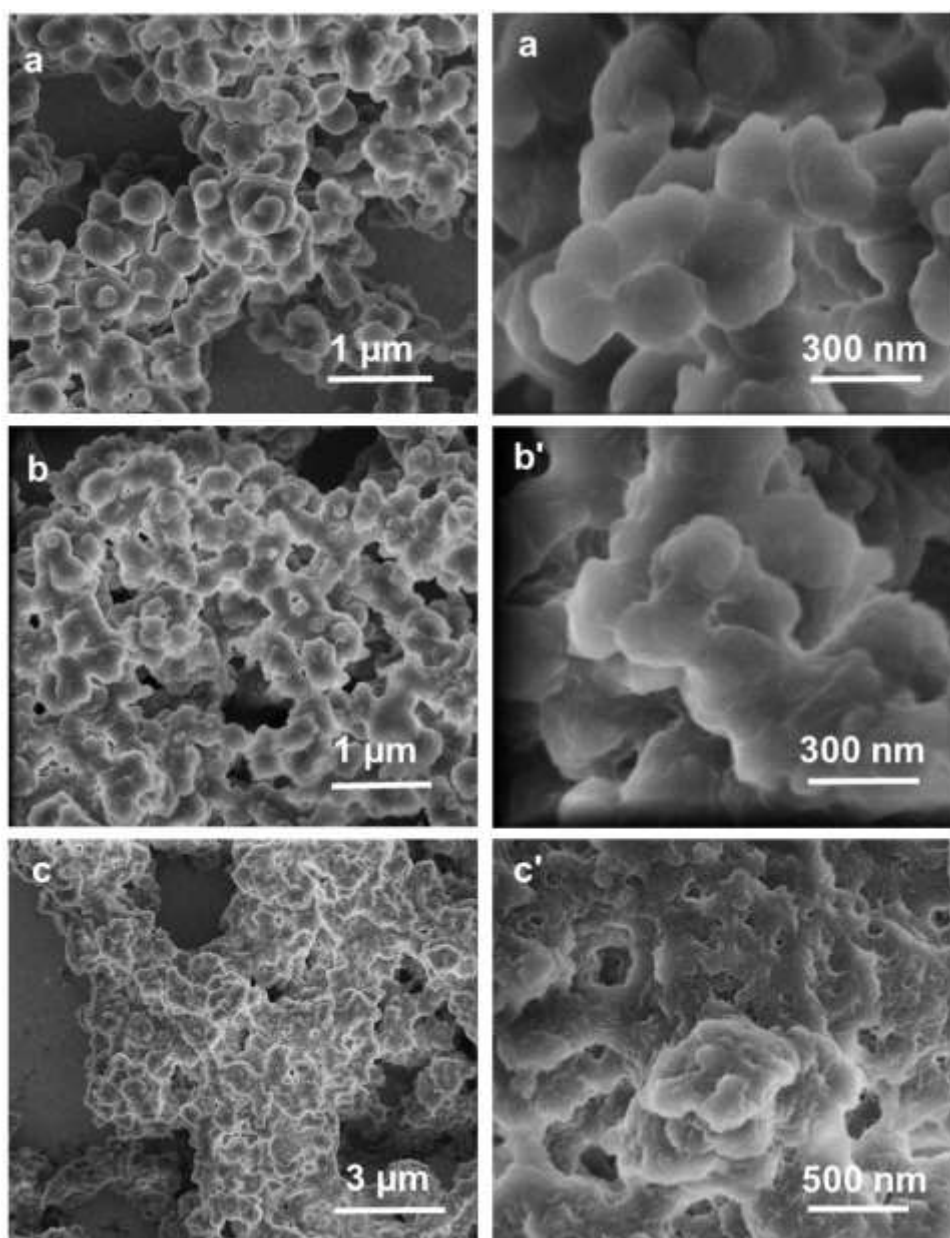
Figure 3.4-2. The NIPAM-MA-BIS gels' SEM images at the BIS cross-linking monomer concentration of (a, a') 5, (b, b') 50, and (c, c') 100 mM. Concentrations of the NIPAM and MA monomers in the solution for polymerization were 25 mM each.
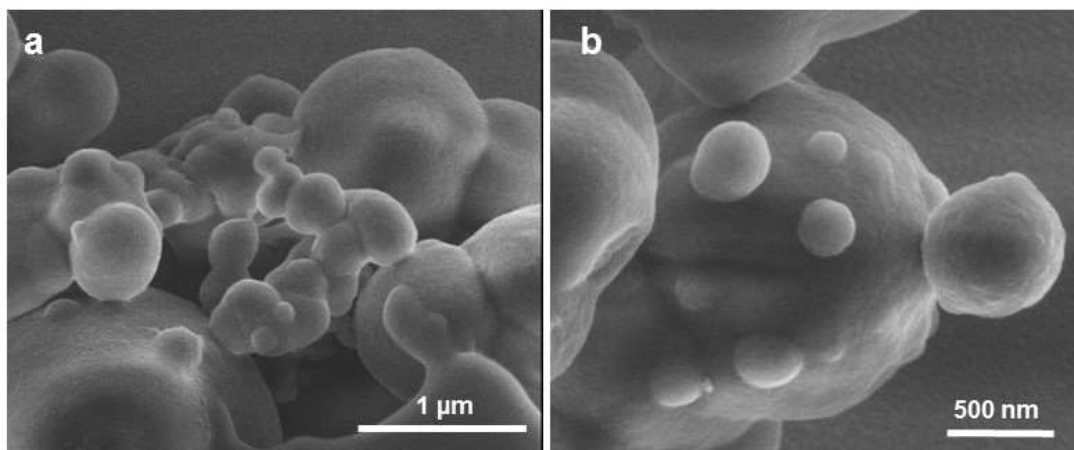
Figure 3.4-3. SEM images of gel particles prepared after inhibiting with 15 mM hydroquinone monomethyl ether the copolymerization from the aqueous solution of 25 mM NIPAM, 25 mM MA, and 50 mM BIS.
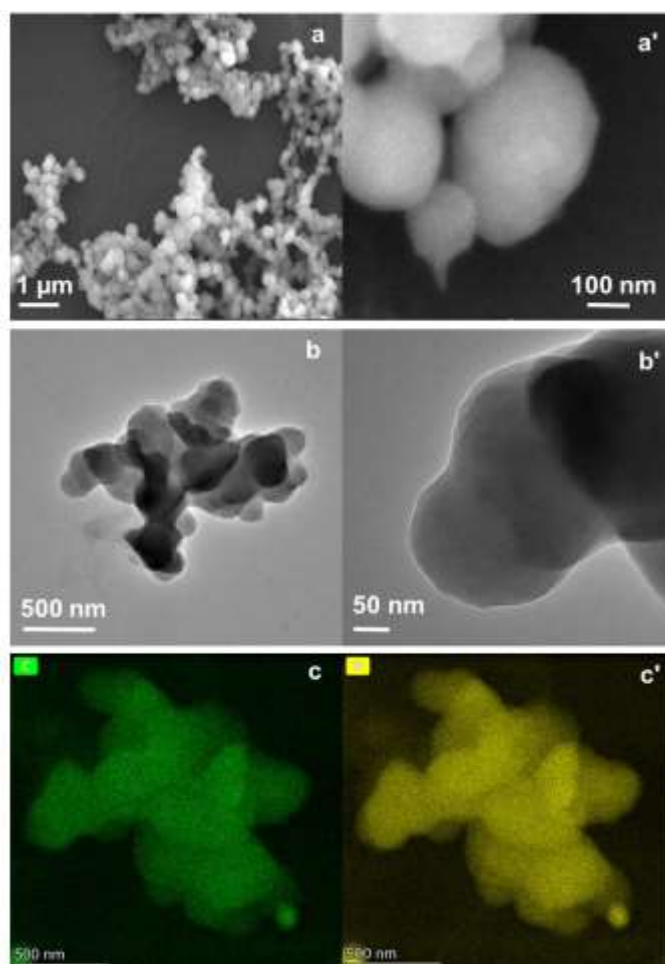
Figure 3.4-4. The (a, a') SEM and (b, b') TEM images of the NIPAM-MA-BIS gel particles prepared at the monomers' concentrations of 20, 20, and 10 mM, respectively. (c, c') Mapping the elemental distribution of the NIPAM-MA-BIS gel particle; carbon (green) and nitrogen (yellow).
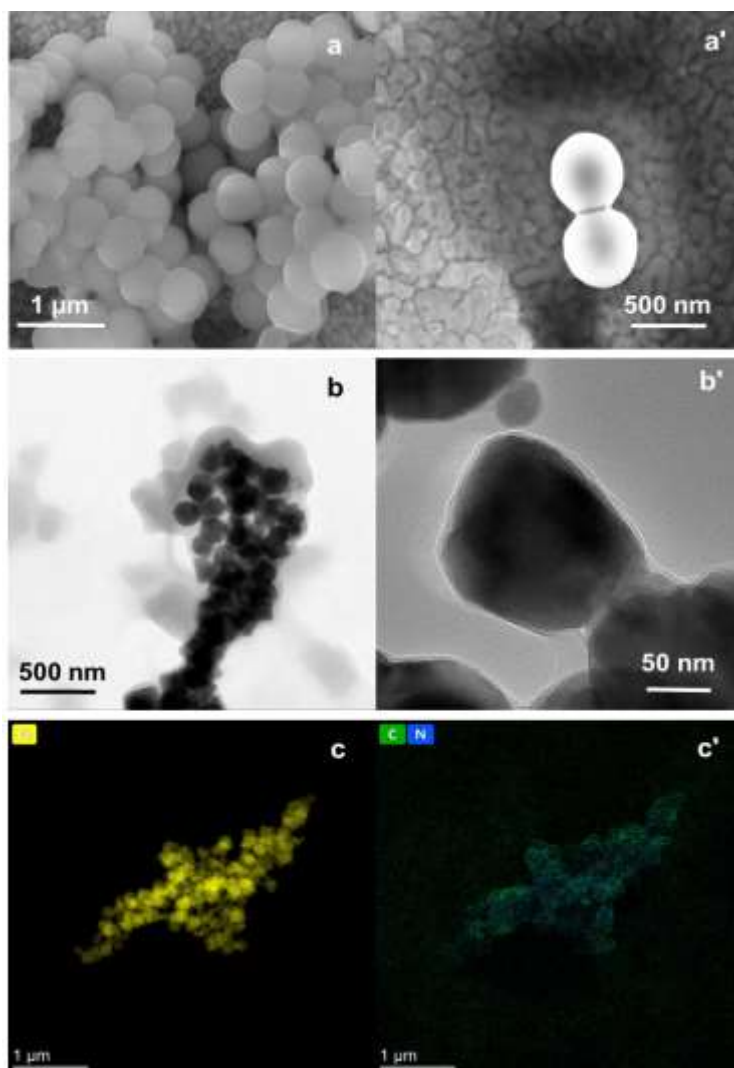
Figure 3.4-5. (a, a') SEM images of the NIPAM-MA-BIS film-coated SiO$_2$ particles. (b, b') TEM images of the NIPAM-MA-BIS film-coated magnetic nanoparticles. (c, c') Mapping the elemental distribution of NIPAM-MA-BIS gel particles, carbon (green) and nitrogen (blue), prepared using the aqueous solution of 20 mM NIPAM, 20 mM MA, and 10 mM BIS.

3.4.3 FTIR spectroscopy characterizing of gel particles

FTIR spectroscopy was used to identify functional groups present in the NIPAM-MA-BIS gel microparticles (Figure 3.4-6). The two bands at 2925 and 2980 cm^{-1} were in the spectrum for the C-H bond's asymmetric and symmetric stretching vibrations, respectively. The broad and intense band at 3327 cm^{-1} was associated with the N-H bond stretching. At 1388 and 1538 cm^{-1}, the respective C-N stretching vibration and N-H bending vibration bands were present. The split band at ~1650 cm^{-1} corresponds to the amide I and amide II bands of NIPAM within the nanogel particles. The band at 1700 cm^{-1} is associated with the carbonyl group stretching vibration, and the sharp band at 1160 cm^{-1} is assigned to the C–N bond vibration of

MA in the nanogel particles. These results confirm successful monomers' copolymerization leading to gel formation.
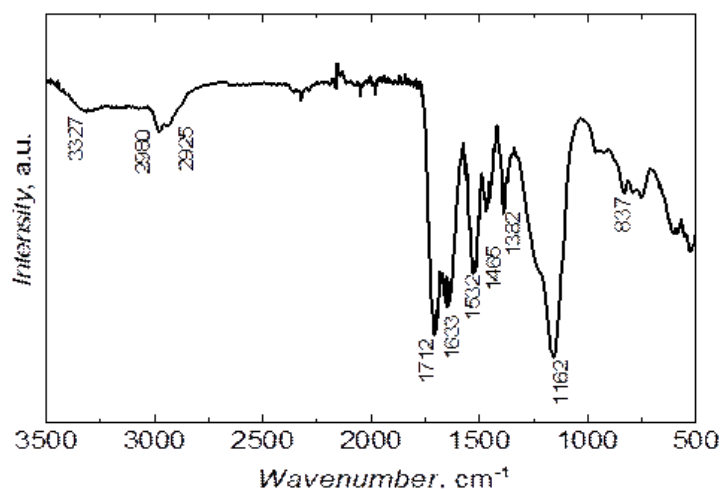
Figure 3.4-6. The FTIR transmission spectrum of the NIPAM-MA-BIS microgel prepared by electrochemically initiated copolymerization from the aqueous solution of 20 mM NIPAM, 20 mM MA, and 10 mM BIS.

3.4.4 Dynamic light scattering (DLS) studying gel particles in solutions of different pH

Polyacrylamide gel particles' properties are pH-dependent.[325, 339, 340] For instance, the particles' hydrophobic nature at low pH can be changed to hydrophilic at high pH, e.g., in a phosphate buffer solution. The size of the gel particles is smaller if the dispersion solution's pH is higher (Figure 3.4-7). The apparent pK_a of MA is 4.25. Therefore, protonated -COOH groups of MA molecules promote gel particles aggregation at low pH. At pH exceeding this pK_a value, the deprotonated -COO⁻ groups decrease gel aggregation because of coulombic repulsion. Another possible explanation for the smaller gel size at higher pH could be polymer chain opening and conforming into shorter globular chains. Furthermore, gel particles exhibit random Brownian motion at all pH values. Their autocorrelation function's decay is shown in Figure 3.4-8.
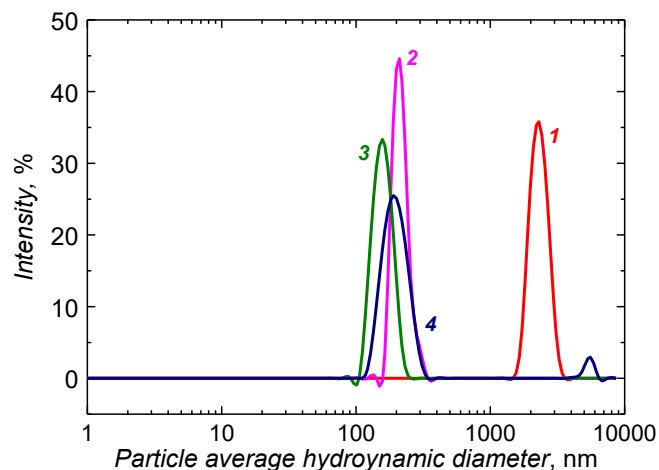
pH	Z_{avg}, (nm)	PDI
4.0	2142	0.133
6.0	522	0.620
7.0	201	0.417
8.0	214	0.480

Z_{avg} – particle average hydrodynamic diameter, PDI – polydispersity index.

Figure 3.4-7. The DLS analysis of NIPAM-MA-BIS gel microparticles dispersed in solutions of pH of (curve *1*) 4.0, (curve *2*) 6.0, (curve *3*) 7.0, and (curve *4*) 8.0, as well as particle parameters at different pH values.
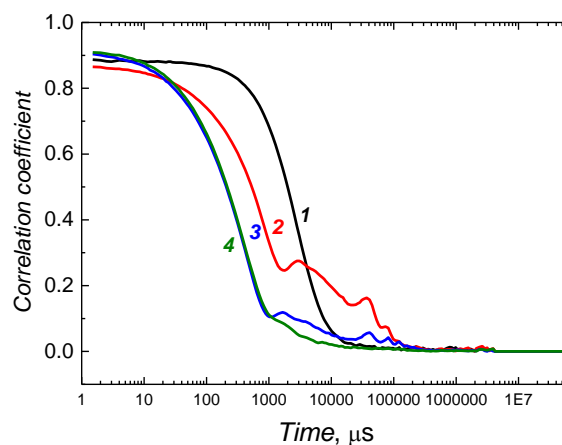
Figure 3.4-8. The time dependence of the correlation coefficient for NIPAM-MA-BIS gel microparticles in suspensions of pH of (curve *1*) 4.0, (curve *2*) 6.0, (curve *3*) 7.0, and (curve *4*) 8.0. The NIPAM-MA-BIS gel was prepared by electrochemically initiated copolymerization from the aqueous solution of 20 mM NIPAM, 20 mM MA, and 10 mM BIS.

3.4.5 Biocompatibility testing with the MTT proliferation/(metabolic activity) assay

For the prepared gel NPs' use as a 3D culture basement membrane-like ECM matrix, first, in vitro cytotoxicity assays were performed on two different cell lines, i.e., MDA-MB-231 (triple-negative breast cancer) and HeLa (cervical cancer) using the MTT proliferation/(metabolic activity) assay (Figure 3.4-9). Both cell lines were seeded on 96-well plates 24 h before the experiment. Afterward, the dose-dependent cytotoxicity assay was performed for a predefined time to determine the cell viability relative to the control. As the control, measurements were performed for untreated cells. The percentage of viable cells was calculated from the absorbance measurements data. NIPAM-MA-BIS gel NPs dispersed in acidic and neutral solutions are nontoxic and highly biocompatible for both cell lines in the concentration range of 20,000 to 39 ng/mL.

The percentage of viable cells in each sample compared to the control was calculated from the absorbance measurement data using the equation:

$$Viability\ [\%] = \frac{Actual\ viability - Average\ viability_{\text{negative control}}}{Average\ viability_{\text{positive control}} - Average\ viability_{\text{negative control}}} \qquad \text{Eq. 3.1}$$

The obtained values from five repeats were then averaged. The IC$_{50}$ concentration value was determined from a plot of cell viability as a function of nanoparticle concentration. A logistic dose-response four-parameter function, derived from Origin software, was fitted to the data. The IC$_{50}$ values were read from the logarithmic concentration scale for a point within the linear range of the fitted curve, corresponding to 50% cell viability as a function of gel NPs' concentration (Figure 3.4-10). Cell viability significantly decreased for the highest concentrations, vis., by 33% of living cells for 1000 µg/mL (Figure 3.4-10). The results agree well with literature data,[341, 342] indicating that the polyacrylamide gel prepared is compatible with cells. The IC$_{50}$ value of 485 µg/mL determined is solely due to covering the surface available to the cells, resulting in a lack of access to oxygen and nutrients (Figure 3.4-11). Two independent cytotoxicity assays were performed to test NIPAM-MA-BIS gel NPs dispersed in acidic and basic solutions. Figures 4a and 4b show cell viability as a function of the NPs' concentration. The results suggest that the NIPAM-MA-BIS gel NPs dispersed in acidic and neutral solutions are nontoxic and highly biocompatible for both cell lines in the 20,000 to 39 ng/mL concentration range.
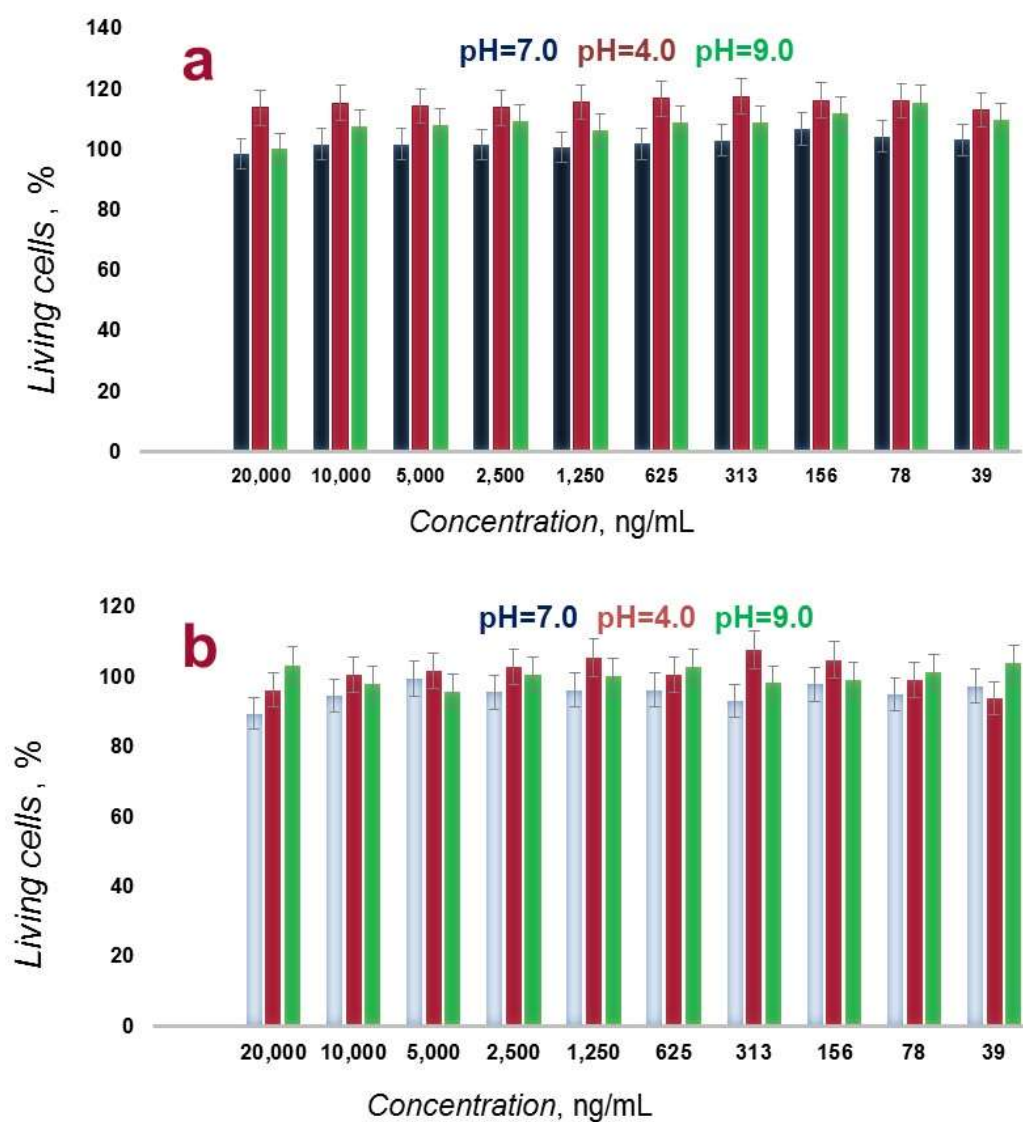
Figure 3.4-9. Histograms of MTT viability assay results of NIPAM-MA-BIS gel nanoparticles for (a) cervical cancer and (b) triple-negative breast cancer cell lines as a function of gel concentration. Different column colours refer to different pH values.
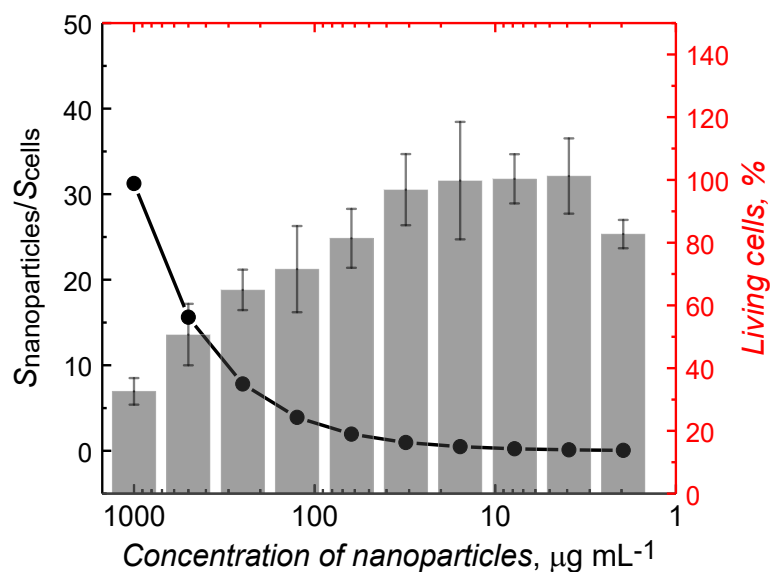
Figure 3.4-10. HeLa cells viability as a function of nanoparticles' concentration. The black curve shows the ratio of the surface area occupied by nanoparticles to the surface area available to cells ($S_{nanparticles}/S_{cells}$).
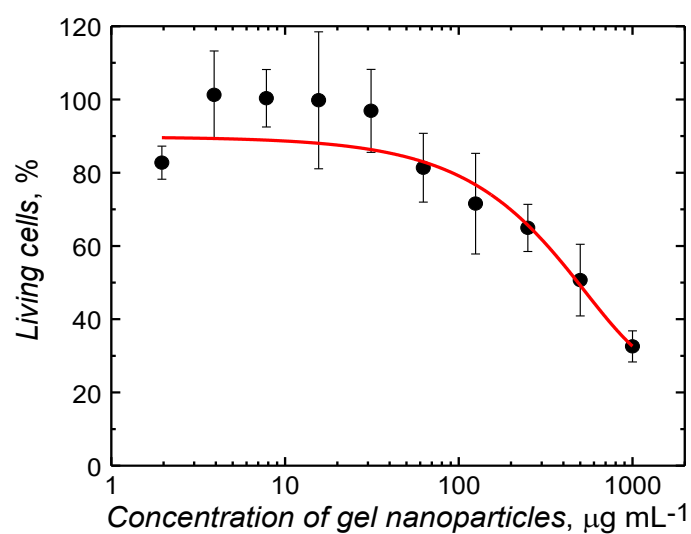
Figure 3.4-11. Viability of HeLa cells incubated for 24 h with NIPAM-MA-BIS gel nanoparticles as a function of gel nanoparticles' concentration, with the IC_{50} value of 485 µg mL^{-1}, based on the MTT assay.

3.4.6 Long-term three-dimensional (3D) cell culture

Two model cell lines, HeLa and MDA-MB-231, were seeded with NIPAM-MA-BIS, MNP-NIPAM-MA-BIS, and SiO$_2$-NIPAM-MA-BIS nanogels to check their usability for 3D cell cultures. The cultures were maintained for three weeks, with untreated cells seeded on the glass as the control. Half of the cell culture medium was replaced every second day (Figures 3.4-12, 3.4-13, and 3.4-14). For each gel, two variants were considered, i.e., gel particles dispersed in solutions of pH = 4.0 and 7.0, and both were maintained at a neutral medium during the long-term cell culture.

3D CM images of the cultures performed on the SiO$_2$-NIPAM-MA-BIS gel NPs are presented in Figure 3.4-14, while similar data concerning the MNP-NIPAM-MA-BIS and NIPAM-MA-BIS particles at two different pH values are demonstrated in Figures 3.4-12 and 3.4-13. Apparently, core-shell and gels NPs supported the formation of thick and viable tissues of HeLa and MDA-MB-231 cells. Moreover, MDA-MB-231 cells formed complex 3D structures, where clusters of viable cells were surrounded by necrotic tissue. Moreover, the cells number and viability were significantly higher in the core-shell gel NPs supported cultures than in the controls.

The 3D XYZ images were converted to 2D, XZ, or YZ projections using Imaris software (Figure 3.4-15a) to obtain quantitative information on the tissue formation progress. Next, viable tissues' thickness was determined from the 2D projections. These determinations' results are presented in Figures 3.4-15b and 3.4-15c.

The absolute thickness of the tissues revealed a difference in growth dynamics between HeLa and MDA-MB-231 cells (Figure 3.4-15b). During the first two weeks of culture, the control MDA-MB-231 cells without gel particles grew to form layers thicker than those formed by the HeLa cells. The MDA-MB-231 control cells massively degenerated and necrosed during the third week, while HeLa cells continued growing (Figure 3.4-14).
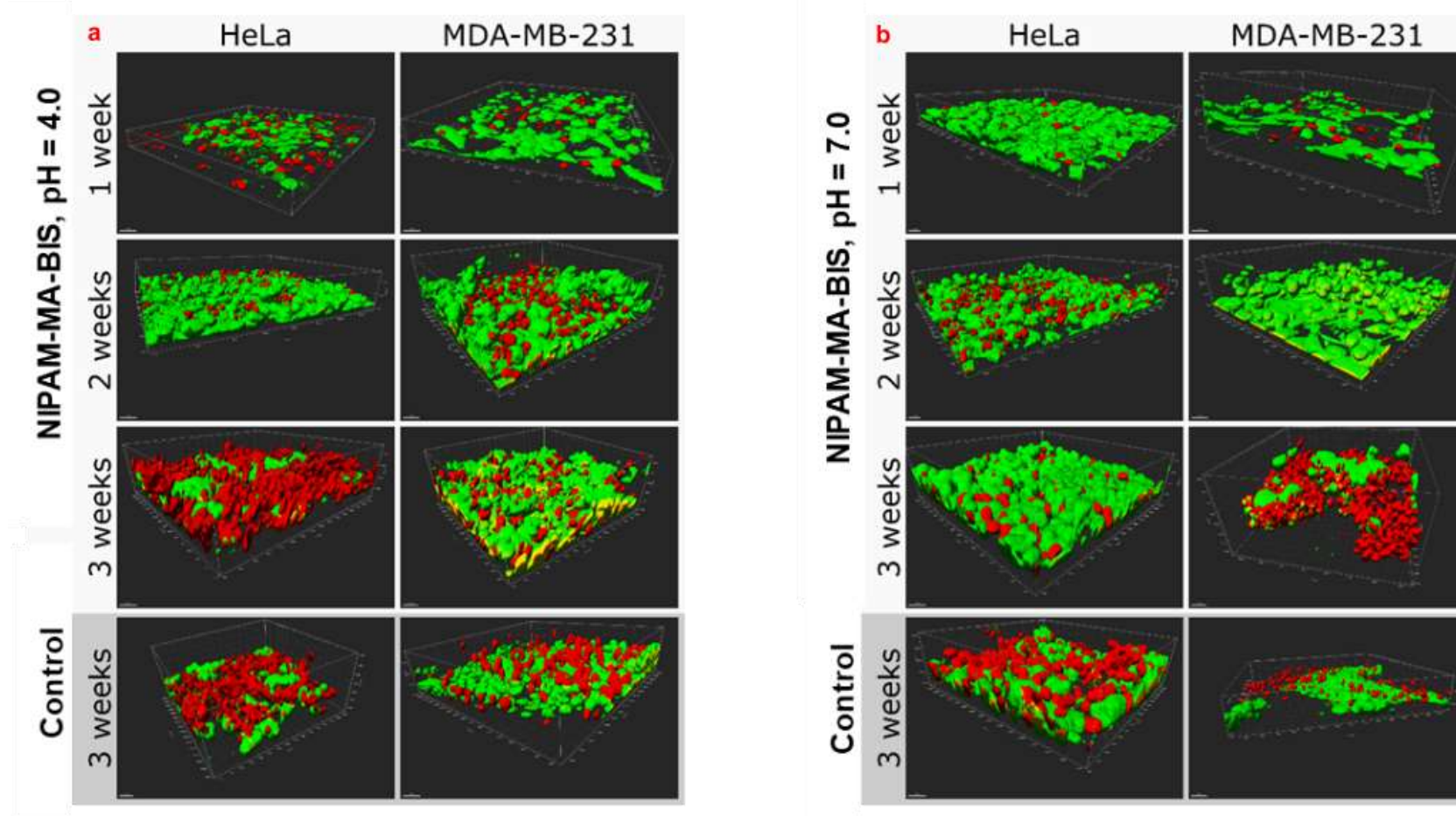
Figure 3.4-12. Confocal microscopy images of the long-term 3D tissue culture on the **NIPAM-MA-BIS** nanoparticles. Gel nanoparticles were dispersed in solutions of pH of (a) 4.0 and (b) 7.0. Green objects are viable cells stained with calcein-AM, and red objects are nuclei of dead cells stained with propidium iodide. Scale horizontal bars correspond to 30 μm.
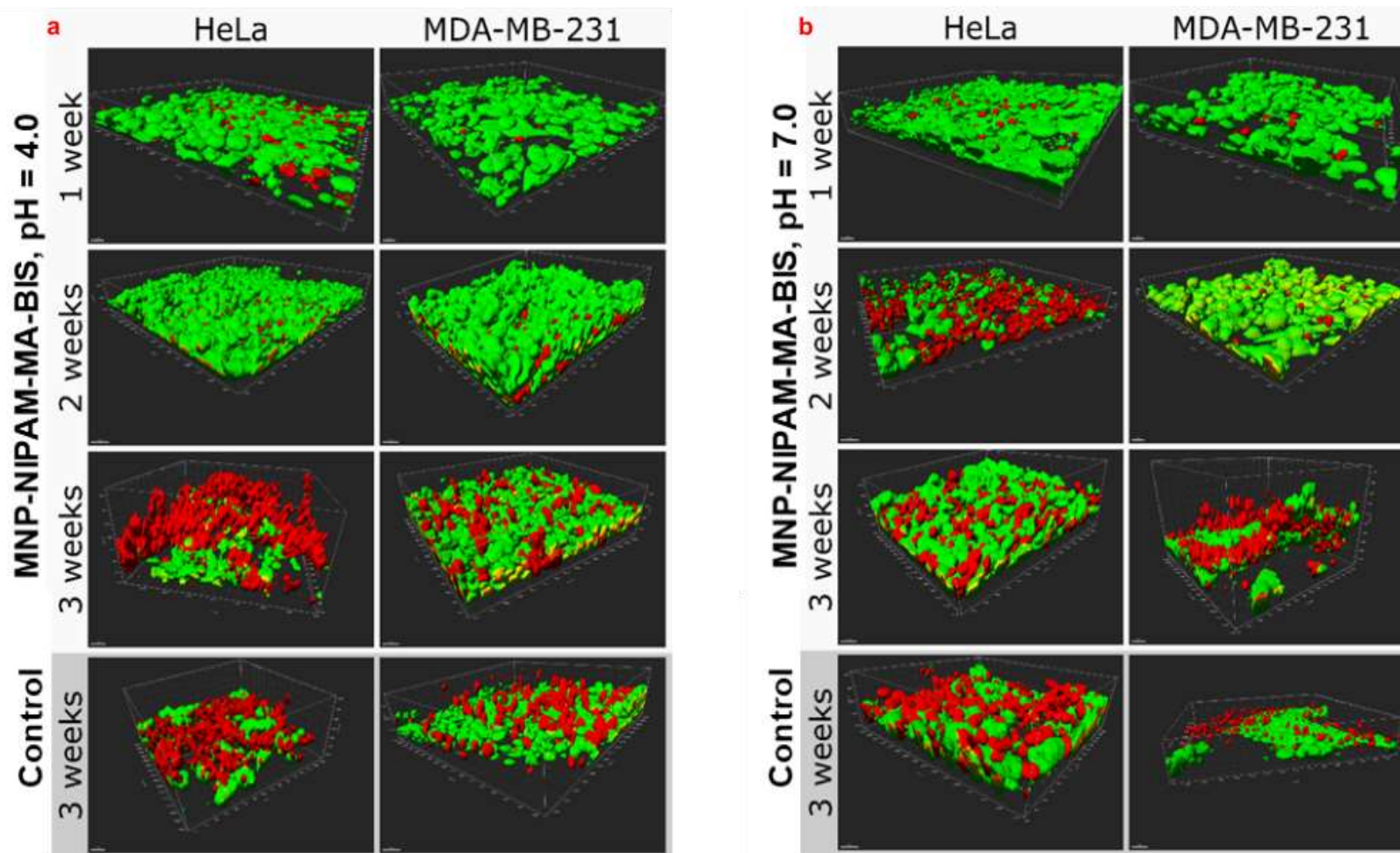
Figure 3.4-13. Confocal microscopy images of the long-term 3D tissue culture on MNP-NIPAM-MA-BIS core-shell nanoparticles. Gel nanoparticles were dispersed in solutions of pH of (a) 4.0 and (b) 7.0. Green objects are viable cells stained with calcein-AM, and red objects are nuclei of dead cells stained with propidium iodide. Scale horizontal bars correspond to 30 μm.
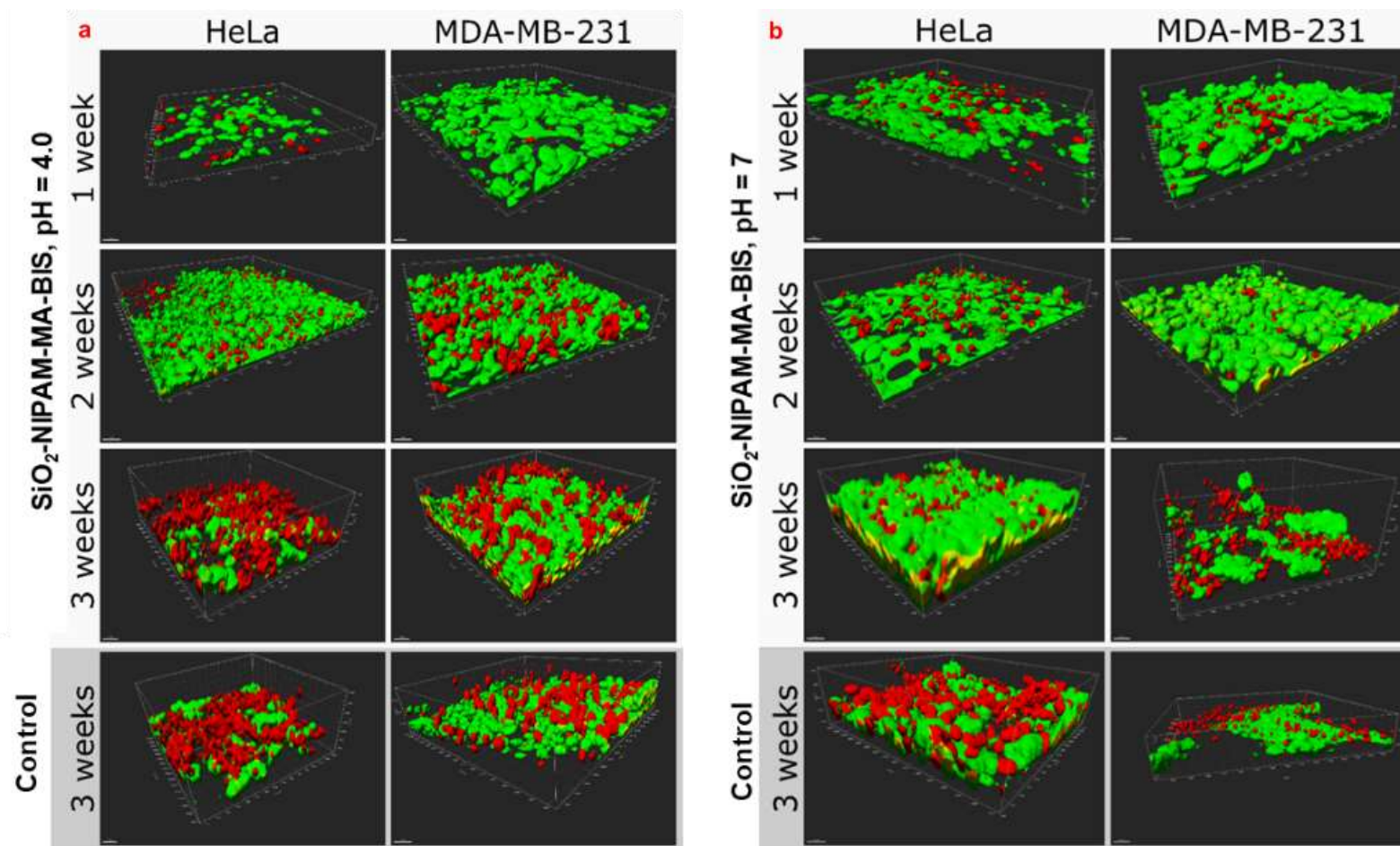
Figure 3.4-14. Confocal microscopy images of the long-term 3D tissue culture on SiO$_2$-NIPAM-MA-BIS core-shell nanoparticles. Gel particles were dispersed in solutions of pH of (a) 4.0 and (b) 7.0. Green objects are viable cells stained with calcein-AM, and red objects are nuclei of dead cells stained with propidium iodide. Scale horizontal bars correspond to 30 μm.

Comparing the glass-supported cultures with the gel-supported cultures leads to the following conclusion. At the initial stage of culture (the first week), there was no significant difference in culture morphology, suggesting no preference for the gel support over the glass support, and the cells formed monolayers. However, gel-supported cultures grew thicker during subsequent weeks, while control cultures gradually degenerated. Seemingly, overconfluent cells adhered to the gel support, spread, and formed extensive 3D structures. Moreover, the nanogels' porosity afforded sufficient oxygen and nutrient delivery, as viable cells were detected in the whole tissue (over 150 μm thick in the MNP-NIPAM-MA-BIS gel NPs). On the other hand, overconfluent cells in glass controls underwent anoikis (apoptosis in response to inappropriate cell-support interactions). Evidently, core-shell gels are a promising tool for studying more complex 3D cell cultures.

Besides, the gel-supported 3D cultures growth was proportional to the control in the case of HeLa cells. Gel-supported MDA-MB-231 cells developed much more complex and expended structures than the control. This development was particularly pronounced in the third culture week when the control degenerated (Figure 3.4-15c). Presumably, gel NPs' support extended the 3D structure growth in the case of insufficient adhesion to the glass 2D supports. Moreover, the SiO_2-NIPAM-MA-BIS and MNP-NIPAM-MA-BIS core-shell gel NPs provided support much more beneficial for complex 3D tissue structures (Figure 3.4-15c).
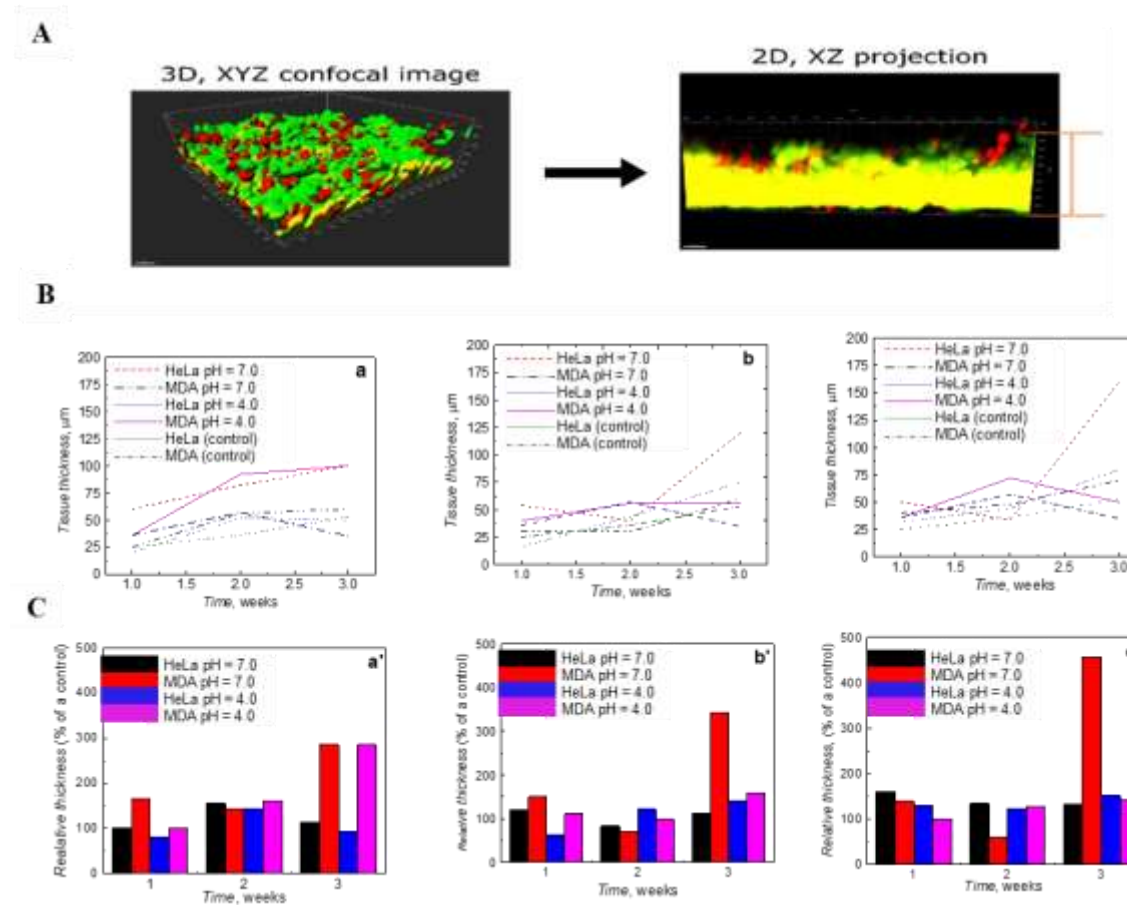
Figure 3.4-15. Quantitative analysis of tissue thickness growth during long-term cell culture in gels. (A) The measurement principle illustrated by 3D confocal microscopy images converted to their 2D projections with Imaris software. Then, the thickness of the viable (green) tissue was measured from the 2D image. (B) Measurements results, involving absolute thickness of the cell cultures over gel nanoparticles, comparison to the related controls of (a) NIPAM-MA-BIS, (b) SiO$_2$-NIPAM-MA-BIS, and (c) MNP-NIPAM-MA-BIS. (C) The relative 3D cultures thickness change with time, calculated as the fraction of the related controls of (a') NIPAM-MA-BIS, (b') SiO$_2$-NIPAM-MA-BIS, and (c') MNP-NIPAM-MA-BIS.

4. Conclusions and future outlook

Escherichia coli is a well-known pathogen responsible for various foodborne diseases and neurological disorders. An electrochemical MIP chemosensor for selective the *E. coli* E2152 strain determination was devised, engineered, and tested. To this end, an *E. coli* E2152 strain was successfully imprinted in a polymer using electrochemically initiated polymerization. 2-Aminophenyl boronic acid was used as the functional monomer and aniline as the cross-linking monomer. The SEM images showed that the bacteria template was fully entrapped in the resulting molecularly imprinted polymer matrix in a single step. The adopted three-step procedure of removing bacteria from the MIP matrix to vacate molecular cavities in the MIP appeared successful. SEM imaging confirmed efficient template extraction. The target *E. coli* E2152 strain was determined up to 2.9×10^4 cells mL^{-1} with an MIP film-coated electrode. The interference study indicated that the cell surface compositions mainly governed their binding behavior.

The results showed that the real-time method could be considered a highly effective alternative to commonly used *E. coli* E2152 strain determination methods involving analytical techniques, such as real-time PCR, flow cytometry, ELISA, MALDI TOF-MS, and HPLC. Although featuring several limitations, conventional biochemical identification tools are still essential for determining nonculturable microorganisms and accurately detecting microbial threats. However, they mostly fail for complex samples because of possible interference in the background, usually overcome through chromatography-based techniques. Therefore, it is necessary to choose practical and inexpensive methods for *E. coli* E2152 strain selective identification and determination in real-time. An inexpensive analytical method exploiting different cell surface properties can be an excellent substitute for conventional biochemical approaches for effortless and quick pathogen identification in real-time.

In the second part of the present research, an effective strategy to elaborate and devise a simple and cost-efficient electrochemical chemosensor for GABA determination in a clinical analysis context is reported. The electrochemical polymerization under potentiodynamic conditions was used to prepare a chemosensor for GABA using molecular imprinting. Detailed computational modeling helped select efficient synthetic receptors for MIP preparation. The procedure developed for a conventional Pt disk electrode was extended to result in disposable commercial IDEs suitable for POC applications. The studies using artificial serum samples confirmed the possibility of the chemosensor application for real samples analyses. CI and EIS

techniques appeared most suitable and convenient, revealing excellent imprinting and chemosensors' detectability, sensitivity, linearity, and selectivity.

MIP chemosensors demonstrate outstanding potential in today's research to determine biocompounds because of their high physicochemical stability and affordability. Moreover, biocompounds' determination is an equally important concern like pathogen identification for proper clinical diagnostics, food safety control, and environmental monitoring. Undoubtedly, the MIP artificial biological receptors show high selectivity and affinity to several biocompound ligands under both physiological and non-physiological conditions. A new MIP recognition artificial receptor for the GABA biomarker determination, devised in the present work, shows the importance of the MIP approach for potential effective indirect determination of non-electroactive biologically significant compounds in POC devices.

In the final part of the present research, a simple green synthesis procedure was developed to prepare more advanced eco-friendly gel structures for microbiological applications. Electrochemistry is successfully exploited to pursue an alternative way to prepare different polyacrylamide microgels and core-shell particles. Surfaces of different inorganic cores were grafted with the NIPAM-MA-BIS copolymer shells of the nanometre order thickness with various monomer combinations under hydrodynamic conditions. The gel NPs' morphology depended on the electroinitiation potential and the BIS cross-linking monomer concentration in the solution for polymerization. The BIS concentration dominantly influenced gel particles' morphology.

Moreover, this concentration defined gel solubility. Low gel density helped incur the softness that further facilitated the ion diffusion. Therefore, gel NPs could mimic the biological environment for tissue culture and exhibit biocompatibility. The NIPAM-MA-BIS gel NPs support extended 3D structure growth compared to the control. In all gel systems, SiO_2-NIPAM-MA-BIS and MNP-NIPAM-MA-BIS core-shell gel NPs provided support much more beneficial than the conventional glass support for complex 3D tissue structures. SEM and STEM imaging confirmed the syntheses of the gel microparticles and core-shell NPs of different morphologies and coatings. The DLS analyses indicated that the microgels were stable in neutral aqueous solutions. The FTIR and ^{13}C NMR spectra directly evidenced that MA was successfully copolymerized with the NIPAM and BIS monomers. Moreover, the TGA and DTGA analyses demonstrated that the microgels' thermal stability was comparable to the stability of the analogous microgels prepared according to literature procedures.

The devising and fabricating of supramolecular nanomaterials, prepared without any harmful additives, opens an attractive route for nanogels application in preparing nano-devices

and bioengineering. Due to the combined properties of nanotechnology and cross-linking gel-like materials, it can be effectively used in biomedical science. Here prepared under hydrodynamic conditions, nanogels can respond to environmental stimuli like pH change. Moreover, the nanogels are biocompatible in studies in vitro. Thus, they can be employed as nanocarriers for the targeted delivery of genes, drugs, and proteins. In addition, these nanogels can be prepared as 3D cell-like structures that can be further explored in tissue engineering. Most importantly, the proposed electrochemically initiated nanogel preparation under hydrodynamic conditions makes them potential candidates for preparing nanogel sensory elements of chemo- and biosensors in the near future. Finally, the core-shell gel NPs can efficiently be used in *microfluidics*-based *separation* devices to purify, e.g., proteins and nucleic acids, and identify and separate potential biomarkers.

5. **References**

6. 1. Mullen, K.; Rabe, J. P., Macromolecular and supramolecular architectures for molecular electronics. *Ann. N. Y. Acad. Sci.* **1998**, *852*, 205-218.

2. Schulz, D.; Patil, A. O., Functional Polymers: An Overview. *Int. Funct. Polym.* **1998**, *704*, 1-14.

3. Wegner, G., Shape persistent macromolecules as building units of complex supramolecular architectures. *Macromol. Symp.* **1996**, *106*, 415-419.

4. Lanzalaco, S.; Armelin, E., Poly(*N*-isopropylacrylamide) and Copolymers: A Review on Recent Progresses in Biomedical Applications. *Gels* **2017**, *3*, 36.

5. Wang, K.; Amin, K.; An, Z.; Cai, Z.; Chen, H.; Chen, H.; Dong, Y.; Feng, X.; Fu, W.; Gu, J.; Han, Y.; Hu, D.; Hu, R.; Huang, D.; Huang, F.; Huang, F.; Huang, Y.; Jin, J.; Jin, X.; Li, Q.; Li, T.; Li, Z.; Li, Z.; Liu, J.; Liu, J.; Liu, S.; Peng, H.; Qin, A.; Qing, X.; Shen, Y.; Shi, J.; Sun, X.; Tong, B.; Wang, B.; Wang, H.; Wang, L.; Wang, S.; Wei, Z.; Xie, T.; Xu, C.; Xu, H.; Xu, Z.-K.; Yang, B.; Yu, Y.; Zeng, X.; Zhan, X.; Zhang, G.; Zhang, J.; Zhang, M. Q.; Zhang, X.-Z.; Zhang, X.; Zhang, Y.; Zhang, Y.; Zhao, C.; Zhao, W.; Zhou, Y.; Zhou, Z.; Zhu, J.; Zhu, X.; Tang, B. Z., Advanced functional polymer materials. *Mater. Chem. Front.* **2020**, *4*, 1803-1915.

6. LaFreniere, J. M. J.; Roberge, E. J.; Halpern, J. M., Review—reorientation of polymers in an applied electric field for electrochemical sensors. *J. Electrochem. Soc.* **2020**, *167*, 037556.

7. Işık, D.; Quaas, E.; Klinger, D., Thermo- and oxidation-sensitive poly(meth)acrylates based on alkyl sulfoxides: dual-responsive homopolymers from one functional group. *Polym. Chem.* **2020**, *11*, 7662-7676.

8. Men, W.; Zhu, P.; Dong, S.; Liu, W.; Zhou, K.; Bai, Y.; Liu, X.; Gong, S.; Zhang, S., Layer-by-layer pH-sensitive nanoparticles for drug delivery and controlled release with improved therapeutic efficacy in vivo. *Drug Delivery* **2020**, *27*, 180-190.

9. Xiang, T.; Wang, L.-R.; Ma, L.; Han, Z.-Y.; Wang, R.; Cheng, C.; Xia, Y.; Qin, H.; Zhao, C.-S., From Commodity Polymers to Functional Polymers. *Sci. Rep.* **2014**, *4*, 4604.

10. Bhawani, S. A.; Nisar, M.; Tariq, A.; Alotaibi, K. M.; Asaruddin, M. R., Chapter Seven - Enzyme-responsive polymer composites and their applications. In *Smart Polymer Nanocomposites*, Bhawani, S. A.; Khan, A.; Jawaid, M., Eds. Woodhead Publishing: 2021; pp 169-182.

11. Xiang, Z.; Liu, M.; Song, J., Stimuli-responsive polymeric nanosystems for controlled drug delivery. *Appl. Sci.* **2021**, *11*, 9541.

12. Hu, J.; Liu, S., Engineering responsive polymer building blocks with host-guest molecular recognition for functional applications. *Acc. Chem. Res.* **2014**, *47*, 2084-2095.

13. Sharma, P. S.; Dabrowski, M.; D'Souza, F.; Kutner, W., Surface development of molecularly imprinted polymer films to enhance sensing signals. *TrAC-Trends Anal. Chem.* **2013**, *51*, 146-157.

14. Takeuchi, T.; Haginaka, J., Separation and sensing based on molecular recognition using molecularly imprinted polymers. *J. Chromatogr. B* **1999**, *728*, 1-20.

15. Abdollahi, E.; Khalafi-Nezhad, A.; Mohammadi, A.; Abdouss, M.; Salami-Kalajahi, M., Synthesis of new molecularly imprinted polymer via reversible addition fragmentation transfer polymerization as a drug delivery system. *Polymer* **2018**, *143*, 245-257.

16. Bagheri, N.; Khataee, A.; Habibi, B.; Hassanzadeh, J., Mimetic Ag nanoparticle/Zn-based MOF nanocomposite (AgNPs@ZnMOF) capped with molecularly imprinted polymer for the selective detection of patulin. *Talanta* **2018**, *179*, 710-718.

17. Jahanban-Esfahlan, A.; Roufegarinejad, L.; Jahanban-Esfahlan, R.; Tabibiazar, M.; Amarowicz, R., Latest developments in the detection and separation of bovine serum albumin using molecularly imprinted polymers. *Talanta* **2020,** *207*, 120317.

18. Moein, M. M., Advancements of chiral molecularly imprinted polymers in separation and sensor fields: A review of the last decade. *Talanta* **2021,** *224*, 121794.

19. Wilbraham, L.; Berardo, E.; Turcani, L.; Jelfs, K. E.; Zwijnenburg, M. A., High-throughput screening approach for the optoelectronic properties of conjugated polymers. *J. Chem. Inf. Model.* **2018,** *58*, 2450-2459.

20. Zhang, L.; Zhu, C.; Chen, C.; Zhu, S.; Zhou, J.; Wang, M.; Shang, P., Determination of kanamycin using a molecularly imprinted SPR sensor. *Food Chem.* **2018,** *266*, 170-174.

21. Owens, G. J.; Singh, R. K.; Foroutan, F.; Alqaysi, M.; Han, C.-M.; Mahapatra, C.; Kim, H.-W.; Knowles, J. C., Sol-gel based materials for biomedical applications. *Prog. Mater. Sci.* **2016,** *77*, 1-79.

22. Sun, M.; Lee, J.; Chen, Y.; Hoshino, K., Studies of nanoparticle delivery with in vitro bio-engineered microtissues. *Bioact. Mater.* **2020,** *5*, 924-937.

23. Abdullah, M. F.; Nuge, T.; Andriyana, A.; Ang, B. C.; Muhamad, F., Core-Shell Fibers: design, roles, and controllable release strategies in tissue engineering and drug delivery. *Polymers* **2019,** *11*, 2008.

24. Kim, S. M.; Patel, M.; Patel, R., PLGA core-shell nano/microparticle delivery system for Biomedical Application. *Polymers* **2021,** *13*, 3471.

25. Wang, C.; Dong, W.; Li, P.; Wang, Y.; Tu, H.; Tan, S.; Wu, Y.; Watanabe, M., Reversible ion-conducting switch by azobenzene molecule with light-controlled sol–gel transitions of the PNIPAm ion gel. *ACS Appl. Mater. Interfaces* **2020,** *12*, 42202-42209.

26. Yuba, E., Development of functional liposomes by modification of stimuli-responsive materials and their biomedical applications. *J. Mater. Chem. B* **2020,** *8* (6), 1093-1107.

27. Kwon, Y.; Choi, Y.; Jang, J.; Yoon, S.; Choi, J., NIR Laser-Responsive PNIPAM and gold nanorod composites for the engineering of thermally reactive drug delivery nanomedicine. *Pharmaceutics* **2020,** *12*, 204.

28. Doberenz, F.; Zeng, K.; Willems, C.; Zhang, K.; Groth, T., Thermoresponsive polymers and their biomedical application in tissue engineering – a review. *J. Mater. Chem. B* **2020,** *8* , 607-628.

29. Aisenbrey, E. A.; Murphy, W. L., Synthetic alternatives to matrigel. *Nat. Rev. Mater.* **2020,** *5*, 539-551.

30. Liu, Y.; Mao, S.; Zhu, L.; Chen, S.; Wu, C., Based on tannic acid and thermoresponsive microgels design a simple and high-efficiency multifunctional antibacterial coating. *Eur. Polym. J.* **2021,** *153*, 110498.

31. Ahmad, H. M. N.; Dutta, G.; Csoros, J.; Si, B.; Yang, R.; Halpern, J. M.; Seitz, W. R.; Song, E., Stimuli-responsive templated polymer as a target receptor for a conformation-based electrochemical sensing platform. *ACS Appl. Polym. Mater.* **2021,** *3*, 329-341.

32. Shu, T.; Hu, L.; Shen, Q.; Jiang, L.; Zhang, Q.; Serpe, M. J., Stimuli-responsive polymer-based systems for diagnostic applications. *J. Mater. Chem. B* **2020,** *8*, 7042-7061.

33. Giobbe, G. G.; Crowley, C.; Luni, C.; Campinoti, S.; Khedr, M.; Kretzschmar, K.; De Santis, M. M.; Zambaiti, E.; Michielin, F.; Meran, L.; Hu, Q.; van Son, G.; Urbani, L.; Manfredi, A.; Giomo, M.; Eaton, S.; Cacchiarelli, D.; Li, V. S. W.; Clevers, H.; Bonfanti, P.; Elvassore, N.; De Coppi, P., Extracellular matrix hydrogel derived from decellularized tissues enables endodermal organoid culture. *Nat. Commun.* **2019,** *10*, 5658.

34. Chen, W.; Tian, X.; He, W.; Li, J.; Feng, Y.; Pan, G., Emerging functional materials based on chemically designed molecular recognition. *BMC Mater.* **2020,** *2*, 1.

35. Abbasy, L.; Mohammadzadeh, A.; Hasanzadeh, M.; Razmi, N., Development of a reliable bioanalytical method based on prostate specific antigen trapping on the cavity of molecularly imprinted polymer towards sensing of PSA using binding affinity of PSA-MIP receptor: A novel biosensor. *J. Pharm. Biomed. Anal.* **2020,** *188*, 113447.

36. Piletska, E.; Kumire, J.; Sergeyeva, T.; Piletsky, S., Rational design and development of affinity adsorbents for analytical and biopharmaceutical applications. *J. Chin. Adv. Mater. Soc.* **2013,** *1* (3), 229-244.

37. Wulff, G., Molecular recognition in polymers prepared by imprinting with templates. In *Polymeric Reagents and Catalysts,* American Chemical Society: 1986; Vol. 308, pp 186-230.

38. Sellergren, B.; Ekberg, B.; Mosbach, K., Molecular imprinting of amino acid derivatives in macroporous polymers: Demonstration of substrate- and enantio-selectivity by chromatographic resolution of racemic mixtures of amino acid derivatives. *J. Chromatogr. A* **1985,** *347*, 1-10.

39. Gui, R.; Guo, H.; Jin, H., Preparation and applications of electrochemical chemosensors based on carbon-nanomaterial-modified molecularly imprinted polymers. *Nanoscale Adv.* **2019,** *1*, 3325-3363.

40. BelBruno, J. J., Molecularly Imprinted Polymers. *Chem. Rev.* **2019,** *119*, 94-119.

41. Sharma, P. S.; Iskierko, Z.; Pietrzyk-Le, A.; D'Souza, F.; Kutner, W., Bioinspired intelligent molecularly imprinted polymers for chemosensing: A mini review. *Electrochem. Commun.* **2015,** *50*, 81-87.

42. Liu, Z.; He, H., Synthesis and applications of boronate affinity materials: From class selectivity to biomimetic specificity. *Acc. Chem. Res.* **2017,** *50*, 2185-2193.

43. Herrera-Chacón, A.; Cetó, X.; del Valle, M., Molecularly imprinted polymers - towards electrochemical sensors and electronic tongues. *Anal. Bioanal. Chem.* **2021,** *413*, 6117-6140.

44. Fujii, Y.; Matsutani, K.; Kikuchi, K., Formation of a specific co-ordination cavity for a chiral amino acid by template synthesis of a polymer Schiff base cobalt(III) complex. *J. Chem. Soc., Chem. Commun.* **1985**, 415-417.

45. Mosbach, K., Molecular imprinting. *Trends Biochem. Sci.* **1994,** *19*, 9-14.

46. Haupt, K.; Mosbach, K., Molecularly imprinted polymers and their use in biomimetic sensors. *Chem. Rev.* **2000,** *100*, 2495-2504.

47. Sellergren, B.; Andersson, L., Molecular recognition in macroporous polymers prepared by a substrate analog imprinting strategy. *J. Org. Chem.* **1990,** *55*, 3381-3383.

48. Qi, P.; Wang, J.; Wang, L.; Li, Y.; Jin, J.; Su, F.; Tian, Y.; Chen, J., Molecularly imprinted polymers synthesized via semi-covalent imprinting with sacrificial spacer for imprinting phenols. *Polymer* **2010,** *51*, 5417-5423.

49. Lübke, M.; Whitcombe, M. J.; Vulfson, E. N., A novel approach to the molecular imprinting of polychlorinated aromatic compounds. *J. Am. Chem. Soc.* **1998,** *120*, 13342–13348.

50. Moreira Gonçalves, L., Electropolymerized molecularly imprinted polymers: perceptions based on recent literature for soon-to-be world-class scientists. *Curr. Opin. Electrochem.* **2021,** *25*, 100640.

51. Cheubong, C.; Takano, E.; Kitayama, Y.; Sunayama, H.; Minamoto, K.; Takeuchi, R.; Furutani, S.; Takeuchi, T., Molecularly imprinted polymer nanogel-based fluorescence

sensing of pork contamination in halal meat extracts. *Biosens. Bioelectron.* **2021,** *172*, 112775.

52. Cui, F.; Zhou, Z.; Zhou, H. S., Molecularly imprinted polymers and surface imprinted polymers based electrochemical biosensor for infectious diseases. *Sensors* **2020,** *20*, 996.

53. Gutiérrez-Climente, R.; Clavié, M.; Dumy, P.; Mehdi, A.; Subra, G., Sol–gel process: the inorganic approach in protein imprinting. *J. Mater. Chem. B* **2021,** *9*, 2155-2178.

54. Paruli, E., III; Soppera, O.; Haupt, K.; Gonzato, C., Photopolymerization and photostructuring of molecularly imprinted polymers. *ACS Appl. Polym. Mater*. **2021,** *3*, 4769-4790.

55. Balamurugan, S.; Spivak, D. A., Molecular imprinting in monolayer surfaces. *J. Mol. Recognit.* **2011,** *24*, 915-929.

56. Renkecz, T.; László, K.; Horváth, V., Molecularly imprinted microspheres prepared by precipitation polymerization at high monomer concentrations. *Mol. Imprinting* **2014,** *2*, 1-17.

57. Lu, H.; Tian, H.; Wang, C.; Xu, S., Designing and controlling the morphology of spherical molecularly imprinted polymers. *Mater. Adv.* **2020,** *1*, 2182-2201.

58. Saylan, Y.; Erdem, Ö.; Inci, F.; Denizli, A., Advances in biomimetic systems for molecular recognition and biosensing. *Biomimetics* **2020,** *5*, 20.

59. Song, Z.; Li, J.; Lu, W.; Li, B.; Yang, G.; Bi, Y.; Arabi, M.; Wang, X.; Ma, J.; Chen, L., Molecularly imprinted polymers based materials and their applications in chromatographic and electrophoretic separations. *TrAC-Trends Anal. Chem.* **2021**, 116504.

60. Guoning, C.; Hua, S.; Wang, L.; Qianqian, H.; Xia, C.; Hongge, Z.; Zhimin, L.; Chun, C.; Qiang, F., A surfactant-mediated sol-gel method for the preparation of molecularly imprinted polymers and its application in a biomimetic immunoassay for the detection of protein. *J Pharm Biomed Anal* **2020,** *190*, 113511.

61. Moein, M. M.; Abdel-Rehim, A.; Abdel-Rehim, M., Recent applications of molecularly imprinted sol-gel methodology in sample preparation. *Molecules* **2019,** *24*, 2889.

62. Allegretto, J. A.; Giussi, J. M.; Moya, S. E.; Azzaroni, O.; Rafti, M., Synthesis and characterization ofthermoresponsive ZIF-8@PNIPAm-co-MAAmicrogel composites with enhanced performanceas an adsorption/release platform. *RSC Adv.* **2020,** *10*, 2453-2461

63. Söylemez, M. A.; Güven, O.; Barsbay, M., Method for preparing a well-defined molecularly imprinted polymeric system via radiation-induced RAFT polymerization. *Eur. Polym. J.* **2018,** *103*, 21-30.

64. Barsbay, M.; Güven, O., Nanostructuring of polymers by controlling of ionizing radiation-induced free radical polymerization, copolymerization, grafting and crosslinking by RAFT mechanism. *Radiat. Phys. Chem.* **2020,** *169*, 107816.

65. Miura, Y., Controlled polymerization for the development of bioconjugate polymers and materials. *J. Mater. Chem. B* **2020,** *8*, 2010-2019.

66. Kidakova, A.; Boroznjak, R.; Reut, J.; Öpik, A.; Saarma, M.; Syritski, V., Molecularly imprinted polymer-based SAW sensor for label-free detection of cerebral dopamine neurotrophic factor protein. *Sens. Actuators B* **2020,** *308*, 127708.

67. Qu, Y.; Qin, L.; Liu, X.; Yang, Y., Reasonable design and sifting of microporous carbon nanosphere-based surface molecularly imprinted polymer for selective removal of phenol from wastewater. *Chemosphere* **2020,** *251*, 126376.

68. Sonawane, S. L.; Asha, S. K., Probing cavity versus surface preference of fluorescent template molecules in molecularly imprinted polystyrene microspheres. *J. Polym. Sci. A* **2017,** *55*, 1558-1565.

69. Wang, Y.; Zhou, J.; Zhang, B.; Tian, L.; Ali, Z.; Zhang, Q., Fabrication and characterization of glutathione-imprinted polymers on fibrous SiO2 microspheres with high specific surface. *Chem. Eng. J.* **2017,** *327*, 932-940.

70. Michaudel, Q.; Kottisch, V.; Fors, B. P., Cationic polymerization: From photoinitiation to photocontrol. *Angew. Chem., Int. Ed.* **2017,** *56*, 9670-9679.

71. Frick, E.; Schweigert, C.; Noble, B. B.; Ernst, H. A.; Lauer, A.; Liang, Y.; Voll, D.; Coote, M. L.; Unterreiner, A.-N.; Barner-Kowollik, C., Toward a Quantitative Description of Radical Photoinitiator Structure–Reactivity Correlations. *Macromolecules* **2016,** *49*, 80-89.

72. Poma, A.; Guerreiro, A.; Whitcombe, M. J.; Piletska, E. V.; Turner, A. P. F.; Piletsky, S. A., Solid-phase synthesis of molecularly imprinted polymer nanoparticles with a reusable template - "Plastic Antibodies." *Adv. Funct. Mater.* **2013,** *23*, 2821-2827.

73. Malitesta, C.; Mazzotta, E.; Picca, R. A.; Poma, A.; Chianella, I.; Piletsky, S. A., MIP sensors--the electrochemical approach. *Anal. Bioanal. Chem.* **2012,** *402*, 1827-46.

74. Sharma, P. S.; Pietrzyk-Le, A.; D'Souza, F.; Kutner, W., Electrochemically synthesized polymers in molecular imprinting for chemical sensing. *Anal. Bioanal. Chem.* **2012,** *402*, 3177-3204.

75. Alanazi, K.; Cruz, A. G.; Masi, S. D.; Voorhaar, A.; Ahmad, O. S.; Cowen, T.; Piletska, E.; Langfor, N.; Coats, T. J.; Sims, M. R.; A.Piletsky, S., Disposable paracetamol sensor based on electroactive molecularly imprinted polymer nanoparticles for plasma monitoring. *Sens. Actuators B* **2021,** *329*, 129128.

76. Sergeyeva, T. A.; Piletsky, S. A.; Brovko, A.; Slinchenko, E. A.; Sergeeva, L. M.; El'skaya, A. V., Selective recognition of atrazine by molecularly imprinted polymer membranes. Development of conductometric sensor for herbicides detection. *Anal. Chim. Acta* **1999,** *392*, 105-111.

77. Cieplak, M.; Kutner, W., Artificial biosensors: How can molecular imprinting mimic biorecognition? *Trends Biotechnol.* **2016,** *34*, 922-941.

78. Gao, M.; Gao, Y.; Chen, G.; Huang, X.; Xu, X.; Lv, J.; Wang, J.; Xu, D.; Liu, G., Recent advances and future trends in the detection of contaminants by molecularly imprinted polymers in food samples. *Front. Chem.* **2020,** *8*, 1142.

79. Ribeiro, J. A.; Fernandes, P. M. V.; Pereira, C. M.; Silva, F., Electrochemical sensors and biosensors for determination of catecholamine neurotransmitters: A review. *Talanta* **2016,** *160*, 653-679.

80. Lopez, J. G.; Piletska, E. V.; Whitcombe, M. J.; Czulak, J.; Piletsky, S. A., Application of molecularly imprinted polymer nanoparticles for degradation of the bacterial autoinducer *N*-hexanoyl homoserine lactone. *Chem. Commun.* **2019,** *55*, 2664-2667.

81. Herrera-Chacón, A.; Dinç-Zor, Ş.; del Valle, M., Integrating molecularly imprinted polymer beads in graphite-epoxy electrodes for the voltammetric biosensing of histamine in wines. *Talanta* **2020,** *208*, 120348.

82. Herrera-Chacon, A.; González-Calabuig, A.; Campos, I.; del Valle, M., Bioelectronic tongue using MIP sensors for the resolution of volatile phenolic compounds. *Sens. Actuators B* **2018,** *258*, 665-671.

83. Roushani, M.; Saedi, Z.; Hamdi, F.; Dizajdizi, B. Z., Preparation an electrochemical sensor for detection of manganese (II) ions using glassy carbon electrode modified with multi-walled carbon nanotube-chitosan-ionic liquid nanocomposite decorated with ion imprinted polymer. *J. Electroanal. Chem.* **2017,** *804*, 1-6.

84. Vidal, J.-C.; Garcia-Ruiz, E.; Castillo, J.-R., Recent advances in electropolymerized conducting polymers in amperometric biosensors. *Microchim. Acta* **2003,** *143*, 93-111.

85. Riskin, M.; Tel-Vered, R.; Bourenko, T.; Granot, E.; Willner, I., Imprinting of molecular recognition sites through electropolymerization of functionalized Au nanoparticles: development of an electrochemical TNT sensor based on π-donor-acceptor interactions. *J. Am. Chem. Soc.* **2008,** *130*, 9726-9733.

86. Zembrzuska, D.; Kalecki, J.; Cieplak, M.; Lisowski, W.; Borowicz, P.; Noworyta, K.; Sharma, P. S., Electrochemically initiated co-polymerization of monomers of different oxidation potentials for molecular imprinting of electroactive analyte. *Sens. Actuators B* **2019,** *298*, 126884.

87. Maria, C. G. A.; K B, A.; Rison, S.; Varghese, A.; George, L., Molecularly imprinted PEDOT on carbon fiber paper electrode for the electrochemical determination of 2,4-dichlorophenol. *Synth. Met.* **2020,** *261*, 116309.

88. Ozcelikay, G.; Kurbanoglu, S.; Zhang, X.; Kosak Soz, C.; Wollenberger, U.; Ozkan, S. A.; Yarman, A.; Scheller, F. W., Electrochemical MIP sensor for butyrylcholinesterase. *Polymers* **2019,** *11*, 1970.

89. Ng, K. L.; Khor, S. M., Graphite-based nanocomposite electrochemical sensor for multiplex detection of adenine, guanine, thymine, and cytosine: A biomedical prospect for studying DNA damage. *Anal. Chem.* **2017,** *89*, 10004-10012.

90. Hulanicki, A.; Glab, S.; Ingman, F., Chemical sensors: definitions and classification. *Pure Appl. Chem.* **1991,** *63*, 1247 - 1250.

91. Cowen, T.; Karim, K.; Piletsky, S., Computational approaches in the design of synthetic receptors – A review. *Anal. Chim. Acta* **2016,** *936*, 62-74.

92. Huynh, T.-P.; Sharma, P. S.; Sosnowska, M.; D'Souza, F.; Kutner, W., Functionalized polythiophenes: Recognition materials for chemosensors and biosensors of superior sensitivity, selectivity, and detectability. *Prog. Polym. Sci.* **2015,** *47*, 1-25.

93. Karim, K.; Cowen, T.; Guerreiro, A.; Piletska, E.; Whitcombe, M. J.; Piletsky, S. A., A protocol for the computational design of high affinity molecularly imprinted polymer synthetic receptors. *J. Biotechnol. Biomater.* **2017** 3, 001–007

94. Mayeux, R., Biomarkers: potential uses and limitations. *NeuroRx* **2004,** *1*, 182-8.

95. Lu, L., Recent advances in synthesis of three-dimensional porous graphene and its applications in construction of electrochemical (bio)sensors for small biomolecules detection. *Biosens. Bioelectron.* **2018,** *110*, 180-192.

96. Alimohammadi, Z.; Pourmoslemi, S., Selective extraction of zolpidem from plasma using molecularly imprinted polymer followed by high performance liquid chromatography. *Microchem. J* . **2021,** *162*, 105844.

97. Chmangui, A.; Driss, M. R.; Touil, S.; Bermejo-Barrera, P.; Bouabdallah, S.; Moreda-Piñeiro, A., Aflatoxins screening in non-dairy beverages by Mn-doped ZnS quantum dots – Molecularly imprinted polymer fluorescent probe. *Talanta* **2019,** *199*, 65-71.

98. Guć, M.; Schroeder, G., Molecularly imprinted polymers and magnetic molecularly imprinted polymers for selective determination of estrogens in water by ESI-MS/FAPA-MS. *Biomolecules* **2020,** *10*, 672.

99. Wang, S.; Jiang, M.; Ju, Z.; Qiao, X.; Xu, Z., A flow-injection chemiluminescent biomimetic immunoassay method using a molecularly imprinted polymer as a biomimetic antibody for the determination of trichlorfon. *Food Agric. Immunol.* **2018,** *29*, 159-170.

100. Seguro, I.; Pacheco, J. G.; Delerue-Matos, C., Low Cost, Easy to prepare and disposable electrochemical molecularly imprinted sensor for diclofenac detection. *Sensors* **2021,** *21*, 1975.

101. Leibl, N.; Haupt, K.; Gonzato, C.; Duma, L., Molecularly imprinted polymers for chemical sensing: A tutorial review. *Chemosensors* **2021,** *9*, 123.

102. Roushani, M.; Zalpour, N., Selective detection of Asulam with in-situ dopamine electropolymerization based electrochemical MIP sensor. *React. Funct. Polym.* **2021,** *169*, 105069.

103. Elugoke, S. E.; Adekunle, A. S.; Fayemi, O. E.; Akpan, E. D.; Mamba, B. B.; Sherif, E.-S. M.; Ebenso, E. E., Molecularly imprinted polymers (MIPs) based electrochemical sensors for the determination of catecholamine neurotransmitters – Review. *Electrochem. Sci. Adv.* **2021,** *1*, e2000026.

104. Ou, Y.; Buchanan, A. M.; Witt, C. E.; Hashemi, P., Frontiers in electrochemical sensors for neurotransmitter detection: towards measuring neurotransmitters as chemical diagnostics for brain disorders. *Anal. Methods* **2019,** *11*, 2738–2755.

105. Bhat, R.; Axtell, R.; Mitra, A.; Miranda, M.; Lock, C.; Tsien, R. W.; Steinman, L., Inhibitory role for GABA in autoimmune inflammation. *Proc. Natl. Acad. Sci. USA* **2010,** *107*, 2580-2585.

106. Prévot, T.; Sibille, E., Altered GABA-mediated information processing and cognitive dysfunctions in depression and other brain disorders. *Mol. Psychiatry* **2021,** *26*, 151–167.

107. Horder, J.; Petrinovic, M. M.; Mendez, M. A.; Bruns, A.; Takumi, T.; Spooren, W.; Barker, G. J.; Künnecke, B.; Murphy, D. G., Glutamate and GABA in autism spectrum disorder - a translational magnetic resonance spectroscopy study in man and rodent models. *Transl. Psychiatry* **2018,** *8:106*, 106.

108. Hossain, I.; Tan, C.; Doughty, P. T.; Dutta, G.; Murray, T. A.; Siddiqui, S.; Iasemidis, L.; Arumugam, P. U., A novel microbiosensor microarray for continuous ex-vivo monitoring of gamma-aminobutyric acid in real-time. *Front. Neurosci.* **2018,** *12*, 500.

109. Doughty, P. T.; Hossain, I.; Gong, C.; Ponder, K. A.; Pati, S.; Arumugam, P. U.; Murray, T. A., Novel microwire-based biosensor probe for simultaneous real-time measurement of glutamate and GABA dynamics in vitro and in vivo. *Sci. Rep.* **2020,** *10*, 12777

110. Moldovan, N.; Blaga, I.-I.; Billa, S.; Hossain, I.; Gong, C.; Jones, C. E.; A.Murray, T.; Divan, R.; Siddiqui, S.; Arumugam, P. U., Brain-implantable multifunctional probe for simultaneous detection of glutamate and GABA neurotransmitters. *Sens. Actuators B* **2021,** *337*, 129795.

111. Silva, D. M. F.; Ferraz, V. P. F.; Ribeiro, Â. M., Improved high-performance liquid chromatographic method for GABA and glutamate determination in regions of the rodent brain. *J. Neurosci. Meth.* **2009,** *177*, 289-293.

112. Dawson, L. A.; Organa, A. J.; Winter, P.; Lacroix, L. P.; Shilliam, C. S.; Heidbreder, C.; Shaha, A. J., Rapid high-throughput assay for the measurement of amino acids from microdialysates and brain tissue using monolithic C18-bonded reversed-phase columns. *J. Chromatogr. B* **2004,** *807*, 235-241.

113. Le, P. H.; Verscheure, L.; Le, T. T.; Verheust, Y.; Raes, K., Implementation of HPLC analysis for γ-aminobutyric acid (GABA) in fermented food matrices. *Food Anal. Meth.* **2020,** *13*, 1190-1201

114. Lach, P.; Cieplak, M.; Noworyta, K. R.; Pieta, P.; Lisowski, W.; Kalecki, J.; Chitta, R.; D'Souza, F.; Kutner, W.; Sharma, P. S., Self-reporting molecularly imprinted polymer with the covalently immobilized ferrocene redox probe for selective electrochemical sensing of p-synephrine. *Sens. Actuators B* **2021,** *344*, 130276.

115. Sharma, P. S.; Garcia-Cruz, A.; Cieplak, M.; Noworyta, K. R.; Kutner, W., Gate effect' in molecularly imprinted polymers: the current state of understanding. *Curr. Opin. Electrochem.* **2019,** *16*, 50-56.

116. Pinalli, R.; Pedrini, A.; Dalcanale, E., Biochemical sensing with macrocyclic receptors. *Chem. Soc. Rev.* **2018,** *47*, 7006-7026.

117. Belbruno, J. J., Molecularly imprinted polymers. *Chem. Rev.* **2018,** *119*, 94–119.

118. Wang, T.; Muthuswamy, J., Immunosensor for detection of inhibitory neurotransmitter γ-aminobutyric acid using quartz crystal microbalance. *Anal. Chem.* **2008,** *80*, 8576-8582.

119. Jinnarak, A.; Teerasong, S., A novel colorimetric method for detection of gamma-aminobutyric acid based on silver nanoparticles. *Sens. Actuators B* **2016,** *229*, 315-320.

120. Huang, Y.; Ding, M.; Guo, T.; Zhang, N.; Tian, Z.; Sun, L.-P.; Guan, B.-O., Ultrasensitive and label-free detection of γ-aminobutyric acid using fiber-optic interferometric sensors functionalized with size-selective molecular sieve arrays. *Sens. Actuators B* **2017,** *244*, 934-940.

121. Hussain, M. M.; Asiri, A. M.; Uddin, J.; Rahman, M. M., An enzyme-free simultaneous detection of γ-aminobutyric acid and testosterone based on copper oxide nanoparticles. *RSC Adv.* **2021,** *11*, 20794-20805.

122. Lee, J.-H.; Chae, E.-J.; Park, S.-j.; Choi, J.-W., Label-free detection of γ-aminobutyric acid based on silicon nanowire biosensor. *Nano Convergence.* **2019,** *6*, 13.

123. Iwai, N. T.; Kramaric, M.; Crabbe, D.; Wei, Y.; Chen, R.; Shen, M., GABA detection with nano-ITIES pipet electrode: A new mechanism, water/DCE–octanoic acid interface. *Anal. Chem.* **2018,** *90*, 3067-3072.

124. Alamry, K. A.; Hussein, M. A.; Choi, J.-w.; El-Said, W. A., Non-enzymatic electrochemical sensor to detect γ-aminobutyric acid with ligand-based on graphene oxide modified gold electrode. *J. Electroanal. Chem.* **2020,** *879*, 114789.

125. Lim, J.-W.; Kang, I.-J., Fabrication of Chitosan-Gold Nanoshells for γ-aminobutyric acid detection as a surface-enhanced Raman scattering substrate. *Bull. Korean Chem. Soc.* **2015,** *36*, 672-677.

126. Hossain, I.; Tan, C.; Doughty, P. T.; Dutta, G.; Murray, T. A.; Siddiqui, S.; Iasemidis, L.; Arumugam, P. U., A novel microbiosensor microarray for continuous ex vivo monitoring of gamma-aminobutyric acid in real-time. *Front. Neurosci.* **2018,** *12*.

127. Monfared, A. M. T.; Tiwari, V. S.; Trudeau, V. L.; Anis, H., Surface-enhanced Raman scattering spectroscopy for the detection of glutamate and gamma-aminobutyric acid in serum by partial least squares analysis. *IEEE Photonics J.* **2015,** *7*, 1-16.

128. Sangubotla, R.; Kim, J., A facile enzymatic approach for selective detection of γ-aminobutyric acid using corn-derived fluorescent carbon dots. *Appl. Surf. Sci.* **2019,** *490*, 61-69.

129. Zhao, F.; Yoo, J.; Kim, J., Fabrication of the optical fiber GABA sensor based on the NADP+-functionalized quantum dots. *J. Nanosci. Nanotechnol.* **2016,** *16*, 1429-1432.

130. El-Said, W. A.; Alshitari, W.; Choi, J.-w., Controlled fabrication of gold nanobipyramids/polypyrrole for shell-isolated nanoparticle-enhanced Raman spectroscopy to detect γ-aminobutyric acid. *Spectrochim. Acta A* **2020,** *229*, 117890.

131. Sekioka, N.; Kato, D.; Kurita, R.; Hirono, S.; Niwa, O., Improved detection limit for an electrochemical γ-aminobutyric acid sensor based on stable NADPH detection using an electron cyclotron resonance sputtered carbon film electrode. *Sens. Actuators B* **2008,** *129*, 442-449.

132. Prasad, B. B.; Prasad, A.; Tiwari, M. P., Highly selective and sensitive analysis of γ-aminobutyric acid using a new molecularly imprinted polymer modified at the surface of abrasively immobilized multi-walled carbon nanotubes on pencil graphite electrode. *Electrochim. Acta* **2013,** *102*, 400-408.

133. Zheng, X.; Lin, R.; Zhou, X.; Zhang, L.; Lin, W., Electrochemical sensor of 4-aminobutyric acid based on molecularly imprinted electropolymer. *Anal. Methods* **2012,** *4*, 482-487.

134. Pingarrón, J. M.; Yáñez-Sedeño, P.; Campuzano, S., New tools of Electrochemistry at the service of (bio)sensing: From rational designs to electrocatalytic mechanisms. *J. Electroanal. Chem.* **2021,** *896*, 115097.

135. Bauer, M.; Wunderlich, L.; Weinzierl, F.; Lei, Y.; Duerkop, A.; Alshareef, H. N.; Baeumner, A. J., Electrochemical multi-analyte point-of-care perspiration sensors using on-chip three-dimensional graphene electrodes. *Anal. Bioanal. Chem.* **2021,** *413*, 763-777.

136. Hong, C.-C.; Chen, C.-P.; Horng, J.-C.; Szu-YigChen, Point-of-care protein sensing platform based on immuno-like membrane with molecularly-aligned nanocavities. *Biosens. Bioelectron.* **2013,** *50*, 425-430.

137. Maxwell, E. J.; Mazzeo, A. D.; Whitesides, G. M., Paper-based electroanalytical devices for accessible diagnostic testing. *MRS Bull.* **2013,** *38*, 309-314.

138. Li, D.; Batchelor-McAuley, C.; Chen, L.; Compton, R. G., Band electrodes in sensing applications: Response characteristics and band fabrication methods. *ACS Sens.* **2019**, *4*, 2250-2266.

139. Rana, S.; Page, R. H.; McNeil, C. J., Impedance spectra analysis to characterize interdigitated electrodes as electrochemical sensors. *Electrochim. Acta* **2011,** *56*, 8559–8563.

140. Lisdat, F.; Schäfe, D., The use of electrochemical impedance spectroscopy for biosensing. *Anal. Bioanal. Chem.* **2008,** *391*, 1555-1567.

141. Cui, B.; Liu, P.; Liu, X.; Liu, S.; Zhang, Z., Molecularly imprinted polymers for electrochemical detection and analysis: progress and perspectives. *J. Mater. Res. Technol.* **2020,** *9*, 12568-12584.

142. Ankeny, J. S.; Court, C. M.; Hou, S.; Li, Q.; Song, M.; Wu, D.; Chen, J. F.; Lee, T.; Lin, M.; Sho, S.; Rochefort, M. M.; Girgis, M. D.; Yao, J.; Wainberg, Z. A.; Muthusamy, V. R.; Watson, R. R.; Donahue, T. R.; Hines, O. J.; Reber, H. A.; Graeber, T. G.; Tseng, H. R.; Tomlinson, J. S., Circulating tumour cells as a biomarker for diagnosis and staging in pancreatic cancer. *Br. J. Cancer* **2016,** *114*, 1367-1375.

143. Boschetti, E.; D'Amato, A.; Candiano, G.; Righetti, P. G., Protein biomarkers for early detection of diseases: The decisive contribution of combinatorial peptide ligand libraries. *J. Proteomics* **2018,** *188*, 1-14.

144. Leinwand, J. C.; Miller, G., Microbes as biomarkers and targets in pancreatic cancer. *Nat. Rev. Clin. Oncol.* **2019,** *16*, 665-666.

145. Wang, X.; Li, X.; Liu, S.; Ren, H.; Yang, M.; Ke, Y.; Huang, L.; Liu, C.; Liu, B.; Chen, Z., Ultrasensitive detection of bacteria by targeting abundant transcripts. *Sci. Rep.* **2016,** *6*, 20393.

146. Galikowska, E.; Kunikowska, D.; Tokarska-Pietrzak, E.; Dziadziuszko, H.; Łoś, J. M.; Golec, P.; Węgrzyn, G.; Łoś, M., Specific detection of Salmonella enterica and *Escherichia coli* strains by using ELISA with bacteriophages as recognition agents. *Eur. J. Clin. Microbiol. Infect. Dis.* **2011,** *30*, 1067-1073.

147. Le, T. N.; Tran, T. D.; Kim, M. I., A convenient colorimetric bacteria detection method utilizing chitosan-coated magnetic nanoparticles. *Nanomaterials* **2020,** *10*, 92.

148. Ahmed, A.; Rushworth, J. V.; Hirst, N. A.; Millner, P. A., Biosensors for whole-cell bacterial detection. *Clin. Microbiol. Rev.* **2014,** *27* 631-646.

149. Piletsky, S.; Canfarotta, F.; Poma, A.; Bossi, A. M.; Piletsky, S., Molecularly imprinted polymers for cell recognition. *Trends Biotechnol.* **2020,** *38*, 368-387.

150. Pan, J.; Chen, W.; Ma, Y.; Pan, G., Molecularly imprinted polymers as receptor mimics for selective cell recognition. *Chem. Soc. Rev.* **2018,** *47*, 5574-5587.

151. Bowler, P. G.; Duerden, B. I.; Armstrong, D. G., Wound microbiology and associated approaches to wound management. *Clin. Microbiol. Rev.* **2001,** *14*, 244-269.

152. Huang, H.-K.; Cheng, H.-W.; Liao, C.-C.; Lin, S.-J.; Chen, Y.-Z.; Wang, J.-K.; Wang, Y.-L.; Huang, N.-T., Bacteria encapsulation and rapid antibiotic susceptibility test using a microfluidic microwell device integrating surface-enhanced Raman scattering. *Lab. Chip* **2020,** *20*, 2520-2528

153. Lenti, M. V.; Mengoli, C.; Vernero, M.; Aronico, N.; Conti, L.; de Andreis, F. B.; Cococcia, S.; Di Sabat, A., Preventing infections by encapsulated bacteria through vaccine prophylaxis in inflammatory bowel disease *Front. Immunol.* **2020,** *11*, 485.

154. Ramanavicius, S.; Ramanavicius, A., Conducting polymers in the design of biosensors and biofuel cells. *Polymers* **2021,** *13*, 49.

155. She, Z.; Topping, K.; Shamsi, M. H.; Wang, N.; Chan, N. W. C.; Kraatz, H.-B., Investigation of the utility of complementary electrochemical detection techniques to examine the in vitro affinity of bacterial flagellins for a toll-like receptor 5 biosensor. *Anal. Chem.* **2015,** *87*, 4218-4224.

156. Cui, F.; Zhou, Z.; Zhou, H. S., Molecularly imprinted polymers and surface imprinted polymers based electrochemical biosensor for infectious diseases. *Sensors* **2020,** *20*, 996.

157. Ahari, H.; Hedayati, M.; Akbari-adergani, B.; Kakoolaki, S.; Hosseini, H.; Anvar, A., Staphylococcus aureus exotoxin detection using potentiometric nanobiosensor for microbial electrode approach with the effects of pH and temperature. *Int. J. Food Prop.* **2017,** *20*, S1578-S1587.

158. Amiri, M.; Bezaatpour, A.; Jafari, H.; Boukherroub, R.; Szunerits, S., Electrochemical methodologies for the detection of pathogens. *ACS Sens.* **2018,** *3*, 1069-1086.

159. Saylan, Y.; Erdem, Ö.; Cihangir, N.; Denizli, A., Detecting Fingerprints of waterborne bacteria on a sensor. *Chemosensors* **2019,** *7*, 33.

160. Shen, X.; Svensson Bonde, J.; Kamra, T.; Bülow, L.; Leo, J. C.; Linke, D.; Ye, L., Bacterial imprinting at pickering emulsion interfaces. *Angew. Chem., Int. Ed.* **2014,** *53*, 10687-10690.

161. Rogovina, L. Z.; Slonimskii, G. L., Formation, structure, and properties of polymer gels. *Russ. Chem. Rev.* **1974,** *43*, 503-523.

162. Tanaka, T., Collapse of gels and the critical endpoint. *Phys. Rev. Lett.* **1978,** *40*, 820-823.

163. Spychalska, K.; Zając, D.; Baluta, S.; Halicka, K.; Cabaj, J., Functional polymers structures for (bio)sensing application—A Review. *Polymers* **2020,** *12*, 1154.

164. Di Chenna, P. H., Gels as Templates for the Syntheses of shape-controlled nanostructured materials. *Gels* **2018,** *4*, 10.

165. Zhang, K.; Lackey, M. A.; Cui, J.; Tew, G. N., Gels based on cyclic polymers. *J. Am. Chem. Soc.* **2011,** *133*, 4140-4148.

166. Moeinzadeh, S.; Khorasani, S. N.; Ma, J.; He, X.; Jabbari, E., Synthesis and Gelation characteristics of photo-crosslinkable star poly(ethylene oxide-co-lactide-glycolide acrylate) macromonomers. *Polymer* **2011,** *52*, 3887-3896.

167. Salehi, P.; Makhoul, G.; Roy, R.; Malhotra, M.; Mood, Z. A.; Daniel, S. J., Curcumin loaded NIPAAM/VP/PEG-A nanoparticles: physicochemical and chemopreventive properties. *J. Biomater. Sci. Polym. Ed.* **2013,** *24*, 574-88.

168. Wei, J.; Yu, Y., Photodeformable polymer gels and crosslinked liquid-crystalline polymers. *Soft Matter* **2012,** *8*, 8050-8059.

169. Graessley, W. W. In *Entangled linear, branched and network polymer systems — Molecular theories*, synthesis and degradation rheology and extrusion, berlin, Heidelberg, 1982//; Springer Berlin Heidelberg: Berlin, Heidelberg, 1982; pp 67-117.

170. Peppas, N. A.; Huang, Y., Polymers and gels as molecular recognition agents. *Pharm. Res.* **2002,** *19*, 578-587.

171. Zhou, X.; Liu, B.; Yu, X.; Zha, X.; Zhang, X.; Chen, Y.; Wang, X.; Jin, Y.; Wu, Y.; Chen, Y.; Shan, Y.; Chen, Y.; Liu, J.; Kong, W.; Shen, J., Controlled release of PEI/DNA complexes from mannose-bearing chitosan microspheres as a potent delivery system to enhance immune response to HBV DNA vaccine. *J. Controlled Release* **2007,** *121*, 200-207.

172. Hasirci, V.; Yilgor Huri, P.; Endoğan, T.; Eke, G.; Hasirci, N., Polymer fundamentals: Polymer Synthesis. 2017.

173. Paquet, C.; Paton, A.; Kumacheva, E., Chapter 7 - Materials with structural hierarchy and their optical applications. In *Frontiers of nanoscience*, Wilde, G., Ed. Elsevier: 2009; Vol. 1, pp 298-325.

174. Hazot, P.; Chapel, J. P.; Pichot, C.; Elaissari, A.; Delair, T., Preparation of poly(*N*-ethyl methacrylamide) particles via an emulsion/precipitation process: The role of the crosslinker. *J. Polym. Sci. A* **2002,** *40*, 1808-1817.

175. Hoare, T.; Pelton, R., Functional group distributions in carboxylic acid containing poly(*N*-isopropylacrylamide) microgels. *Langmuir* **2004,** *20*, 2123-2133.

176. Yuan, H. G.; Kalfas, G.; Ray, W. H., Suspension polymerization. *J. Polym. Sci. C* **1991,** *31*, 215-299.

177. Wood, C. D.; Cooper, A. I., Synthesis of macroporous polymer beads by suspension polymerization using supercritical carbon dioxide as a pressure-adjustable porogen. *Macromolecules* **2001,** *34*, 5-8.

178. Alehosseini, E.; Jafari, S. M., Micro/nano-encapsulated phase change materials (PCMs) as emerging materials for the food industry. *Trends Food Sci. Technol.* **2019,** *91*, 116-128.

179. Ko, J. A.; Park, H. J.; Hwang, S. J.; Park, J. B.; Lee, J. S., Preparation and characterization of chitosan microparticles intended for controlled drug delivery. *Int. J. Pharm.* **2002,** *249*, 165-174.

180. Fernandez, V. V. A.; Tepale, N.; Sánchez-Díaz, J. C.; Mendizábal, E.; Puig, J. E.; Soltero, J. F. A., Thermoresponsive nanostructured poly(*N*-isopropylacrylamide) hydrogels made via inverse microemulsion polymerization. *Colloid Polym. Sci.* **2006,** *284*, 387-395.

181. Lesage de la Haye, J.; Martin-Fabiani, I.; Schulz, M.; Keddie, J. L.; D'Agosto, F.; Lansalot, M., Hydrophilic macroraft-mediated emulsion polymerization: synthesis of latexes for cross-linked and surfactant-free films. *Macromolecules* **2017,** *50*, 9315-9328.

182. Zhou, C.; Chen, Y.; Huang, M.; Ling, Y.; Yang, L.; Zhao, G.; Chen, J., A new type of dual temperature sensitive triblock polymer (P(AM-co-AN)-b-PDMA-b-PNIPAM) and its self-assembly and gel behavior. *New J. Chem.* **2021,** *45*, 5925-5932.

183. Thiele, S.; Andersson, J.; Dahlin, A.; Hailes, R. L. N., Tuning the thermoresponsive behavior of surface-attached pnipam networks: varying the crosslinker content in si-ATRP. *Langmuir* **2021,** *37*, 3391-3398.

184. Semsarilar, M.; Abetz, V., Polymerizations by RAFT: Developments of the technique and its application in the synthesis of tailored (co)polymers. *Macromol. Chem. Phys.* **2021,** *222*, 2000311.

185. Yan, S.; Wu, Q.; Chang, A.; Lu, F.; Xu, H.-C.; Wu, W., Electrochemical synthesis of polymer microgels. *Polym. Chem.* **2015,** *6*, 3979-3987.

186. Vijh, A. K.; Conway, B. E., Electrode kinetic aspects of the Kolbe reaction. *Chem. Rev.* **1967,** *67*, 623-664.

187. Naga, N.; Ito, M.; Mezaki, A.; Tang, H.-C.; Chang, T.-F. M.; Sone, M.; Nageh, H.; Nakano, T., Morphology control and metallization of porous polymers synthesized by Michael addition reactions of a multi-functional acrylamide with a diamine. *Materials* **2021,** *14*, 800.

188. Zhang, K.; Lackey, M. A.; Cui, J.; Tew, G. N., Gels Based on Cyclic Polymers. *J. Am. Chem. Soc.* **2011,** *133*, 4140-4148.

189. Luo, Z.; Xue, K.; Zhang, X.; Lim, J. Y. C.; Lai, X.; Young, D. J.; Zhang, Z.-X.; Wu, Y.-L.; Loh, X. J., Thermogelling chitosan-based polymers for the treatment of oral mucosa ulcers. *Biomater. Sci.* **2020,** *8*, 1364-1379.

190. Zhang, Y.; Xie, S.; Zhang, D.; Ren, B.; Liu, Y.; Tang, L.; Chen, Q.; Yang, J.; Wu, J.; Tang, J.; Zheng, J., Thermo-responsive and shape-adaptive hydrogel actuators from fundamentals to applications. *Eng. Sci.* **2019,** *6*, 1-11.

191. Lv, X.; Tang, Y.; Tian, Q.; Wang, Y.; Ding, T., Ultra-stretchable membrane with high electrical and thermal conductivity via electrospinning and in-situ nanosilver deposition. *Compos. Sci. Technol.* **2020,** *200*, 108414.

192. Li, Y.; Yin, X.-F.; Chen, F.-R.; Yang, H.-H.; Zhuang, Z.-X.; Wang, X.-R., Synthesis of magnetic molecularly imprinted polymer nanowires using a nanoporous alumina template. *Macromolecules* **2006,** *39*, 4497-4499.

193. Jeon, S.; Han, P.; Jeong, J.; Hwang, W. S.; Hong, S. W., Highly aligned polymeric nanowire etch-mask lithography enabling the integration of graphene nanoribbon transistors. *Nanomaterials* **2021,** *11*, 33.

194. Long, J. W., Architectural design, interior decoration, and three-dimensional plumbing en route to multifunctional nanoarchitectures. *Acc. Chem. Res.* **2007,** *40*, 854-862.

195. El-Enany, G.; Lacey, M. J.; Johns, P. A.; Owen, J. R., In situ growth of polymer electrolytes on lithium ion electrode surfaces. *Electrochem. Commun.* **2009,** *11*, 2320-2323.

196. Lee, J.; Panzer, M. J.; He, Y.; Lodge, T. P.; Frisbie, C. D., Ion gel gated polymer thin-film transistors. *J. Am. Chem. Soc.* **2007,** *129*, 4532-4533.

197. Yang, Y.-H.; Bolling, L.; Haile, M.; Grunlan, J. C., Improving oxygen barrier and reducing moisture sensitivity of weak polyelectrolyte multilayer thin films with crosslinking. *RSC Adv.* **2012,** *2*, 12355-12363.

198. Tanaka, M.; Nakahata, M.; Linke, P.; Kaufmann, S., Stimuli-responsive hydrogels as a model of the dynamic cellular microenvironment. *Polym. J.* **2020,** *52*, 861-870.

199. Mello, H. J. N. P. D.; Mulato, M., Effect of aniline monomer concentration on PANI electropolymerization process and its influence for applications in chemical sensors. *Synth. Met.* **2018,** *239*, 66-70.

200. Mujahid, A.; Dickert, F. L., Surface acoustic wave (SAW) for chemical sensing applications of recognition layers. *Sensors* **2017,** *17*, 2716.

201. Wang, Y.; Liu, A.; Han, Y.; Li, T., Sensors based on conductive polymers and their composites: a review. *Polym. Int.* **2020,** *69*, 7-17.

202. Shahid, M.; Farooqi, Z. H.; Begum, R.; Arif, M.; Wu, W.; Irfan, A., Hybrid microgels for catalytic and photocatalytic removal of nitroarenes and organic dyes from aqueous medium: A review. *Crit. Rev. Anal. Chem.* **2020,** *50*, 513-537.

203. Gao, Q.; Zhang, C.; Wang, M.; Wu, Y.; Gao, C.; Zhu, P., Injectable pH-responsive poly (γ-glutamic acid)-silica hybrid hydrogels with high mechanical strength, conductivity and cytocompatibility for biomedical applications. *Polymer* **2020,** *197*, 122489.

204. Shao, Y.; Bai, H.; Wang, H.; Fei, G.; Li, L.; Zhu, Y., Magnetically sensitive and high template affinity surface imprinted polymer prepared using porous TiO2-coated magnetite-silica nanoparticles for efficient removal of tetrabromobisphenol A from polluted water. *Adv. Compos. Hybrid Mater.* **2021**.

205. Taniguchi, A.; Tamura, S.; Ikegami, T., The relationship between polymer structures on silica particles and the separation characteristics of the corresponding columns for hydrophilic interaction chromatography. *J. Chromatogr. A* **2020,** *1618*, 460837.

206. Wang, F.; Sun, Y.; Guo, X.; Li, D.; Yang, H., Preparation and graft modification of hierarchically porous ferriferrous oxide for heavy metal ions adsorption. *J. Sol-Gel Sci. Technol.* **2020,** *96*, 360-369.

207. Alemán, J. V.; Chadwick, A. V.; He, J.; Hess, M.; Horie, K.; Jones, R. G.; Kratochvíl, P.; Meisel, I.; Mita, I.; Moad, G.; Penczek, S.; Stepto, R. F. T., Definitions of terms relating to the structure and processing of sols, gels, networks, and inorganic-organic hybrid materials (IUPAC Recommendations 2007). *Pure Appl. Chem.* **2007,** *79*, 1801-1829.

208. Carter, P.; Bhattarai, N., Chapter 7 - Bioscaffolds: fabrication and performance. in *engineered biomimicry*, Lakhtakia, A.; Martín-Palma, R. J., Eds. Elsevier: Boston, 2013; pp 161-188.

209. Cuggino, J. C.; Molina, M.; Wedepohl, S.; Igarzabal, C. I. A.; Calderón, M.; Gugliotta, L. M., Responsive nanogels for application as smart carriers in endocytic pH-triggered drug delivery systems. *Eur. Polym. J.* **2016,** *78*, 14-24.

210. Vinogradov, S. V.; Bronich, T. K.; Kabanov, A. V., Nanosized cationic hydrogels for drug delivery: preparation, properties and interactions with cells. *Adv. Drug Delivery Rev.* **2002,** *54*, 135-47.

211. Spiridonov, V.; Panova, I.; Kusaia, V.; Makarova, L.; Romodina, M.; Fedyanin, A.; Pozdnyakova, N.; Shibaeva, A.; Zezin, S.; Sybachin, A.; Yaroslavov, A., Doxorubicin loaded magnetosensitive water-soluble nanogel based on NIPAM and iron (3+) containing nanoparticles. *Macromol. Symp.* **2020,** *389*, 1900072.

212. Duro-Castano, A.; Sousa-Herves, A.; Armiñán, A.; Charbonnier, D.; Arroyo-Crespo, J. J.; Wedepohl, S.; Calderón, M.; Vicent, M. J., Polyglutamic acid-based crosslinked doxorubicin nanogels as an anti-metastatic treatment for triple negative breast cancer. *J. Control. Release* **2021,** *332*, 10-20.

213. Zhou, D.; Liu, S.; Hu, Y.; Yang, S.; Zhao, B.; Zheng, K.; Zhang, Y.; He, P.; Mo, G.; Li, Y., Tumor-mediated shape-transformable nanogels with pH/redox/enzymatic-sensitivity for anticancer therapy. *J. Mater. Chem. B* **2020,** *8*, 3801-3813.

214. Clegg, J. R.; Sun, J. A.; Gu, J.; Venkataraman, A. K.; Peppas, N. A., Peptide conjugation enhances the cellular co-localization, but not endosomal escape, of modular poly(acrylamide-co-methacrylic acid) nanogels. *J. Controlled Release* **2021,** *329*, 1162-1171.

215. Keskin, D.; Zu, G.; Forson, A. M.; Tromp, L.; Sjollema, J.; van Rijn, P., Nanogels: A novel approach in antimicrobial delivery systems and antimicrobial coatings. *Bioact. Mater.* **2021,** *6*, 3634-3657.

216. Zhang, Q.; Guo, Y.; Zhu, L.; Liu, X.; Yang, J.; Li, Y.; Zhu, X.; Zhang, C., A nucleic acid nanogel dually bears siRNA and CpG motifs for synergistic tumor immunotherapy. *Biomater. Sci.* **2021,** *9*, 4755-4764.

217. Kordalivand, N.; Tondini, E.; Lau, C. Y. J.; Vermonden, T.; Mastrobattista, E.; Hennink, W. E.; Ossendorp, F.; Nostrum, C. F. v., Cationic synthetic long peptides-loaded nanogels: An efficient therapeutic vaccine formulation for induction of T-cell responses. *J. Controlled Release* **2019,** *315*, 114-125.

218. Litowczenko, J.; Gapiński, J.; Markiewicz, R.; Woźniak, A.; Wychowaniec, J. K.; Peplińska, B.; Jurga, S.; Patkowski, A., Synthesis, characterization and in vitro cytotoxicity studies of poly-*N*-isopropyl acrylamide gel nanoparticles and films. *Mater. Sci. Eng. C* **2021,** *118*, 111507.

219. Mohammadi, M.; Arabi, L.; Alibolandi, M., Doxorubicin-loaded composite nanogels for cancer treatment. *J. Controlled Release* **2020,** *328*, 171-191.

220. Sung, B.; Kim, M.-H.; Abelmann, L., Magnetic microgels and nanogels: Physical mechanisms and biomedical applications. *Bioeng. Transl. Med.* **2021,** *6*, e10190.

221. García, M. C.; Cuggino, J. C., 12 - Stimulus-responsive nanogels for drug delivery. In *Stimuli-responsive polymeric nanocarriers for drug delivery applications, Volume 1*, Makhlouf, A. S. H.; Abu-Thabit, N. Y., Eds. Woodhead Publishing: 2018; pp 321-341.

222. Zhu, X.; Sun, Y.; Chen, D.; Li, J.; Dong, X.; Wang, J.; Chen, H.; Wang, Y.; Zhang, F.; Dai, J.; Pirraco, R. P.; Guo, S.; Marques, A. P.; Reis, R. L.; Li, W., Mastocarcinoma therapy synergistically promoted by lysosome dependent apoptosis specifically evoked by 5-Fu@nanogel system with passive targeting and pH activatable dual function. *J. Controlled Release* **2017,** *254*, 107-118.

223. Siirilä, J.; Hietala, S.; Ekholm, F. S.; Tenhu, H., Glucose and maltose surface-functionalized thermoresponsive poly(n-vinylcaprolactam) nanogels. *Biomacromolecules* **2020,** *21*, 955-965.

224. Stawicki, B.; Schacher, T.; Cho, H., Nanogels as a versatile drug delivery system for brain cancer. *Gels* **2021,** *7*, 63.

225. Sana, S. S.; Arla, S. K.; Badineni, V.; Boya, V. K. N., Development of poly (acrylamide-co-diallyldimethylammoniumchloride) nanogels and study of their ability as drug delivery devices. *SN Appl. Sci.* **2019,** *1*, 1716.

226. Tarabukina, E.; Seyednov, E.; Filippov, A.; Constantin, M.; Harabagiu, V.; Fundueanu, G., Thermoresponsive properties of *N*-isopropylacrylamide with methacrylic acid copolymer in media of different acidity. *Macromol. Res.* **2017,** *25*, 680-688.

227. Cuggino, J. C.; Blanco, E. R. O.; Gugliotta, L. M.; Alvarez Igarzabal, C. I.; Calderón, M., Crossing biological barriers with nanogels to improve drug delivery performance. *J. Controlled Release* **2019,** *307*, 221-246.

228. El-Zeiny, H. M.; Abukhadra, M. R.; Sayed, O. M.; Osman, A. H. M.; Ahmed, S. A., Insight into novel β-cyclodextrin-grafted-poly (*N*-vinylcaprolactam) nanogel structures as advanced carriers for 5-fluorouracil: Equilibrium behavior and pharmacokinetic modeling. *Colloids Surf. A* **2020,** *586*, 124197.

229. Prusty, K.; Swain, S. K., Release of ciprofloxacin drugs by nano gold embedded cellulose grafted polyacrylamide hybrid nanocomposite hydrogels. *Int. J. Biol. Macromol.* **2019,** *126*, 765-775.

230. Shanks, N.; Greek, R.; Greek, J., Are animal models predictive for humans? *Philos. Ethics, Humanit. Med.* **2009**, *4*.

231. Marconi, G. D.; Porcheri, C.; Trubiani, O.; Mitsiadis, T. A., Three-dimensional culture systems for dissecting notch signalling in health and disease. *Int. J. Mol. Sci.* **2021,** *22*, 12473.

232. Bartosh, T. J.; Ylostalo, J. H.; Mohammadipoor, A.; Bazhanov, N.; Coble, K.; Claypool, K.; Lee, R. H.; Choi, H.; Prockop, D. J., Aggregation of human mesenchymal stromal cells

(MSCs) into 3D spheroids enhances their antiinflammatory properties. *Proc. Natl. Acad. Sci. USA* **2010,** *107*, 13724-9.

233. Gähwiler, B. H.; Capogna, M.; Debanne, D.; McKinney, R. A.; Thompson, S. M., Organotypic slice cultures: a technique has come of age. *Trends Neurosci.* **1997,** *20*, 471-477.

234. Lancaster, M. A.; Knoblich, J. A., Organogenesis in a dish: Modeling development and disease using organoid technologies. *Science* **2014,** *345,* 1247125-1

235. Lancaster, M. A.; Renner, M.; Martin, C.-A.; Wenzel, D.; Bicknell, L. S.; Hurles, M. E.; Homfray, T.; Penninger, J. M.; Jackson, A. P.; Knoblich, J. A., Cerebral organoids model human brain development and microcephaly. *Nature* **2013,** *501*, 373-379.

236. Eiraku, M.; Takata, N.; Ishibashi, H.; Kawada, M.; Sakakura, E.; Okuda, S.; Sekiguchi, K.; Adachi, T.; Sasai, Y., Self-organizing optic-cup morphogenesis in three-dimensional culture. *Nature* **2011,** *472*, 51-6.

237. Przyborski, S. A., Differentiation of human embryonic stem cells after transplantation in immune-deficient mice. *Stem Cells* **2005,** *23*, 1242-50.

238. Sato, T.; Vries, R. G.; Snippert, H. J.; van de Wetering, M.; Barker, N.; Stange, D. E.; van Es, J. H.; Abo, A.; Kujala, P.; Peters, P. J.; Clevers, H., Single Lgr5 stem cells build crypt-villus structures in vitro without a mesenchymal niche. *Nature* **2009,** *459*, 262-265.

239. Rustad, K. C.; Wong, V. W.; Sorkin, M.; Glotzbach, J. P.; Major, M. R.; Rajadas, J.; Longaker, M. T.; Gurtner, G. C., Enhancement of mesenchymal stem cell angiogenic capacity and stemness by a biomimetic hydrogel scaffold. *Biomaterials* **2012,** *33*, 80-90.

240. Huch, M.; Koo, B. K., Modeling mouse and human development using organoid cultures. *Development* **2015,** *142*, 3113-25.

241. Astashkina, A. I.; Mann, B. K.; Prestwich, G. D.; Grainger, D. W., A 3-D organoid kidney culture model engineered for high-throughput nephrotoxicity assays. *Biomaterials* **2012,** *33*, 4700-11.

242. Murphy, W. L.; McDevitt, T. C.; Engler, A. J., Materials as stem cell regulators. *Nat. Mater.* **2014,** *13*, 547-557.

243. Vazin, T.; Schaffer, D. V., Engineering strategies to emulate the stem cell niche. *Trends Biotechnol.* **2010,** *28*, 117-124.

244. Tan, S.; Barker, N., Engineering the niche for stem cells. *Growth Factors* **2013,** *31*, 175-184.

245. Giobbe, G. G.; Crowley, C.; Luni, C.; Campinoti, S.; Khedr, M.; Kretzschmar, K.; De Santis, M. M.; Zambaiti, E.; Michielin, F.; Meran, L.; Hu, Q.; van Son, G.; Urbani, L.; Manfredi, A.; Giomo, M.; Eaton, S.; Cacchiarelli, D.; Li, V. S. W.; Clevers, H.; Bonfanti, P.; Elvassore, N.; De Coppi, P., Extracellular matrix hydrogel derived from decellularized tissues enables endodermal organoid culture. *Nat. Commun.* **2019,** *10*, 5658.

246. Aisenbrey, E. A.; Murphy, W. L., Synthetic alternatives to Matrigel. *Nat. Rev. Mater.* **2020,** *5*, 539-551.

247. Guvendiren, M.; Burdick, J. A., Stiffening hydrogels to probe short- and long-term cellular responses to dynamic mechanics. *Nat. Commun.* **2012,** *3*.

248. Kuhlman, W.; Taniguchi, I.; Griffith, L. G.; Mayes, A. M., Interplay between PEO tether length and ligand spacing governs cell spreading on RGD-modified PMMA-g-PEO comb copolymers. *Biomacromolecules* **2007,** *8*, 3206-3213.

249. Vincent, L. G.; Choi, Y. S.; Alonso-Latorre, B.; del Álamo, J. C.; Engler, A. J., Mesenchymal stem cell durotaxis depends on substrate stiffness gradient strength. *Biotechnol. J.* **2013,** *8*, 472-484.

250. Bao, W.; Li, M.; Yang, Y.; Wan, Y.; Wang, X.; Bi, N.; Li, C., Advancements and frontiers in the high performance of natural hydrogels for cartilage tissue engineering. *Front. Chem.* **2020,** *8*.

251. Zhu, J.; Marchant, R. E., Design properties of hydrogel tissue-engineering scaffolds. *Expert Rev. Med. Devices* **2011,** *8*, 607-626.

252. Echeverria, C.; Fernandes, S. N.; Godinho, M. H.; Borges, J. P.; Soares, P. I. P., Functional stimuli-responsive gels: hydrogels and microgels. *Gels* **2018,** *4*, 54.

253. Roach, P.; Eglin, D.; Rohde, K.; Perry, C. C., Modern biomaterials: a review—bulk properties and implications of surface modifications. *J. Mater. Sci. Mater. Med.* **2007,** *18*, 1263-1277.

254. Kurimoto, R.; Kanie, K.; Idota, N.; Hara, M.; Nagano, S.; Tsukahara, T.; Narita, Y.; Honda, H.; Naito, M.; Ebara, M.; Kato, R., Combinational effect of cell adhesion biomolecules and their immobilized polymer property to enhance cell-selective adhesion. *Int. J. Polym. Sci.* **2016,** *2016*, 2090985.

255. Cai, S.; Wu, C.; Yang, W.; Liang, W.; Yu, H.; Liu, L., Recent advance in surface modification for regulating cell adhesion and behaviors. *Nanotechnol. Rev.* **2020,** *9*, 971-989.

256. Murphy, C. M.; Matsiko, A.; Haugh, M. G.; Gleeson, J. P.; O'Brien, F. J., Mesenchymal stem cell fate is regulated by the composition and mechanical properties of collagen–glycosaminoglycan scaffolds. *J. Mech. Behav. Biomed. Mater.* **2012,** *11*, 53-62.

257. Zhang, Z.; Ni, J.; Chen, L.; Yu, L.; Xu, J.; Ding, J., Encapsulation of cell-adhesive RGD peptides into a polymeric physical hydrogel to prevent postoperative tissue adhesion. *J. Biomed. Mater. Res. B* **2012,** *100B*, 1599-1609.

258. Crosslinking and mechanical properties significantly influence cell attachment, proliferation, and migration within collagen glycosaminoglycan scaffolds. *Tissue Eng. B* **2011,** *17*, 1201-1208.

259. Xu, X.; Liu, Y.; Fu, W.; Yao, M.; Ding, Z.; Xuan, J.; Li, D.; Wang, S.; Xia, Y.; Cao, M., Poly(*N*-isopropylacrylamide)-based thermoresponsive composite hydrogels for biomedical applications. *Polymers* **2020,** *12*, 580.

260. Rana, M. M.; Rajeev, A.; Natale, G.; De la Hoz Siegler, H., Effects of synthesis-solvent polarity on the physicochemical and rheological properties of poly(*N*-isopropylacrylamide) (PNIPAm) hydrogels. *J. Mater. Res. Technol.* **2021,** *13*, 769-786.

261. Francius, G.; Polyakov, P.; Merlin, J.; Abe, Y.; Ghigo, J.-M.; Merlin, C.; Beloin, C.; Duval, J. F. L., Bacterial surface appendages strongly impact nanomechanical and electrokinetic Properties of *Escherichia coli* cells Subjected to osmotic stress. *PLoS ONE* **2011,** *6*, e20066.

262. Ross-Murphy, S. B., Dynamic light scattering. B. J. Berne and R. Pecora, John Wiley, New York, 1976, pp. 376. Price £16.50. *Br. Polym. J.* **1977,** *9*, 177-177.

263. Wyatt, P. J., Differential light scattering and the measurement of molecules and nanoparticles: A review. *Anal. Chim. Acta* **2021,** *7-8*, 100070.

264. Bloomfield, V. A., Quasi-elastic light scattering applications in biochemistry and biology. *Annu. Rev. Biophys.* **1981,** *10*, 421-450.

265. Rochas, C.; Geissler, E., Measurement of dynamic light scattering intensity in gels. *Macromolecules* **2014,** *47*, 8012-8017.

266. Brabazon, D.; Raffer, A., Chapter 3-Advanced characterization techniques for nanostructures. in *emerging nanotechnologies for manufacturing*, Ahmed, W.; Jackson, M. J., Eds. William Andrew Publishing: Boston, 2010; pp 59-91.

267. Went, M.; Vos, M.; Elliman, R., Electron inelastic mean free path in solids as determined by electron Rutherford back-scattering. *J. Electron Spectrosc. Relat. Phenom.* **2007,** *156*, 387-392.

268. Zhou, W.; Apkarian, R.; Wang, Z. L.; Joy, D., Fundamentals of scanning electron microscopy (SEM). In *Scanning microscopy for nanotechnology*, Springer: 2006; pp 1-40.

269. Fay, F.; Linossier, I.; Langlois, V.; Haras, D.; Vallee-Rehel, K., SEM and EDX analysis: Two powerful techniques for the study of antifouling paints. *Prog. Org. Coat.* **2005,** *54*, 216-223.

270. Binnig, G.; Quate, C. F.; Gerber, C., Atomic Force Microscope. *Phys. Rev. Lett.* **1986,** *56*, 930-933.

271. Sudarsan, V., Chapter 4 - Materials for hostile chemical environments. In *materials under extreme conditions*, Tyagi, A. K.; Banerjee, S., Eds. Elsevier: Amsterdam, 2017; pp 129-158.

272. Redondo-Morata, L. In *High-speed atomic force microscopy probing the dynamics of biomolecules*, *Biofisica* **2018,** *10,* 15-21.

273. Schreiber, S. L.; Kotz, J. D.; Li, M.; Aubé, J.; Austin, C. P.; Reed, J. C.; Rosen, H.; White, E. L.; Sklar, L. A.; Lindsley, C. W.; Alexander, B. R.; Bittker, J. A.; Clemons, P. A.; de Souza, A.; Foley, M. A.; Palmer, M.; Shamji, A. F.; Wawer, M. J.; McManus, O.; Wu, M.; Zou, B.; Yu, H.; Golden, J. E.; Schoenen, F. J.; Simeonov, A.; Jadhav, A.; Jackson, M. R.; Pinkerton, A. B.; Chung, T. D.; Griffin, P. R.; Cravatt, B. F.; Hodder, P. S.; Roush, W. R.; Roberts, E.; Chung, D. H.; Jonsson, C. B.; Noah, J. W.; Severson, W. E.; Ananthan, S.; Edwards, B.; Oprea, T. I.; Conn, P. J.; Hopkins, C. R.; Wood, M. R.; Stauffer, S. R.; Emmitte, K. A., Advancing biological understanding and therapeutics discovery with small-molecule probes. *Cell* **2015,** *161*, 1252-65.

274. Kissinger, P. T.; Heineman, W. R., Cyclic voltammetry. *ACS J. Chem. Educ.* **1983,** *60*, 702.

275. Lasia, A., Electrochemical impedance spectroscopy and its applications. In *Modern aspects of electrochemistry*, Conway, B. E.; Bockris, J. O. M.; White, R. E., Eds. Springer US: Boston, MA, 2002; pp 143-248.

276. Chang, B.-Y.; Park, S.-M., Electrochemical impedance spectroscopy. *Annu. Rev. Anal. Chem.* **2010,** *3*, 207-229.

277. Randles, J. E. B., Kinetics of rapid electrode reactions. *Discuss. Faraday Soc.* **1947,** *1*, 11-19.

278. Berggren, C.; Bjarnason, B.; Johansson, G., Capacitive biosensors. *Electroanalysis* **2001,** *13*, 173-180.

279. Marć, M.; Kupka, T.; Wieczorek, P. P.; Namieśnik, J., Computational modeling of molecularly imprinted polymers as a green approach to the development of novel analytical sorbents. *TrAC-Trends Anal. Chem.* **2018,** *98*, 64-78.

280. Abdel Ghani, N. T.; Mohamed El Nashar, R.; Abdel-Haleem, F. M.; Madbouly, A., Computational design, synthesis and application of a new selective molecularly imprinted polymer for electrochemical detection. *Electroanalysis* **2016,** *28*, 1530-1538.

281. Nicholls, I. A.; Andersson, H. S.; Charlton, C.; Henschel, H.; Karlsson, B. C. G.; Karlsson, J. G.; O'Mahony, J.; Rosengren, A. M.; Rosengren, K. J.; Wikman, S., Theoretical and computational strategies for rational molecularly imprinted polymer design. *Biosens. Bioelectron.* **2009,** *25*, 543-552.

282. Frisch, M. J.; Trucks, G. W.; Schlegel, H. B.; Scuseria, G. E.; Robb, M. A.; Cheeseman, J. R.; Scalmani, G.; Barone, V.; Petersson, G. A.; Nakatsuji, H.; Li, X.; Caricato, M.; Marenich, A. V.; Bloino, J.; Janesko, B. G.; Gomperts, R.; Mennucci, B.; Hratchian, H. P.; Ortiz, J. V.; Izmaylov, A. F.; Sonnenberg, J. L.; Williams-Young, D.; Ding, F.;

Lipparini, F.; Egidi, F.; Goings, J.; Peng, B.; Petrone, A.; Henderson, T.; Ranasinghe, D.; Zakrzewski, V. G.; Gao, J.; Rega, N.; Zheng, G.; Liang, W.; Hada, M.; Ehara, M.; Toyota, K.; Fukuda, R.; Hasegawa, J.; Ishida, M.; Nakajima, T.; Honda, Y.; Kitao, O.; Nakai, H.; Vreven, T.; Throssell, K.; Montgomery, J. A., Jr., J.E.P.; Ogliaro, F.; Bearpark, M. J.; Heyd, J. J.; Brothers, E. N.; Kudin, K. N.; Staroverov, V. N.; Keith, T. A.; Kobayashi, R.; Normand, J.; Raghavachari, K.; Rendell, A. P.; Burant, J. C.; Iyengar, S. S.; Tomasi, J.; Cossi, M.; Millam, J. M.; Klene, M.; Adamo, C.; Cammi, R.; Ochterski, J. W.; Martin, R. L.; Morokuma, K.; Farkas, O.; Foresman, J. B.; Fox, D. J., *Gaussian 16, Revision C.01. Gaussian, Inc.,* Wallingford CT. **2016**.

283. Lach, P.; Sharma, P. S.; Golebiewska, K.; Cieplak, M.; D'Souza, F.; Kutner, W., Molecularly imprinted polymer chemosensor for selective determination of an *n*-nitroso-l-proline food toxin. *Chem. Eur. J.* **2017,** *23*, 1942-1949.

284. Polsky, R.; Harper, J. C.; Wheeler, D. R.; Arango, D. C.; Brozik, S. M., Electrically addressable cell immobilization using phenylboronic acid diazonium salts. *Angew. Chem.* **2008,** *120*, 2671-2674.

285. Aytaç, S.; Kuralay, F.; Boyacı, İ. H.; Unaleroglu, C., A novel polypyrrole–phenylboronic acid based electrochemical saccharide sensor. *Sens. Actuators B* **2011,** *160*, 405-411.

286. Rick, J.; Chou, T.-C., Using protein templates to direct the formation of thin-film polymer surfaces. *Biosens. Bioelectron.* **2006,** *22*, 544-549.

287. Ren, L.; Liu, Z.; Liu, Y.; Dou, P.; Chen, H. Y., Ring-opening polymerization with synergistic co-monomers: access to a boronate-functionalized polymeric monolith for the specific capture of cis-diol-containing biomolecules under neutral conditions. *Angew. Chem.* **2009,** *121*, 6832-6835.

288. Golabi, M.; Kuralay, F.; Jager, E. W. H.; Beni, V.; Turner, A. P. F., Electrochemical bacterial detection using poly(3-aminophenylboronic acid)-based imprinted polymer. *Biosens. Bioelectron.* **2017,** *93*, 87-93.

289. Andreyev, E. A.; Komkova, M. A.; Nikitina, V. N.; Zaryanov, N. V.; Voronin, O. G.; Karyakina, E. E.; Yatsimirsky, A. K.; Karyakin, A. A., Reagentless polyol detection by conductivity increase in the course of self-doping of boronate-substituted polyaniline. *Anal. Chem.* **2014,** *86*, 11690-11695.

290. MacDiarmid, A. G.; Epstein, A. J., Polyanilines: a novel class of conducting polymers. *Faraday Discuss.* **1989,** *88*, 317-332.

291. Yan, J.; Springsteen, G.; Deeter, S.; Wang, B., The relationship among pKa, pH, and binding constants in the interactions between boronic acids and diols—it is not as simple as it appears. *Tetrahedron* **2004,** *60*, 11205-11209.

292. Nikitina, V. N.; Zaryanov, N. V.; Kochetkov, I. R.; Karyakina, E. E.; Yatsimirsky, A. K.; Karyakin, A. A., Molecular imprinting of boronate functionalized polyaniline for enzyme-free selective detection of saccharides and hydroxy acids. *Sens. Actuators B* **2017,** *246*, 428–433.

293. Matsushita, M.; Kuramitz, H.; Tanaka, S., Electrochemical oxidation for low concentration of aniline in neutral pH medium: Application to the removal of aniline based on the electrochemical polymerization on a carbon fiber. *Environ. Sci. Technol.* **2005,** *39*, 3805–3810.

294. Golabi, M.; Kuralay, F.; Jager, E. W. H.; Beni, V.; Turner, A. P. F., Electrochemical bacterial detection using poly(3-aminophenylboronic acid)-based imprinted polymer. *Biosens. Bioelectron.* **2017,** *93*, 87-93.

295. Wu, J.; Wang, R.; Lu, Y.; Jia, M.; Yan, J.; Bian, X., Facile preparation of a bacteria imprinted artificial receptor for highly selective bacterial recognition and label-free impedimetric detection. *Anal. Chem.* **2019,** *91*, 1027-1033.

296. Cheng, Z.; Wang, E.; Yang, X., Capacitive detection of glucose using molecularly imprinted polymers. *Biosens. Bioelectron.* **2001,** *16*, 179-185.

297. Malev, V. V.; Kondratiev, V. V., Charge transfer processes in conducting polymer films. *Russ. Chem. Rev.* **2006,** *75*, 147-160.

298. Erridge, C.; Bennett-Guerrero, E.; Poxton, I. R., Structure and function of lipopolysaccharides. *Microb. Infect.* **2002,** *4*, 837–851.

299. Heinrichs, D. E.; Yethon, J. A.; Whitfield, C., Molecular basis for structural diversity in the core regions of the lipopolysaccharides of *Escherichia coli* and *Salmonella enterica*. *Mol. Microbiol.* **1998,** *30*, 221-232.

300. Caffrey, P.; Owen, P., Purification and *N*-terminal sequence of the a subunit of antigen 43, a unique protein complex associated with the outer membrane of *Escherichia coli*. *J. Bacteriol.* **1989,** *171*, 3634-3640.

301. Henderson, I. R.; Meehan, M.; Owen, P., Antigen 43, a phase-variable bipartite outer membrane protein, determines colony morphology and autoaggregation in *Escherichia coli* K-12. *FEMS Microbiol. Lett.* **1997,** *149*, 115-120.

302. Heras, B.; Totsika, M.; Peters, K. M.; Paxman, J. J.; Gee, C. L.; Jarrott, R. J.; Perugini, M. A.; Whitten, A. E.; Schembri, M. A., The antigen 43 structure reveals a molecular Velcro-like mechanism of autotransporter-mediated bacterial clumping. *Proc. Natl. Acad. Sci. USA* **2014,** *111*, 457–462.

303. Jacquot, A.; Sakamoto, C.; Razafitianamarahavo, A.; Caillet, C.; Merlin, J.; Fahs, A.; Ghigo, J.-M.; Duval, J. F. L.; Beloinc, C.; Francius, G., The dynamics and pH-dependence of Ag43 adhesins' self-association probed by atomic force spectroscopy. *Nanoscale* **2014,** *6*, 12665-12681.

304. Aprikian, P.; Interlandi, G.; Kidd, B. A.; Trong, I. L.; Tchesnokova, V.; Yakovenko, O.; Whitfield, M. J.; Bullitt, E.; Stenkamp, R. E.; Thomas, W. E.; Sokurenko, E. V., The bacterial fimbrial tip acts as a mechanical force sensor. *PLoS Biol.* **2011,** *9*, e1000617.

305. Jacquot, A.; Sakamoto, C.; Razafitianamaharavo, A.; Caillet, C.; Merlin, J.; Fahs, A.; Ghigo, G.; Beloin, C.; Duval, J. F. L.; Francius, G., Dynamic modulation of fimbrial extension and fimH-mannose binding force on live bacteria under pH changes: A molecular atomic force microscopy analysis. *J. Biomed. Nanotechnol.* **2014,** *10*, 3361-3372.

306. Gao, L.; Lu, X.; Liu, H.; Li, J.; Li, W.; Song, R.; Wang, R.; Zhang, D.; Zhu, J., Mediation of extracellular polymeric substances in microbial reduction of hematite by *Shewanella Oneidensis* MR-1. *Front. Microbiol.* **2019,** *10*, 575.

307. Subramanian, S. B.; Yan, S.; Tyagi, R. D.; Surampalli, R. Y., Extracellular polymeric substances (EPS) producing bacterial strains of municipal wastewater sludge: Isolation, molecular identification, EPS characterization and performance for sludge settling and dewatering. *Water Res.* **2010,** *44*, 2253-2266.

308. Lawrence, J. R.; Swerhone, G. D. W.; Kuhlicke, U.; Neu, T. R., In situ evidence for metabolic and chemical microdomains in the structured polymer matrix of bacterial microcolonies. *FEMS Microbiol. Ecol.* **2016,** *92*, 1-12.

309. Sonohara, R.; Muramatsu, N.; Ohshima, H.; Kondo, T., Difference in surface properties between *Escherichia coli* and *Staphylococcus aureus* as revealed by electrophoretic mobility measurements. *Biophys. Chem.* **1995,** *S5*, 273-277.

310. Gaboriaud, F.; Gee, M. L.; Strugnell, R.; Duval, J. F. L., Coupled electrostatic, hydrodynamic, and mechanical properties of bacterial interfaces in aqueous media. *Langmuir* **2008,** *24*, 10988-10995.

311. Ederer, J.; Janos, P.; Ecorchard, P.; Tolasz, J.; Stengl, V.; Benes, H.; Perchaczc, M.; Pop-Georgievskid, O., Determination of amino groups on functionalized graphene oxide for

polyurethane nanomaterials: XPS quantitation vs. functional speciation. *RSC Adv.* **2017,** *7*, 12464-12473.

312. Kehrer, M.; Duchoslav, J.; Hinterreiter, A.; Cobet, M.; Mehic, A.; Stehrer, T.; Stifter, D., XPS investigation on the reactivity of surface imine groups with TFAA. *Plasma Process. Polym.* **2019,** *16*, e1800160.

313. Kaniewska, K.; Karbarz, M.; Stojek, Z., Electrochemical attachment of thermo- and pH sensitive interpenetrating-polymers-network hydrogel to conducting surface. *Electrochim. Acta* **2015,** *179*, 372-378.

314. Bonham, J. A.; Faers, M. A.; Duijneveldt, J. S. v., Non-aqueous microgel particles: synthesis, properties and applications. *Soft Matter* **2014,** *10*, 9384-9398.

315. Ribeiro, C. A.; Martins, M. V. S.; Bressiani, A. H.; Bressiani, J. C.; Leyva, M. E.; Queiroz, A. A. A., Electrochemical preparation and characterization of PNIPAM-HAp Scaffolds for bone tissue engineering. *Mater. Sci. Eng. C* **2017,** *81*, 156-166.

316. Ise, T.; Nagaoka, K.; Osa, M.; Yoshizaki, T., Cloud points in aqueous solutions of poly(*N*-isopropylacrylamide) synthesized by aqueous redox polymerization. *Polymer J.* **2011,** *43*, 164-170.

317. Downey, J. S.; Frank, R. S.; Li, W.-H.; Stöver, H. D. H., growth mechanism of poly(divinylbenzene) microspheres in precipitation polymerization. *Macromolecules* **2004,** *37*, 9746–9752.

318. Bai, F.; Yang, X.; Huang, W., Synthesis of narrow or monodisperse poly(divinylbenzene) microspheres by distillation−precipitation polymerization. *Macromolecules* **2004,** *37*, 9746-9752.

319. Plamper, F. A.; Richtering, W., Functional microgels and microgel systems. *Acc. Chem. Res.* **2017,** *50*, 131-140.

320. Diez-Pena, E.; Quijada-Garrido, I.; Frutos, P.; Barrales-Rienda, J. M., Thermal properties of cross-linked poly(*N*-isopropylacrylamide)[P(*N*-iPAAm)], poly(methacrylic acid) [P(MAA)], their random copolymers [P(*N*-iPAAm-co-MAA)], and sequential interpenetrating polymer networks (IPNs). *Macromolecules* **2002,** *35*, 2667-2675.

321. Holley, D. W.; Ruppel, M.; Mays, J. W.; Urban, V. S.; D.Baskaran, Polystyrene nanoparticles with tunable interfaces and softness. *Polymer* **2014,** *55*, 58-65.

322. Conley, G. M.; Aebischer, P.; Nöjd, S.; Schurtenberger, P.; Scheffold, F., Jamming and overpacking fuzzy microgels: deformation, interpenetration, and compression. *Sci. Adv.* **2017,** *3*, e1700969.

323. Pan, Y. V.; Wesley, R. A.; Luginbuhl, R.; Denton, D. D.; Ratner, B. D., Plasma polymerized *N*-isopropylacrylamide: synthesis and characterization of a smart thermally responsive coating. *Biomacromolecules* **2001,** *2*, 32-36.

324. Chung, P.-W.; Kumar, R.; Pruski, M.; Lin, V. S.-Y., Temperature responsive solution partition of organic-inorganic hybrid poly(*N*-isopropylacrylamide)-coated mesoporous silica nanospheres. *Adv. Funct. Mater.* **2008,** *18*, 1390-1398.

325. Gao, X.; Cao, Y.; Song, X.; Zhang, Z.; Xiao, C.; He, C.; Chen, X., pH- and Thermo-responsive poly(*N*-isopropylacrylamide-co-acrylic acid derivative) copolymers and hydrogels with LCST dependent on pH and alkyl side groups. *J. Mater. Chem. B* **2013,** *1*, 5578-5587.

326. Schilli, C. M.; Zhang, M.; Rizzardo, E.; Thang, S. H.; Chong, Y. K.; Edwards, K.; Karlsson, G.; Müller, A. H. E., A new double-responsive block copolymer synthesized via RAFT polymerization: Poly(*N*-isopropylacrylamide)-block-poly(acrylic acid). *Macromolecules* **2004,** *37*, 7861-7866.

327. Hong, C.-Y.; Li, X.; Pan, C.-Y., Smart core-shell nanostructure with a mesoporous core and a stimuli-responsive nanoshell synthesized via surface reversible addition-fragmentation chain transfer polymerization. *J. Phys. Chem. C* **2008,** *112*, 15320–15324.

328. Yang, Y.; Yan, X.; Cui, Y.; He, Q.; Li, D.; Wang, A.; Fei, J.; Li, J., Preparation of polymer-coated mesoporous silica nanoparticles used for cellular imaging by a ''graft-from'' method. *J. Mater. Chem.* **2008,** *18*, 5731-5737.

329. Yang, J.; Shen, D.; Zhou, L.; Li, W.; Li, X.; Yao, C.; Wang, R.; El-Toni, A. M.; Zhang, F.; Zhao, D., Spatially confined fabrication of core-shell gold nanocages@mesoporous silica for near-infrared controlled photothermal drug Release. *Chem. Mater.* **2013,** *25*, 3030-3037.

330. Allegretto, J. A.; Giussi, J. M.; Moya, S. E.; Azzaroni, O.; Rafti, M., Synthesis and characterization of thermoresponsive ZIF-8@PNIPAm-co-MAA microgel composites with enhanced performance as an adsorption/release platform. *RSC Adv.* **2020,** *10*, 2453-2461

331. Pourjavadi, A.; Kohestanian, M.; Streb, C., pH and thermal dual-responsive poly(NIPAM-co-GMA)-coated magnetic nanoparticles via surface-initiated RAFT polymerization for controlled drug delivery *Mater. Sci. Eng. C* **2020,** *108*, 110418.

332. Omer, M.; Haider, S.; Park, S.-Y., A novel route for the preparation of thermally sensitive core-shell magnetic nanoparticles. *Polymer* **2011,** *52*, 91-97.

333. Chang, B.; Chen, D.; Wang, Y.; Chen, Y.; Jiao, Y.; Sha, X.; Yang, W., Bioresponsive controlled drug release based on mesoporous silica nanoparticles coated with reductively sheddable polymer shell. *Chem. Mater.* **2013,** *25*, 574-585.

334. Crassous, J. J.; Mihut, A. M.; Dietsch, H.; Pravaz, O.; Ackermann-Hirschi, L.; Hirtc, A. M.; Schurtenbergera, P., Advanced multiresponsive comploids: from design to possible applications. *Nanoscale* **2014,** *6*, 8726-8735.

335. Baeza, A.; Guisasola, E.; Ruiz-Hernández, E.; Vallet-Regí, M., Magnetically triggered multidrug release by hybrid mesoporous silica nanoparticles. *Chem. Mater.* **2012,** *24*, 517-524.

336. Yasmeen, N.; Kalecki, J.; Borowicz, P.; Kutner, W.; Sharma, P. S., Electrochemically initiated synthesis of polyacrylamide microgels and core-shell particles. *ACS Appl. Polym. Mater.* **2022,** *4*, 452-462.

337. Becker, H.; Vogel, H., The role of hydroquinone monomethyl ether in the stabilization of acrylic acid. *Chem. Eng. Technol.* **2006,** *29*, 1227-1231.

338. Chavda, H.; Patel, C., Effect of crosslinker concentration on characteristics of superporous hydrogel. *Int. J. Pharm. Investig.* **2011,** *1*, 17-21.

339. Yin, X.; Hoffman, A. S.; Stayton, P. S., Poly(N-isopropylacrylamide-co-propylacrylic acid) copolymers that respond sharply to temperature and pH. *Biomacromolecules* **2006,** *7*, 1381–1385.

340. Wood, K. M.; Stone, G. M.; Peppas, N. A., Wheat germ agglutinin functionalized complexation hydrogels for oral insulin delivery. *Biomacromolecules* **2008,** *9*, 1293–1298.

341. Barz, M.; Tarantola, M.; Fischer, K.; Schmidt, M.; Luxenhofer, R.; Janshoff, A.; Theato, P.; Zentel, R., From defined reactive diblock copolymers to functional HPMA-based Self-assembled nanoaggregates. *Biomacromolecules* **2008,** *9*, 3114-3118.

342. Kamei, S.; Kopecek, J., Prolonged blood circulation in rats of nanospheres surface-modified with semitelechelic poly[N-(2-hydroxypropyl)methacrylamide]. *Pharm. Res.* **1995,** *12*, 663-668.